CHROMIUM-FREE CONVERSION COATING OF ALUMINIUM-COPPER ALLOYS

A thesis submitted to The University of Manchester for the degree of Doctor of Philosophy
in the Faculty of Engineering and Physical Sciences

2010

FAITH GEORGE

SCHOOL OF MATERIALS

CONTENTS

Word Count = 76,640

LIST OF TABLES

LIST OF FIGURES

ABSTRACT

Aluminium alloys are frequently pre-treated by a conversion coating before application of an organic coating in order to improve the corrosion resistance and adhesive properties of the surface and the corrosion resistance provided by the system. Chromate-containing conversion coatings are commonly used for this purpose. However, legislation limits future use of hexavalent chromium compounds due to their toxic and carcinogenic nature. Therefore, alternative, so-called chromium-free conversion coatings are being developed that are more environmentally-compliant.

The purpose of the present work has therefore been to contribute to a better understanding of how the aluminium substrate affects the formation and properties of conversion coatings for adhesive bonding. In particular, a chrome-free zirconium-based conversion treatment process has been investigated as a possible replacement for conventional chromate conversion treatment. The influence of the conversion time on the thickness of the formed layer on pure aluminium was investigated using complementary surface analytical techniques. The conversion time was varied between 30 and 600 seconds.

In this study, the structure and composition of zirconium-based chromium-free conversion coatings on magnetron sputtered superpure aluminium and a range of aluminium-copper alloys were characterised as a function of immersion time in the aqueous conversion bath to understand the mechanism of coating formation and protection. However, the presence of copper significantly influences the coating development and ultimately the performance of the conversion coatings formed on binary copper-containing aluminium alloys.

The morphology and composition of the coatings have been probed using transmission electron microscopy, Rutherford backscattering spectroscopy and glow discharge optical emission spectroscopy, with loss of substrate through growth of the conversion coating also quantified. A comparison of the RBS spectra obtained for the superpure aluminium specimens after different immersion times revealed that zirconium (Zr) and oxygen (O) peaks were wider for longer immersion times, indicating thickening of the coating with increased immersion times. Thus, increasing the immersion time resulted in an increase in coating thickness but little change in coating composition occurred as determined by the RBS RUMP simulations. Alloying decreases the coating thickness, as well as metal consumption.

Here, aspects of the corrosion behaviour of superpure aluminium and aluminium-copper alloys were also considered using electronoptical, electrochemical and surface analytical probing. The influence that short and prolonged treatment times exert on the performances of such conversion coating is discussed. The conversion coating formed after 60 s and 180 s of immersion in the zirconium-based conversion coating bath provide good corrosion resistance which can be attributed to the high stability of the compounds that constitute the surface oxide layer, and good adhesion properties.

DECLARATION

No portion of the work referred to in the thesis has been submitted in support of an application for another degree or qualification of this or any other university or other institute of learning.

COPYRIGHT STATEMENT

i. The author of this thesis (including any appendices and/or schedules to this thesis) owns certain copyright or related rights in it (the "Copyright") and she has given The University of Manchester certain rights to use such Copyright, including for administrative purposes.

ii. Copies of this thesis, either in full or in extracts and whether in hard or electronic copy, may be made **only** in accordance with the Copyright, Designs and Patents Act 1988 (as amended) and regulations issued under it or, where appropriate, in accordance with licensing agreements which the University has from time to time. This page must form part of any such copies made.

iii. The ownership of certain Copyright, patents, designs, trade marks and other intellectual property (the "Intellectual Property") and any reproductions of copyright works in the thesis, for example graphs and tables ("Reproductions"), which may be described in this thesis, may not be owned by the author and may be owned by third parties. Such Intellectual Property and Reproductions cannot and must not be made available for use without the prior written permission of the owner(s) of the relevant Intellectual Property and/or Reproductions.

iv. Further information on the conditions under which disclosure, publication and commercialisation of this thesis, the Copyright and any Intellectual Property and/or Reproductions described in it may take place is available in the University IP Policy (see http://www.campus.manchester.ac.uk/medialibrary/policies/intellectual-property.pdf), in any relevant Thesis restriction declarations deposited in the University Library, The University Library's regulations (see http://www.manchester.ac.uk/library/aboutus/regulations) and in The University's policy on presentation of Theses.

DEDICATION

To my ever loving and wonderful family, I couldn't have done it without you.

ACKNOWLEDGEMENTS

I would like to express my heartfelt thanks and gratitude to my supervisor, Professor George Thompson for his support, excellent advice, inspiring encouragement and guidance over the past four years. He has constantly inspired me and given me encouragement throughout the course of this research work. I am deeply indebted to him and without his help and guidance this work would not have been possible. I would also like to acknowledge and thank Professor Peter Skeldon for his supervision, kind support and helpful suggestions on my research.

I also wish to thank Dr Yanwen Liu who I have had many useful and intriguing discussions with during the early stages of the research. I wish to acknowledge Dr Xiaorong Zhou for his assistance with the filiform corrosion tests. My thanks also go to Judith Shackleton and Gary Harrison for their kind assistance with the XRD technique and processing of the data. Administrative help from Sandra Kershaw is also acknowledged. Furthermore, thanks to everyone at the Corrosion and Protection Centre for making these four years a pleasant experience. I treasure this priceless experience here and will always remember that I am from the Corrosion and Protection Centre.

I would like to express my heartfelt thanks and love to my parents Mr and Mrs Omowaiye and my siblings for their immense love and support. In addition, I really appreciate all the kind assistance from those who deserve mention but are not named here. To the friends who supported and encouraged me in my trying times, I would like to say a big thank you.

My most sincere thanks go to my best friend and love, Friday George. Without his support and love, this work would not have been completed.

My greatest thanks goes to Jehovah God for his loving kindness.

CHAPTER 1

1 INTRODUCTION

Aluminium and its alloys are considered to be the most versatile engineering materials across a broad range of applications [1-15]. Aluminium is a key component in so many aspects of our life. Its unique combination of properties makes it ideal for an almost endless range of applications and an essential part of modern living. Although pure aluminium is too soft to be used as a heavy duty material for large structures, it possesses excellent corrosion resistance that is attributed to the formation of a highly protective barrier oxide film on the bare metal surface almost immediately in a wide variety of environments.

High strength aluminium alloys can be produced by addition of appropriate alloying elements, such as copper, magnesium and zinc and by suitable heat treatment procedures. Due to their lightness, strength, stiffness as well as corrosion resistance, electrical conductivity, high ductility and non-toxic properties, interest in the application of these alloys for specific engineering purposes is growing rapidly in a wide range of industries. The combination of lightness, strength and workability makes aluminium the ideal material for mass-produced commercial aircraft. Alloys used typically for aerospace applications include the damage tolerant AA2xxx-series and the high strength AA7xxx-series [16]. Strong aluminium alloys take the extraordinary pressures and stresses involved in high altitude flying; wafer-thin aluminium panels keep the cold out and the air in [17]. Many internal fittings, like the seating on planes, are made from aluminium to save weight and therefore fuel consumption, reduce emissions and increase the aircraft's payload [6, 18]. As environmental issues such as global warming have been spotlighted in recent years, aluminium alloys have begun to be used in automobile body panels to reduce overall body weight, thereby improving fuel economy and running performance [19]. It has been calculated that during the life of a single vehicle, there will be a saving of 6 to 12 times the energy it took to produce the primary aluminium metal used to construct the car [20]. Every tonne of aluminium that is used in place of a tonne of heavier materials will save 20 tonnes of carbon dioxide over the lifetime of the vehicle [20].

Copper is one of the principal alloying elements of aluminium alloys [21]. The Al-Cu alloys offer an excellent ratio of weight to mechanical properties and, for this reason, they are commonly employed in the aeronautical industry for numerous structural components [22]. However, copper reduces the corrosion resistance of aluminium [21-24] more than any of the common alloying elements. This alloying element, added to improve the mechanical properties of commercial copper-containing aluminium alloys, can be precipitated as second-phase particles or inclusion. Second phase particles or inclusions are usually noble with respect to the aluminium matrix, thereby facilitating corrosion, or enrich the corrosion product thereby possibly inhibiting the corrosion rate [8, 25-27].

Studies of the corrosion and stability of high strength age-hardened aluminium alloys, such as AA2xxx and AA7xxx series alloys, are of considerable interest because of their wide usage as structural materials in aeronautical industry. Many of these alloys have increased corrosion susceptibilities compared with pure aluminium [2, 28]. AA2xxx series of aluminium alloys are among the most corrosion prone commercial alloys in common use [25]. The inhomogeneous distribution of copper in the alloy microstructure has been shown to be a major cause for the low resistance to pitting and stress corrosion cracking [25]. Specifically, the concentration of copper in second-phase particles and the local depletion of copper in certain microstructural regions establish local galvanic cells resulting in localised attack [29, 30], especially in media that contain chlorides, due principally to the heterogeneous microstructure of the alloy [22]. It is well known that Cu-containing species, such as intermetallics on aluminium substrates can promote pitting at adjacent sites [31]. Bohni and Uhlig [32], observed that the presence of just a few ppm of Cu^{2+} ions can raise the corrosion potential of Al in 0.1 M NaCl to the pitting potential (E_p). Hence, with aluminium alloys, second phase materials are important in corrosion and protection processes, since the surface composition is altered locally, thus, differing electrochemical responses are expected across the surface [33-38].

Furthermore, the effect of alloy content [32, 39], electrolyte [40] and heat treatment [41] on pitting and repassivation of aluminium alloys in halide media have been reported. Alloying elements, impurities and age-hardening treatments can result in the formation of intermetallic precipitates in the alloy, which when exposed to a corrosive environment lead to highly localised attack, such as pitting, stress corrosion cracking

and corrosion fatigue. Aggressive anions, such as the halides, induce breakdown of the protective passive film [42, 43] and can result in catastrophic failure of the material. Several studies [29, 39, 40, 44] have been devoted to investigating the role of chloride ions in the breakdown of the passive film, repassivation and initiation of localised corrosion of aluminium and high-strength aluminium alloys. It has been suggested that pits can be initiated in aluminium even in the complete absence of Cl^- when copper ions are available [13, 45].

Since the AA2xxx series of aluminium alloys has the highest copper content as a group, AA2024 aluminium alloy, which is one of the most widely used high strength aluminium-based alloys in aircraft, provides a ready source for copper-containing inclusions in the protective oxide surface film[1]. Therefore, the present extensive use of this alloy and similar aluminium alloys with relatively high copper content has serious consequences for the integrity of aircraft structural materials, when the operational service life of aircraft is extended far beyond its design life [1].

For many years, the treatment of aluminium and its alloys for corrosion protection has involved processes where chromate species have played a key role in achieving the desired corrosion protection [46]. Conversion coatings formed on aluminium and its alloys, by treating in chromate-fluoride baths, have found extensive industrial applications as a result of their ability to provide improved corrosion resistance, in part through their suitability for the adhesive application of paints and other organic layer [14]. The high corrosion resistance offered by chromate films is attributed to the presence of both hexavalent and trivalent chromium species in the conversion coating. The use and disposal of chromium and chromium compounds have received much regulatory attention because of the toxicity and carcinogenicity of chromium. As a result of this, the uses of hexavalent chromium compounds have recently been overshadowed by the environmental problems associated with it, and hence, a substantial effort have been on developing new, effective and environmentally-friendly protective coating [24].

Although extensive research work has been directed towards the identification of a viable substitute for chromate, successes have been limited. Many of the environmentally-friendly conversion treatments alternatives proposed have problems matching the many advantages of chromate conversion coatings in providing excellent

corrosion protection and adhesion. Such environmentally-friendly conversion coatings should be able to inhibit corrosion by maintaining the polarisation resistance of the oxide layer and thus preventing chloride ion penetration of the protective oxides.

Unlike conversion coatings based on rare earth metals (REM), existing reports on experimental work published in the literature on zirconium-based conversion coating is very limited, with many uncertainties regarding the effect different concentration levels of copper in the alloy have on the thickness of the coating formed on the alloy substrates. In this study, an environment-friendly, zirconium-based conversion coating is proposed for the protection of aluminium and Al-Cu alloys. The present work was undertaken to obtain a more complete and consistent information on the composition and formation of zirconium-based conversion coatings on superpure aluminium and Al-Cu alloys of a range of compositions, and the influence of the alloy microstructure on their corrosion behaviour. It is shown in this work that ZrO_2 plays a significant role in the corrosion protection process. Potential-time data were combined with data from polarisation tests to investigate the extent to which different immersion times and copper concentrations in the alloy substrates affect the corrosion resistance provided by the coating layer formed. Structure and chemistry of zirconium-based conversion layers were characterised as a function of immersion time in the aqueous conversion bath to understand the mechanism of film formation. Characterisation was performed by glow discharge optical emission spectroscopy, atomic force microscopy, Rutherford backscattered spectroscopy, scanning electron microscopy and transmission electron microscopy. The effect of immersion time and copper concentration on corrosion resistance were monitored by electrochemical and scanning electron microscopy. The corrosion behaviour of conversion coated substrates was evaluated by means of an anodic and cathodic polarisation tests in 3.5wt.% NaCl, and compared with that of untreated aluminium.

CHAPTER 2

2 LITERATURE SURVEY

2.1 Introduction

Aluminium supports an air-formed oxide film which provides a barrier between the aluminium surface and the prevailing environment, thus protecting the metal from further oxidation. This self-protecting characteristic gives aluminium its high intrinsic corrosion resistance. However, the barrier is far from perfect; the films on the aluminium surface contains myriads of flaws or defects which may be activated in corrosive environments, and allow environmental access to the metal surface. An important point is that such flaws provide easy paths for electronic conduction in the otherwise insulating oxide covering the aluminium substrate [47]. When aluminium is exposed to an environment conducive to pitting attack, all the flaws in the surface oxide film can be considered as potential pit sites. Hence, defects in oxide films, which results from a local breakdown of the oxide film, contribute to localised corrosion of aluminium substrates. Consequently, the corrosion and filming behaviour of aluminium and its alloys have received detailed fundamental and practical scrutiny [48]. Additionally, the air-formed film is chemically reactive in aqueous solutions over a wide range of pH, thus enabling oxide thinning to proceed in solutions of relatively low and high pH values and significant hydration at intermediate pH values. The ability to control this reaction is used in treatments such as conversion coating of aluminium [47]. A conversion coating is often applied on aluminium and its alloys in order to improve their resistance to corrosion and to improve adhesion of subsequently applied organic finishes.

The primary objective of this survey is therefore to review systematically the following aspects: the mechanical, physical and chemical properties of aluminium and its alloys; the corrosion behaviour of aluminium and its alloys in different environments, especially in the presence of halide ions; the effect of alloying additions on the corrosion behaviour of aluminium and its alloys; corrosion protection of aluminium and

aluminium alloys by chemical conversion coatings; and a study of the composition and structure of zirconium-based conversion coatings as a viable alternative to chromate-containing conversion coatings.

2.1.1 Background

Aluminium is the third most abundant element comprising about 8% by mass of the Earth's crust and is therefore, the most abundant structural metal. In nature, however, it only exists in very stable combinations with other materials (particularly as silicates and oxides) and it was not until 1808 that its existence was first established by Sir Humphrey Davy, who originally called it aluminum. It took many years of painstaking research to "unlock" the metal from its ore and even more years to produce a viable, commercial production process. In 1821 Bertheir discovered, outside a small village in the south of France, a clay-like material that contained 40-60% alumina, either as the trihydrate gibbsite ($Al(OH)_3$) or as the monohydrates boehmite (γ-AlO(OH)) and diaspore (α-AlO(OH)). He gave this ore the name bauxite. The term bauxite refers to an ore or to a mixture of minerals rich in hydrated oxides, formed of aluminous rocks. Four years later in 1825, the Danish scientist Oersted produced the first samples of pure aluminium by reducing (through a painstaking process of heating) anhydrous aluminium chloride with potassium amalgam [49]. Between the years of 1827 and 1845, Wöhler improved this process by substituting potassium for the amalgam and finding a better method for the dehydration step of the final aluminium product. Wöhler was also able to establish the specific gravity or density of aluminium, demonstrating the metal's lightweight and malleability properties [50].

It was not until 1854 that the first process was developed which could produce commercial quantities of aluminium. Henri Sainte-Claire Deville (France) improved on the Wöhler method by substituting the expensive potassium with the much more affordable sodium by using sodium aluminium chloride instead of just aluminium chloride. In 1885, the Cowle brothers produced the first aluminium alloys containing iron and copper, soon after which, the invention of the dynamo made a cheaper supply of electricity available [51].

Following the development of large-scale equipments for generating electrical power in 1886 [50], two scientists, Hall and Héroult, working independently, developed and

patented a new process for direct electrolytic decomposition of aluminium oxide (Al_2O_3) [52] that would become the only method used today. The Hall-Héroult process was enhanced with the evolution of the Bayer process [53] which produces aluminium oxide from bauxite, which is used in the Hall-Héroult process. When the Hall-Héroult process was developed, the aluminium industry was born and this process of extracting aluminium from its ore has been able to withstand many years and attempts to rewrite or add to it and remains the fundamental basis of all commercial aluminium production today.

2.1.2 Aluminium and its properties

The properties of aluminium alloys depend on a complex interaction of chemical composition and microstructural features developed during solidification, thermal treatment and, for wrought alloys, deformation processing [54]. Aluminium has a unique and unbeatable combination of properties that make it a versatile, highly usable and attractive construction material. The properties of aluminium depend, to a large extent, on the purity of the metal. This may vary from ordinary aluminium of commercial purity to super-purity aluminium. The three main properties on which the application of aluminium is based are its low density of approximately 2.7 g/cm^3, the high mechanical strength achieved by suitable alloying and heat treatments, and the relatively high corrosion resistance of the pure metal [51]. However, there are several other properties that make aluminium one of the most heavily used metals. These properties can be divided into two broad categories, namely physical properties and chemical properties. Further valuable features can be obtained by various treatments of the metal; these are discussed further when the applications of aluminium and its alloys are considered.

2.1.2.1 Aluminium and aluminium alloys: physical, mechanical and chemical properties

Aluminium (Al) is a silvery-white metal of atomic number 13 and atomic weight of 26.9815 g/mol. It has the face-centred cubic crystal structure (Figure 2.1) over the whole temperature range up to the melting point. This type of crystal structure is the most packed cubic lattice. The closest distance between two atoms in the aluminium structure is 2.863Å at room temperature [54], and aluminium has a stacking-fault

energy of 200 mJ/m^2. It is a light metal which can be given tremendous strength by alloying. Aluminium conducts heat and electricity, reflects light and radiant energy and resists corrosion. It is also non-magnetic, non-toxic, and can be formed by all known metal working processes. Alloying, cold working and heat-treating can be used to tailor the properties of aluminium. The tensile strength of pure aluminium is around 90 MPa but this can be increased to over 700 MPa for some heat-treatable alloys. Extrusions of the right alloy and design are as strong as structural steel. Currently, alloys of the 7000 series can be aged to attain strength levels of the order of 0.7 to 0.8 GPa [55]. However, at this strength level, their application is limited by factors such as fracture toughness and strain localisation of environmentally-sensitive cracking [55].

The Young's modulus for aluminium (E = 70,000 MPa) is one-third that of steel. This means that the moment of inertia has to be three times as great for an aluminium extrusion to achieve the same deflection as a steel profile. Hence, aluminium behaves elastically under static and dynamic loading conditions, with the ability to resume its shape and size. The thermal and electrical conductivities are very good compared to that of copper. Naturally easy to manipulate, aluminium offers optimal design flexibility to engineers and architects. It can be fabricated into a wide variety of forms, including foil, sheets, geometric shapes, rods and wires, and is a popular choice for complex hollow extrusions. High machinability and plasticity also make it ideal for cutting, drilling, punching, hammering and bending.

Aluminium extruding is a versatile metal-forming process that enables designers, engineers, and manufacturers to take full advantage of a wide array of physical characteristics. Good malleability, which is a necessity for aluminium extruding, allows bending and other forming operations in both hot and cold conditions. Complex shapes can be realised in one-piece extruded aluminium sections without having to effect mechanical joining methods. The resultant profile typically is stronger than a comparable assemblage and is less likely to leak or slacken over time. Aluminium, when used in sheet, coil or extruded form, has a number of advantages over other metals and materials. Although other materials may offer some of the beneficial characteristics of aluminium, they cannot provide the full range of benefits that aluminium offers. A summary of some important physical properties are shown in Table 2.1; however, these properties are affected by the purity of aluminium.

Table 2.2 lists the designations, characteristics and forms of some widely used alloys. The 1000, 3000 and 5000 series alloys have their properties adjusted by cold work, usually by cold rolling. The properties of these alloys depend upon the degree of cold work and whether any annealing or stabilising thermal treatment follows the cold work. A standardised nomenclature is used to describe these conditions.

Table 2.1 Typical properties of aluminium

Property	Value
Atomic Number	13
Atomic Weight (g/mol)	26.9815
Valency	3
Crystal Lattice	Face centred cubic
Melting Point (°C)	660.2
Boiling Point (°C)	2480
Mean Specific Heat (0-100°C) (cal/g.°C)	0.219
Thermal Conductivity (0-100°C) (cal/cms. °C)	0.57
Co-Efficient of Linear Expansion (0-100°C) ($x10^{-6}$/°C)	23.5
Electrical Resistivity at 20°C (μΩcm)	2.69
Density (g/cm^3)	2.6898
Modulus of Elasticity (GPa)	70
Poissons Ratio	0.34

With the flexibility of compositions, degree of cold work and variation of annealing and temperature, a wide range of mechanical properties can be achieved especially in sheet products (see Table 2.3 (a) and 2.3 (b)). The AA2xxx, AA4xxx, AA6xxx, AA7xxx and

AA8xxx series alloys respond in this way. The wide choice of alloy compositions, solution heat treatment temperatures and times, quench rates from temperature, choice of artificial ageing treatment and degree to which the final product has been deformed, permit a wide range of properties to be achieved.

Table 2.2 Some common aluminium alloys and their characteristics [56]

Alloy	Characteristics	Form
AA1050/1200	Good formability, weldability and corrosion resistance	S,P
AA2014	Heat treatable, high strength, non-weldable and Poor corrosion resistance.	E,P
AA3103/3003	Non-heat treatable, medium strength work hardening alloy, good weldability, formability and corrosion resistance.	S,P,E
AA5251/5052	Non-heat treatable. Medium strength work hardening alloy. Good weldability, formability and corrosion resistance.	S,P
AA5454*	Non-heat treatable. Good weldability and corrosion resistance.	S,P
AA5083*/5182	Non-heat treatable. Good weldability and corrosion resistance. Very resistant to sea water, industrial atmospheres. A superior alloy for cryogenic use (in annealed condition)	S,P.E
AA6063*	Heat treatable. Medium strength alloy. Good weldability and corrosion resistance. Used for intricate profiles.	E
AA6061*/6082*	Heat treatable. Medium strength alloy. Good weldability and corrosion resistance.	S,P,E
AA6005	Heat treatable. Properties very similar to 6082. Preferable as air quenchable, therefore has less distortion problems. Not notch sensitive.	E
AA7020	Heat treatable. Age hardens naturally therefore will recover properties in heat affected zone after welding. Susceptible to stress corrosion. Good ballistic deterrent properties.	P.E
AA7075	Heat treatable. Very high strength. Non-weldable. Poor corrosion resistance.	E,P

* signifies the most commonly used alloys; S, P and E represent sheet, plate and extrusions respectively.

Table 2.3 (a) Mechanical properties of selected aluminium alloys [55, 56].

Alloy	Temper	Proof Stress 0.2% (MPa)	Tensile Strength (MPa)	Shear Strength (MPa)	Elongation A5 (%)	Hardness Vickers (HV)
AA1050A	H12	85	100	60	12	30
	H14	105	115	70	10	36
	H16	120	130	80	7	-
	H18	140	150	85	6	44
	0	35	80	50	42	20
AA2011	T3	290	365	220	15	100
	T6	300	395	235	12	115
AA3103	H14	140	155	90	9	46
	0	45	105	70	29	29
AA4015	0	45	110-150	-	20	30-40
	H12	110	135-175	-	4	45-55
	H14	135	160-200	-	3	-
	H16	155	185-225	-	2	-
	H18	180	210-250	-	2	-
AA5083	H32	240	330	185	17	95
	0/H111	145	300	175	23	75

Table 2.3 (b) Mechanical properties of selected aluminium alloys [55, 56]

Alloy	Temper	Proof Stress 0.2% (MPa)	Tensile Strength (MPa)	Shear Strength (MPa)	Elongation A5 (%)	Hardness Vickers (HV)
AA5251	H22	165	210	125	14	65
	H24	190	230	135	13	70
	H26	215	255	145	9	75
	0	80	180	115	26	46
AA5754	H22	185	245	150	15	75
	H24	215	270	160	14	80
	H26	245	290	170	10	85
	0	100	215	140	25	55
AA6063	0	50	100	70	27	85
	T4	90	160	11	21	50
	T6	210	245	150	14	80
AA6082	0	60	130	85	27	35
	T4	170	260	170	19	75
	T6	310	340	210	11	100
AA6262	T6	240	290	-	8	-
	T9	330	360	-	3	-
AA7075	0	105-145	225-275	150	9	65
	T6	435-505	510-570	350	5	160

Regarding its chemical properties, aluminium falls into Group Three of the Periodic Table, with 13 protons and 14 neutrons, giving it a mass of 27. Aluminium has the electronic orbital configuration $1s^2 2s^2 2p^6 3s^2 3p^1$. The three electrons in the outer orbit give the aluminium atom a valence of +3. Therefore, aluminium usually exists as Al^{3+} species in compounds. The formation of trivalent involves large amount of energy and it usually forms covalent bonds through sp^2 hybridization. The large positive charge, however, can be stabilised by water molecules arranged in octahedral co-ordination, $[Al(H_2O)_6]^{3+}$. The water of hydration exists both in aqueous solutions and some of the aluminium salts, such as alums.

Aluminium is a reactive metal that will easily form an oxide/hydroxide film when it is exposed to water at room temperature [57]. At neutral pH, the film formed is insoluble and grows to a sufficient thickness that limits reactivity of the aluminium substrate. However, the stability (solubility) of the film formed is dependent on the pH of the solution. Aluminium, at near-neutral pH conditions, is expected to form a passivating barrier film, which limits corrosion, however, the corrosion rate increases as the pH changes away from the near-neutral condition. The growth of the passivating film is driven by electrochemical reactions. The reason behind the increase in corrosion is that the formation of hydroxide [57]:

$$Al + 3H_2O \rightarrow Al(OH)_3 + 3H^+ + 3e^- \quad (2.1)$$

at neutral pH, when a crack in the passive film is produced, is replaced by metal dissolution according to the reaction:

$$Al \rightarrow Al^{3+} + 3e^- \quad (2.2)$$

at low pH or the formation and dissolution of the film

$$Al + 3OH^- \rightarrow Al(OH)_3 + 3e^- \quad (2.3a)$$

$$Al(OH)_3 + OH^- \rightarrow Al(OH)_4^- \quad (2.3b)$$

Despite being high in the reactivity series, aluminium is resistant to corrosion because of the thin layer of aluminium oxide (Al_2O_3), which forms on its surface in air. The oxide layer protects the underlying metal and renders it inert to any further reaction. However, aluminium is not resistant to corrosion in many mineral acids, except for

acids with strong oxidising properties [54]. The action of such acids depends on their concentrations. Aluminium is slowly attacked by most dilute acids and rapidly dissolves in concentrated hydrochloric acid, producing hydrogen:

$$2Al(s) + 6HCl(aq) \rightarrow AlCl_3(aq) + 3H_2(g) \quad (2.4)$$

While aluminium readily dissolves in dilute nitric, it is rendered passive in concentrated nitric acid due to the formation of aluminium oxide layer which protects the metal from further oxidation. Typical passivation concentrations range from 18% to 22% by weight.

$$Al + HNO_3 \rightarrow \text{Passivation} \quad (2.5)$$

In dilute sulphuric acid (from 1% up to 20%), all grades of aluminium, including high purity aluminium, have low resistance to corrosion even at room temperature [54]. Aluminium liberates hydrogen on reaction with dilute sulphuric acid. Suphur dioxide is liberated on reaction with concentrated sulphuric acid:

$$2Al + 3H_2SO_4\,[dil] \rightarrow Al_2(SO_4)_3 + 3H_2 \quad (2.6)$$

$$2Al + 6H_2SO_4\,[conc] \rightarrow Al_2(SO_4)_3 + 6H_2O + 3SO_2 \quad (2.7)$$

The alkalis are usually reactive to aluminium. Aluminium dissolves in strong alkali solutions to give colourless aluminates. Even high purity aluminium is vigorously attacked by alkalis such as sodium and potassium hydroxide to yield hydrogen and the aluminate ion.

$$2Al(s) + 2NaOH(aq) + 6H_2O \rightarrow 2Na[Al(OH)_4](aq) + 3H_2(g) \quad (2.8)$$

$$2Al + 2KOH + 2H_2O \rightarrow 2KAlO_2 + 3H_2 \quad (2.9)$$

Addition of a small amount of alkali to an aluminium salt solution precipitates aluminium hydroxide. On addition of further alkali, the hydroxide dissolves to form the aluminate ion.

Aluminium is also an expensive reducing agent. It is used for reduction of oxides of highly reactive metals. However, these metals need to be below aluminium in the reactivity series.

$$Cr_2O_3 + 2Al \xrightarrow{Heat} Al_2O_3 + 2Cr \quad (2.10)$$

$$Fe_2O_3 + 2Al \xrightarrow{Heat} Al_2O_3 + 2Fe \quad (2.11)$$

Aluminium has a very high resistance to concentrated hydrogen peroxide. It is characterised by good resistance to many organic compounds including acetaldehyde, formaldehyde and tetrachloride glycerine and also has good resistance to petroleum products.

2.1.2.2 Alumina: physical and chemical properties

Alumina or aluminium oxide (Al_2O_3) possesses strong ionic interatomic bonding, giving rise to its desirable material characteristics. Chemical and thermal stability, relatively good strength, thermal and electrical insulation characteristics combined with availability in abundance have made aluminium oxide attractive for engineering applications [58-60]. It occurs in two crystalline forms, alpha (α) and gamma (γ) alumina. Alpha alumina is composed of colourless hexagonal crystal structure, with a rhombohedral (corundum) structure consisting of 10 atoms (Figure 2.2). Four of these atoms are aluminium; six are oxygen. Gamma alumina (γ-Al_2O_3) is composed of minute colourless cubic crystals with specific gravity of about 3.6 that are transformed to α-Al_2O_3 form at high temperatures (above 450^0C). Alumina is an insulator, relatively inert chemically [61], and has a high melting point. It is insoluble in water and organic liquids and very slightly soluble in strong acids and alkalis. High purity alumina resists attack by all gases except wet fluorine and it is resistant to all common reagents except hydrofluoric acid and phosphoric acid. Elevated temperature attack occurs in the presence of alkali metal vapours, particularly at lower purity levels.

In the corundum structure, the aluminium atom is octahedrally coordinated with oxygen atoms. According to Feret et al [62] the corundum structure can be visualised as layers of hexagonal close-packed oxygen atoms with small aluminium atoms in two-thirds of the octahedrally coordinated holes between the oxygen atoms. The atomic positions consist of 12 aluminium atoms and 18 oxygen atoms. The unit cell dimensions are: a=b=4.7588 Å and c=12.992 Å.

When a freshly abraded aluminium surface is exposed to the atmosphere, it is immediately covered with a thin film of aluminium oxide (1-3 nm thick), which quickly

re-forms when damaged, thus protecting the metal from further environmental attack. An important feature of the alumina film formed on aluminium is that its molecular volume is stoichiometrically 1.5 times that of the metal consumed in oxidation [51]. This shows that the oxide film is under compressive stress, and will cover the aluminium surface continuously as well as cope with a certain amount of substrate deformation without rupturing [51]. Today, many protective coatings for aluminium and its alloys are based on this protective surface layer.

Films produced by reaction of aluminium oxide with water are of importance in corrosion [63]. Aluminium oxide reacts readily with water to form hydroxide. According to Hart [64], at temperatures below 60^0C, film growth proceeds in three stages: (1) "amorphous", $Al(OH)_3$, (2) boehmite, γ-AlO(OH), (3) bayerite, β-$Al_2O_3.3H_2O$, the final film thus consisting of three layers. Vedder and Alwitt [65, 66] suggested that the important steps involved in the aluminium-water reaction are: (1) formation of an amorphous oxide, (2) dissolution of this oxide, and (3) precipitation of aluminium hydroxide.

In step (1), the amorphous oxide is continuously replenished by an electrochemical process in which barrier film growth is the anodic half-cell reaction, coupled with the cathodic reduction of water [66]. In step (2), the exact nature of the oxide dissolution process is not known, but it involves the hydrolysis of surface Al-O bonds. The particular hydrolysed aluminium species found in solution depends on temperature, pH, and aluminium concentration [66]. In dilute solutions at 25^0C, the major aluminium monomer species varies with pH in the following manner: Al^{+3} for pH<3, $Al(OH)^{+2}$; for pH 4-5, $Al(OH)_2^+$; for pH 5-6; and $Al(OH)_4^-$ for pH>6.5. The hydrolysed species may be produced by the following surface reactions [66]:

$$Al_2O_3 + 3H_2O \rightarrow 2Al(OH)^{+2} + 4OH^- \quad (2.12)$$

$$Al_2O_3 + 3H_2O \rightarrow 2Al(OH)_2^+ + 2OH^- \quad (2.13)$$

$$Al_2O_3 + 5H_2O \rightarrow 2Al(OH)_4^- + 2H^+ \quad (2.14)$$

The formation of aluminium anions, $Al(OH)_4^-$, at reduced pH, is favoured by increasing temperature. For example, at 25^0C, gibbsite ($Al_2O_3.3H_2O$) is in equilibrium with 10^{-4} M $Al(OH)_4^-$ at about pH 10 but, at 100^0C, this equilibrium is achieved at about pH 7 [67].

Thus, with increasing temperature and pH, the most likely surface hydrolysis shifts from reaction (1) through (2) to (3).

At higher aluminium concentrations and elevated temperatures, hydrolysed aluminium readily forms polynuclear complexes which appear to be transitory species that eventually coalesce to form a solid phase. Complex cations as large as $[Al_{14}(OH)_{34}]^{+8}$ have been identified Mesmer and Baes [68], and it has been suggested that this species is the precursor of boehmite precipitation under hydrothermal conditions [69]. However, it has not been demonstrated that such complexes are involved in step (3) – precipitation, leading to film growth but, according to Alwitt [66], this is certainly a possibility.

2.1.3 Importance of aluminium

The role aluminium plays in everyday life is such that it is difficult to realise that the metal was still a comparative rarity in the early 1900's. Almost 19 million tonnes of primary aluminium are presently used in the western World alone. Through the development of a wide range of alloys, very varied strength and ductility can be achieved and this has led to the many current applications today [51]. These range from the use of very thin foil material in the packaging industry, ductile materials for drink containers, and highly conductive alloys for electrical purposes, to relatively low-strength alloys for the building industry and high strength materials for aircraft and armoured vehicles [51]. Aluminium is 100 percent recyclable, with minimal downgrading of its qualities [52, 70]. In addition to primary production, more than 7 million tonnes of aluminium are produced from recyclable scrap. The re-melting of aluminium requires only about 5 percent of the energy required to initially produce the primary metal [70]. Hence, the proportion of aluminium produced from scrap (secondary aluminium) is rising rapidly. In addition to its high scrap-value, other properties contributing to the widespread application of aluminium and its alloys are the non-toxic and colourless nature of its corrosion product which makes aluminium a very versatile material.

2.1.4 Structure, morphology and grain size

The structural morphologies play an important role in the corrosion behaviour of aluminium alloys. Several different structural morphologies may develop due to a wide range of operational conditions and various growth forms during solidification [71] of aluminium castings. It is well-known that the structural integrity of shaped castings is closely related to their thermal behaviour during solidification [71-73]. Osorio et al [71] observed that structural morphologies depend on the operational conditions imposed by the metal/mould system. The grain structure of a casting may take many forms during solidification and is usually characterised by both the macrostructure and the microstructure [71]. While the microstructure can be classified into cell/dendrite and eutectic morphologies, the macrostructure generally consists of three distinct zones. These are the chill, columnar, and equiaxed zones respectively. The origin of each one has been the subject of intense experimental and theoretical investigation because of the well known correlation between grain structures and mechanical properties of aluminium alloys [74, 75]. According to Osorio et al [71], coarse equiaxed grains tend to improve the corrosion resistance compared with fine equiaxed grains. The observed decrease in corrosion resistance was found to be in the order of coarse equiaxed > coarse columnar > fine equiaxed > fine columnar structures. This can be attributed to the grain boundaries energy level due to plastic deformation and defects.

For aluminium alloys, the influence of grain size is connected to the role (in terms of corrosion performance) of the solute(s), which segregate to the grain boundaries. The grain size affects many properties of the aluminium alloys [76]. In particular, as the grain size increases, the strength characteristics decrease [77] while the corrosion resistance improves. There is a well-known relationship called the Hall-Petch equation [78, 79], that shows the yield strength is proportional to the reciprocal of the square root of the grain diameter. For cast alloys, however, it is not always true that the alloy strength improves with decreasing grain size. A number of studies [72, 80, 81] have focused on the effect of microstructure and particularly dendrite spacing on mechanical properties. These studies have shown that in order to control the properties of cast alloys, it is necessary to understand the mechanism and characterisation of primary and secondary dendrite spacings during the solidification of alloys.

2.1.5 Aluminium alloy designations

Aluminium alloys are usually classified with respect to the fabrication process (cast alloys and wrought (mechanically worked) alloys) [82]. These two classes can be further subdivided into families of alloys based on chemical composition and finally on temper designation [83]. Temper designations are used to identify the condition of the alloy, that is the amount of cold work the alloy has undergone or its heat treatment condition. The latter is subdivided into heat-treatable and non-heat treatable alloys and into various forms produced by mechanical working [84]. The age hardened alloys are usually more corrosion resistant and more amenable to corrosion protection than the hardened alloys [85].

For wrought alloys, a four-digit system is used to produce a list of wrought composition families. In this four digit system, the first digit identifies the major alloying element(s) while the remaining three digits are used as serial numbers to identify particular alloy types as shown in the following:

AA1xxx series alloys: Controlled, unalloyed 99% pure aluminium or higher. This series is characterised by excellent resistance to corrosion and high thermal and electrical conductivity but poor mechanical properties. The last two of the four digits indicate the minimum percentage of aluminium. For example, AA1070 indicates aluminium purity of 99.70%. The second digit indicates modifications in impurity limits or alloying elements. When the second digit is zero, this indicates unalloyed aluminium having natural impurity limits. Integers 1-9 indicate special control of one or more individual impurities or alloying elements.

AA2xxx series alloys: Alloys in which copper is the principal alloying element, although other elements, notably magnesium, may be specified [52, 84]. This series has high-strength and is heat-treatable, but has low corrosion resistance, and is subject to intergranular attack and is difficult to inhibit [85].

AA3xxx series alloys: Alloys in which manganese is the principal alloying element. This series generally can not be heat-treated [85]. The alloys are characterised by relatively good corrosion resistance and moderate strength, and the alloys can be protected in certain media.

AA4xxx series alloys: Alloys in which silicon is the principal alloying element. Silicon added to aluminium substantially lowers the melting point without causing the resulting alloys to become brittle [84]. The AA4xxx series alloys are both heat-treatable and non-heat treatable alloys. The main difference between the heat-treatable and non-heat-treatable AA4xxx series is that the non-heat treatable alloys contain aluminium with silicon as the principal alloying element with no other elements added that could allow heat treatability. The heat-treatable 4xxx series alloys contain silicon and also controlled additions of magnesium and/or copper, which provide the material with the opportunity to respond to, and increase its strength through, heat treatment. The AA4xxx alloy series has good corrosion resistance and can be inhibited [85].

AA5xxx series alloys: Alloys in which magnesium is the principal alloying element. These are non-heat treatable. Magnesium has a high solubility in aluminium. When the magnesium content in the alloy is greater than 3.5%, the excess magnesium precipitates as Mg_5A_{l8}. Chromium is also a common additive, and appears as a fine dispersoid of $Cr_2Mg_3Al_{18}$ [86]. These alloys are characterised by good corrosion resistance and moderate strength. However, under certain conditions of loading, they are subject to stress corrosion cracking [85].

AA6xxx series alloys: Alloys in which magnesium and silicon are the principal alloying elements. They are precipitation hardened, with Mg_2Si as the hardening precipitate. If there is a low alloy concentration of magnesium and silicon, then all the Mg_2Si can be dissolved during solution heat treatment and used in the precipitation hardening reaction [86]. The alloys offer moderate strength with good ductility in the heat-treated and aged condition. These alloys have good corrosion resistance and may be protected effectively.

AA7xxx series alloys: Alloys in which zinc is the principal alloying element, but other alloying elements such as copper, magnesium, chromium and zirconium may be specified [52, 84]. They can be divided into two subfamilies depending on the percentage of copper as the third alloying element. Al-Zn-Mg-Cu alloys are the highest strength alloys after heat treatment, but they are not corrosion resistant. Al-Zn-Mg alloys are corrosion resistant. They are readily heat-treated without the strict precautions of solution heat-treating temperature causing eutectic melting [86].

AA8xxx series alloys: Alloys characterising miscellaneous compositions [52] which may include tin and some lithium compositions. Lithium has a considerably lower density than aluminium and because its solubility is also relatively high, it can be alloyed with aluminium in sufficient quantities to give a significant reduction in density (typically about 10% less than other aluminium alloys) [87]. The characteristics of this series depend on the major alloying element.

The cast alloy designation system also has four digits, and the first digit specifies the major alloying constituent(s). The first digit indicates the alloy group while the second and third digits identify the specific aluminium alloy or, for the aluminium 1xx.1 series, it indicates purity. However, a decimal point is used between the third and fourth digits to make clear that these are designations used to identify alloys in the form of castings or ingots [88]. The fourth digit indicates the production form: xxx.0 indicates castings and xxx.1, for the most part, indicates ingots having limits for alloying elements the same as or very similar to those for the alloy in the form of casting. A fourth digit of the xxx.2 is used to indicate that the ingot has composition limits; this typically represents the use of tighter limits on certain impurities to achieve specific properties in the finished cast products produced from that ingot. Alloy families for casting compositions include the following [52]:

1xx.x: Controlled unalloyed (pure) compositions.

2xx.x: Alloys in which copper is the principal alloying element. Other alloying elements may be specified.

3xx.x: Alloys in which silicon is the principal alloying element. The other alloying additions such as copper and magnesium are specified. The 3xx.x series comprises nearly 90% of all shaped castings produced.

4xx.x: Alloys in which silicon is the principal alloying element.

5xx.x: Alloys in which the principal alloying element is magnesium.

6xx.x: Unused

7xx.x: Alloys in which zinc is the principal alloying element. Other alloying elements such as copper and magnesium may be specified.

8xx.x: Alloys in which the principal alloying element is tin.

2.1.6 Effects of composition and microstructure on corrosion

AA1xxx wrought alloys: This series conforms to composition specifications that set maximum individual, combined, and total contents for several elements present as natural impurities in the smelter - grade or refined aluminium used in production of these products. Corrosion resistance of all the composition of AA1xxx is very high. However, under many conditions, the corrosion resistance of this series decreases slightly with increasing alloy content. Iron, silicon and copper are the elements present in the largest percentages. The copper and part of the silicon are in solid solution. The second-phase particles present contain either iron or iron and silicon – Al_6Fe, Al_3Fe, and Al_{12} Fe_3Si_2 – all of which are cathodic to the aluminium matrix [52].

AA2xxx wrought alloys and AA2xx.x cast alloys: These series are less resistant to corrosion than alloys of other series, which contain much reduced contents of copper. Alloys of this type were the first heat-treatable, high-strength aluminium based materials and they have been used widely for years in structural applications, particularly in aircraft and aerospace applications [10]. Electrochemical effects on corrosion can be stronger in these alloys than in other aluminium alloys because of two factors; significant change in electrode potential with variations in amount of copper in solid solution and, under some conditions, the presence of non uniformities in solid solution concentration [52]. The general resistance to corrosion decreases with increasing copper content. This is not primarily attributed to these solid solution or second phase solution potential relationships. It is attributed to galvanic cells created by formation of minute copper particles or films deposited on the alloy surface as a result of corrosion.

AA2xxx wrought alloys containing lithium: Addition of lithium decreases the density and increases the elastic modulus of aluminium alloys, thus making aluminium-lithium alloys a good choice for replacing the existing high-strength alloys, primarily in aerospace applications. Although lithium is highly reactive, addition of up to 3% lithium to aluminium shifts the pitting potential of the solid solution only slightly in the anodic direction [89]. In an extensive corrosion investigation of several binary and ternary aluminium-lithium alloys, Niskanen et al [90] found that modification of the

microstructure to promote formation of the δ phase (AlLi), reduces the corrosion resistance of the alloy in 3.5% NaCl solution. It was concluded that an understanding of the δ phase is central to an understanding of the corrosion behaviour of these alloys [52, 90].

AA3xxx wrought alloys: Wrought alloys of the AA3xxx series have very high resistance to corrosion. Manganese is present in the aluminium solid solution, in submicroscopic particles of precipitates and in larger particles of Al_6(Mn,Fe) or Al_2(Mn,Fe)3Si phases, both of which have solution potentials almost similar to that of the solid solution matrix [52]. Thus, these constituents are not significant sites for corrosion initiation. The 3xxx series, like pure aluminium, does not incur any of the more serious forms of localised corrosion, and pitting corrosion is the principal type of corrosion encountered. The addition of about 1.25% manganese increases strength without impairing ductility [84].

AA4xxx wrought alloys and AA3xx.x and AA4xx.x cast alloys: Silicon is present as second-phase constituent particles in aluminium wrought alloys of the AA4xxx series used in brazing and welding alloys, and in cast alloys of the AA3xx.x and AA4xx.x series. Although the effect of silicon on the corrosion resistance of these alloys is minimal because the silicon particles are highly polarised, the corrosion resistance of AA3xx.x castings alloys is strongly affected by copper content, which can be as high as 5% in some compositions, and also by levels of impurity. Modifications of certain basic alloys have more restrictive limits on impurities, which benefit corrosion resistance and mechanical properties [52].

AA5xxx wrought alloys and AA5xx.x cast alloys: Wrought Alloys of the AA5xxx series and cast alloys of the AA5xx.x series have high resistance to corrosion. This accounts in part for their use in a wide variety of building products and chemical processing and food handling equipment, as well as applications involving exposure to seawater [52]. When magnesium is present in amounts that either remain in solid solution or partially precipitate as Al_8Mg_5 particle, dispersed uniformly throughout the alloy matrix, the alloy is as resistant to corrosion as commercially pure aluminium.

AA6xxx wrought alloys: The heat-treatable wrought alloys of the AA6xxx series have moderately high strength and very good resistance to corrosion. The Mg_2Si phase, which is the basis for precipitation hardening, is unique in that it is an ionic compound

and, not only is it anodic to aluminium but it is also reactive in acidic solutions. Since these alloys are normally used in the heat-treated condition, no detrimental effects result from the principal alloying elements (magnesium and silicon) or from the supplementary elements (chromium, manganese, or zirconium) which are added to control grain structure. Copper additions, which enhance strength in many of these alloys, are limited to small amounts to minimise effects on corrosion resistance [52]. When the copper level is higher than 0.5%, some intergranular corrosion can occur in some of the tempers (T4 and T6), but this does not result in susceptibility to exfoliation or SCC [91]. When the magnesium and silicon contents in a balanced AA6xxx alloy are in proportion to form only Mg_2Si, corrosion by intergranular penetration is minimal in most commercial environments. However, if the alloy contains silicon level beyond that needed to form Mg_2Si, or if it contains a high level of cathodic impurities, susceptibility to intergranular corrosion increases [92].

AA7xxx wrought alloys and AA7xx.x cast alloys: The AA7xxx wrought and AA7xx.x cast alloys, because of their zinc contents, are anodic to AA1xxx wrought aluminium and to other aluminium alloys [52]. They are among the aluminium alloys that are most susceptible to stress corrosion cracking (SCC). Stress corrosion cracking of aluminium alloys is discussed in detail in section 2.2.8. Resistance to general corrosion of the copper-free wrought AA7xxx alloys is good, approaching that of the wrought AA3xxx, AA5xxx and AA6xxx alloys. The addition of copper as one of the alloying elements in Al-Zn-Mg alloys greatly improves the mechanical strength of AA7xxx series alloys by precipitation hardening [93]. The peak-aged T6 temper provides the maximum mechanical strength [93]. However, copper-containing AA7xxx alloys in the T6 temper (AA7xxx-T6) are very susceptible to various forms of localised corrosion in chloride environments, such as pitting, crevice corrosion, intergranular corrosion (IGC), and exfoliation corrosion [93]. The copper-containing alloys of the AA7xxx series, such as AA7049, AA7050, AA7075, and AA7178 have lower resistance to general corrosion than those of the same series that do not contain copper [52]. The AA7xxx series of alloys are more resistant to general corrosion than AA2xxx series of alloys, but less resistant than wrought alloys of other groups. Copper, in both wrought and cast alloys of the aluminium-zinc-magnesium-copper type, reduces resistance to general corrosion; however, these alloy composition are beneficial from the standpoint of resistance to

SCC since copper additions makes it possible for these alloys to be precipitated at higher temperatures.

2.1.7 Aluminium and its applications

Aluminium and its alloys are used widely in aerospace, automotive, architectural, lithographic, packaging [94], electrical and electronic applications. The alloy selected for any particular application depends on factors such as the mechanical and physical properties required, the material cost and the service environment involved [51]. The AA2xxx series (Al-Cu alloys) is used mainly in the aircraft industry, and the AA3xxx series (Al-Mn alloys) is widely employed in the canning industry. Recently, the AA4xxx series alloys have been in a greater demand for architectural applications (e.g. architectural lighting) because of the appearance (colour) which can be obtained when anodic coatings are applied. The AA5xxx series (Al-Mg alloys) are widely used in marine applications [85], where low density materials, good mechanical properties and better resistance to corrosion are desired. They can also be used unprotected for structural and architectural applications. The AA6xxx series (Al-Mg-Si alloys) are common extrusion alloys used particularly in the building industry. Due to their high mechanical strength and comparatively low density, the AA7xxx series (Al-Zn-Mg) of aluminium alloys is very attractive for aircraft structures. In particular, copper-containing alloys, such as AA7075, AA7050, AA7029, AA7010, or AA7349 have the best mechanical properties [95]. In these alloys, the mechanical strength is greatly improved by precipitation hardening.

2.2 Forms of Corrosion of Aluminium Alloys

Aluminium alloys may corrode through several different pathways [96]. Recognising the pathway or the forms of aluminium corrosion is an important step in determining the appropriate remedy for each problem [96]. When a metal is placed in an aqueous environment it can behave in three ways: corrode, show immunity or passivate [97]. The level of acidity or alkalinity of the environment significantly affects the corrosion behaviour of aluminium alloys.

Corrosion resistance of aluminium alloys is related to various factors including:

- The metal composition
- The type of environment in which it is used
- Service conditions, including temperature and moisture
- The method that may be used for joining the products
- Intended service life of the structure and maintenance programme.

Pourbaix diagrams can provide valuable information in the study of corrosion phenomena. The conditions for thermodynamic stability of protective oxide films on aluminium alloys are expressed by the Pourbaix diagram (Figure 2.3). This diagram shows the thermodynamic stability of aluminium species as a function of potential and pH. The pH (x-axis) varies from acidic at low pH to alkaline at high pH. The region of water stability is bounded by the dashed lines labelled (a) and (b) [96]. Line (a) is the hydrogen line below which water is no longer stable and decomposes into hydrogen (H_2) and OH^- (alkalisation); and line (b) is the oxygen line above which water is unstable and decomposes into oxygen (O_2) and H^+ (acidification). In acidic environments, aluminium dissolves as Al^{3+} ions and, in alkaline environments, aluminium dissolves as AlO_2^- ions.

$$Al_2O_2 + H_2O \rightarrow 2AlO_2^- + 2H^+ \quad (2.15)$$

In neutral solutions (pH range of about 4-8.5), the hydroxide is insoluble which makes the aluminium surface passive. However, the limits of this range vary somewhat with temperature, the specific form of oxide film present on aluminium surface, and with the presence of substances that can form soluble complexes or insoluble salts with aluminium [52].

The electrochemical equations governing the corrosion of aluminium alloys are 2.16 – 2.18. The reaction for anodic dissolution is shown in equation (2.16). However, if oxygen is present, the cathodic reaction involves the reduction of oxygen to hydroxyl anions as shown in equation (2.17). The oxygen reduction at the cathode is a fairly rapid reaction when it occurs on impurities such as iron or copper precipitates in the aluminium matrix, hence for this reason, single phase aluminium alloys usually have greater corrosion resistance than aluminium alloys which contains second-phase

intermetallic particles [96]. In the absence of oxygen, the second possible cathodic reaction in water is hydrogen evolution (Eq. 2.18).

$$Al \rightarrow Al^{3+} + 3e- \quad \text{(anodic reaction)} \tag{2.16}$$

$$O_2 + 2H_2O + 4e- \rightarrow 4OH \quad \text{(cathodic reaction)} \tag{2.17}$$

$$2H + 2e- \rightarrow H_2 \quad \text{(cathodic reaction)} \tag{2.18}$$

In general, corrosion of a metal proceeds when five conditions are met [98]. An active corrosion site consists of an anode, cathodic, continuous electrical contact between the anode and cathode, continuous electrolyte and a cathodic reactant such as O_2, H_2O or H_2 [98].

Many years of experience with applications in building, commercial vehicles, shipbuilding, outdoor installations and highway equipment, using aluminium alloys from the AA1xxx, AA2xxx, AA5xxx and AA6xxx series, have shown their outstanding corrosion resistance when exposed to urban, marine and other hostile environments. Alloys from the AA2xxx and AA7xxx series, on the other hand, are not employed in certain applications such as shipbuilding or building and construction.

2.2.1 Uniform corrosion

Uniform corrosion, or general corrosion, is a corrosion process exhibiting uniform thinning that proceeds evenly over the entire surface area or a large fraction of the total area [84]. Uniform corrosion of aluminium is rare, except in special, highly acidic or alkaline environments [52]. However, if the surface oxide film is soluble in the environment, as in phosphoric acid or sodium hydroxide, aluminium dissolves uniformly at a steady rate [52]. In the case of aluminium alloys, differences in electrical potential can occur on the surface of a piece of aluminium alloy due to small differences in chemical composition, phase differences, amount of cold work, etc. These differences set up small corrosion cells, each with an anode and cathode. Corrosion continues until the metal is consumed or the corrosive film formed on the surface sets up a barrier to the electrolyte. The breakdown of protective coating systems on structures often leads to this form of corrosion [84]. General corrosion commonly occurs on metal surfaces having a uniform chemical composition and microstructure. Dissolution is most uniform

in pure aluminium and the next most uniform are dilute alloys and the non heat-treatable alloys [91]. Heat-treatable alloys often show some surface roughness, especially when thick cross-sections are etched because variable dissolution rates result in thickness variations in solid solution concentration of the alloying elements and the distribution of constituent particles [52].

2.2.2 Pitting corrosion

Pitting may occur in most metals with protective film, but it is particularly characteristic of aluminium and aluminium alloys. It is a localised form of corrosion [99] by which cavities, i.e. "holes" are produced in the material. Pitting corrosion is caused primarily by variations in the grain structure between adjacent areas on the metal surfaces that are in contact with a corrosive environment. For aluminium alloys, pitting corrosion has been found to initiate at the intermetallic compounds [100]. Therefore, depending on the composition of the alloys and the environment, the pitting corrosion might initiate preferentially on different intermetallic particle types, resulting in different electrochemical behaviour [101]. Pitting is first noticeable as a white or grey powdery deposit, similar to dust, that blotches the surface. When the superficial deposit is removed, the pits can be seen in the surface. These pits may appear either as relatively shallow indentations or as deeper cavities of small diameters. The morphology of an individual pit is controlled by the nature and intensity of attack [97]. For aluminium and its alloys, two types of pit morphologies are usually observed; crystallographic and hemispherical pits. For example, in hydrochloric acid, cubic pits form because of the preferential attack in the {100} crystallographic orientation; where moisture is present, attack is concentrated in the {111} direction and octahedral pits result [102]. In near-neutral chloride-containing environments, the mouths of the pits tend to be circular and the cross-sections roughly hemispherical [97]. The presence of an aggressive anion is a necessary condition for pitting corrosion to occur. Many studies [31, 40, 43, 103-108] have shown that such aggressive anions for aluminium and its alloys include; Cl^-, Br^-, I^-, ClO_4^-, IO_3^-, NO_3^-, SO_4^{2-}.

The process of pit initiation can be divided into several steps: the induction period, pit initiation and propagation processes. Each step may be stifled and thus pit repassivation may occur [109]. Pitting can penetrate several millimetres during a short period if the

conditions are extremely unfavourable. It can be described in terms of four distinct and consecutive stages [110, 111]:

- ❖ Processes occurring on the passive film, at the boundary of the passive film and the solution.
- ❖ Processes occurring within the passive film, when no visible microscopic changes occur in a film.
- ❖ Formation of so-called metastable pits which initiate and grow for a short period of time below the critical pitting potential and then repassivate (this is an intermediate step in pitting)
- ❖ Stable pit growth, above a certain potential termed the critical pitting potential.

The rapid anodic dissolution of aluminium when exposed to aggressive anions such as Cl^- appears to be due to the ability of the chlorine ion to influence the nature of the passive oxide films [112] formed on aluminium and its alloys. It usually starts with the local breakdown of the passive film [113] (from a weak point in the oxide), and after initiation, the reactions within the pit reduce the pH and increase the chloride concentration and in this way sustain the reaction. The pit is the anode, while the unaffected area surrounding the point of penetration (flaw in protective oxide) is the cathode of a cell whose electrolyte is the corrosive solution (which contains an aggressive anion (e.g. Cl^-)). On aluminium covered by protective films, the surface area available for cathodic reactions is very large compared with that available for the anodic reaction which is commonly initiated at flaws in the protective film. As a result, the current per unit area of the cathodic surface remains low and large areas of the metal surface may be exposed to cathodic reaction accelerators in the aggressive solution (e.g. oxidising agent) and thereby stimulate the anodic reaction. The anodic current density is high, and sufficient metal is soon removed to form a depression in the surface, unless corrosion products stifle the reaction [114]. In many cases, oxygen combines with aluminium ions produced by corrosion to form protection oxide films. However, if the oxygen available is insufficient or if the corrosion product formed is not protective, the pit grows and a cavity is soon formed in which oxygen is not easily replenished and thus, is soon exhausted. Moreover, corrosion current causes any chloride ions present to migrate to the anode. These ions tend to destroy the protective qualities of any films

which may still be present and they also acidify the solution in the pit [114]. The combination of large cathodic and small anodic areas, oxygen exhaustion, chloride accumulation and acidicity of solution in the pit, produce an intensely localised form of attack. The overall result on the corrosion rate depends on whether it is the anodic retardation or cathodic stimulation that is dominant [114].

Nitrate ions are usually considered as being among the most effective inhibitors of the pitting corrosion of aluminium by chlorides [32, 115]. However, copper-rich particles act as preferential sites for pitting due to the aggressiveness of nitrate ions towards these intermetallics. It has been shown [116, 117] that in specific electrolyte mixtures, i.e., specific concentrations and specific [NaCl]/[$NaNO_3$] ratios, the corrosion rates of AA7075 and AA2024 aluminium alloys are increased by an order of magnitude over that in NaCl solutions of the same concentrations. The results were related to the reactivity of nitrate ions toward intermetallic compounds [116].

2.2.3 Crevice corrosion

Crevice corrosion is a localised form of corrosive attack. It can be considered as a particular form of pitting which occurs between faying surfaces (e.g., in threaded or flanged connections), usually due to oxygen concentration cell effects. This form of corrosion is usually associated with a stagnant solution on the micro-environmental level [84]. Such stagnant microenvironments tend to occur in crevices (shielded areas) such as those formed under gaskets, washers, insulation material, fastener heads, surface deposits, disbanded coatings, threads, lap joints and clamps [84]. Examples of deposits that may produce crevice (or deposit attack) are sand, dirt, corrosion products, and other solids [118]. The deposit acts as a shield and creates a stagnant condition [118]. Crevice corrosion is initiated by changes in local chemistry within the crevice:

- Depletion of inhibitor in the crevice
- Depletion of oxygen in the crevice
- A shift to acid conditions in the crevice
- Build-up of aggressive ion species (e.g. chloride) in the crevice

Usually, crevice corrosion is considered to be due to oxygen concentration cell effects. It also arises because of acidity changes in the crevice, build-up of ions in the crevice, or depletion of an inhibitor. This explains why crevice corrosion is observed on materials like stainless steels in deaerated chloride solutions, where no oxygen concentration cell exists. In this case, so-called "occluded cell" corrosion processes (with increase of acidity and build-up of ions in the crevice) are operational, similar to the pitting corrosion process.

Crevice corrosion occurs in narrow metal to metal or non-metal to metal gaps, where the convection of water is hampered and specific crevice chemistry which is different from the environment is allowed to develop. Aggressive ions like chlorides must be present in the bulk electrolyte. The oxygen in the bottom of the crevice is consumed and an anodic area is developed adjacent to the oxygen depleted zone. Crevice corrosion develops in a similar manner to pitting corrosion after the initiation stage, with a gradual decrease of pH and an increase of the chloride concentrate ion within the crevice. Crevice corrosion is normally not a serious problem on aluminium in the absence of aggressive ions, because of the very stable aluminium oxide. However, in a crevice, there is a possibility for accumulation of moisture because of capillary forces and deposits with corrosive or hygroscopic species. In this way there will be a constant corrosive environment in the crevice which eventually can breakdown the oxide layer.

Crevice corrosion can also occur during storage of aluminium, for example water staining which creates dark stains as a result of a surface etching caused by water trapped between the adjacent surfaces. It is most commonly seen on sheet products and is mainly an aesthetic problem since the mechanical integrity of the water stained aluminium is rarely impaired. A further problem is the accumulation of corrosion products in narrow crevices which can finally deform the structure in extreme cases.

2.2.4 Intergranular corrosion

Intergranular corrosion (IGC) is localised attack along the grain boundaries, or immediately adjacent to grain boundaries [84, 119, 120] of some alloys while the bulk of the grains is not attacked under specific conditions. During heat treatment, aluminium alloys are heated to a temperature that dissolves the alloying elements. As the metal cools, the alloying elements combine to form other compounds. If the cooling

rate is slow, they form predominantly at the grain boundaries. The compounds formed differ electrochemically from the metal adjacent to the grain boundaries. These altered compounds can be either anodic or cathodic to the adjoining areas, depending on their composition. The presence of an electrolyte will only complete the cycle for corrosion to take place, thus resulting in an attack on the anodic area. This attack may be relatively rapid and can exist without visible evidence. Corrosion products building up along these grain boundaries exert pressure between the grains, as the corrosion advances; it reveals itself by lifting of the surface grains of the metal by the force of expanding corrosion products present at the grain boundaries just below the surface [84]. This advanced stage of intergranular attack is referred to as exfoliation corrosion. Recognition and necessary corrective action to immediately correct such serious instances of corrosion are vital. This type of attack can seriously weaken structural members before the volume of corrosion products accumulate on the surface and the damage becomes apparent. Aluminium alloys can be susceptible to intergranular corrosion depending on heat treatment.

In order to understand the susceptibility of aluminium alloys towards IGC, Guillaumin and Mankowski [4] studied the corrosion behaviour of AA2024-T351 alloy in 1 M NaCl solution. They found that the Al_2CuMg hardening precipitates encountered in the alloy matrix are surrounded by a dispersoid-free zone. Hence, the galvanic couples; dispersoid-free zone/the rest of the alloy matrix, and dispersoid-free zone/S phase particles cause the dissolution of the matrix surrounding the particles. The formation of intermetallic precipitates such as Al_2Cu and Al_2CuMg in the vicinity of grain boundaries makes these zones depressed in Cu content [121]. Thus, the grain boundaries become more anodic than the grain bulk. Hence copper-containing aluminium alloys (AA2xxx series) with certain heat treatments, are sensitive to intergranular corrosion (IGC).

Sinyavskii et al. [113] showed that intergranular corrosion can proceed on aluminium alloys in either of two forms, namely crystallographic or structure-decomposition IGC. The first is characteristic of low-alloy or pure aluminium and is controlled by recrystallisation process [113]. High-angle boundaries of growing recrystallised grains accumulate numerous vacancies which partly coagulate, thus causing thermodynamic instability of the boundaries, and their electrode potential approaches the potential of

active corrosion [113]. The second is characteristic of medium- or high-alloy aluminium and is controlled by peculiarities of the decomposition of the supersaturated solid solutions [113].

In aluminium alloys, intergranular attack usually results from the establishment of local cells along grain boundaries in which second phase, intermetallic precipitates concentrate [84]; these are either anodic or cathodic to the bulk of the grain. Susceptibility to intergranular corrosion is mainly dependent upon alloy composition and heat-treatment. AA1xxx and AA3xxx series aluminium alloys are generally not susceptible to intergranular attack since grain boundary precipitates either do not arise, or they have the a similar solution potential to the surrounding metal. This form of corrosion can be very dangerous because the attack can proceed undetected through the material and may deteriorate the mechanical properties of the metal and cause fracture without any visible exterior signs of corrosion.

2.2.5 Exfoliation corrosion

Exfoliation corrosion is a further form of severe intergranular corrosion associated with high-strength aluminium alloys [84]. Generally, exfoliation corrosion occurs when there is a combination of three factors: a highly directional microstructure, a preferential anodic path and a specific type of corrosive environment [110, 122]. Exfoliation corrosion proceeds in layers parallel to the surface in the rolling direction [123], the layers will flake because of the pressure from the corrosion products. It exhibits itself by the “lifting up” of the surface grains of the metal by means of the force of the expanding corrosion products present at the grain boundaries just below the surface [124]. The corrosion products force metal away from the body of the material and give rise to a layered or leaf-like appearance ("exfoliation") in unrecrystallised alloys. Exfoliation corrosion is a visible evidence of intergranular corrosion and is more often seen on extruded sections where grain thicknesses are usually less than rolled forms [124]. Alloys that have been extruded or otherwise worked heavily, with a microstructure of elongated, flattened grains, are particularly prone to this damage [84]. This form of corrosion is associated with a marked directionality of the grain structure [110]. In aircraft materials, exfoliation corrosion is most common in the heat-treatable Al-Zn-Mg-Cu (AA7xxx series), Al-Cu-Mg (AA2xxx series), and Al-Mg alloys. Exfoliation

corrosion has also been observed in Al-Mg-Si alloys [110] and some cold worked AA5xxx alloys. Care must be taken over heat treatment where maximum resistance to exfoliation is usually achieved before maximum resistance to stress corrosion cracking [97]. For example, precipitation treatments used to produce a T76 temper in AA7xxx alloys, which use times and temperatures intermediate to those of T6 (peak aged-maximum strength) and T73 (increased resistance to stress corrosion cracking) treatments, provide excellent resistance to exfoliation but only intermediate resistance to stress corrosion [97].

Alloys that are susceptible to intergranular corrosion may also experience exfoliation corrosion when heavily cold worked. The attack is not usually as serious as intergranular corrosion because it is easier to observe. However, localised effects can be dramatic, such as in the case of fasteners and rivets which are subjected to cold work during assembly and subsequently exposed to service conditions which can give rise to grain boundary precipitation. The cold worked head of the fastener can become completely detached in extreme cases.

2.2.6 Filiform corrosion

One of the most common forms of corrosion occurring on coated aluminium and aluminium alloys is filiform corrosion (FFC) [125]. It is characterised by an active corrosion cell that propagates across the metal surface underneath the coating [126], leaving a tail filled with corrosion products [127, 128]. The mode of attack is similar to pitting corrosion in that the front of the attack is supported by moisture which penetrates the surface layer and becomes depleted of oxygen making the area anodic. Essentially, filiform corrosion is a type of “oxygen concentration cell” in which the anodic area is the head of the filament and the cathode is the area surrounding it, including the tail. In appearance, filiform corrosion on aluminium alloys resembles long thin, thread-like filaments, often up to several centimetres long, but less than 1 millimetre wide. A filament consists of two visually distinguishable parts: an active head, where dissolution of the metal occurs, and a trailing tail, composed of dry corrosion products [127]. The filaments are generally white, with a grey head. This head forms the active corrosion site, with corrosion propagation and filament growth taking place here. Filament heads are electrolyte-filled, containing metal cations and aggressive anions (such as Cl^-), and

typically exhibit a low pH (as low as pH 1) toward their leading edge as a consequence of cation hydrolysis [129, 130]. Conversely, filament tails are filled with dry, porous, corrosion product. It is generally believed that filament advance is driven by differential aeration arising from facile mass transport of gaseous oxygen (O_2) through the filament tail [129, 130]. This implies that the principal site of cathodic oxygen reduction must lie toward the trailing edge and that of anodic metal dissolution toward the leading edge of the filament head [131]. Filament advance on aluminium alloys is thought to involve anodic undercutting of the organic coating [129, 130, 132-134]. However, increased coating adhesion tends to reduce filament propagation rates, possibly because of the way in which coating adhesion and coating deformability influence the shape of the filament-head electrolyte droplet [131].

Filiform corrosion is almost always initiated at defects in the coating and propagates in the presence of aggressive chloride ions, oxygen, and sufficient relative humidity [128]. It is generally considered to result from contamination on the metal surface and will only propagate in humid conditions [135]. It depends on the relative moisture of the air and the quality of the surface treatment preparation prior to coating. The type of pre-treatment used prior to painting has a very important influence on the subsequent occurrence of filiform corrosion [135]. While this form of corrosion rarely, if ever, leads to a working failure, the consequences can be severe for any decorative function [125]. It has been unclear whether the range of behaviour of aluminium alloys are caused by differences in the alloy compositions or by some feature of their microstructure or surface condition [135]. However, according to Leth-Olsen and Nisancioglu [136], the chemical composition of the substrate is believed to play an important role on resistance to filiform corrosion.

The literature reveals that susceptibility of aluminium alloys to filiform corrosion attack is more closely related to the condition of the original surface layer than to the microstructure of the substrate [135]. This is due to the presence in the near-surface regions of high temperature oxides, rolling lubricants and other contaminants from processing. Copper and iron-containing aluminium alloys can lead to the formation of galvanic cells between intermediate compounds and the matrix. These events govern the local breakdown of protective coatings on such aluminium alloys. It is also well known

from the literature that the composition of aluminium alloy, particularly copper and iron contents, has a direct and dominant effect on the growth rate of filiform corrosion.

Afseth et al [137-141] have found a strong relationship between the presence of deformed layers and filiform corrosion susceptibility of AA3xxx and AA5xxx series aluminium alloys. The hot-rolled material is more susceptible to filiform corrosion attack than the cold-rolled material, and the susceptibility increases more with heat-treatment [137, 139, 141]. The microstructure of AA3005 alloy reveals the presence of fine intermetallic phases within the thin deformed layer, although the investigation could not establish significant change in solid solution manganese content at the alloy surface [137]. Caustic etching improved the filiform susceptibility of the alloy by removal of the active surface layer [141]. Etching also removed the substrate sensitivity to heat-treatment, thus indicating that the enhanced precipitation is associated with the deformed layer [142]. By cold-rolling a corrosion-resistant etched sample, the sensitivity to filiform attack after heat-treatment can be reintroduced[141]. The effect is associated with the precipitation of intermetallic particles during thermo-mechanical processing [142]. The particles increase cathodic activity of the surface and act as pit initiation sites. It is also thought that precipitation causes solute depletion of the matrix [142, 143]. The use of an inhibiting primer or a conversion coating can be effective protection against filiform corrosion attack.

2.2.7 Galvanic corrosion

Galvanic corrosion takes place between two different metals, alloys, or coatings, which are coupled together electrically in the presence of a common electrolyte. Galvanic effect can also arise due to differences in metal composition and as a result of varying composition in the region of grain boundaries for the same metal. Each metal has a potential different from any other metal when placed in an electrolyte, thus setting up an electrochemical corrosion cell [84]. Almost any lack of homogeneity of the aluminium alloy surface or its environment may initiate a galvanic corrosion attack by causing a difference in potential. The magnitude of this potential difference between the alloy surfaces will determine which areas of the metal are the cathodes and which areas are anodes, and the rate at which corrosion occurs at the anode. Contact between dissimilar

metals may also cause galvanic current to flow, due to the difference in potentials of the two metals.

For galvanic corrosion to occur, the following three conditions must exist:

- There must be two electrochemically dissimilar metals present
- There must be an electrically conductive path between the two metals
- There must be a conducive path for the metal ions to move from the more anodic metal to the more cathodic metal.

The degree to which aluminium corrodes when coupled with a more cathodic metal depends on the degree to which it is polarised in the galvanic cell [52]. The metal or alloy possessing the more negative (active) potential tends to suffer accelerated corrosion i.e. the material is consumed by anodic dissolution [84], while the metal or alloy possessing the more positive (noble) potential tends to remain practically unaffected.

To protect metals or alloys from an aqueous environment or the atmosphere, a variety of coatings have been applied to the surface of such metals or alloys [144]. In the presence of an electrolyte, which could be a thin film of moisture, galvanic action between coating and substrate is an important factor in determining the protection offered by most coatings [144]. Galvanic corrosion of aluminium by more cathodic metals in solutions of non-halide salts is usually less than in solutions of halide ones because the aluminium is less likely to be polarised to its pitting potential [52]. In any environment, galvanic corrosion is reduced by removal of the cathodic reactant.

2.2.8 Stress corrosion cracking

Many alloys exhibit excellent resistance to stress corrosion cracking in all standard tempers; however, high strength aluminium alloys, which are of primary interest in aerospace applications, must be approached cautiously. Stress corrosion cracking (SCC) is the formation of brittle cracks in a normally sound material through the simultaneous influence of tensile stress and a corrosive environment [145]. This stress can either be applied (external load), or can be residual stress in the metal (e.g., due to production process or heat treatment). In most cases, stress corrosion cracking has been associated

with the process of active path corrosion which involves accelerated corrosion along a path of higher than normal corrosion susceptibility, with the bulk of the material typically being passive. The most common active path is the grain boundary [146], where segregation of impurity elements can make it marginally more difficult for passivation to occur. There are some essential conditions that must be present for stress corrosion cracking to occur:

- A susceptible material
- An environment that causes stress corrosion cracking for that material and
- Sufficient tensile stress to induce stress corrosion cracking

The last often involves residual fabrication stresses, especially at weldments. Several investigations have indicated that stress corrosion cracking is strongly affected by alloy composition, microstructure, heat treatment, and to a lesser degree, the stress intensity [147-149]. Aluminium alloys containing more than 3% wt Mg or 1-2% wt Zn are susceptible to stress corrosion cracking in both atmospheric and water exposures due to supersaturation of solid solution and increased tendency of magnesium atoms to precipitate at grain boundaries [148]. However, it was reported that zinc addition of 1-2 % wt improves SCC resistance of Al-Mg alloys, due to the formation of stable Al-Zn-Mg phases at grain boundaries [148]. Low strength alloys and commercially pure aluminium are (much more) resistant to stress corrosion cracking. Several literatures also reported the poor resistance to stress corrosion cracking exhibited by aluminium alloys containing appreciable amounts of soluble alloying elements, such as AA2xxx series, copper-bearing AA7xxx and AA8xxx series alloys [120, 149]. It is assumed that, for Al-Cu alloys (AA2xxx series), stress corrosion cracking occurs through an anodic dissolution mechanism, whereas hydrogen embrittlement is the cause of cracking in higher strength [Al-Zn-Mg (-Cu)] alloys. Hence, anodic dissolution is generally favoured in AA2xxx series aluminium alloys while hydrogen embrittlement cracking is favoured in the AA7xxx series.

The embrittlement of aluminium alloys by hydrogen involves the ingress of hydrogen from the environment (through corrosion) into the susceptible alloys, which can seriously reduce the ductility and load-bearing capacity, causing cracking and brittle failures at stresses below the yield stress of aluminium alloys. In this case, the cathodic

reaction during SCC is the reduction of hydrogen, and the hydrogen evolved enters the alloy and induces initiation and propagation of the crack through diffusion and enrichment of hydrogen atoms at the crack tip during the process of SCC [150]. For stress corrosion cracking controlled by anodic dissolution, the cathodic process does not involve the reduction of hydrogen or hydrogen from the cathodic reaction is not sufficient to induce hydrogen embrittlement. The precipitation of electrochemically more noble phases at grain boundaries leads to the depletion of the more noble element in the area adjacent to the grain boundary. The depleted zones have a lower potential than the precipitates and this way, an anodic path along the grain boundaries is formed which causes the grain boundary regions to dissolve preferentially. The applied stress continually ruptures the oxide film in the grain boundary region, enabling or enhancing anodic dissolution, and crack propagation occurs along the grain boundaries. Anodic dissolution of active intermetallic phases or grain boundaries, and effects of copper enrichment around, or in, particles on localised galvanic corrosion cells are examples where anodic dissolution dominates the crack growth process. A typical example for this is the copper-rich intermetallic phases (Al_3Cu or Al_3CuMg) at grain boundaries of a sensitised 2xxx – series alloy.

In practice, stress corrosion cracking is mainly encountered in the heat treated, high-strength alloys. Such cracking is a problem, for example, in marine and aircraft structures where a high strength-to-weight ratio is required. In particular, stress corrosion cracking of high strength AA7xxx series aluminium poses a continuing issue for the aerospace industry [151]. A typical susceptible material is AA7075-T6. However, the same alloy, but in the T73 temper, has good resistance to environmental cracking.

Intergranular corrosion is strongly involved in stress corrosion cracking of aluminium alloys together with pitting corrosion, which is important during the crack initiation phase and in forming local occluded corrosion cells for creating a locally acidified occluded environment. In general, aluminium alloys containing appreciable amounts of soluble alloying elements such as copper, magnesium, silicon, and zinc are sensitive to stress corrosion cracking. Stress corrosion cracking of aluminium alloys is almost exclusively intergranular and it is generally thought that grain boundaries form an anodic path for stress corrosion cracking growth under the combined influence of stress

and a favourable environment. Therefore, stress corrosion cracking of aluminium alloys may be prevented by cathodic protection or with a suitable heat treatment, thus making the microstructure less sensitive to stress corrosion cracking. Application of protective coatings for aluminium alloys is a further useful and important method in avoiding stress corrosion cracking susceptibility [148].

2.3 Corrosion Behaviour of Copper-containing Aluminium Alloys

There is significant interest in the corrosion behaviour of copper-containing aluminium alloys[152]. Copper, whether it is present at matrix regions or as a constituent of secondary phases, is generally considered to affect the corrosion resistance. Generally, the microstructure of the aluminium alloys has a large influence on their corrosion behaviour. The dominant feature of alloy microstructures is the distribution of second-phase particles that contains high concentrations of alloying and impurity elements [153]. These particles often exhibit distinctly different electrochemical characteristics compared to the surrounding matrix microstructure. In particular, the presence of intermetallic compounds of copper, which act as cathodic sites, play an important role in the corrosion behaviour of aluminium alloys [154] and they can give rise to localised corrosion, such as pitting, intergranular, stress corrosion and exfoliation, because of the formation of galvanic cells. The shape, size and chemical composition of the intermetallic particles are determined by the processing route (heat treatment and forming) carried out on the aluminium alloy [155]. Furthermore, the corrosion behaviour of copper-containing aluminium alloys depends on the chemical composition of the media since species such as chlorides are aggressive towards the aluminium matrix and the copper-rich particles. On the other hand, sulphates, which can also be aggressive to copper-rich intermetallic particles, have an inhibitive effect on the corrosion of the aluminium matrix [156-158].

2.3.1 Effects of alloying elements

The effect of copper on the pitting potential of aluminium-copper alloys is predominantly of interest since it gives a clue for the possible mechanism of pitting. The pitting potential of solution-treated aluminium-copper alloys (alloys water quenched from 539^0C, with the copper retained in solid solution), increases with increasing

copper content [29, 159]. The effect is stronger for the first 1% Cu addition, with the pitting potential dependence becoming almost linear for increased copper contents, up to 5% [29]. The highest pitting potential value was limited by solubility of copper in aluminium [159] and ageing of the alloy affected the pitting potential. The pitting potential of the aged alloy was found to be determined by the copper content of the solute depleted zones formed during ageing [29].

Many studies have shown that gains in mechanical properties derived from copper alloying and ageing results in a decrease in corrosion resistance of copper-containing aluminium alloys due to the formation of copper-rich intermetallic particles. These particles (discussed in detail in section 2.3.2) provide sites for oxygen reduction, increase the alloy corrosion potential, and localise electrochemical activity on the alloy surface in a way that leads to enhanced corrosion susceptibility compared to other aluminium alloys [153, 160-168]. However, an effect of copper alloying addition which is not as widely appreciated is the inhibition of localised corrosion in its initial stages [161, 169-171]. This effect is observed almost exclusively in Al-Cu solid solutions [161, 171]. A multi-electrode approach was used by Kim and Buchheit [161] to collect statistically large populations of pitting potential measurements on Al 99.999, Al-0.2Cu, Al-2.0Cu and Al-2.0Zn solid solution alloys. The results obtained established that copper dissolved in solid solution ennobles the pitting potential compared with Al 99.999, while Zn reduces the pitting potential. Ramgopal and Frankel [171] developed a more clear-cut interpretation of the inhibiting effect of copper in Al-Cu solid solutions based on the measurement of the anodic polarisation response of artificial crevices using a decreasing potential scanning approach. Based on their results, copper ennobles aluminium dissolution kinetics by increasing the exchange current density and the Tafel slope of the dissolution partial reaction. This increases the repassivation potential and reduces the dissolution kinetics producing the observed inhibiting effect.

2.3.2 Effects of intermetallics

Intermetallic compounds can be defined as an ordered alloy phase formed between two or more metallic elements. These particles are either intentionally developed in order to obtain the desired mechanical properties or they are present in the alloys as natural impurities. Many authors [4, 25, 154, 155, 172, 173] have discussed the importance of

intermetallic particles as initiation sites for corrosion. Intermetallic particles can exhibit two modes of behaviour: passive and active. Passive behaviour is characterised by relatively noble corrosion potentials (E_{corr}) and low dissolution rates [174]. The active behaviour on the other hand, is characterised by active corrosion potential and large dissolution currents [174]. The susceptibility of aluminium alloys to localised corrosion strongly depends on the distribution and electrochemical properties of intermetallic compounds and second phase particles [160, 175]. The electrochemical responses of copper-rich intermetallic particles have received particular attention, since they can be preferred cathodes [163, 176]. The role of particles in relation to corrosion are often described in the context of their galvanic relationship with their surrounding matrix phase, solute depleted zone, or other intermetallic particles present. Furthermore, noble elements, especially if present as precipitated constituents, actually leads to an increase in the corrosion susceptibility of copper-containing aluminium alloys, as a result of the formation of localised galvanic couples [102, 155, 177, 178]. Several studies have shown that the susceptibility of commercial Al-Cu alloys to corrosion is principally due to copper-rich, magnesium-rich and iron-rich intermetallics.

Cast alloys generally contain a high concentration of intermetallic particles which, to some extent, govern the mechanical and physical properties of these alloys. Intermetallic particles generally found in cast alloys are the copper-rich, iron-rich and magnesium-rich intermetallics. In the following sections, the effect of the presence of copper-rich and iron-rich intermetallic on the electrochemical properties of copper-containing aluminium alloys will be discussed.

2.3.2.1 Copper-rich intermetallics - Al_2Cu (θ phase)

A considerable number of studies [31, 176, 179] have been carried out in order to assess the electrochemical behaviour and effect of Al_2Cu intermetallics on corrosion behaviour of Al-Cu alloys, especially AA2xxx aluminium alloys. Scully et al. [180] examined the relevance of Al_2Cu intermetallic compounds to the localised corrosion of aluminium alloys. They found that the open circuit potentials of the Cu and Al_2Cu are $\geq$ 0.75 V more positive than that of Al in inert solutions ranging from pH 2 to 12 [174, 180, 181]. The relationship between E_{pit} and the concentration of chloride ions is:

$$E_{pit}\ [V_{Hg/Hg2SO4}] \rightarrow -1.120 - 0.121 \log [Cl^-] \qquad (2.19)$$

Comparing equation 2.19 to the open circuit potentials obtained from their study, Scully et al. [180] concluded that the open circuit potentials of Al_2Cu in solutions of near-neutral pH are more positive than or equal to the E_{pit} for pure Al over a broad range of Cl^- concentrations. This confirms the widely held view that galvanic coupling of Al_2Cu intermetallic particles to the Al-rich α-phase will promote pitting and deposition corrosion [174, 176, 180, 181]. Deposition corrosion is a special case of galvanic corrosion that takes the form of pitting. It occurs when particles of a more cathodic metal in solution plate out on an aluminium surface to set up local galvanic cells [52]. Corrosion of alloys due to deposition appears to stem from dealloying of intermetallic particles as well as from solid solutions [177]. For Al-Cu alloys, deposition corrosion involves dissolution of copper by corrosion and replating of copper elsewhere on the alloy surface [177, 181]. Replated copper is a far more efficient catalyst for hydrogen and oxygen reduction than an oxide-covered surface on aluminium, and this increased cathodic efficiency stimulates further alloy corrosion [177]. The gap in understanding deposition corrosion in aluminium alloys has existed in relation to how copper is oxidised from the alloy during a corrosion process that occurs hundreds of millivolts negative to the oxidation potential of copper [177, 181, 182]. Copper deposition was studied by Obispo et al. [183], on AA2024 aluminium alloy in 3.5% (0.6 M) NaCl solutions, ranging in pH from 3 to 11. They observed that variations in the pH can alter the integrity and morphology of copper deposits which, in turn, can affect the efficiency of pitting corrosion. That is, nodular copper deposits formed in acidic NaCl environments may be more adherent than those in neutral or basic environments, thereby influencing the frequency of corrosion pits in the matrix [183]. According to Annamalai et al. [184, 185], temperature also has an important influence on copper deposition.

2.3.2.2 Copper-rich intermetallics - Al_2CuMg (S phase)

A further, important copper-rich intermetallic particle is the S phase (Al_2CuMg). These particles are the ones most often observed in AA2024-T3 alloys [186]. The importance of anodic S phase particles (Al_2CuMg) as initiation sites for severe pitting corrosion of copper-containing aluminium alloys when exposed to aggressive environments has been discussed in several papers [4, 25, 183, 187, 188]. The mechanism for pitting associated with S phase intermetallic particles in AA 2024-T3 has been discussed by Buchheit et al

[25]. In summary, they found that corrosion of AA 2024-T3 starts from the dealloying of anodic S phase particles as a result of galvanic corrosion driven by the galvanic couple of anodic S phase and the cathodic aluminium matrix. This resulted in the formation of copper-rich particle remnants in 0.1 M NaCl, which was also confirmed by Zhu and van Ooij [187]. As dealloying continues, the S phase remnants become copper-rich and finally turn into cathodes towards the adjacent Al matrix. Consequently, the opposite galvanic couple of anodic Al matrix and cathodic copper-rich S phase remnant is established [187]. This would lead to another galvanic corrosion, causing dissolution of the surrounding Al matrix [25]. This explanation is not fully supported by the experimental evidence of the study carried out by Zhu and van Ooij [187], although several other authors [4, 189, 190] are in agreement. This gives rise to the question whether or not the galvanic corrosion suggested by Buchheit et al [25] is the primary cause for the severe Al dissolution around the S phase particles? An alternative explanation given by Zhu and van Ooij [187], is that the α-Al matrix is most likely to experience a severe cathodic dissolution due to the local alkalization formed along the dealloying of S phase in the early stages (3.5 hours of immersion in a 0.6 M NaCl solution (pH 6.5)). The overall cathodic dissolution of the surrounding Al matrix consists of the following two simultaneous processes: (1) chemical dissolution of the Al oxide layer; and (2) electrochemical formation of a new layer of Al oxide by the oxidation of the bare Al matrix [187].

However, Schmutz and Frankel [173, 191] supported the explanation given by Buchheit et al [25], that dealloying by preferential dissolution of aluminium and magnesium is responsible for copper enrichment on the surface of the intermetallic particles. The latter showed that dealloying of Al-Cu-Mg particles produces copper particles that are no longer attached to the metal surface, which results in redistribution of copper around the intermetallics. Copper enrichment of S-phase particles after corrosion tests can be explained in two ways, namely, selective dissolution of Al and Mg while Cu remains in the S-phase, or dissolution of the particle followed by copper redeposition [188].

Nitrate ions, which are known to be efficient inhibitors for aluminium, are very aggressive species towards copper. Hence, due to their high copper content and to their less protective oxide film, Al-Cu-Mg intermetallic particles act as anodic sites and are preferentially dissolved, the cathodic reaction being the reduction of nitrate ions. Al, Cu,

and Mg from the particles are dissolved and, when the applied potential is sufficiently low, copper becomes redeposited on and around the particles [188]. The particle with the copper layer becomes more noble in comparison with the adjacent matrix and thus induces the dissolution of the surrounding matrix and simultaneously, nitrate ions induce pitting of the copper enriched particles which continue dissolving [188]. Therefore, Al-Cu-Mg particles act successively as anodic and cathodic sites until they are completely dissolved. However, at high potentials no copper redeposition occurred and nitrate ions protected the AA2024 aluminium alloy from pitting [188]. When Blanc et al [188], performed the same experiment in nitrite solution, copper-rich particles again dissolved but only pitting of the matrix was observed due to the lower amount of hydroxyl ions produced by the cathodic reduction, i.e., nitrite reduction. This shows that nitrite ions are less effective inhibitors of pitting corrosion for 2024 aluminium alloy than nitrate ions.

2.3.2.3 Iron-rich intermetallics

Iron is the dominant impurity found in commercial grade aluminium and aluminium alloys [192, 193]. The solubility of iron in the solid state is very low; hence, most of the iron present in aluminium alloys appears as an intermetallic second phase in combination with aluminium and other elements. It forms intermetallic second phase particles such as Al_7Cu_2Fe, $Al_{23}CuFe_4$, Al_5FeSi, AlSiMgFe, and Al_3Fe depending on the composition of the parent alloy and heat treatment. There is general consensus that iron-rich intermetallics act as local cathodes promoting dissolution of the surrounding matrix. Obispo et al. [183, 192] studied copper deposition on AA2024-T3 aluminium alloys, using TEM/EDX along with a replica-based lift-off technique to enhance the particle and surface debris resolution. They observed large copper clusters deposited on iron-rich or iron-containing areas when AA2024-T3 was immersed in 0.6 M NaCl solutions. They suggested that copper reduction from solution is an electrochemical displacement reaction which is very likely to occur on cathodic particles by oxidization or dealloying of electroactive elements such as iron (Fe) from the particles. A cluster of nodular particles was also displayed on the surface of the dealloyed S phase remnant [187]. This might indicate that, after dealloying to a certain extent, the S phase remnant becomes so cathodic towards the aluminium matrix that it turns into a favourable site for copper reduction.

Recently, Bethencourt et al [22] studied the behaviour of AA2017 alloy in 0.59 M NaCl solution. They observed that Copper-rich intermetallic particles are cathodic with respect to the matrix, and a reaction of reduction of oxygen takes place over these. The associated anodic reaction is the oxidation of the matrix. The authors [22] also observed that the local increase in pH resulted in the dissolution of the layer of oxide and of the matrix that surrounds the intermetallics. According to these authors and several other authors [22, 25, 187, 194], a notable fact in the behaviour of the iron-rich intermetallics is the effect of copper. Small superficial particles rich in copper were observed on the alloy matrix, particularly over the iron-rich intermetallic particles. These authors concluded that the copper originates from Al(Cu,Mg) intermetallics and once the Al and Mg in these particles have been removed, the remaining copper is dissolved due to its porous structure. Hence, this copper in solution is then reduced on cathodic sites such as the Al(Cu,Fe,Mn) intermetallics and thus, appears in the form of nodules. These small nodules were seen deposited preferentially on iron-rich intermetallic particles, while no deposition was observed on Al(Cu,Mg). Bethencourt et al [22] were able to confirm that the layer of oxide formed around the Al(Cu,Mg) intermetallics is rich in copper, while the layer present around the iron-rich intermetallics is less rich in copper. Copper deposition onto iron-rich intermetallics as noted by Obispo et al [183] and Chen et al. [195], may involve a reaction of the form:

$$Cu^{2+} + Fe \rightarrow Fe^{2+} + Cu \qquad (2.20)$$

where the iron-rich particles become the more electropositive substrate [183].

2.4 Corrosion Protection by Conversion Coatings

2.4.1 Introduction

A metal conversion treatment is a specially formulated mixture of inorganic chemicals which react with the metal surface to produce a strongly adherent, corrosion-inhibiting conversion coating on the metal surface. This treatment changes the immediate surface layer of metal into a film of metallic oxide or compound which provides improved corrosion resistance compared with the natural metal oxide film, and it provides an effective base or key for supplementary protection such as paints. They differ from anodic coatings in that conversion coatings are formed by a non-electrolytic (no applied

power) chemical reaction at the surface of the aluminium, whereas anodic coatings are formed using external electrical power [52]. However, conversion coatings are much thinner than anodic coatings and are consequently less durable [97]. Thus, conversion coatings usually form the base for the application of paints or other organic coatings. The main advantages of chemical conversion processes are lower operating and capital costs, as well as speed [10, 196] when compared with anodising. The strength and durability of an adhesively bonded repair depend partly on the adhesive and partly on the metal and its surface pre-treatment. Many pre-treatments have been developed to increase the initial strength and durability of bonds to aluminium and its alloys. Penetration of the adhesive into the pores of the surface film is an important feature of a durable bond [197]. Penetration depends not only on the pore dimensions, but also on the contact angle between the adhesive and substrate, the adhesive viscosity and the viscosity-time characteristics at the temperature of application [197].

2.4.2 Conversion coating of aluminium and its alloys

Before an organic coating is applied, aluminium alloys are often treated by conversion coating to convert the metal substrate to a corrosion resistant surface that more easily accepts and bonds to subsequently applied coatings [198, 199]. This method of protecting aluminium and its alloys from corrosion by conversion coatings has been in use since 1915 [200]. There are three main types of surface pre-treatment based on the following [198]:

- The thickening of the natural oxide film
- The production of a precipitated film of heavy metal phosphates and/or chromates; and non-chromium processes
- The use of synthetic organic polymers

The ideal pre-treatment film possesses the following properties [51]:

1. It should be continuous and impervious to gas and liquids
2. It should be inert or almost insoluble in its environment
3. It should not electrolytically accelerate the attack on the basis metal

4. It should be resistant to mechanical damage such as abrasion or scratching or, if weak and thin, it should be self-healing

5. It should bond readily with paints and other organic finishing materials.

The factors that are of importance are primarily the type and conditions of the conversion process and to a lower degree, types and microstructure of the underlying alloy [201].

2.4.3 Surface chemistry of adhesion to aluminium

Ideally, conversion coatings not only provide some enhancement to the corrosion resistance of the substrate but also function predominantly to increase the adhesion of the subsequent organic layers. Adhesion of coatings to aluminium surfaces undoubtedly depends on the environment, the surface cleanliness, the area of real contact, the properties of the solids and the interface, and modes of junction rupture. The effective rate of permeation from the external environment to the metal surface depends primarily on:

- The thickness of the coating
- The diffusivity and solubility within the homogeneous polymer, and
- The presence of macro- and micro-defects in the coating

Diffusivity and solubility of pollutants are mostly determined by the chemical nature of the polymeric layer and the effective cross-linking achieved during curing of alloys. The use of a coating that is too thin produces uncovered metal peaks and/or thinned polymeric areas. Adhesion across an interface occurs by physical and chemical bond formation [202]. Chemical bonding involves covalent bond formation between the substrate and the adhesive, while physical bonding can involve mechanical interlocking or adsorption due to dispersive or donor-acceptor interactions [202]. Surface treatments usually involve a number of steps carried out under strictly controlled conditions and times [203]. They can be roughly broken down into a cleaning step to remove oils, greases, and dirt; a step in which the existing oxide is removed; in the same or a following step, a new, tailored oxide or conversion coating is formed [203]. In general, the more demanding the environment and/or mechanical performance required, the

more extensive the pre-treatment procedure [203]. For example, the requirements placed on a structural bond in an aircraft will be significantly greater than those required for a packaging laminate, and this is usually reflected by the pre-treatment process adopted.

2.4.4 Mechanism of film formation

The natural oxide film present on all aluminium surfaces is responsible for the comparatively high corrosion resistance of the metal [51, 204]. The thickness of the oxide film varies, depending on alloy composition and processing or exposure conditions but is normally in the range of 5-15 nm [51]. However, the oxidation of aluminium surface stops after this thickness range is reached because the film formed is substantially non-porous and will not allow the passage of the solution to the metal surface [51]. In order to obtain thicker films, it is necessary to include reactants in the solution which will continue to penetrate through the growing film, or that will result in the formation of a film which remains sufficiently porous to allow continued growth [51]. Maintenance of these conditions requires careful control of the pre-treatment solution pH. If the pH is too high or too low, the material formed by reaction with the surface will simply dissolve in the solution and no further film growth will take place [51]. As a result of this, commercially suitable solutions are usually inhibited alkaline solutions or weak dilute acids, such as hydrofluoric, fluosilic, chromic or tartaric acids, which form complex ions. Lithium hydroxides also have a good potential as film forming agents on aluminium substrates. When aluminium substrates react with different pre-treatment formulations, the driving force for film growth is usually provided by an electrochemical process. Film formation occurs through interaction of fluorides in solution (conversion bath) with oxide and hydroxides in the surface of the metal substrate. An understanding of surface characteristics achieved by the different aluminium pre-treatments should help in studying the properties and characteristics of conversion layers formed on aluminium alloys.

Conversion coatings can be applied to aluminium alloys by conventional techniques (rinse, immersion or spray) or by non-rinse processes. An important criterion for non-rinse formulations is that they do not leave water soluble salts in the pre-treatment film following reaction with the metal surface [51]. As a result, some formulations developed for rinse application are not suitable as non-rinse [51]. Non-rinse processes

give films of a generally uniform composition throughout the full film thickness apart from some concentration of the polymeric species in the surface regions of the film [51]. The thickness of the conversion film formed using the non-rinse processes can be controlled by the formulation concentration or by the thickness of solution applied to the surface. Fluorides in conversion bath solutions thin the natural oxide film originally present on the aluminium surface and maintain a thin oxide at the interface between the growing pre-treatment film and the metal substrate by removing any oxides or hydroxides formed. Diffusion of reactants through the gelatinous growing film provides a mechanism for the continuation of film growth on surfaces already covered with a layer of reaction products [51]. Corrosion resistant films can be formed on aluminium and aluminium alloys using formulations comprising metals selected from zirconium, titanium, hafnium, aluminium, silicon, germanium, tin and boron and aromatic sulphonic acid polymers and co-polymers, complex fluorides of boron, silicon, titanium, zirconium or hafnium have been used in pre-treatments [51].

2.4.5 Mechanism of inhibition

Conversion coating of a metal substrate results when the physical or chemical properties of the metal surface is altered by immersion in suitable conversion bath solution to form a partial or complete protective film at the metal-solution interface. The protective film formed is really a reaction product which includes a portion of the base metal as one of the components of the inert film which is commonly known as conversion coating. The mechanism of inhibition of aluminium surface by conversion coating treatments has been the subject of several researches. Several mechanisms have been proposed to explain how and why conversion coatings protect the substrate metals from corrosion. These mechanisms include; barrier layer protection, active corrosion protection, anodic inhibition and cathodic inhibition.

The adsorption theory suggests that the action of inhibitors in suppressing corrosion is based on their adsorption at the metal-solution interface [159]. It was postulated [205, 206] that the inhibitor ions chemisorb on the metal surface, which reduces the chemical activity of the metal [159]. For instance, the mechanism of corrosion inhibition of high strength aluminium alloys by hexavalent chromium containing conversion coatings entails a reduction and irreversible adsorption of Cr^{III} to the surface of the metal to

block sites of adsorption and the release of oxo-Cr(VI) anions that migrate to defects in the coating. Inhibition of the alloy then occurs as a result of the hexavalent chromium compounds adsorbing irreversibly on micro-cathodes on the alloy. This slows the rate-determining oxygen reduction half of the electrochemical corrosion reaction, since oxygen chemisorption is prevented and it becomes a much weaker oxidising agent.

2.4.6 Chromate conversion coatings

Chromate conversion coatings have been widely applied for corrosion protection of aluminium alloys owing to their self-healing nature, ease of application, high electric conductivity and their high efficiency/cost ratio [207]. This type of conversion coating effectively protects aluminium alloys against localised corrosion and promotes excellent adhesion to paints and adhesives [208]. Due to its toxicity and carcinogenic nature, hexavalent chromium is now recognised as a significant threat to both human health and the environment [198, 208-210]. Recent legislation imposes strong limitations in the future use of chromates, e.g. in the automotive and aerospace industries [208]. A number of alternatives for chromate conversion coatings have been developed in recent years [211]. However, none of these appear to match the performance and versatility of the chromate-based conversion processes [208]. The performance of the chromate conversion coatings has been attributed to several factors [208], some of which are listed below [212]:

- Chromate conversion coatings contain residual hexavalent chromium which provides a barrier that separates aggressive environments from the aluminium substrates [203].
- Hexavalent chromium compounds adsorb on aluminium oxides so as to minimise the otherwise positive surface charge, which makes the films less susceptible to adsorption of chloride.
- It provides barrier protection of aluminium matrix due to its hydrophobic character.
- It is stable over a wide pH range.

- Coatings appear to be self-healing due to storage and release of Cr^{VI} species that diffuse to the defect and react with the bare aluminium to form hydrated Cr^{III} oxide which prevents pit initiation.

Fundamental knowledge of mechanisms of chromate conversion coating formation and protection afforded to the metal substrate is a top priority and a prerequisite in developing successful environmentally-friendly conversion coatings (chromate replacements) for different applications. Furthermore, identification of non-chromate based conversion coatings for aluminium and its alloys requires a clear understanding of the mechanism by which hexavalent chromium compounds inhibit and form protective films on aluminium and its alloys [212]. Thus, increased understanding of the mechanisms of nucleation, growth, and corrosion protection of the chromate conversion coatings, is crucial in order to gain insight into steps necessary to reproduce their excellent properties with other systems, which are characterised by a less detrimental impact on health and environment [213].

2.4.6.1 Mechanism of film formation

Previous studies have shown that the morphology of the chemical conversion coating is strongly dependent on the crystallographic orientation of the substrate. This, in turn, appears to control the preferential deposition of the hydrated chromium oxide at grain boundaries or cellular boundaries. Such boundaries for the most part, contain the presumed flaw sites due to the impurity segregation in the metal substrate. Based on these observations, a mechanism of conversion coating growth has been progressed. Chromate conversion coating on aluminium alloys is generated by the reaction of the alloy with an acidic solution containing dichromate. The formation of chromate conversion coating on aluminium alloys requires the presence of fluoride at a pH of 1.2 -1.9, to thin the oxide on the surface, thus allowing the charge transfer reactions to proceed [198, 208]. The chromate-fluoride baths contain about 3 to 4 g/l of chromic acid, 3 to 5 g/l of sodium dichromate, and about 1 g/l sodium fluoride [214]. Most CCCs are produced from these proprietary solutions. However, many contain ferricyanide accelerators [51]. Such accelerated baths contain about 2 to 5 g/l of potassium ferricyanide [214]. The solutions are normally operated at room temperature [51]. Exposure of aluminium to a dichromate-containing CCC solution results in

simultaneous oxidation of aluminium in the presence of complexing F^- and reduction of the chromate to Cr(III) (a protective hydrated film):

$$2Al + 3H_2O \rightarrow Al_2O_3 + 6H^+ + 6e^- \quad (2.21)$$

$$Al_2O_3 + 6HF \rightarrow 2AlF_3 \text{ (soluble)} + 3H_2O \quad (2.22)$$

$$Cr_2O_7^{2-} + 8H^+ + 6e^- \rightarrow Cr_2O_3.H_2O + 3H_2O \quad (2.23)$$

Film growth proceeds by direct contact of the solution with the metal surface through immersion, where aluminium oxide on the surface must be thinned to allow chemical reactions to proceed. Thus, the processes of CCC growth are envisaged as follow [94]:

- Initial chemical reactions of the solution species with the alumina film thus thinning the film
- Ionic transport proceeds to reform the film (anodic process)
- Deposition of $Cr_2O_3.nH_2O$ with any hydrogen evolution (cathodic process) at impurity sites
- The coating developed at cathodic sites, spreads over the surface, thus hindering anodic process
- Stifling of the anodic process
- Conversion coating reaches a limiting thickness of about 400 nm

During the early stages of film formation, the deposition CCC on intermetallic particles can occur at a different rate to that found on the aluminium matrix surface [51]. On thicker films, the particle can be smaller in size than those beneath [51]. As the film thickness increases, a tendency for the film to crack and form a “mud crack” morphology increases [51]. Mud cracking occurs as a result of shrinkage of the film as the large amounts of water trapped between the particles in the gel deposited (conversion film) on aluminium surface are removed during drying [51] and this can increase during ageing. Diffusion of reactants through the gelatinous film provide a mechanism for the continuation of film growth on surfaces already covered with a layer of reaction products [51].

For high purity aluminium, with relatively few impurity segregates, sites of ready electron conduction are in poor supply [94]. For this situation, the chemical reaction of fluoride species with the alumina film proceeds to give an alumina film of reduced thickness, which enables electron tunnelling [94]. Thus, coating formation proceeds as considered previously, although the detailed mechanism is subtly different from that of [94] lower purity aluminium (alloys).

The morphology and composition of the chromate conversion film can be influenced by the formulation of the bath, although structurally the films are composed of amorphous, hydrated $Cr_2O_3.nH_2O$ with an underlying, thin Al_2O_3 layer which has been penetrated by fluoride species [94]. In the presence of phosphate species, generating the very important and very widely used chromate-phosphate conversion coating system, the $Cr_2O_3.nH_2O$ material is replaced by solid chromium phosphate of unknown water content [94]. The common understanding of the structure, chemistry, and performance of CCC has been developed through examination of coatings applied by immersion processing normally under ideal or near-ideal conditions [210]. In addition to substrate microstructure, preceding chemical treatment and formulations of the conversion bath may significantly affect the coating structure [208]. The factors affecting growth rate of CCCs (using acid process) are as follows:

- *Temperature* – thicker coatings are obtained at lower temperature.
- *pH* – coatings produced above pH 2.5 are thinner and less protective.
- *Concentration of fluoride* – too high a concentration results in powdery and thin coatings which give poor corrosion resistance.

2.4.6.2 Film composition and structures

The chromate conversion coatings are essentially amorphous, with composition and structure affected by the preceding chemical treatment and composition of the conversion bath [208, 215]. Abd Rabbo et al. [215] studied the conversion coating development on aluminium in chromate/fluoride solutions using secondary ion mass spectrometry. The conversion coating obtained consists largely of chromium-containing material [215]. After natural immersion of aluminium specimens for 1-15 minutes in a chromate/fluoride conversion solution at a temperature of 293K, it was found that the

film is mostly amorphous but contains a cellular-like structure, with aluminium and fluoride being concentrated in the inter-cellular regions, probably in the form of a complex oxyfluoride. The literature also suggests that CCCs consist of particles ranging in size from 10 nm to 60 nm in layers [24].

The structure and chemical composition of CCCs have been the subject of numerous studies [175, 216-219]. The results of these studies show CCCs to be a mixture of chromium oxides (γ-$CrOOH.nH_2O$), other components from the conversion bath (F^- and $[Fe(CN6)]^{3-}$), and components from the substrate. Chromium is present in CCC as both Cr^{3+} and Cr^{6+}, with Cr^{6+} predominantly in the outer layer [175]. It is generally considered that the molecular structure of the CCC is composed of a precipitated hydrated Cr^{3+} compound, which adsorbs the Cr^{6+} [217, 218, 220]. Further studies by Treverton and Davies [221] showed that conversion coatings developed in chromate baths comprises of a largely hydrated chromium oxide, whereas those formed in the chromate-phosphate treatments are essentially hydrated chromium phosphate.

2.4.6.3 Effect of intermetallics

The growth of chemical conversion coatings on high strength copper-containing aluminium alloys such as AA2024 and AA7075 is complicated by their heterogeneous microstructure, which includes a matrix phase and a variety of intermetallic particles of varying sizes and electrochemical behaviour. Several studies [34-36, 222, 223] have been undertaken to determine the influence of copper-rich and iron-rich intermetallic particles on the formation of chromate-based conversion coatings. Meng et al. [222] suggested that the CCC formation on intermetallic particles is dependent on several factors, such as electrochemical reactivity of the intermetallics, local pH, and the reaction between the intermetallic particles (present in copper-containing aluminium alloys) and the bath composition. Waldrop and Kendig [223] studied the nucleation and growth of CCCs on AA2024-T3 aluminium alloys using atomic force microscopy (AFM). The CCC deposited on the aluminium matrix phase was found to nucleate and grow very fast in the form of nodules. Nucleation and growth of the conversion coating was observed to be faster on Al-Fe-Cu-Mn particles than on Al-Cu-Mg. This is due to the fact that Al-Fe-Cu-Mn intermetallic particles are more cathodically active than the matrix while the Al-Cu-Mg intermetallics are less cathodically active than the matrix

thus supporting slow growth of coating [223]. Hence, the results from the authors indicate that Al-Fe-Cu-Mn intermetallics particles accelerate cathodic reaction of chromate-based conversion treatment but Al-Cu-Mg intermetallics inhibit the reaction. A similar study of the nucleation and growth of CCCs formed on AA2024-T3 was conducted by Brown and Kobayashi [224] using AFM, field-enhanced scanning electron microscopy (FE-SEM) and transmission electron microscopy (TEM). They observed that the growth of CCCs on Al-Cu-Mg intermetallic particles was sustained by anodic dissolution, while the coating growth on Al-Cu-Fe-Mn particles was enhanced by localised dissolution of copper-depleted zones at the periphery of Al-Cu-Fe-Mn intermetallic particles. The authors [224] also concluded that CCC formation and growth of on intermetallic particles strongly depend on the size, shape and composition intermetallic particles. This result is consistent with the observation by Hagans and Haas [34] for the CCC on intermetallic particles present in AA2024-T3 aluminium alloys. They observed that the surface of the alloys appear to oxidise in two discrete steps; the matrix rapidly oxidise followed by slower oxidation copper-rich and iron-rich intermetallics under chromating bath conditions. These authors [34] also proposed that ferricyanide interact with copper-rich particles to form $Cu_4Fe(CN)_6$ or $Cu_2Fe(CN)_6$ and that these compounds promote corrosion resistance by eliminating the galvanic couple that would otherwise form between the noble intermetallic particles and the matrix.

McGovern et al. [36] investigated the CCC formation on bulk synthesised Al-Cu-Mg ingot and AA2024-T3 using Raman spectroscopy. They observed that the CCC formation on Al-Cu-Mg and Al-Cu-Fe-Mn intermetallics was suppressed compared to the matrix. They also found that the higher the Cu content in the intermetallic phases, the thinner the CCC formed due to passivation by adsorbed ferricyanide. When cathodic intermetallics such as Al_3Fe, Al_7Cu_2Fe and θ-phase Al_2Cu were coupled separately with AA1100, Juff et al. [35] observed that the coatings formed on the matrix were ten times thicker than that formed on the intermetallic phases and the coating formation increased linearly with immersion time. Vasquez et al. [225, 226] proposed a refined view of CCCs formed on AA2024-T3. They suggested that CCCs formed on AA2024-T3 are heterogeneous, with the thickness of coatings on θ- and S-phase intermetallic particles observed to be one-tenth that on the matrix. The thickness of the CCC on $Al_{20}Cu_2(MnFe)_3$ intermetallics was found to be non-uniform compared with that formed on the matrix. The cyanide-enriched oxide films formed on the intermetallic particles

were different from those formed on the matrix, and Cr was depleted in the oxide formed on Copper-rich intermetallics.

Baek and Frankel [227] investigated the effect of chromate on the cathodic corrosion rate of thin-film analogues of pure Al, Al-4%Cu, AA2024-T3 alloy, and Al_2Cu intermetallics, with or without chromate using an electrochemical quartz crystal microbalance (EQCM). They suggested that the presence of chromate effectively decreases the net cathodic current densities on the more noble phases such as Cu and $Al_{20}Cu(MnFe)_3$. The presence of chromate was also observed to decrease the anodic reaction rate of Al_2CuMg intermetallics. The minimised oxygen reduction reaction on the θ-phase Al_2Cu and the Al-Cu-Fe-Mn phase by chromate species generates less hydroxyl ions, which attack the surrounding Al matrix and intermetallics and thus, suppresses further development of catalytic Cu on the alloy surface [227]. S-phase particles, which can provide a source for copper redistribution after it is dealloyed and thus generate more active cathodic sites for oxygen reduction reaction are anodically inhibited which further decreases the active sites for oxygen reduction [227]. These combined effects, according to Baek and Frankel [227] make chromate-based conversion coatings a very efficient oxygen reduction inhibitor and subsequently corrosion inhibitor for AA2024 aluminium alloys.

2.4.6.4 Effect of alloying elements

The corrosion protection provided by chromium-based conversion coatings on aluminium alloys can be influenced by many factors such as alloy composition, microstructure and enrichments of the alloying elements within the alloy. The microstructure and morphology of the surface of aluminium alloys is are factors that affect the nucleation, growth and protective properties of chromate conversion coatings. The investigation of CCC on aluminium alloys has been focused on the influence of the substrate microstructure on the nucleation and growth of the chromate conversion film.

Liu et al. [228] studied the growth kinetics of chromate/fluoride conversion coatings on high purity aluminium, Al–2.3at.%Cu, Al–1.9at.%Au and Al–20at.%Au alloys. They found that the addition of copper and gold to aluminium reduces the kinetics of growth of the coating. In the case of gold, increased addition further slows coating development [228]. The results showed enrichments of copper and of gold developing in the alloy

beneath the coating. The reduced rate of growth of conversion coatings on the alloys may be due to thermodynamic and kinetic factors [228]. The enrichment of the copper in the alloy leads to a positive shift in the corrosion potential of Al–Cu alloys, which may indicate a shift in the equilibrium potential of the anodic reaction [228]. Such a shift, expected also for Al–Au alloys, during conversion treatment will reduce the thermodynamic driving force for coating formation that may reduce the kinetics of growth [228]. Enrichment of copper on the surface during pre-treatment and CCC processing plays a critical role in coating formation and performance of the treated substrate [203]. For the Al–1.9at.%Au alloy, gold is present as metal nanoparticles, rather than an ionic species. Although depending on the conditions at the alloy/coating interface, the possibility of direct incorporation of nanoparticles of copper can not be ruled out. These nanoparticles could present a physical barrier to ionic transport in the coating. However, the volume of particles in the coating is low, and the population density is probably too low to affect significantly the kinetics of coating growth [228]. For the Al–20at.%Au alloy, there is a much greater possibility of physical hindrance of ion transport in the coating, although pathways around particles still appear to be present [228]. Thus, the slower rate coating of the aluminium alloys, compared with that of the high-purity aluminium, suggests that the enrichment of the alloying element leads to the reduction in growth rate of coatings [228]. The presence of Cr(VI) species in the hydrated Cr(III) oxide of the coating material [218, 229] can be explained by transport of Cr(VI) species through the coating to sites of coating formation near the alloy. With thickening and possible ageing of the coating, the transport of Cr(VI) species is expected to slow, thereby reducing the rate of coating growth [228].

Chromate conversion coatings on Al–Cu and Al–Au alloys contain increased numbers of cathodic sites following achievement of the relevant maximum enrichments of the alloys [228]. Several possibilities may then arise: the particles may physically weaken the bonding of the coating to the substrate; enhanced reduction of chromate may generate new coating material at a relatively high rate within the existing coating, with stresses leading to detachment; hydrogen gas may be evolved with pressures mechanically disrupting the pre-existing and newly forming coating near the alloy/coating interface [228]. Such hydrogen gas evolution may explain the modified appearance of coating material formed at times after the initial detachment, with channels possibly then allowing release of gas to the solution without major disruption

of the coating [228]. Increased evolution of hydrogen may also slow down coating growth if the rate of reaction is under anodic control.

In recent studies, the influence of alloy metallurgy in the formation of CCCs on aluminium has been addressed, particularly for the high-strength AA2024-T3 alloy. Waldrop and Kendig [223] studied the nucleation of chromate conversion coating using Al 2024-T3 alloy. They reported a significant difference in coating nucleation behaviour on the alloy matrix and on two distinct intermetallic phases. After a short immersion in a chromate bath, the film nucleation was reported to be faster on the Al-Cu–Fe–Mn particles than on the aluminium matrix, whereas that on the Al-Cu–Mg particles was considerably slower [223]. Other studies reported that the final coating thickness on the intermetallic particles was less than on the alloy matrix [36, 214].

It appears that coating nucleation and growth on AA2024-T3 alloy is influenced strongly by the size, shape and composition of the intermetallic particles present as well as the composition of the neighbouring matrix region. In general, it is observed that the final coating thickness on Cu- and Fe-containing particles is significantly thinner than on the aluminium matrix [36, 208]. Brown and Kobayashi [224] revealed that initial stages of CCC growth on a clean and fresh AA2024-T3 alloy surface take place at coarse Al_6(Cu,Fe,Mn) particles and over an outer lying matrix region surrounding the particles [224]. Coating growth was supported by anodic dissolution of aluminium from a copper-depleted matrix zone immediately adjacent to the particles [208]. Liu et al. [230] compared the formation of chromate/fluoride conversion coatings on solid-solution binary Al-Cu alloys with that on commercial 2014-T6 alloys. They found that the initial growth of chromate/fluoride conversion coatings formed on solid-solution binary Al-Cu alloys develops with oxidation of aluminium only, while copper enriches in the alloy to the required level for its incorporation into the coating [230]. This leads to an associated loss of coating material, thus limited subsequent thickening of the coating. Conversion coating of commercial AA2014-T6 alloy was shown to result in regions of relatively thin and thick coating material which mainly reflect the local distributions of copper and the influence of copper on the development of the coating layer [230].

Meng and Frankel [93] investigated the effect of copper content on chromate conversion coating protection of AA7xxx-T6 aluminium alloys. They found that each CCC-treated

AA7xxx-T6 alloy exhibits only one breakdown potential, which is slightly higher than the second breakdown potential for the bare (untreated) alloy [93]. They concluded that alloyed copper has different effects on CCC protection: copper is beneficial to CCC protection for coating formed on polished AA7xxx-T6 alloy, but copper is detrimental if it is enriched on the surface prior to CCC formation [93].

2.4.7 Zirconium-based conversion coatings

The heavy restrictions on the use and disposal of chromate containing conversion coating have led to an exhaustive search to find suitable replacements [98]. Several alternative conversion coatings (often called chromium-free conversion coatings) processes which can be used to provide improved corrosion protection of aluminium alloys have been developed. One of these alternatives is surface treatment based on group IV-A fluorides. Among these alternative conversion coatings developed so far, only those based on zirconium salts gain wide acceptance [231]. Zirconium-based conversion coatings improve corrosion protection and paint adhesion of aluminium alloys. The corrosion resistance of these coatings is not considered to match that of chromate conversion coatings [35]. However, they have not been tested over the wide range of environments in which chromate conversion coatings have proved effective [51].

2.4.7.1 Mechanism of film formation

Zirconium-based conversion coating on aluminium alloys is generated by the reaction of the alloy substrate with a zirconium-based bath. Film formation occurs by interaction of the fluorozirconate with hydroxides at the surface of the metal substrate. Zirconium-based conversion coating is assumed to form by the precipitation of zirconium oxide due to an increase in pH (hydrogen evolution at cathodic sites leads to a local increase in pH) of the bath solution at the metal oxide/liquid interface. The solubility of the coating compound decreases when the pH increases, resulting in precipitation of coating material.

One of the first zirconium-based conversion baths contained boric acid, a source of fluoride, a source of zirconium, and nitric acid for pH adjustment. A typical example contains [51]:

- 0.4 g/l K_2ZrF_6
- 5.0g/l H_2BO_3
- 10.0g/l KNO_3
- 0.4ml HNO_3 (4N)

The solution is used at a pH of 3-5 and at a temperature of 50-65^{0}C [51]. According to Deck et al. [232], treatments must be applied at pH values less than approximately 4.5 because of insufficient solubility in less acid environments. Formulations can be applied by conventional techniques (rinse, immersion or spray) or by non-rinse processes [51]. An important criterion for no-rinse formulations is that they do not leave water soluble salts in the conversion film following reaction with aluminium surface [51]. Non-rinse versions of the zirconium-based conversion coating are similar to the rinse formulations, but often result in the deposition of thicker films on the metal surface [51]. Non-rinse applications give films of a generally uniform composition throughout the full film thickness [51] apart from some concentration of the polymeric species in the surface regions of the film [51]. Film formation occurs through interaction of fluorozirconate with hydroxides in the surface of the metal substrate. Some replacement of oxides with fluorides in surface regions of the film also occurs, but the majority of the film analyses as a mixture of zirconium and aluminium oxyfluorides [51]. The literature showed that the double-layered coating films formed by immersion processes (rinsed) are not being found in films deposited by no-rinse processes. Clearly, the coating does not develop in a similar manner to Cr_2O_3 or $CrPO_4$ coating since ZrO_2 type material can only be produced by interfacial pH changes [35].

Zirconium-based conversion coatings based on ammonium zirconium carbonates can give effective coating performance on aluminium alloys. Such formulations also contain polyacrylic esters or salts, and can be applied by spray, immersion or flow coating contacting methods. The coating can also be used to enhance the corrosion performance of conventional chromate and phosphate processes [51]. Because of their high formability, conversion films formed using this formulation can show good coating adhesion.

2.4.7.2 Film composition and structures

Zirconium, aluminium, oxygen and fluorine are the main constituents of the conversion film, with zirconium accounting for about 36% of the total weight [51]. It has been considered that zirconium species are bonded to the hydrated aluminium film covering the aluminium surface [51]. From in-depth elemental profiles through the resultant film, the film has been considered to be multi-layered, with Al_2O_3 adjacent to the aluminium surface, a Zr/O/F containing outer layer and ZrO_2 sandwiched between the previous layers. The literature reveals that zirconium is always present in its dioxide form ZrO_2, and some hydroxy-oxide or hydroxyfluoride may also be present depending on the composition of the conversion bath [233]. Recently, Survilience et al. [234] studied the effect of ZrO_2 particles added to Cr(VI) bath on the corrosion properties of chromium-based conversion coatings, they observed that ZrO_2 particles enhance the corrosion resistance of chromium coating.

Schram et al. [231] studied the composition of a commercial zirconium-based conversion coating (Alodine 4830/4831) which contains mainly a fluorinated zirconium salt and a water soluble polymer. They reported a two-layered structure for zirconium-based conversion coating, in which the inner region (close to the metal interface) contains only Al and O, while the outer region (closer to the outer surface) contains a fluorinated zirconium compound as well as a polymeric compound. They also concluded that the thickness of the conversion layer formed on AA1050 aluminium alloy was nearly independent of the conversion time.

In order to characterise the microstructure and chemical composition of zirconium-titanium based conversion coating, Nordlien et al. [199], studied the formation mechanism of these films on AA6060 using a commercial Alodine 2840 bath. They reported preferential nucleation of the zirconium-titanium oxide films due to its growth on and around intermetallic particles and this resulted in reduced cathodic activity of the particle. Thus, passivation of the cathodes in this manner constituted a limitation in the formation of a good quality conversion layer [199].

While a few investigations [51, 199, 235] have been carried out on the formation of zirconium-titanium conversion coatings, limited information is available in the accessible literatures regarding zirconium-based conversion coatings. Further

investigation needs to be carried to investigate the mechanism of inhibition; effect of copper-rich and iron-rich intermetallics; and the effect of alloy composition on the formation and protection of zirconium-based conversion coating as a possible alternative to chromium-based conversion coatings.

2.4.8 Other non-chromate conversion coatings

Hexavalent-chromium-based conversion coating systems have been used for over 60 years, providing excellent corrosion resistance and paint adhesion characteristics when used with aluminium and its alloys [214]. Hence, chromium-based conversion coatings have been the standard against which other conversion coatings have been judged. Any replacement coating process must be designed to duplicate these characteristics as closely as possible. Thus, alternative processes for chromate conversion coatings on aluminium alloy surfaces represent a research challenge for environmental reasons. The hexavalent chromium present in several coating systems is known to be carcinogenic and environmentally hazardous [236]. This is the reason why the development, testing and usage of chromate-free conversion coating systems are increasing. Presently, CCC remains an essential component in effective corrosion protection systems on aluminium alloys [210] for many applications. In order for candidate non-chromate conversion coatings to gain attention as viable candidates for many applications, they must meet the performance characteristic of CCC and must be environmentally friendly. Alternative processes have been developed, giving rise to the following chromium-free conversion coating processes;

- Zirconium-based conversion coating
- Titanium-based conversion coating
- Permanganate conversion coating
- Cobalt-based conversion coating
- Cerium-based conversion
- Ammonium-zirconium carbonate conversion coating
- Lithium-based conversion coating

Zirconium-based conversion coating has been discussed in the preceding section. Attention is now given to other non-chromate conversion coating systems.

2.4.8.1 Titanium-based conversion coatings

Recent studies into non-chromate conversion coatings have identified several potential bath chemistries that might replace conventional chromate-based baths. Titanium-based conversion coatings are gaining increased acceptance as viable alternatives to chromate conversion coatings with several studies having been carried out on these coatings. Some studies reported that, for no-rinse treatments prepared from hexafluorotitanic acid, H_2TiF_6, a steady increase in the pitting potential is seen during immersion in 5 g l^{-1} or 35 g l^{-1} NaCl solutions, with an increasing separation between pitting potential and corrosion potential over time (indicating a decreasing tendency to pitting) [237]. Furthermore, much lower corrosion rates were found compared with the bare as-cleaned alloy. In order to improve the characteristics of such films, various polymers have been added to the treatment in order to provide chrome-equivalent corrosion protection and to facilitate the adhesion of paint [232].

Several studies have focused on the properties and effect of coatings incorporating tannic acid (TA) and polyacrylic acid (PAA) in the bath formulations. Smit et al. [237] used polarisation curves to assess the effect of organic additives on the performance of titanium-based conversion coatings. They found that when either tannic acid or poly(acrylic acid) was incorporated into no-rinse conversion coatings based on H_2TiF_6, they performed better than coatings without inhibitor on first exposure, giving higher pitting potentials and lower corrosion currents. However, longer exposure led to a deterioration in performance [237]; eventually, protection was worse than for coatings without organic additives as shown by the lower pitting potential, decreased separation between pitting and corrosion potential, and higher corrosion currents, than coatings from H_2TiF_6 alone [237]. Several authors have suggested that dissolution of the organic components occurs from such coatings during immersion [238-240] and this may be responsible for deterioration in performance. At short immersion times, coatings of PAA or TA provide improved anodic inhibition to either bare alloy or simple coatings of H_2TiF_6 alone, as shown by the decreased anodic currents and increased corrosion potential.

Acidic and alkaline titanium-based formulations have been developed for immersion or solution pretreatment [51]. Alkaline solution (pH between 11.5 and 13.5) contains titanium ions and a complexing agent. After rinsing, the conversion film formed is treated in an acid solution containing tannin or tannic acid [51]. Most acidic titanium-based formulations are based on hexafluorotitanic acid and may also contain tannin or tannic acid as well as organic acids, polymers and other metal oxides. Many titanium-based bath formulations are similar to zirconium-based conversion coating formulations, apart from the replacement of fluorozirconate (ZrF_6^{2-}) by fluorotitanates (TiF_6^{2-}).

The performance of several titanium-based conversion coatings has been studied by Fedrizzi et al. [241]. They reported that fluorotitanate or fluorozirconate coatings can give similar performance to conventional chromate-based treatments, when used as pre-treatment for an organic coating. Smit et al. [242] studied the performance and characteristics of a no-rinse titanium-based conversion coating on AA3003 aluminium alloy. They concluded that the application of a H_2TiF_6 based conversion coating to AA3003 aluminium alloy improves the anodic inhibition of the alloy and reduces the corrosion current density [242].

High resolution XPS studies of films formed by fluorotitanate formulations suggest that the overall film forming reaction is [2]:

$$H_2TiF_6 + 2Al_2O_3 \rightarrow 4AlOF + TiOF_2 + H_2O \quad (2.24)$$

A combination of XPS, Auger depth profiles and chemical analysis suggests that the surface region of the film comprises [2]:

$$4AlOF.TiOF_2.H_2O \quad (2.25)$$

The composition of the majority of the film is given by the following:

$$Al_2O_3.4AlOF.TiOF_2.H_2O \quad (2.26)$$

2.4.8.2 Permanganate conversion coating

Passing across the third row of transition metals, from left to right, there is much similarity between the elements in terms of their chemical and physical characteristics,

until iron is reached [214]. Thus, the conversion coatings produced by hexavalent chromium compounds are, as expected, similar to those produced by heptavalent manganese [214] found in permanganate conversion coating. Similar to the chemistry of hexavalent chromium compounds, the heptavalent-manganese-based conversion coating contains a blend of manganese of various oxidation states and aluminium oxides. Higher oxidation state manganese oxides are reduced to a lower oxidation state, as necessary, in order to prevent oxidation of the aluminium, just as higher-oxidation-state chromium oxides are reduced in the hexavalent conversion coating system [214]. Permanganate conversion coating formulations give a yellow-gold colour, which is similar to that of the chromium conversion coating system. The main difference between the two conversion coating systems is that hexavalent chromium conversion coating system produces a protective inorganic polymer, unlike the heptavalent manganese-based system. This reduces the protective properties of the permanganate conversion coating. Unlike chromate conversion coatings, permanganate films do not lose their corrosion resistance when heated above 65^0C [51].

Permanganate conversion coating is generated in a five-step process, involving a solvent clean, alkaline clean, rinse, treatment in permanganate solution, and a final rinse. The conversion bath is acidic (pH 2.5-4.0) and contains aluminium nitrate ($Al[NO_3]_3$) and potassium permanganate ($KMnO_4$). The preferred operating temperature is between 60^0C and 65^0C and the selected deoxidizer is nitric acid/bromate (HNO_3/BrO_3^-)-based [214]. The primary component of most pre-treatment formulations are potassium and sodium permanganate [51]. Because of their non-toxicity, permanganate-based formulations do not present the effluent disposal and handling problems associated with hexavalent chromium treatments.

Danilidis et al. [243], examined the properties of manganese-based conversion treatment on an Al-Mn alloy. They found that conversion coating formed a uniform, dense, thin (15-20 nm), and well-adhering layer on the metal substrate. They further concluded that the manganese-based conversion coating in many respects resembles that of chromium-based films [243]. Hamdy and Beccaria [244] investigated the effect of permanganate treatment on the corrosion behaviour of aluminium composites under different conditions. They showed that permanganate treatment improves the corrosion protection of aluminium composites in NaCl solution by forming a compact passive

film of manganese oxides over the aluminium oxide layer [244]. The corrosion protection obtained after 3 hours of treatment at neutral pH is better than that obtained at pH 8 [244]. Furthermore, they concluded that the surface of manganese oxide layer has a dual effect on the corrosion inhibition of aluminium composites. Due to the 'basic' electron donor properties of Mn ions, they inhibit the adsorption of chloride ions and, owing to their buffer action, the local acidic sites were reduced; hence, the resistance to localised corrosion was increased [244].

2.4.8.3 Cobalt-based conversion coating

Cobalt-based conversion coatings have been developed primarily for the aircraft industry as possible replacements for chromate-based formulations [51]. This coating process is currently finding application in the marine and automotive industries. The conversion coating contains a trivalent or tetravalent cobalt/valence stabiliser complex. The coating formulations are prepared by dissolution of Co(III) salts and a metal acetate (e.g. Na, Mg or Ca acetate) to form a solution of cobalt (III) hexacarboxylate complex [51]. Bath formulations based on cobalt acetate give the best overall performance, but the best paint performance is obtained using cobalt nitrate [51]. Conversion coating can be applied on aluminium surfaces by immersion, hand or spray processes. Other variations to cobalt-based processes, claimed to be commercially practicable for the aircraft industry, involve contacting the metal surface with an aqueous solution prepared by reacting [51]:

- A cobalt (II) salt
- An ammonium salt
- One or more complexing agents selected from a soluble metal carboxylate, a soluble metal nitrile or ammonia
- A water soluble amine
- An oxidising agent

Hughes et al. [245] examined the development of the deoxidation, cobalt-containing conversion coating and sealing steps on AA2024-T3 alloy and AA7075-T6 alloy. This resulted in the growth of an open porous oxide structure over the matrix of the alloy.

They found that increasing immersion time resulted in an increase in thickness of conversion layer but little change in the composition of the coating.

The main component of the coating formed in all cases is aluminium oxide, but they also contain a mixture of cobalt oxides: CoO, Co_2O_3 and Co_3O_4 [51]. Aluminium oxide is the main component at the interface between the film and metal substrate, while Co_2O_3 and Co_3O_4 are concentrated at the surface of the film, and the centre regions contains a mixture of all four oxides [51].

2.4.8.4 Cerium-based conversion coatings

Lanthanides ions, such as Ce^{3+}, Y^{3+}, La^{3+}, Pr^{3+} and Nd^{3+}, form insoluble hydroxides, have a low toxicity and their ingestion or inhalation is not considered harmful to health [246, 247]. Hence, some of the most promising chromate replacement conversion coatings are derived from these rare-earth elements, particularly cerium (Ce), which is relatively abundant in nature and offers the best degree of inhibition due to the formation of a compact film of cerium oxide and hydroxides. Corrosion protective film can be simply formed by immersion of an aluminium alloy in a solution containing 100-1000 ppm cerium chloride [51]. Two different theories, based on XPS studies [248, 249], were postulated to explain the formation of a mixed Ce(III)/Ce(IV) hydrated oxide in the presence of oxygen. The first theory asserts that local increase of pH caused by the oxygen reduction reaction enables the precipitation of solid Ce(III) hydroxide, which finally oxidises to hydrated CeO_2 [250, 251]. Conversely, Aldykiewicz et al. [252] proposed that the first step of film formation involves the oxidation of Ce(III) to Ce(IV) in solution, which can in turn, precipitate as insoluble CeO_2 due to a local pH increase as a result of the cathodic oxygen reduction.

Many studies have been undertaken on the mechanism of inhibition of cerium conversion coatings deposited on copper-containing aluminium alloys in aqueous solutions containing cerium salts. Aldykiewicz, et al. [252] suggested that the inhibition of the aluminium alloys is achieved by deposition of a cerium-rich film on the copper-containing intermetallics which blocks the cathodic reduction of oxygen at these sites.

Inhibition of corrosion by cerium is also believed to involve decreasing the rate of cathodic oxygen (O_2) reduction by precipitation of Ce(III) hydroxide ($Ce[OH]_3$) at

regions of high pH [51, 253]. This mechanism requires the activation across the metal surface of many electrochemical cells associated with microscopic features such as grain boundaries, precipitates, constituent phases and inclusion, or submicroscopic features such as flaws in existing naturally occurring oxide films [249]. The cathodic processes generate alkaline conditions close to the metal surface [249]. These conditions lead to localised precipitation of an hydrated cerium oxide and the formation of the film. Film formation can be accelerated by cathodic treatment in cerium chloride or cerious nitrate dissolved in butoxyethanol, but the film formed provides reduced corrosion inhibition to the aluminium substrate [51].

However, it is worth mentioning that in spite of the simplicity of the process involved in the formation of cerium-based conversion coatings on aluminium alloys, it is commercially unattractive due to the long duration of time required for the conversion treatment. A first attempt to reduce the duration of treatment was based on galvanostatically polarising the aluminium surface in aqueous $CeCl_3$ bath [247] or in a solution of cerium salts in organic solvents. However, the necessity of high direct current (DC) potentials in tandem with a volatile organic solvent makes the industrial application of this method difficult [247]. A conversion coating based on the use of aqueous solutions of $CeCl_3$ and hydrogen peroxide was later developed to produce passivating films in much shorter time [209, 254] on aluminium alloys by increasing the temperature of the cerium-based bath. Mansfeld et al. [255, 256] proposed the immersion in boiling aqueous cerium salts solutions in combination with an anodic treatment in 0.1 M Na_2MoO_4, however, the industrial application of this process is complicated by both the use of the boiling bath as well as the additional cost from the anodic step. Wilson and Hinton [257] developed and patented a less complicated method involving the addition of hydrogen peroxide (H_2O_2) to cerium chloride bath to form a cerium oxide/hydroxide film on Al-Cu alloys in a very short time (approximately 10 min). The acceleration effect of H_2O_2 may simply be related to the rapid increase in pH caused by its reduction that favours the precipitation of cerium oxide/hydroxide [247]. Hydrogen peroxide also enhances the oxidation of Ce(III) to Ce(IV) ions in solution and this results in an hydroxide film containing cerium mainly in the 4-valent state, as observed by XPS studies [247, 254].

For copper-containing alloys, AA2024-T3 and AA7075-T6, improved corrosion performance is achieved by electrochemically removing surface copper-containing intermetallics prior to processing [51]. From the XPS results obtained, the mechanism of cerium-based conversion coating formation can be speculated. The H_2O_2 is the oxidizing agent, while Ce(III) is a reducing agent. Ce(III) is oxidised to Ce(IV) and Ce(IV) is stable in the solution, thus changing the solution from colourless to yellow. Anodic dissolution occurs at different locations according to:

$$Al \rightarrow Al^{3+} + 3e^- \quad (2.27)$$

While, at the cathode, hydrogen evolution or reduction of peroxide and oxygen in the solution according to:

$$2H^+ + 2e^- \rightarrow H_2 \quad (2.28)$$

$$H_2O_2 + 2H^+ + 2e^- \rightarrow 2H_2O \quad (2.29)$$

$$O_2 + 4H^+ + 4e^- \rightarrow 2H_2O \quad (2.30)$$

Wang et al. [258], used electrochemical methods and immersion tests to study the kinetics of the cerium chemical conversion coating formation and their corrosion resistance in 3.5% sodium chloride (NaCl) solution on aluminium alloy AA2024-T3. They suggested that a simple cerium conversion coating process for AA2024-T3 alloy involved immersing the alloy in a solution containing 10 g/l $CeCl_3.7H_2O$, 40 ml/l H_2O_2 (30 wt%), and 2 g/l $ZnCl_2$ at room temperature for 6-10 minutes , keeping the pH of the solution at 3. They found that the conversion coatings were composed of spherical particles which contain higher contents of oxygen and cerium than other sites [258]. The $ZnCl_2$ effectively accelerated the rate of coating formation, thus shortening the treatment time [258].

2.4.9 Health considerations

The use of chemical conversion coatings on aluminium alloys to achieve long-term corrosion resistance as well as the base for application of organic materials (particularly paints and lacquers) has found widespread applications. The use of chemical conversion coatings that do not contain harmful chemicals that can endanger human health and pollute the environment is of particular interest to the Federal Environmental Agencies,

aerospace and transport industries. At the core of the problem is the demonstration of human health effects associated with exposure to hexavalent chromium [259]. Since hexavalent chromium is a human carcinogen, concern exists not only about workplace exposure at high level, but also environmental exposure at much lower levels [259]. Hexavalent chromium or chromate is currently the most effective way to inhibit corrosion of aluminium alloys [98]. The Environmental Protection Agency (EPA) is the main regulator of chromate uses and emissions through several different acts including the Clean Water Act, the Comprehensive Environmental Response, Compensation and Liability Act (CRCLA) and Toxic Substances Control Act (TSCA) [260]. National emission standards for hazardous air pollutants (NESHAP) were proposed for chromium along with 188 other hazardous air pollutants (HAP) listed in the Clean Air Act [98]. Unfortunately, the same properties that make Cr^{6+} a superior corrosion inhibitor are also responsible for it being environmentally unsafe. It is the strong oxidation properties of chromates that have brought much scrutiny concerning their use [98]. It appears that Cr^{6+} does not intimately react with human DNA, but instead goes through a reduction to Cr^{5+} which is responsible for the DNA damage (mutation in bacteria and transformation of mammalian cells) [261]. Chromate exposure is primarily through inhalation, ingestion and through skin contact. The most common effect of exposure to chromate is lung cancer, but the toxicological effects are not limited to cancer alone [260]. Although there is speculation that eventually chromates will be completely banned from use, the current legislative trend is following the same path as volatile organic compounds (VOCs) [98] in the sense that they are reduced significantly but not totally eradicated.

The economic and environmental burden of using chromates has drastically affected the aerospace industry due to its dependence on the use of aluminium based alloys in manufacturing aircrafts [98]. Environmentally, the industry must deal with lower limits of exposure to workers as well as controlled release and clean-up of by-products an waste generated by its use [98]. This concern has produced a cascade of consequences, including [259]:

- Increased liability for claims of workplace and environmental exposure
- Increased cost for tracking inventories, monitoring emissions, reporting usage of chromium compounds, and disposal of solid waste containing chromium

- ❖ More stringent disposal limits for discharges of dissolved chromium in wastewater.

Therefore, environmentally acceptable alternatives for chromate-containing conversion coatings that exhibit the same corrosion resistance as chromate coatings are needed.

2.4.10 Introduction to present work

Due to the current push to replace chromium-based conversion coatings, special attention has been paid to alternative, so-called chromium-free conversion coatings, which are more environmentally-friendly than hexavalent chromate conversion coatings. A vast variety of coating bath exists accompanied by pre-treatment and post treatment processes. Some of these alternative coating chemistries have been reported to have good corrosion resistance, but the processes either have too many steps or involve high temperature steam or boiling water, which makes them expensive and sometimes impractical for industrial applications.

Zirconium-based conversion coating is one of the possible candidates that might be able to replace hexavalent chromate-based conversion coatings. In order to ultimately achieve a chromate-free corrosion inhibitor, it very important to gain a complete understanding of zirconium-based conversion coating interaction and protection mechanisms of aluminium alloys and its constituent particles. This type of conversion coating system is a comparatively recent development compared to chromium-based conversion coatings and limited information is available in accessible literatures about its morphology, composition, mechanism of inhibition and other characteristics. Hence, a great deal still needs to be learned about the coating formation and degree of protection provided by zirconium-based baths on different aluminium alloy systems, particularly copper-containing aluminium alloy, which is one of the most widely used high strength aluminium-based alloys in aircraft and it provides a ready source for Cu-containing inclusions in the protective oxide surface film. Therefore, the present extensive use of this alloy and similar aluminium alloys with relatively high Cu content should have serious consequences for the integrity of aircraft structural materials, when the operational service life of aircraft is extended far beyond its design life.

The primary goal of this research effort was to develop, characterise and evaluate conversion coatings based on zirconium bath formulations as a substitute for chromate systems. An additional objective is to investigate some of the more fundamental aspects of the phenomena involved in the formation of zirconium-based protective films on aluminium and copper-containing aluminium alloys. In order to gain full insight into the effects of copper on Al-Cu solid solution alloys, the present work displays an overview of the results recently obtained relating to the effect of copper alloying element on the zirconium conversion coating of aluminium-copper alloys. The growth of zirconium-based conversion coatings on magnetron sputtered superpure aluminium and a range of binary aluminium-copper alloys of a variation of %Cu composition were examined as a function of immersion time in the aqueous bath. The use of sputtering-deposited metastable alloys, free from significant amounts of second phase, allows relatively precise measurement of thickness changes of the deposit due to growth of the coating, by transmission electron microscopy [228]. By combining the information obtained from several analytical approaches, it is intended to develop a comprehensive and consistent model accounting for the effect of solid solution alloying elements on the behaviour of binary Al-Cu alloys in zirconium-based conversion coating bath.

In order to understand the electrochemical behaviour and influence of the conversion bath on the protection of aluminium and copper-containing aluminium alloys, the corrosion behaviour of the specimens was studied in sodium chloride electrolyte following conversion coating, to investigate in more detail the mechanisms affecting corrosion inhibition under these conditions. A suite of aluminium and Al-Cu alloys specimens, all of which had been immersed for selected times in zirconium-based conversion coatings followed by salt spray testing of selected specimens were also investigated. For a complete understanding of the inhibition action from zirconates, inhibition must be viewed through the prism of electrochemical differences between the matrix and constituent particles. The goal is that zirconium-based conversion coatings, tailored and maximised for specific environments may be able to provide comparable inhibition as chromium-based conversion coatings over narrow but acceptable environmental windows.

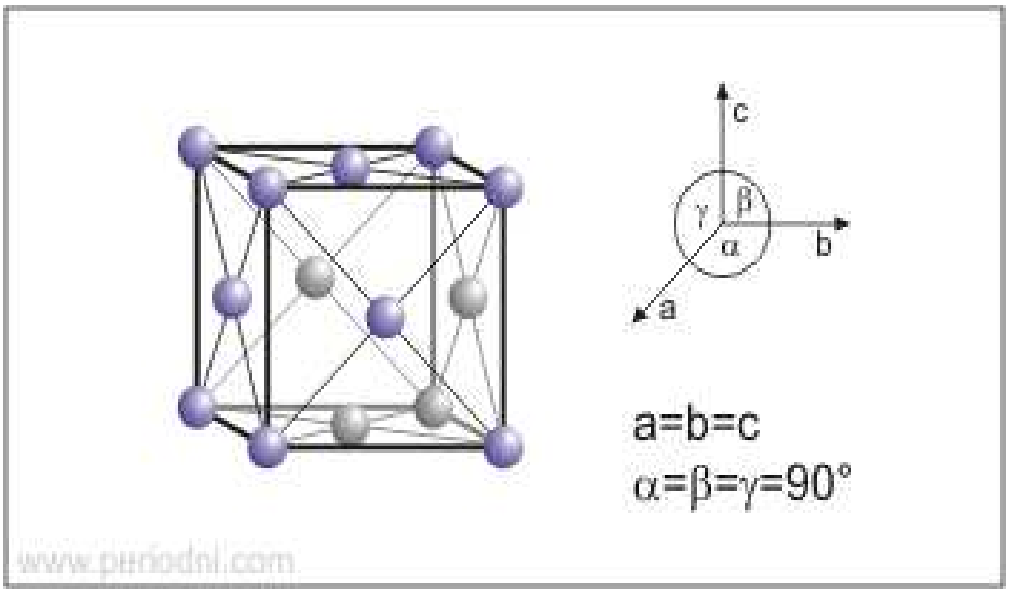

Figure 2.1 Crystalline structure of aluminium, showing (a) face-centred cubic structure and (b) orientation of crystal

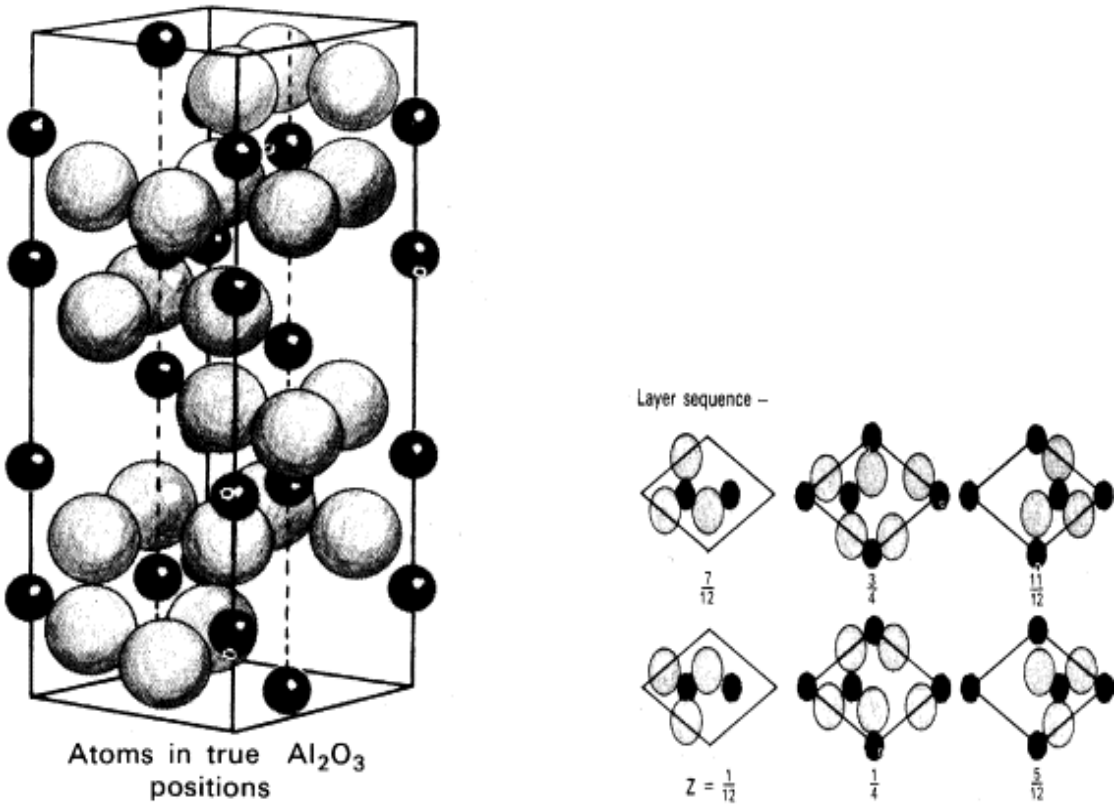

Figure 2.2 The corundum structure [62] ●-aluminium; ○-oxygen

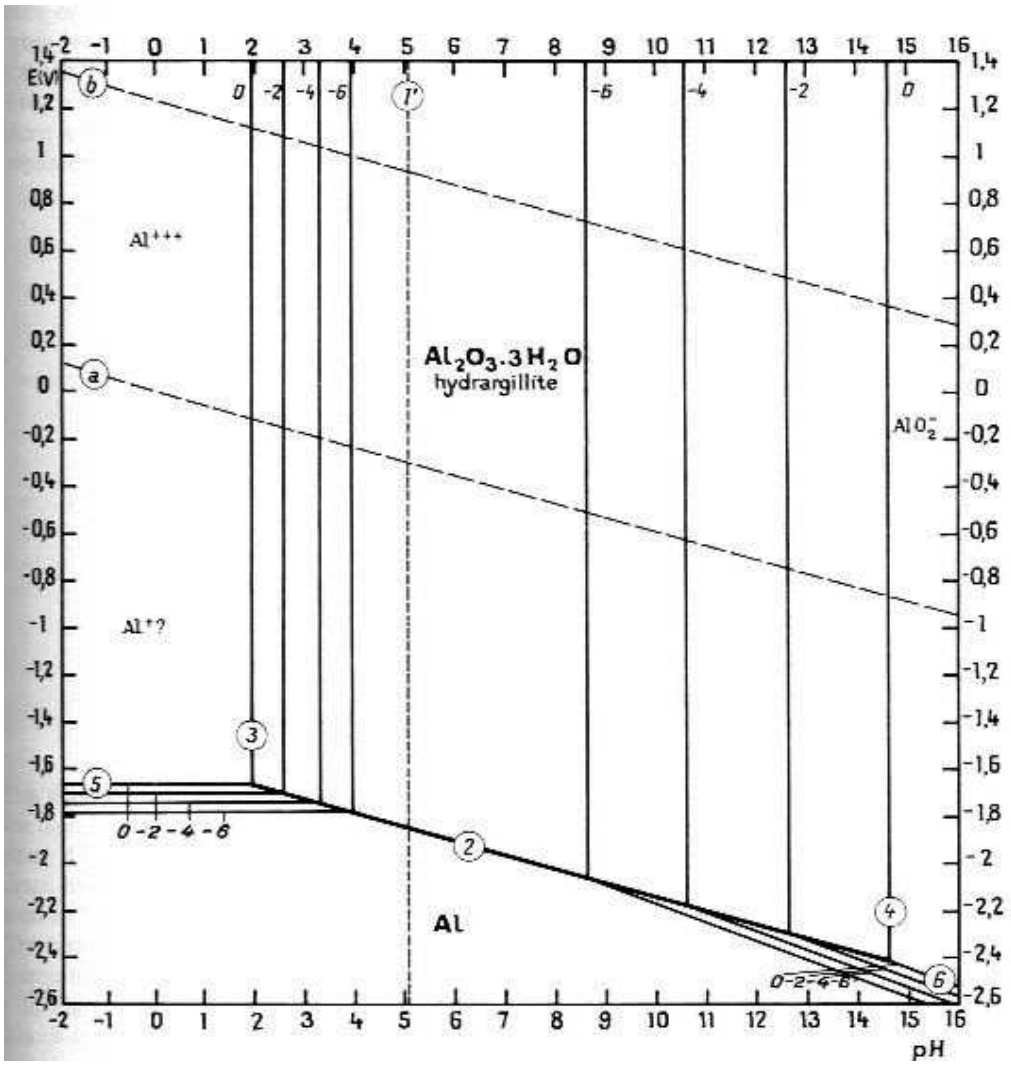

Figure 2.3 The Pourbaix diagram for aluminium with an hydragillite ($Al_2O_3.3H_2O$) film at 25^0C (www.olwnet.rice.edu/)

CHAPTER 3

3 EXPERIMENTAL PROCEDURE

3.1 Introduction

The surface of a solid in contact with a liquid or gaseous phase usually differs substantially from the interior of the solid both in chemical composition and physical properties [262]. Characterisation of the surface properties of aluminium and its alloys is often vital in corrosion, and in adhesion mechanisms. Successful application of various aluminium alloys often requires surface treatment and finishing for cleaning, brightening, wear and corrosion resistance. The details of the materials used in this research, including specimen and solution preparation, the experimental approaches including electrochemical measurements are presented in this chapter. This section also deals with surface preparation and analytical techniques employed in characterising aluminium alloy surfaces.

3.2 Specimen Description

The base material used for this study is superpure aluminium. The main impurities and their percentages are iron (0.004 wt%), copper (0.002 wt%) and silicon (0.003 wt%). Specimens of superpure aluminium (99.99%) in the form of coupons, of dimensions 3.5 cm × 1.7cm, were cut from high purity aluminium sheet of 0.6 mm thickness to provide substrates for sputter deposition and subsequent coatings. Some copper-containing aluminium alloys, deposited by magnetron sputtering, were employed. The materials were deposited using an Atom Tech Limited magnetron sputtering system, with 99.99% Al and 99.99% Cu targets. Materials were deposited on to electropolished superpure aluminium substrates that were attached to a rotating copper table, the temperature of which remained below 308 K.

3.3 Specimen Preparation

As with all pre-treatment systems, the most important aspect is proper cleaning and deoxidisation prior to application of the conversion coating [198]. Residues of oil, grease, marking inks, cutting oils and loose dirt will seriously affect the formation of conversion coatings. Hence, all the metal coupons need to be degreased in acetone in order to remove these contaminants before electropolishing.

3.3.1 Cleaning

Many coating failures can be attributed to poor metal surface preparation. Thus, a crucial requisite for proper coating formation is a clean metal substrate, free from contaminants such as oils, greases, waxes, corrosion products and other particles that soil the metal substrates. An ideal cleaning agent is one which is capable of removing all the contaminants from the metal surface, and thwarts their redeposition or the formation of other detrimental reaction products.

Prior to electropolishing, the surface of the specimens were degreased by rubbing with cotton wool soaked with acetone, followed by rinsing with acetone. Subsequently, the specimens were thoroughly rinsed in deionised water to prevent the dragout of the chemical (acetone) used in cleaning, which may contaminate the subsequent stages. After the rinsing step, the specimens were then dried in a cool air stream.

3.3.2 Electropolishing

Electropolishing is an electrochemical process which involves the application of a direct current (dc) voltage or current to an electrolytic cell in order to promote anodic dissolution in suitable electrolyte. In electropolishing, the metal part is immersed in a temperature controlled bath of electrolyte and subjected to direct current. The metal coupon is made the anode (+) [263] by connecting it to the positive terminal (anode) of a direct current (dc) power supply. The negative terminal is attached to a cathode to which the surface materials removed from the anode are attracted when electric current is applied. Often, the size, position and distance of the cathode to the metal coupon (anode) are controlled during the process in order to achieve the desired level of polish. The surface material is removed by anodic dissolution when a dc current is applied.

Removal of the surface material begins at high points within the microscopic surface texture. The current density is greater at the high points and reduced at the low points. The rate of the electropolishing reaction is directly proportional to the current density. The increased current density at the high points forces the metal to dissolve faster at these points and thus tends to level the surface material. By removing these points, the electropolishing process improves the surface finish, thus leaving a smoother and more reflective surface. This process improves the near surface chemistry of the material, and promotes the formation of an improved corrosion resistant surface layer. After the electropolishing treatment, the metal coupon is passed through a series of steps to neutralise, rinse, clean and dry the surfaces. Adequate rinsing after electropolishing is essential to avoid stains [51].

The controlling operating parameters include the following [51]:

- Applied voltage
- Temperature
- Solubility of aluminium oxide in the solution
- Oxidising power of the solution

Caicedo-Martinez et al. [264] studied the surface nanotextures on aluminium with particular interest in the influence of residual elements (Cu, Fe, Si) present in aluminium, and the additional effects of a deliberate alloying addition of manganese. They concluded that substrate composition does not influence cell size as a result of electropolishing. However, grain-orientation-dependent features persist.

In the present study, spade electrodes, of dimensions 35 × 17 mm, were prepared by cutting the superpure aluminium sheet using a guillotine. The resulting rectangular-shaped specimens were connected to aluminium rods (200 mm length × 3 mm diameter) using crocodile clips. The superpure aluminium spade electrodes were immersed in 20 vol. % perchloric acid in ethanol at a constant voltage of 20 V for 3 minutes and at temperature of 5^0C or less. The electropolishing cell was immersed in an ice bath in order to maintain the temperature of the electropolishing solution at the required temperature of 5^0C. Immediately after electropolishing, the specimens were rinsed in ethanol for 30 s, then in deionised water for 30 s, and finally dried in a cool air stream.

Thus, a microscopically and highly reflective surface is produced, suitable for sputter deposition. After electropolishing, the specimens were stored in a desiccator over silica gel.

3.3.3 Sputtering and sputter deposition

The deposition of the metal layer (Al-Al or Al-Cu) was realised using a magnetron sputter device with a DC sputter source on a laboratory scale. The sputtered metal film was deposited on the surface of the electropolished specimens while they are rotated in the centre of the two targets. The system was evacuated to 2×10^{-7} mbar, with sputtering then carried out at 5.5×10^{-3} mbar. The substrate is enclosed in a vacuum and placed directly in the path of the neutral atoms. The neutral species collide with gas atoms, causing the material to strike the substrate from different directions with a variety of energies. As atoms adhere to the aluminium substrate, a film is formed. The resultant deposits are relatively thin.

In the present study, two series of experiments were conducted. In the first series of sputter deposition, the target used was metallic aluminium of 99.99% purity while, all Al-Cu films were deposited with a dc magnetron sputtering system using a circular aluminium and copper target of 99.99% purity respectively. The target to substrate distance was 1 cm or more depending on the desired copper concentration. The substrates for the deposition were 3.5 × 1.7 cm aluminium coupons, which had been electropolished prior to sputter deposition. The sputtering deposition was carried out in high purity argon (Ar) gas (99.998%). Al films were sputtered from two aluminium (99.99%) targets in high purity argon (99.999%) – nitrogen (99.999%) atmosphere. After sputter deposition, the working areas of the specimens were defined by lacquer 45 [228] and then stored in the desiccator.

3.3.4 Electrode preparation

Spade electrodes of superpure aluminium and binary Al-Cu alloys were prepared from individual rectangular-shaped specimens of dimension 35 mm × 17 mm. The individual surfaces of the rectangular-shaped superpure aluminium were degreased, electropolished, after which, Al or Al-Cu films were deposited on the surface. After the individual specimens were surface treated and immersed in the conversion bath

solution, each specimen was then attached to an aluminium rod (200 mm length × 3 mm diameter) by cutting a notch, approximately 5 mm deep, at one end of the aluminium rod. In order to maintain a good connection between the specimens and the aluminium rod, the diameter of the notch was made narrower compared with the thickness of the specimens. Hence, in the present study, the specimens were gripped by the aluminium rods with the aid of pliers in order to ensure a relatively low resistance between the specimen and the rod. Heat-shrink polyolefin tubing, which fitted tightly to each specimen, was used to sheath the aluminium rods. The resultant spade electrodes were then covered with resin and beeswax (1:3 wt/wt), leaving an exposed working area of approximately 1 cm^2.

3.4 Solution Preparation

Solutions and electrolytes for all experiments were prepared with deionised water using analytical reagent grade chemicals. The aqueous solutions used for the zirconium-based conversion coating process contained 0.0014 M H_2ZrF_6, 5 g/l H_2BO_3, 10 g/l KNO_3 and approximately 0.4 ml HNO_3[4N].

For electrochemical tests and polarisation studies, the testing electrolyte was 3.5 wt.% NaCl solution.

3.5 Zirconium-based Conversion Treatment

The conversion treatment was performed on superpure aluminium and model copper-containing aluminium alloy (Al-1.0at.%Cu, Al-5.0at.%Cu, Al-10at.%Cu and Al-30at.%Cu) formed by magnetron sputtering. The conversion treatment was performed at room temperature by dipping the sputter-deposited metal coupons (35 × 17 mm) in a zirconium bath containing 0.0014 M H_2ZrF_6, 5 g/l H_2BO_3, 10 g/l KNO_3 and 0.4 ml HNO_3[4N]. The temperature and pH of the conversion bath were kept at 55^0C and 2.6 respectively. Specimens were treated for different times (0, 30, 60, 180, 300 and 600 s) in order to investigate how the formation and characteristic of zirconium-based conversion coatings are influenced by immersion time. The specimens were rinsed thoroughly with deionised water after the conversion process, and then dried in a cool air stream. Rinsing thoroughly with deionised water, after immersion in the conversion bath ensured the removal of any acid residues, soluble salts and non-adherent particles

that might be present on the treated metal surface which would otherwise promote blistering of subsequent paint films used for finishing. Treated specimens were kept in a desiccator to minimise aging effects.

3.6 Experimental Approach

3.6.1 Potential-time response

The polarisation behaviour of the untreated and treated metal substrates (electrodes) was performed in a 250 ml cell containing 200 ml of 3.5 wt% NaCl electrolyte. A three-electrode cell configuration consisting of the specimen (standard spade-type electrode) as the working electrode (WE), a platinum electrode as the counter electrode (CE) and a saturated calomel electrode as a reference electrode (RE) was used. The working electrodes, aluminium and Al-Cu spade-type electrodes, were mounted in such a way that only approximately 1 cm^2 of the electrode was in contact with the aggressive solution. The reference electrode was placed as close as possible to the surface of the working electrode. The potentials were monitored and recorded using Gill AC potentiostat (ACM instruments). The electrolyte was freely aerated and all experiments were performed at room temperature.

3.6.2 Polarisation studies

Polarisation studies can provide valuable information regarding the corrosion mechanism, corrosion rate and susceptibility to corrosion of metallic specimens in designated environments.

In the present study, the polarisation studies were carried out in order to examine the effect of the cathodic and anodic behaviour of treated and untreated superpure aluminium as well as the binary Al-Cu model alloys in 3.5 wt% NaCl solution. The polarisation behaviour of each specimen was determined using a spade electrode (specimen) connected to a GillAC potentiostat in a three-electrode cell. A saturated calomel electrode and a platinum electrode were used as reference and counter electrodes respectively. The working electrode was a standard spade-type electrode with a nominal working area of 1 cm^2.

Prior to commencing a polarisation study, it is usual to monitor the open circuit potential or corrosion potential for a period of time in the electrolyte. Monitoring of the potential should be conducted for a sufficiently long period of time in order to ensure that steady-state conditions exist between the specimen and its environment. Hence, in the present study, each of the specimens was immersed in 3.5 wt% NaCl electrolytes for 60 minutes to allow the potential to reach a steady value after which each specimen (spade electrodes) was polarised in the cathodic or anodic direction at a scan rate of 17 mV/min. Cathodic polarisation was carried out from +5 mV to a reverse potential of -1000 mV in the cathodic direction. For anodic polarisation experiments, deaeration was achieved by injecting nitrogen into the electrolyte for 2 hours in order to expel air bubbles. After 2 hours, specimens were immersed in the electrolyte and the open circuit potentials were measured for 60 minutes. Anodic polarisation was carried out from -5 mV to a reverse potential of +1000 mV in the anodic direction.

Anodic polarisation curves provide useful information concerning the potential range over which a material is passive, the ease of achieving passivity, the level of protection afforded by the passive film and the susceptibility to pitting.

3.7 Ultramicrotomy

Ultramicrotomy is a thin sample preparation method for successful transmission electron microscopy (TEM) investigations of metals [265-267]. Many materials in their natural state are too thick to be examined directly with an electron microscope. Ultramicrotomy represents, perhaps, the only technique presently available which allows direct observation of the substrate metal and its surface films, developed during corrosion or filming processes [268]. It provides additional and important advantages in the preparation of clean and microscopically smooth surfaces for both high purity aluminium and aluminium alloys, allowing transmission electron microscopy to be utilised fully in the study of their corrosion and filming behaviour [268]. Ultrathin sections can be created in the range of 10 - 100 nm thick with the use of a diamond knife. The electron transparent ultrathin sections of aluminium alloys can then be penetrated by an electron beam to reveal the intricate morphology. In order to obtain thinner and better quality sections for high resolution observations, it is necessary to use a high quality diamond knife [265]. Two angles are important in the use of a diamond

knife for sectioning, namely the included angle and the clearance angle (Figure 3.1 (a)). The standard included angle used for routine section with Micro Star knives is 45^0. The clearance angle is the angle between the back diamond adjusted to facilitate sectioning depending on the material being sectioned. The metal slices, of thickness in the order of a couple of hundred nanometres, are then retrieved from the water and mounted on a copper grid. The grid should be placed in the water and under the surface, and then it should be lifted up, gently picking up the sections at an angle. The grid is then dried immediately on filter paper as contaminants can land on the specimen if dried in air.

After the conversion coating process, the specimens for ultramicrotomy were cut into narrow strips of dimension 10 × 3 mm, with one end subsequently trimmed to a sharp tip. In order to prepare an embedded hard material, each strip specimen was arranged parallel to the axis of BEEM polyethylene capsules and was encapsulated in an epoxy resin which was formed from DDSA (dodenyl succinic andydride), MNA (methyl nadic anhydride), Agar 100 and BDMA (Benzyl Dimethyl Amine) - epoxy cure accelerator. Each sharp-tipped specimen was then positioned at the centre of the capsule. Curing was undertaken at 60 °C for 24 hours before trimming and sectioning. The resin (hardened) embedded specimens was taken out of the capsule and trimmed using a Leica Ultracut UCT ultramicrotome (Figure 3.1 (b)). The encapsulated specimens were initially trimmed with a glass knife and suitably thin sections, between 5 and 10 nm, thick were prepared by sectioning in a direction approximately parallel to the coating/metal interface with a diamond knife [269]. The cutting speed and section thickness were set at 0.2 mm s^{-1} and 15 nm respectively. The slices produced were collected from a bath of deionised water onto 200 mesh TEM copper grids and later dried at room temperature and stored for subsequent TEM examination.

3.8 Scanning Electron Microscopy and Energy Dispersive X-ray Spectroscopy

The scanning electron microscope (SEM) has long been recognised as a tool to give a simulated ‘visual’ image of a surface, with a magnification which is sufficiently large for both macro- and micro-structures to be studied [270]. The scanning electron microscope (SEM) is a microscope that uses electrons rather than light to form an image. There are many advantages to using the SEM instead of a light microscope. The

SEM has a large depth of field, which allows a large amount of the sample to be in focus at one time. The SEM also produces images of high resolution, which means that closely spaced features can be examined at a high magnification. Preparation of the samples is relatively easy since most SEM only require the sample to be conductive. The combination of higher magnification, larger depth of focus, greater resolution, and ease of sample observation makes the SEM one of the most important tool used in research areas today [271].

Conventional light microscopes use a series of glass lenses to bend light waves and thus create a magnified image. The SEM (Figure 3.2) creates the magnified images by using electrons instead of light waves. It shows very detailed 3-dimensional images at much higher magnifications than is possible with an ordinary light microscope. The images created without light waves are rendered black and white. The specimen (which has been carefully prepared to withstand the vacuum inside the microscope) is then placed inside the microscope's vacuum column through an air-tight door. After the air is pumped out of the column, an electron gun, situated at the top, emits a beam of high energy electrons. This beam travels downward through a series of magnetic lenses which are designed to focus the electrons to a very fine spot. Near the bottom, a set of scanning coils hastens the focused beam back and forth across the specimen. As the electron beam hits each spot on the specimen, secondary electrons are knocked loose from the specimen surface. An electron detector counts these electrons and sends the signals to an amplifier. The final image is built up from the number of electrons emitted from each spot on the specimen. The intensity of the emitted electrons from a specimen of a given homogenous composition depends on the local angle of the surface to the scanning beam moderated by the probability of their reaching the detector [270]. Thus, the image of the surface appears to have been viewed along the axis of the incident beam with a contrast that is expected if the sample is illuminated by a beam of light from the direction of the detector [270].

High resolution images can be produced with field emission gun scanning electron microscope (FEGSEM). The main difference between the SEM and the FEGSEM is the type of electron emitter used. FEGSEM uses a cold cathode field emitter while SEM uses thermionic emitters. FEGSEM instruments also operate in a high vacuum that allows electron movements along the column without scattering and prevents discharges

inside the gun. A narrow probing beam, produced by field emission cathode, provides improved spatial resolution and minimises sample charging and damage.

In order to reveal the surface morphology and to measure the coating layer thickness, scanning electron microscopy was carried on the specimens studied in this work. Samples for SEM were prepared by cutting 1 cm by 1 cm pieces from the specimens. The surface morphology of the aluminium specimens before and after coating was examined by scanning electron microscopy. The micrographs were taken with an Amray 1810 instrument, with resolution of 60 Å, interfaced with an ISIS x-ray microanalysis workstation with a high resolution Gem (Germanium) Ayw (thin windowed) X-ray detector. High resolution images were also taken using FEGSEM instrument Zeiss Evo-50. Energy Dispersive X-ray analyses were carried out at accelerating voltage of 20 kV.

3.9 Transmission Electron Microscopy

Transmission electron microscopy (TEM) is an imaging technique whereby a beam of electrons is focused onto a specimen causing an enlarged version to appear on a fluorescent screen or layer of photographic film. Transmission electron microscopy has been used for decades to examine ultrathin specimens. It is often used to determine the morphology and structure of nanomaterials. This technique requires a clean sample that meets ultra high-vacuum standards in order to provide surface characterisations. Thus, the specimens must be very thin and able to withstand the high vacuum present inside the instrument. In the past, light microscopes have been used mostly for imaging since they are relatively easy to use. However, the maximum resolution of an image is determined by the wavelength of the photons that are being used to probe the sample. The wavelength of light limits resolution in an optical light microscope. The TEM operates on the same basic principles as the light microscope, but uses electrons instead of light. Transmission electron microscopes use electrons as light source and their much reduced wavelength make it possible to achieve resolutions of one thousand times better than with a light microscope. Thus, objects of the order of 10^{-1} nm can be resolved. The schematic diagram of the principal features of a transmission electron microscope is shown in Figure 3.3 (a).

A light source situated at the top of the microscope emits the electrons that travel through the vacuum in the column of the microscope (Figure 3.3 (b)). The TEM uses electromagnetic lenses to focus the electrons into a very thin beam. The electron beam then travels through the specimen to be studied. Depending on the density of the specimen, some of the electrons are scattered and disappear from the beam. At the bottom of the microscope the unscattered electrons hit a fluorescent screen, which gives rise to a "shadow image" of the specimen with its different parts displayed in varied darkness according to their density. The image can be studied directly by the operator or photographed with a camera.

The contrast in a TEM image is not the same as the contrast in a light microscope image. A crystalline material interacts with the electron beam mostly by diffraction rather than absorption, although the intensity of the transmitted beam is still affected by the volume and density of the material through which it passes. The intensity of the diffracted beam depends on the orientation of the planes of atoms in a crystal relative to the electron beam - at certain angles the electron beam is diffracted strongly from the axis of the incoming beam, while at other angles the beam is largely transmitted. Modern TEMs are often equipped with specimen holders that allow the user to tilt the specimen to a range of angles in order to obtain specific diffraction conditions, and apertures placed below the specimen allow the user to select electrons diffracted in a particular direction. A high contrast image can therefore be formed by blocking electrons deflected away from the optical axis of the microscope by placing the aperture to allow only unscattered electrons to pass through. This produces a variation in the electron intensity that reveals information on the crystal structure, and can be viewed on a fluorescent screen, or recorded on photographic film or captured electronically. It is also possible to produce an image from electrons deflected by a particular crystal plane. By either moving the aperture to the position of the deflected electrons, or tilting the electron beam so that the deflected electrons pass through the centered aperture, an image can be formed of only deflected electrons, known as a *dark field* image.

There are a number of drawbacks to the transmission electron microscopy technique. Many materials require extensive sample preparation to produce a specimen thin enough to be electron transparent, which makes TEM analysis a relatively time consuming process with a low throughput of samples. The structure of the sample may

also be changed during the preparation process. Additionally, the field of view is relatively small, raising the possibility that the region analysed may not be characteristic of the whole sample. There is potential that the sample may be damaged by the electron beam, particularly in the case of biological materials.

The surface structure and coating layer thickness of all the specimens were investigated using transmission electron microscopy. Ultramicrotomed thin sections were examined at an accelerating voltage of 120 kV in a JOEL 2000 FX II analytical TEM instrument equipped with an energy dispersive X-ray analysis facilities. Energy dispersive X-ray (EDX) unit connected to the TEM was used to determine the percentage of atomic contents of elements present in the surface of the coated aluminium substrate. Specimens were imaged at an energy electron beam of 2 keV, and the EDX spectra obtained were interpreted by means of the ISIS Data Software.

3.10 Atomic Force Microscopy

Atomic force microscopy (AFM) is a very high resolution scanning probe microscope [272] which makes it a valuable technique for studying micro- and nano-structured surfaces. It is a technique for investigating the surface topography of a sample. An atomic force microscope (Figure 3.4) is simply an extremely small, sharp probe attached to a spring loaded cantilever which moves over the surface of a specimen. Light from a laser shining on the cantilever is detected by a photodiode and the resultant signal generated is interpreted by specialist electronics. The tip is usually made from either a ceramic or semiconducting material, however, recently the tips have been made from cylindrical carbon nanotubes that are much stronger and yet flexible. The sharper the tip, the better the resolution of the final image. The lateral resolution of the image can be as small as the tip radius (typically 5-15 nm), and the vertical resolution can be in the order of angstroms. A standard atomic force microscope can analyse a specimen between 10-20 cm^2 to a resolution of less 0.2 nm.

The principle of operation of a standard atomic force microscope is based on scanning of a sharp tip, mounted on a flexible cantilever across the specimen area. When the tip approaches the surface within a few angstroms, local attractive or repulsive van der Waals forces between the atoms of the tip and the specimen surface is set off which is converted into a bending or deflection of the cantilever. The tip is moved over the

sample by a scanner, typically a piezoelectric transducer, which can make extremely precise movements. The magnitude of the deflection depends on the tip-to-specimen distance (*d*). A laser beam is focused on the backside of the cantilever, which is reflected onto a distant photo-detector. Hence, when the cantilever moves up and down corresponding to the surface contours, the laser beam is also deflected as well. Thus, the deflection of the laser spot on the photo-detector will correspond to the height displacement on the surface of the specimen. The bending or deflection of the cantilever, normal to the specimen surface is usually monitored by an optical lever, although other methods have been investigated [273]. The optical lever consists of a laser focused on the back of the cantilever which is reflected onto a photo-detector (typically a split photodiode). The combination of the sharp tip, the very sensitive optical lever, and the highly precise movements by the scanner, combined with the careful control of van der Waal forces between the tip and the specimen surface, allow the extremely high spatial resolution (on the nanoscale) of AFM.

There are many different operating modes for an AFM. The most commonly used modes of operation of an AFM are the contact mode and the tapping mode. In the contact mode, the cantilever is kept in constant contact with the sample surface by applying a constant force between the cantilever and the surface. The tapping mode is very gentle in contrast to the contact mode. It utilises a piezo crystal to oscillate the cantilever up and down (usually 100-200 nm) only tapping the surface while it scans across the specimen. By controlling how hard the tip is tapped, the AFM can move away from the surface when the cantilever tip feels a ridge, so that it does not hit against the surface when it moves across it. The tapping can be finely tuned by changing the voltage applied to the piezo crystal but a common tapping frequency is mainly between 50-500 MHz. Another mode which is not so common is the non-contact mode [274]. In the non-contact mode the tip stays in close (almost touching) contact to the surface at all times.

Tapping mode AFM was used to characterise the surface topography of the superpure and Al-Cu model alloys before and after different times of immersion in zirconium-based conversion bath. These characterisations were conducted using a Veeco Dimension T^m 3100 multimode atomic force microscope manufactured by Digital Instruments. Quantitative evaluation of the data (image data) was carried out using the

NanoScope III off-line analysis software and the scanning probe image processor (SPIP).The AFM measurements were presented as plan-view and 3-dimensional images.

3.11 Optical Microscopy

Optical microscopy, or light microscopy, refers to the inspection of the specimen at higher magnification using an instrument known as an optical or light microscope. Optical microscopes are the simplest and oldest of the microscopes. It is one of the most versatile, non-destructive analytical tools used to study the microstructure of a great range of materials on the micron and submicron scale. A basic optical microscope has the following components:

- a lamp to illuminate the specimen
- a nose piece to hold 4 to 5 objectives which is used in changing the viewing magnification
- an aperture diaphragm used to adjust the resolution and contrast
- a field diaphragm for adjusting the field of view
- an eye piece to magnify the objective image (usually by 10X) and
- a stage for manipulating the specimen.

During an optical microscope inspection, the specimen is usually mounted on a transparent glass slide and positioned on the movable specimen stage of the microscope and is positioned perpendicularly to the axis of the objective lens. Light from the microscope lamp is focused by the condenser lens onto the specimen, which reflects some light back to the lens. The objective lenses pick up the reflected light transmitted by the specimen and focus it on the focal plane of the objective lens, thus creating a magnified image of the specimen. Usually the image formed on the objective focal plane is magnified by the ocular lens. The light emanating from the already magnified image of the specimen is reflected on the ocular lens which projects it onto a piece of photographic film or a video camera. The image seen in the microscope depends not

only on how the specimen is illuminated and positioned, but on the characteristics of the specimen as well.

The morphology of the treated and untreated specimens after exposure to aggressive electrolytes was examined using an optical microscope (model: Olympus BHM). The imaging system involves a JVC colour video camera (model: TK – C1370) placed on top of the objective portion of the microscope. The camera was connected to a computer in order to record real-time images from the substrates using BDPRO capture software.

3.12 Rutherford Backscattering Spectroscopy

Rutherford Backscattering Spectroscopy (RBS) is a technique that has been widely used for the characterisation of surfaces of single oxides [275] and for studying the materials in thin coatings. It is able to reach buried atomic layers non-destructively and gives information on the stoichiometry and atomic concentrations [276]. The technique uses ion beams with energies in the MeV range to determine the chemical composition of thin films [213]. The energies of the backscattered ions depend on the mass and the distance from the external surface of the atom of collision [213]. The incident ions lose energy during the collision with the atom and also due to passing in and out of the material. The scattering effect is named after Rutherford when the interaction between the incident nucleus and the target nucleus is only due to the Coulomb force [213]. Energy analysis of the backscattered ions by the detection system yields a spectrum in the form of counts versus channel number. The channel number is linearly related to the energy of the backscattered ion, which for a certain element is inversely related to the distance from the external surface. Therefore, knowing the density of the material and the stopping cross section of the element, it is possible to relate the channel number to the distance from the surface [213]. RBS spectra are usually quantified using scattering cross-sections and rump simulation [172].

Rutherford backscattering spectroscopy (RBS) has been used in the present study to examine how changes in processing conditions, particularly the treatment times, influence the coating thickness and zirconium distribution at each processing time. This technique is based on the detection of ions that are elastically backscattered by nuclei of the atoms of a material analysed [275]. The energy and mass of the projectile atoms are known. Then, the composition of the sample examined is calculated through the

measurement of the number of projectile ions backscattered at different energies (backscattered spectrum), and considering the principle of conservation of momentum and energy during the elastic collision of two masses [275]. Equations and constants used for these calculations are included in a computer program called RUMP (Rutherford Universal Manipulation Program) which simulates the experimental backscattering spectrum as a function of the composition of the coated aluminium surfaces studied.

Coatings were analysed by Rutherford backscattering spectroscopy (RBS), using either 1.53 or 1.86 MeV He^+ ions, supplied by the Van de Graaff accelerator of the University of Paris. The diameter of the ion beam was 1 mm. The RBS data were interpreted by the RUMP program.

The channel number of the part of the RBS spectra related to zirconium is transformed in distance from the external surface using the density of pure zirconium oxide. The thickness of the zirconium layer was taken arbitrarily as the distance from the surface at which the counts of backscattered ions, proportional to the density of atom of zirconium, are 30% of the maximum value. Therefore, it is necessary to keep in mind that the measurements of thickness of zirconium-based films obtained from these analyses are only semi-quantitative. This is also due to the fact that the density of pure zirconium oxide was used, whereas the coating layer is a mixture of zirconium oxide and hydroxide. Regardless, the thicknesses of the zirconium-based films from all the specimens were calculated with the same method and therefore comparisons should be possible.

3.13 Nuclear Reaction Analysis

Nuclear reaction analysis (NRA) is a powerful technique for quantification of the concentration or the depth profile of a certain element in a specimen for which the qualitative chemical composition is known, using light ion beams with energies in the range 1 – 10 MeV [277]. It is also a sensitive means of measuring depth profiles of individual isotopes of an element which is not possible using surface analytical techniques such as RBS, Auger electron spectroscopy (AES), or X-ray photoelectron spectroscopy (XPS).

In order to quantify the amount of oxygen in the zirconium-based conversion coatings formed on conversion coated specimens, nuclear reaction analyses were carried out on the superpure aluminium specimens as well as the Al-30at.%Cu alloy specimens in both the as-sputtered and conversion coated conditions. The oxygen content in the zirconium-based conversion coating was measured by NRA using $^{16}O(d, p_1)^{17}O$ with a deuteron beam of 2.43 MeV. Protons were detected at 150^0 to the direction of the incident beam. A mylar film was placed in front of the detector in order to eliminate the signal from elastically scattered deuterons. The amount of oxygen in the conversion layer film was determined from the ratio of the proton yield from the specimen (superpure aluminium or Al-30at.%Cu alloy) to that from an anodised tantalum standard specimen known to contain 5.05×10^{18} oxygen atoms/m^2 to a precision of 3%.

3.14 Glow Discharge Optical Emission Spectroscopy

Glow Discharge Optical Emission Spectroscopy (GDOES) is a rapid analytical technique used for direct bulk analysis and depth profiling analysis of solids (metals, powders, polymers, glasses and ceramics). GDOES employs a glow discharge source and one or more optical spectrometers. A schematic layout is given in Figure 3.5 (a). Since this technique gives composition of materials as elemental depth profiles, conversion coatings currently being developed on aluminium and copper-containing aluminium substrates can be easily studied.

The principle of operation is relatively easy to understand. In GDOES, the specimen to be analysed is brought close to the anode (a copper tube) of a glow discharge source (Figure 3.5 (b)). The copper tube is filled with low pressure argon (~600 Pa) with either a radio frequency (RF) or direct current (DC) voltage applied between the anode and the specimen (cathode). Atomisation of the specimen in GDOES occurs by cathodic sputtering, followed by a transport of the sputtered material in the excitation source [278]. Cathodic sputtering is used to remove material layer by layer from the surface of the specimen. The atoms removed from the metal substrate migrate into the plasma where they are excited through collisions with electrons or metastable carrier gas atoms. The characteristic spectrum emitted by this excited atoms is measured by the spectrometer.

Analytical interpretation of the GDOES data depends on calibration. In order to achieve accuracy over a wide range of materials, the calibration has to be correct, i.e. it must correctly reflect actual relations between the signal response and the composition of the specimens to be analysed. The key to good calibrations is a correct calibration model, i.e. a correct general form of the equations linking the signal response and the composition of the analysed material [278]. Ideally, the calibration model should reflect in a suitable way all processes affecting the signal response - sample atomisation, excitation and conversion of the emitted light into the actually measured signal(s) [279]. Emission intensities depend on the specimen composition in a predictable way, namely, if analysing a specimen M, the intensity $I_{E,M}$ of an emission line of element E depends on the concentration $c_{E,M}$ of the element in that specimen as in the equation below.

$$I_{E,M} = R_E \, c_{E,M} \, q_M \tag{3.1}$$

where q_M is the sputter factor of specimen M and R_E is proportionality factor known as emission yield of that particular line. The sputtering rate q_M is defined as the amount of the material of the specimen sputtered (removed) from the specimen within a time unit. It depends on the matrix and the discharge conditions [280, 281].

In view of the importance of GDOES for precise depth profiling of films materials and the potential of GDOES for depth profiling analysis of films, GDOES spectra of superpure aluminium and Al-Cu alloys were recorded before and after the immersion treatment. The specimens were depth-profiled using a Jobin Yvon GD Profiler 2 RF instrument. The depth profiling analysis of the coatings was carried out at an argon pressure of 700 Pa by applying an RF of 13.56 MHz and a power of 35 W. Light emissions of characteristic wavelengths, associated with the sputtered species, excited mainly by collision with electrons were monitored throughout the analysis with a sampling interval of 0.01 s for depth profiling. The relevant wavelengths (nm) were as follows: aluminium, 396.152; copper, 324.754; oxygen, 130.217; zirconium, 339.198 and boron, 249.678.

3.15 X-ray Diffraction Spectroscopy

X-ray diffraction (XRD) is an indispensible non-destructive tool for the qualitative and quantitative analysis of a wide range of materials. It is used to characterise the crystal

composition, grain size and preferred orientation in polycrystalline or powdered solid specimens. XRD detects the molecular composition and can distinguish among various phases of a compound of a given chemical formula. Structural information on amorphous phases can also be obtained using XRD. X-ray diffractometers consist of three basic elements: an X-ray tube, a specimen holder, and an X-ray detector.

X-ray diffraction spectroscopy is based on constructive interference of monochromatic X-rays and a crystalline specimen. These X-rays are generated by a cathode ray tube, filtered to produce monochromatic radiation, collimated to concentrate, and directed onto the specimen. The geometry of the X-ray diffractometer is such that the specimen rotates in the path of the collimated X-ray beam at an angle θ while the X-ray detector which collects the diffracted X-rays, rotates at an angle of 2θ. The intensity of spatially diffracted X-rays is continuously recorded as the specimen and the detector rotate through their respective angles. The diffraction of X-rays by specimens is described by Bragg's law;

$$n\lambda = 2d \sin\theta \qquad (3.2)$$

Bragg's law relates the wavelength (λ) of electromagnetic radiation to the diffraction angle (θ) and the lattice spacing (d) in a crystalline specimen. When the geometry of the incident X-rays impinging the specimen satisfies the Bragg's law, constructive interference occurs and a peak in intensity occurs. The d-spacing of each peak is then obtained by solving the Bragg's equation for the appropriate value of wavelength (λ). Conversion of the diffraction peaks to d-spacings allows identification of the specimen because each crystal has a set of unique d-spacings. This is usually achieved by comparison of specimen's d-spacings with standard reference patterns. The orientation and relative intensity of the diffraction pattern contain information on the crystallographic structure of the specimens being studied. Through the use of appropriate database, XRD allows researchers to qualitatively (phase analysis) identify the compounds present and quantitatively determine their relative abundance in case a mixture of the latter is under scrutiny.

The structure of sputter-deposited aluminium and aluminium-copper alloys were determined by X-ray diffraction. XRD measurements were performed with a Philips X'Pert – MPD X-ray diffractometer (with a copper tube anode) equipped with a

diffracted-beam curved graphite monochromator. The X-ray photon wavelength was 1.542 Å with a take-off angle of 6^0. The XRD patterns were collected with the X-ray source operating at an accelerating voltage of 45 kV and an emission current of 40 mA. The data were collected in steps of 0.05^0 (2θ) in the 5 to 85^0 (2θ) range with a constant counting time of 30 s per step. The fixed angle of incidence of the X-ray beam was 3^0. The identification of the phase composition of the specimens was done by comparing the measured d-spacings in the diffraction pattern and their integrated intensities with known standards.

3.16 Corrosion Tests

3.16.1 Filiform corrosion test

Assessment of the susceptibility of the specimens to filiform corrosion was done using an accelerated laboratory filiform corrosion test. The specimens were tested in the as-sputtered condition and after conversion coating treatments. Two specimens for each condition were tested. The specimens for filiform corrosion tests were coated using a transparent acrylic coating (Rohm & Haas, Paraloid B48N). The coating was applied with a wire-bar (from Jaguar) and cured at room temperature overnight, leaving a dry film thickness of approximately 20 μm. A 10 mm scribe was made in the coating using a steel tipped scribing tool. Corrosion was initiated by introducing droplets of 16 wt.% HCl solution into the scribe for 2 - 3 minutes. The excess HCl solution was then removed carefully, from the surface after which, the specimens were placed in a humidity chamber, maintained at 40^0C and 80% relative humidity, for 3000 h in accordance with DIN EN ISO 3665 [137].

3.16.2 Salt spray testing

Salt spray (fog) is considered as one of the most useful standards for measuring corrosion resistance in the coating industry. Standard salt fog is the industry's benchmark for obtaining corrosion data. It can be used to test the relative resistance to corrosion of coated and uncoated metallic specimens, when exposed to a salt spray fog at an elevated temperature. Salt spray tests are performed using a special chamber, appropriately named or described as salt spray chamber. The American Society for Testing Materials (ASTM) B117 (Standard Practise for Operating Salt Spray (Fog)

apparatus) was developed as a test to measure the relative effectiveness of coatings to protect the substrate to which the coating is adhered from corrosion. It gives the operating parameters of the salt spray chamber. These parameters are temperature, air pressure, concentration of salt, collection rate etc. The salt solution comprises 5% NaCl in deionised water (with a pH range of 6.5 to 7.2), and the chamber temperature is kept at 35 - 37^0C. The salt solution is atomised in the salt spray chamber such that for each 80 cm^2 of horizontal collection area there will be a collection at a rate of 1 - 2 ml per hour [282]. These parameters have strict operating ranges that must remain in check to ensure proper reproducibility of corrosion data. The duration of the test can range from 8 to over 3000 h, depending on the material being tested. ASTM D1654 standard is the most common evaluation method for ASTM B117.

Salt spray testing in accordance with ASTM B117 standard was used to evaluate uncoated and acrylic coated conversion coated specimens. Prior to initiating the test, the collection rate, and the salt concentration and pH of the collected solution were measured and conformed to the requirements set by the ASTM B117 standard: 1.0 - 2.0 ml of solution per hour in an 80 cm^2 horizontal collection area (based on an average run of 16 h), 5 wt.%, 6.5 - 7.2 pH, respectively. The temperature of the chamber was monitored on a daily basis and was found to maintain the range specified by the ASTM B117 standard. In the present study, test specimens were supported in the test chamber using racks that fix the specimens at an angle of 30^0 from the vertical. All specimens were photographed prior to, during and at the termination of the test. The acrylic-coated coupons for each conversion coating condition were scribed and exposed to 1000 h of salt fog under conditions identical to those of the uncoated specimens. At the end of the test the specimens are carefully removed from the chamber. They are allowed to dry for one hour before rinsing, in order to reduce the risk of removing corrosion products. The assessment of corrosion is performed visually and by digital colour photography to show the extent of corrosion that occurred during the 1000 h of ASTM B117 salt spray testing.

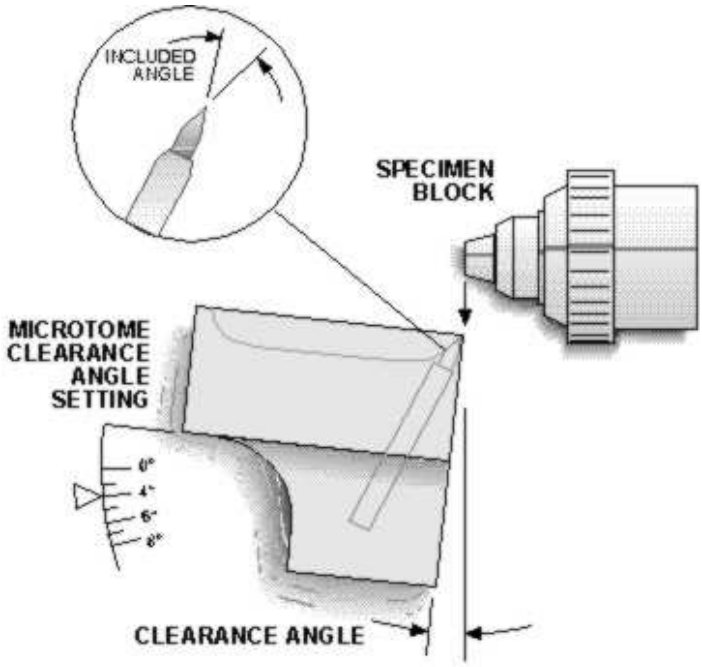

Figure 3.1 (a) Specimen sectioning process (www.microstartech.com), (b) Photo of Leica Ultracut UCT ultramicrotome.

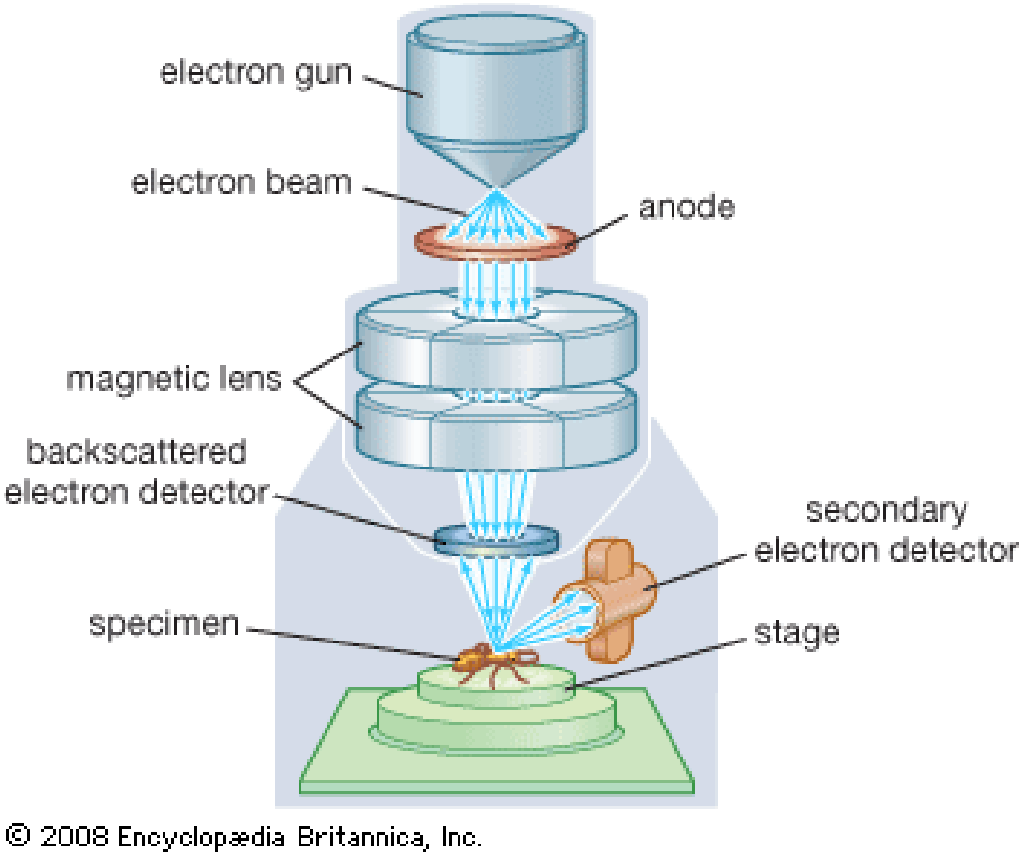

Figure 3.2 Schematic view of the operation of SEM (http://media-2.web.britannica.com/eb-media/88/113688-004-B14FDB14.gif)

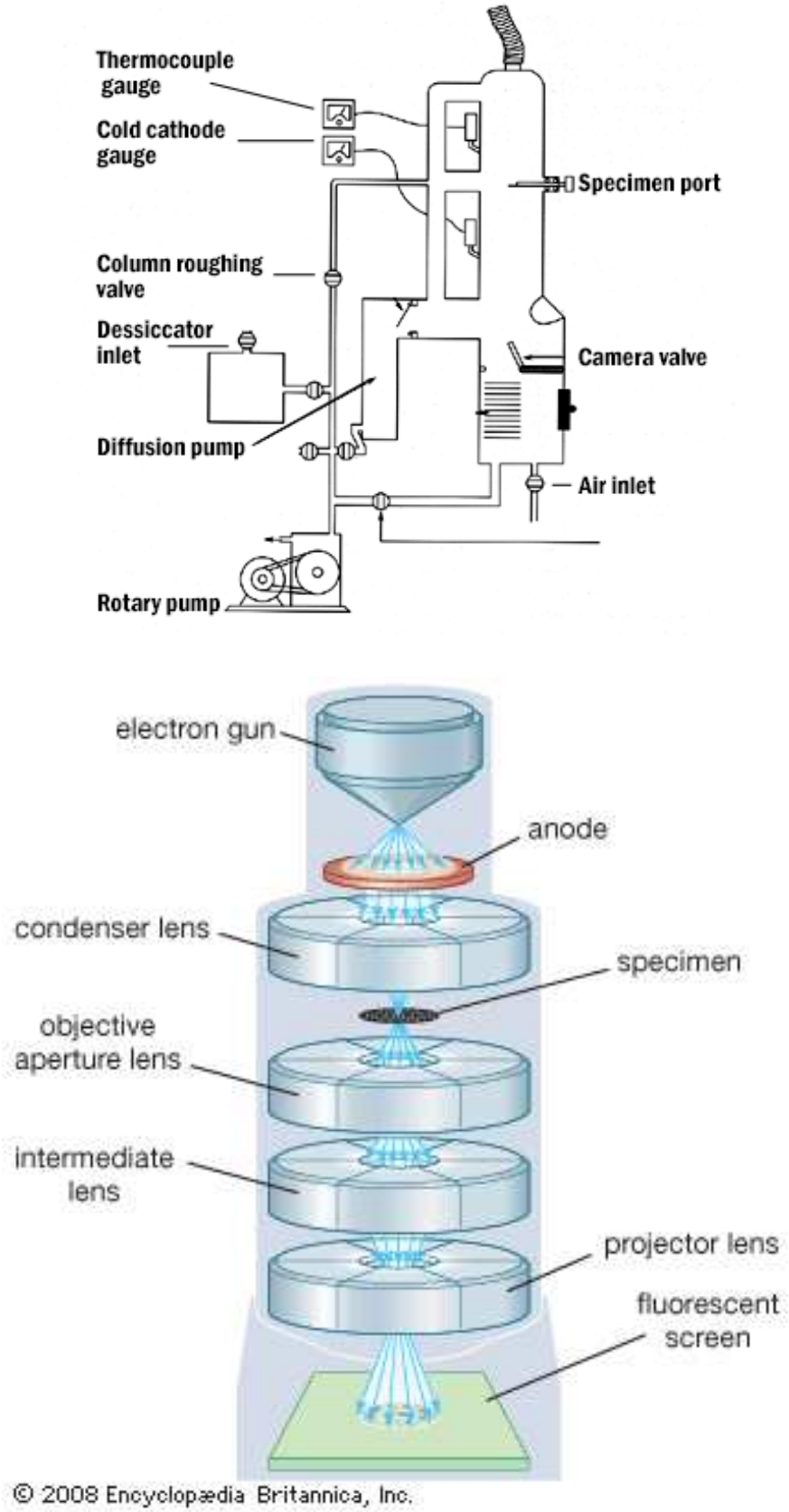

Figure 3.3 Schematic view of (a) principal features of a TEM (b) operation of a TEM (http://media-2.web.britannica.com/eb-media/90/113690-004-CB552E7F.gif)

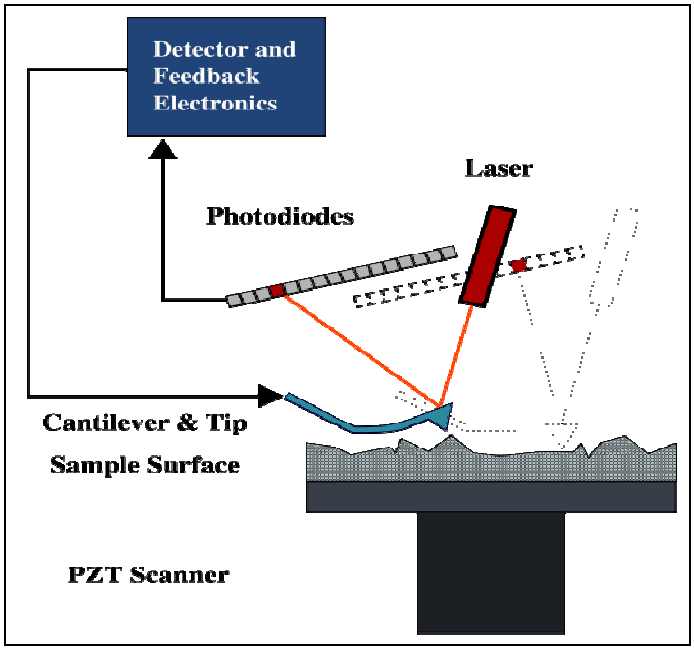

Figure 3.4 (a) A Nanoscope III Multimode AFM and (b) a schematic diagram illustrating the AFM operation.

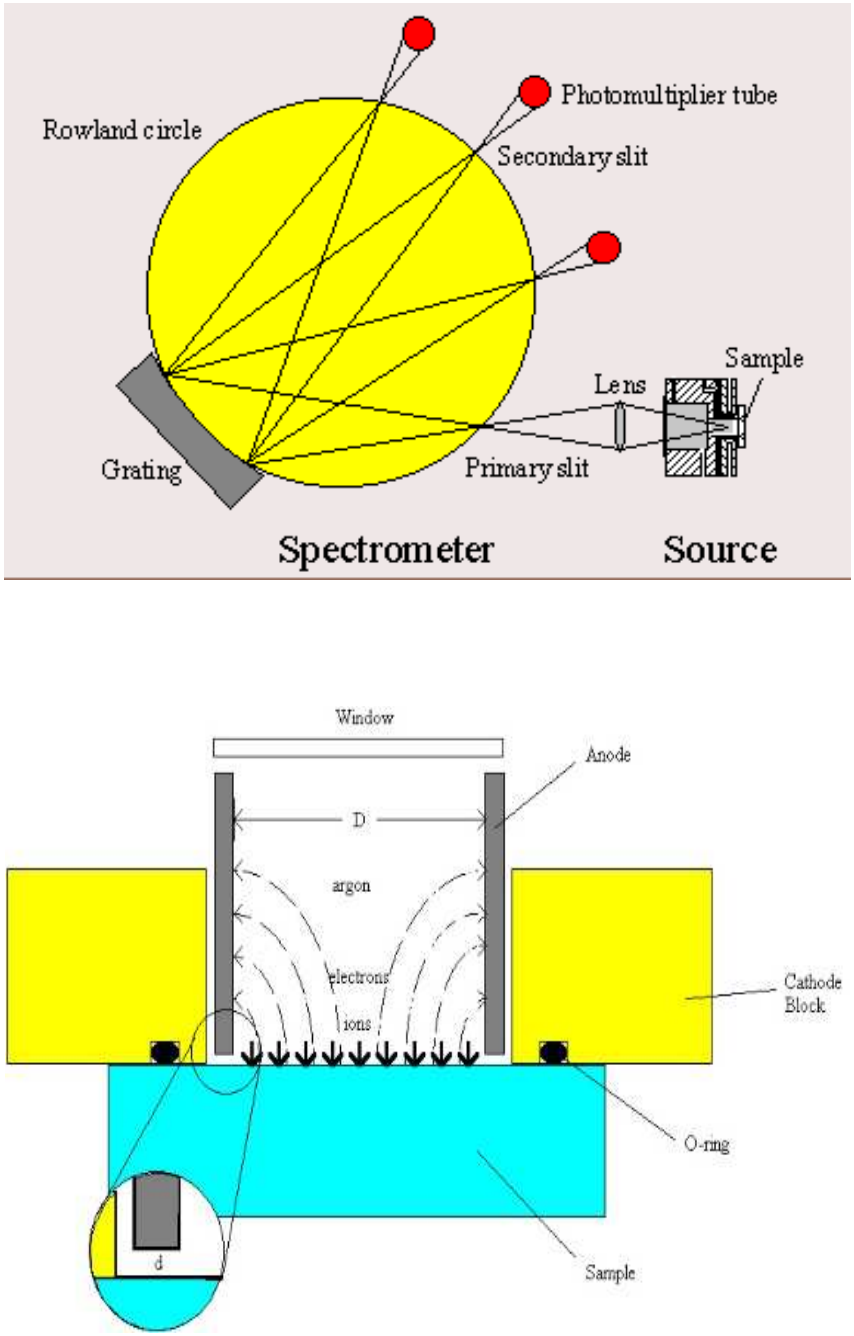

Figure 3.5 Schematic diagrams of (a) GDOES and (b) glow discharge source (www.glow-discharge.com/)

CHAPTER 4

4 ASSESSMENT OF ALUMINIUM AND MODEL ALUMINIUM-COPPER ALLOYS PREPARED BY MAGNETRON SPUTTERING

4.1 Introduction

In this chapter, characterisation of superpure aluminium and aluminium-copper model alloys (Al-1.0at.%Cu, Al-5.0at.%Cu, Al-10at.%Cu and Al-30at.%Cu) in the as-sputtered condition is considered. Optical microscopy, scanning electron microscopy (SEM), transmission electron microscopy (TEM), atomic force microscopy (AFM) and crystallographic measurements by X-ray diffraction spectroscopy (XRD) have been employed. The electrochemical behaviour of the as-sputtered aluminium and aluminium-copper model alloys is also introduced in this chapter.

4.2 Optical Microscopy

4.2.1 Magnetron sputtered superpure aluminium and aluminium-copper model alloys

Optical microscopy was used prior to electrochemical testing to observe surface defects such as scratches and cracks introduced during sputtering and handling. The optical micrographs of the superpure aluminium, Al-1.0at.%Cu, Al-5.0at.%Cu, Al-10at.%Cu and Al-30at.%Cu alloys in the as-sputtered condition are shown Figures 4.1 (a) – 4.1 (e) respectively. The optical micrographs of the aluminium-copper model alloys reveal changes in the surface morphologies with increasing percentage composition of copper the model alloys. Arrays of microscopic grooves were also observed on the aluminium-copper model alloys. These grooves are continuous and parallel to each other with a separation distance of approximately 20 μm. The optical micrograph of the surface of the initial aluminium substrate reveals that the observed grooves are due to the rolling lines on the original surface of the aluminium substrate before sputter deposition.

4.3 Scanning Electron Microscopy

The microstructure and elemental composition of the magnetron sputtered aluminium and copper-containing aluminium alloys were observed with the aid of a scanning electron microscope. An energy dispersive X-ray (EDX) elemental analysis facility was attached to the scanning electron microscopes to utilise its electron beam as source. In EDX analysis, a high energy electron beam is scanned across the specimen, causing the emission of X-rays as excited electrons return to the ground state. The energy of emitted X-ray is dependent on the elemental configuration of the specimens. Oxygen was detected on all the specimens tested except the as-sputtered Al-30at.%Cu alloy specimen. Gaseous incorporation in sputtered films is likely due to the fact that the faster a sputtered film forms on the metal substrate, the more residual gas from the ambient vacuum becomes incorporated into the films.

4.3.1 Magnetron-sputtered superpure aluminium

The surface of the magnetron-sputtered superpure aluminium is shown in Figure 4.2. The superpure aluminium surface morphology appears relatively flat and free from detritus. In order to investigate the local composition of the superpure aluminium specimen, EDX point analyses were carried out. The results from these analyses are given in Table 4.1. The analysis by EDX point measurement confirms the presence of aluminium and oxygen which is likely alumina (Al_2O_3) which possesses strong ionic bonding giving rise to its desirable material characteristics. The slight variation in the composition of the as-sputtered aluminium substrate is likely due to the fact that EDX point analyses were made of interesting features on the metal surface and these have a different composition level which is likely due to impurities on the metal surface.

Table 4.1 EDX analyses of the surface of the superpure aluminium specimen

Spectrum	In stats.	O	Al	Total
Spectrum 1	Yes	0.34	99.66	100.00
Spectrum 2	Yes	0.71	99.29	100.00
Spectrum 3	Yes	0.65	99.35	100.00
Max.		0.71	99.66	
Min.		0.34	97.29	

All results in weight%

4.3.2 Magnetron-sputtered Al-1.0at.%Cu alloy

Figure 4.3 displays the scanning electron micrographs of the alloy after magnetron sputtering. Arrays of microscopic parallel grooves (consistent with the optical microscopy observations) were also observed on Al-1.0at.%Cu model alloy. The EDX results (Table 4.2) confirms the presence and weight percentage of copper in the model alloy from known sputtering parameters as expected. It also reveals the presence of oxygen.

4.3.3 Magnetron-sputtered Al-5.0at.%Cu alloy

Scanning electron images of the surface of the sputter deposited Al-5.0at.%Cu alloy reveal the generally featureless appearance, as depicted in Figure 4.4. The analysis of the EDX spectra reveals the percentage weight composition of the alloy (Table 4.3).

4.3.4 Magnetron-sputtered Al-10at.%Cu alloy

Figure 4.5 shows the scanning electron micrograph of the surface of the as-sputtered Al-10at.%Cu specimen. Table 4.4 shows the elemental composition of the alloy by EDX

analyses. Spectrum 2 and spectrum 4 revealed the presence of some carbon impurities on the surface of the alloy.

Table 4.2 EDX analyses of the surface of the magnetron-sputtered Al-1.0at.%Cu alloy

Spectrum	In stats.	O	Al	Cu	Total
Spectrum 1	Yes	1.48	96.62	1.90	100.00
Spectrum 2	Yes	2.18	95.94	1.88	100.00
Spectrum 3	Yes	0.88	97.28	1.84	100.00
Spectrum 4	Yes	1.12	97.04	1.84	100.00
Max.		2.18	97.28	1.90	
Min.		0.88	95.94	1.84	

All results in weight%

Table 4.3 EDX analyses of the surface of the magnetron-sputtered Al-5.0at.%Cu alloy

Spectrum	In stats.	O	Al	Cu	Total
Spectrum 1	Yes	3.12	89.96	6.92	100.00
Spectrum 2	Yes	1.46	89.77	8.77	100.00
Spectrum 3	Yes	2.50	88.43	9.07	100.00
Max.		3.12	89.96	9.07	
Min.		1.46	88.43	6.92	

All results in weight%

Table 4.4 EDX analyses of the surface of the magnetron-sputtered Al-10at.%Cu alloy

Spectrum	In stats.	C	O	Al	Cu	Total
Spectrum 1	Yes		1.67	79.03	19.30	100.00
Spectrum 2	Yes	0.52	0.71	87.53	11.24	100.00
Spectrum 3	Yes		2.47	78.95	18.58	100.00
Spectrum 4	Yes	2.14	0.24	79.00	18.62	100.00
Max.		2.14	2.47	87.53	19.30	
Min.		0.52	0.24	78.95	11.24	

All results in weight%

4.3.6 Magnetron-sputtered Al-30at.%Cu alloy

The surface of the magnetron-sputtered Al-30at.%Cu alloy is shown in Figure 4.6. The binary alloy surface morphology appears relatively flat, with some cavities developed at local sites. In order to investigate the local composition of the alloy, EDX point and area (22.5 cm^2) analyses were carried out. The EDX results are given in Table 4.5.

Table 4.5 EDX analyses of the surface of the magnetron-sputtered Al-30at.%Cu alloy

Spectrum	In stats.	Al	Cu	Total
Spectrum 1	Yes	63.53	36.47	100.00
Spectrum 2	Yes	63.04	36.96	100.00
Spectrum 3	Yes	59.68	40.32	100.00
Max.		63.53	40.32	
Min.		59.68	36.47	

All results in weight%

4.4 Transmission Electron Microscopy

4.4.1 Magnetron-sputtered superpure aluminium

A transmission electron micrograph of an ultramicrotomed cross section of the as-sputtered superpure aluminium is shown in Figure 4.7. The metal is columnar-grained, with a typical grain width of ~50 nm. The micrograph also confirms the non-uniformity of the specimen surface due to faceting during growth of the sputtered layer. The average thickness of the sputter deposited superpure aluminium is approximately 437.5 nm. The alumina film present on the electropolished aluminium substrate (approximately 3 nm) marks the interface between the sputter deposit and the underlying aluminium substrate.

4.4.2 Magnetron-sputtered Al-1.0at.%Cu alloy

Figure 4.8 shows a transmission electron micrograph of the ultramicrotomed Al-1.0at.%Cu alloy after sputter deposition. The surface of the binary alloy is not as rough as that of the sputter deposited superpure aluminium since the height and width of the metal ridges are not as pronounced as that of the superpure aluminium specimen. The

average thickness of the sputter deposited Al-1.0at.%Cu alloy is approximately 437.5 nm, with a grain width of approximately 31.25 nm.

4.4.3 Magnetron-sputtered Al-5.0at.%Cu alloy

A transmission electron micrograph of the Al-5.0at.%Cu specimen is shown in Figure 4.9. The alloy is columnar-grained, with a typical grain width of ~ 18.75 nm. The average thickness of the alloy is 487.5 nm. The surface of the specimen is rougher than that of the Al-1.0at.%Cu substrate, and the faceted texture is revealed with varied widths between the metal ridges that form the boundaries of the grains. The bases of the faceted texture protrude into the substrate to a depth of approximately 12.5 nm.

4.4.4 Magnetron-sputtered Al-10at.%Cu alloy

Figure 4.10 displays the transmission electron micrograph of the binary alloy after deposition. The alloy surface appears less rough compared to all other specimens except for the Al-30at.%Cu alloy. The surface has a faceted texture of varying dimensions. The average thickness of the sputter deposited Al-10at.%Cu alloy is approximately 362.5 nm.

4.4.6 Magnetron-sputtered Al-30at.%Cu alloy

Figure 4.11 shows the transmission electron micrograph of the binary alloy after deposition. The alloy surface appears relatively flat with minimal hillocks compared with all other specimens. The average thickness of the sputter deposited Al-30at.%Cu binary alloy is approximately 337.5 nm.

4.5 Atomic Force Microscopy

4.5.1 AFM characterisation of as-sputtered superpure aluminium

In order to gain more detailed information on the surface morphology of the superpure aluminium specimen, AFM analysis was performed. The AFM study of the morphology of the superpure aluminium specimen (Figure 4.12) reveals that the surface is not microscopically flat. This result confirms the TEM analysis which revealed the non-uniformity of the specimen surface due to faceting during growth of the sputtered layer.

The sputter deposited superpure aluminium shows clear evidence of hillock protrusions. The grains are relatively large and irregular in shape with clear definitions between the grains. Generally, facet surfaces are revealed, as shown in Figure 4.12 (c). The arithmetic mean roughness (R_a), the root mean square deviation (R_q) and the mean height of the profile within a specimen length (R_z) of 134 nm are 11.36, 14.47 and 11.51 nm respectively. The RMS roughness (R_q) is often larger than the average roughness (R_a), but both parameters show the same roughness tendency. Optimal characterisation of surface texture is expressed with area roughness calculations that are made on the surface of the specimen. If the surface of the specimen is almost flat (graphically the peak values are larger than the valley values), then the arithmetic mean roughness (R_a) value is approximately equal to the RMS roughness (R_q) value.

4.5.2 AFM characterisation of as-sputtered Al-1.0at.%Cu alloy

AFM images of the surface of the magnetron sputtered Al-1.0at.%Cu alloy are shown in Figure 4.13. This figure displays an elongated faceted texture. The roughness analysis reveals an arithmetic mean roughness (R_a) of 4.24 nm, root mean square deviation (R_q) of 5.47 nm and a profile mean height of 5.28 nm. The surface of the superpure aluminium presents a higher roughness than the Al-1.0at%Cu specimen, as revealed by the average roughness (R_a) and RMS roughness (R_q) values reported.

4.5.3 AFM characterisation of as-sputtered Al-5.0at.%Cu alloy

Figures 4.14 (a) – (c) show the typical AFM images of the as-sputtered Al-5.0at.%Cu alloy. The texture of the magnetron sputtered Al-1.0at.%Cu alloy is generally pebble or cell-like. Some particles protrude above the alloy surface by about 33 nm. The AFM roughness analysis reveals an arithmetic mean roughness (R_a) of 7.36 nm, root mean square deviation (R_q) of 9.65 nm and a mean height of 11.44 nm.

4.5.4 AFM characterisation of as-sputtered Al-10at.%Cu alloy

The AFM study of the morphology of the Al-10at.%Cu specimen (Figure 4.15) reveals a fine cellular or scalloped texture. The arithmetic mean roughness (R_a), the root mean square deviation (R_q) and the mean height of the profile within a specimen length (R_z) of 57.72 nm are 5.30, 6.62 and 5.71 nm respectively.

4.5.6 AFM characterisation of as-sputtered Al-30at.%Cu alloy

An atomic force image of the magnetron sputtered Al-30at.%Cu alloy is shown in Figure 4.16. The surface appears relatively smooth with few protuberances from the alloy matrix. The protuberances with an average diameter of about 101 nm (protruding about 14 nm above the alloy matrix) are likely individual grains or due to shadowing effects. The AFM roughness analysis reveals an arithmetic mean roughness (R_a) of 4.06 nm, root mean square deviation (R_q) of 5.47 nm and a mean height of 5.11 nm.

4.6 Crystallographic Measurements by X-ray Diffraction Spectroscopy

The XRD patterns of as-sputtered specimen recorded on the Y plane between $2\theta = 5$ and 85^0 are shown in Figure 4.17 (a) – 4.17 (e). XRD confirmed the preferred orientation of the thin sputtered aluminium films. All specimens demonstrated thin films with crystalline aluminium peaks according to PDF 04-0787. Prominent peaks for {111} and {200} reflections are highlighted on the plots for superpure aluminium (Figure 4.17 (a)). The superpure aluminium film demonstrated the strongest {111} peak height. However, as the copper content increases (Figure 4.17 (b) – (e)), this peak becomes smaller and less defined due to the appearance of other orientation peaks as displayed in Tables 4.6 to 4.10. This reduction in peak intensity for {111} is also an indicator of increased disorder in the film due to the change in the orientation of the grains as the copper content of the alloy is increased. The intensity of the {111} peak is a measure of the preferred orientation of aluminium in the crystalline grains. The presence of intermetallic compounds in Al-Cu binary alloys was also confirmed by the presence of very fine low XRD reflections with low intensity. The primary aluminium (α-Al) solid phase and the secondary θ (Al_2Cu) phase were observed to be present in the binary aluminium-copper alloys.

Table 4.6 Orientation of the as-sputtered superpure aluminium specimen obtained from the XRD pattern in Figure 4.17 (a)

Pos. [°2Th.]	h k l	Rel. Int. [%]
34.6128	-	0.05
38.4979	1 1 1	100.00
44.7295	2 0 0	22.69
65.0510	2 2 0	0.63
78.2045	3 1 1	0.13

Table 4.7 Orientation of the as-sputtered Al-1.0at.%Cu alloy specimen obtained from the XRD pattern in Figure 4.17 (b)

Pos. [°2Th.]	h k l	Rel. Int. [%]
20.7627	1 1 0	0.57
29.5163	-	0.13
38.4902	1 1 1	69.55
44.7383	2 0 0	100.00
47.4093	3 1 0	0.20
65.0963	2 2 0	14.81
69.4503	-	0.51
78.1788	3 1 1	50.06
78.4317	0 0 4	33.26
82.3994	1 1 4	8.49
82.6966	3 2 3	4.99

Table 4.8 Orientation of the as-sputtered Al-5.0at.%Cu alloy specimen obtained from the XRD pattern in Figure 4.17 (c)

Pos. [°2Th.]	h k l	Rel. Int. [%]
20.7281	1 1 0	3.85
29.4166	-	0.60
38.6300	1 1 1	39.51
42.1319	2 2 0	1.74
42.6504	1 1 2	2.47
44.7240	2 0 0	55.75
47.4143	3 1 0	2.24
47.8982	2 0 2	1.74
57.2221	-	0.26
61.4472	-	0.16
65.0962	2 2 0	7.80
67.1841	-	0.26
69.4133	-	0.88
73.5429	-	0.80
74.2105	-	0.91
78.1786	3 1 1	100.00
78.4940	0 0 4	41.64
82.3732	1 1 4	7.65
82.7078	3 2 3	3.59

Table 4.9 Orientation of the as-sputtered Al-10at.%Cu alloy specimen obtained from the XRD pattern in Figure 4.17 (d)

Pos. [°2Th.]	h k l	Rel. Int. [%]
20.7483	1 1 0	0.86
29.5109	2 0 0	0.16
38.5590	1 1 1	24.36
39.8182	-	0.39
42.1382	-	0.44
42.6485	1 1 2	0.56
44.7371	2 0 0	14.53
47.4611	-	0.51
47.9684	-	0.33
57.2087	-	0.06
61.3043	-	0.05
65.0865	2 2 0	2.86
69.4550	-	0.29
73.6061	-	0.34
74.2391	-	0.54
78.1825	3 1 1	100.00
78.5005	3 3 2	42.02
82.3860	1 1 4	4.12
82.7072	3 2 3	2.37

Table 4.10 Orientation of the as-sputtered Al-30at.%Cu alloy specimen obtained from the XRD pattern in Figure 4.17 (e)

Pos. [°2Th.]	h k l	Rel. Int. [%]
20.6194	1 1 0	1.01
38.4590	2 0 0	1.82
42.5557	1 1 2	6.51
44.6899	2 0 0	4.89
47.7594	2 0 2	2.64
57.3977	-	0.16
65.0314	2 2 0	100.00
73.5468	-	0.21
78.1305	3 1 1	20.49

4.7 Electrochemical Behaviour of Aluminium and Al-Cu Model Alloys

In considering the mechanisms of inhibition of corrosion by conversion coatings, it is important to take into consideration the influences of substrate preparation, since pre-treatments give rise to different surface topographies which reflects the manner in which the substrate material is removed.

4.7.1 Open circuit potential measurements

The potential-time response of superpure aluminium and aluminium-copper model alloys in 3.5 wt.% NaCl solution is shown in Figures 4.18 (a) and (b). The variation in open circuit corrosion potential with time for magnetron-sputtered superpure aluminium and the alloys containing 1, 5, 10, 30 at.%Cu recorded during immersion in naturally aerated 3.5 wt.% NaCl solution is shown in Figure 4.18 (a). The superpure aluminium electrode initially adopted a potential of -850 mV (SCE). The potential then decreased slightly to an approximate value of -900 mV (SCE), after 1000 s of immersion in the chloride solution. Thereafter, the potential further decreased to a steady state value of -1280 mV after 6000 s. There was no fluctuation in the observed potential for the aluminium specimen. For the Al-1.0at.%Cu alloy, an initial potential of -744.61 mV was observed, followed by a period of rapid potential fluctuations, after which the observed potential was nearly steady. Subsequently, there was a steep rise in potential, followed by a period of rapid potential fluctuations. In contrast, however, when the alloy copper content was further increased, the open circuit potentials were not stable with fluctuations in potential being more pronounced.

Figure 4.18 (b) shows the potential-time response for superpure aluminium and copper-containing aluminium alloys in nitrogen-deaerated 3.5 wt.% NaCl solution. For superpure aluminium, after the initially adopted open circuit potential of -1473 mV (SCE) at the time of immersion, the potential increased at a relatively reduced rate to -1390 mV after 1000 s; thereafter, the potential decreased from the maximum potential value over the following 1200 s to a steady state value of -1465 mV. The potential-time response of Al-1.0at.%Cu alloy (Figure 4.18 (b)) in nitrogen-deaerated NaCl solution shows an initial potential of -900 mV (SCE) at the time of immersion, after which it decreased at a steep rate to -1290 mV after 1000 s followed by a period of rapid potential fluctuations between -1278.1 mV and -1246.8 mV. The potential of the Al-5.0at.%Cu alloy electrode at the time of immersion was approximately -903 mV (SCE). The potential dropped rapidly to -1122 mV in the early stages of immersion in sodium chloride solution and recovered to -955 mV after 550 s with a subsequent fall to -1135 mV after 2267 s; this was followed by a slight increase of potential with time up to a maximum of -975.6 mV. The potential of the Al-10at.%Cu specimen at the time of immersion was -750 mV (SCE). This potential dropped relatively slowly to a minimum

value of -960 mV after 3600 s, after which the potential was maintained in the range of -950 mV to -913 mV over the period of immersion. The potential-time response of Al-30at.%Cu in 3.5 wt.% sodium chloride solution shows an initial potential of -885 V (SCE) at the time of immersion, followed by a period of rapid potential fluctuations between -765 mV and -860 mV.

The open-circuit corrosion potential of the as-sputtered specimens was obtained from ACM polarisation data analysis software over the 2 hours immersion period in 3.5 wt% NaCl solution. Figure 4.19 illustrates the relationship between the average open-circuit corrosion potential and Al-Cu alloy composition. The results obtained for the superpure aluminium and copper-containing aluminium alloys over a period of 2 hours immersion in deaerated 3.5 wt% NaCl solution revealed that the average potential of the aluminium alloys became increasingly positive as the copper content was increased.

4.8 Cathodic Polarisation

The cathodic polarisation sweeps obtained for the magnetron-sputtered superpure aluminium and selected Al-Cu alloys in aerated 3.5 wt.% NaCl solution are shown in Figure 4.20. For the superpure aluminium specimen, a rapid increase in current density was initially observed close to the open-circuit potential. The cathodic polarisation response revealed a diffusion controlled process from the open circuit potential of -1255 mV to –1500 mV. After -1500 mV, a second cathodic process, i.e. hydrogen evolution commenced. However, the behaviour of the copper-containing alloys revealed a strong diffusion controlled process with relatively small increase in current density being observed for a little increase in potential.

An electrode reaction is considered to be under “diffusion control” when the overall rate of the reaction is controlled by the rate of the diffusion of the reactants to the electrode surface rather than the rate of the reaction itself. This condition occurs when the diffusion rate is much slower than the reaction rate and the diffusion process cannot make the reactants available sufficiently to the electrode surface. The presence of a current density plateau in cathodic polarisation curve indicates that diffusion of oxygen towards the electrode surface acts as the rate-controlling step of the cathodic reaction [283]. The cathodic process during aluminium corrosion in aerated sodium chloride solution is dominated by diffusion of the dissolved oxygen towards the

aluminium electrode surface and the reduction of oxygen (equation 4.1) and then followed by hydrogen evolution.

$$O_2 + 2H_2O + 4e^- \rightarrow 4OH^- \quad (4.1)$$

In Figure 4.20, the cathodic polarisation responses of the Al-Cu binary alloys were similar since diffusion controlled cathodic reactions appeared to be predominant. The polarisation curves obtained for the Al-Cu alloys were observed to be under strong diffusion control compared with that of the superpure aluminium specimen. Hence, the cathodic responses of the alloys show a strong diffusion controlled behaviour, with only a very small increase in current density being observed for a large increase in potential. A further effect of increasing the copper content of the alloy was to shift the cathodic polarisation curves to progressively higher current densities as shown in Figure 4.20.

4.9 Anodic Polarisation

The anodic polarisation sweeps obtained for sputter-deposited superpure aluminium and aluminium-copper alloys after 2 hours immersion in 3.5 wt.% NaCl solution are shown in Figure 4.21. The polarisation curves clearly show a passive current density of approximately 1.65×10^{-7} A/cm for superpure aluminium specimen.

Figure 4.21 showed that as the alloy copper content was increased the anodic polarisation curves were shifted to higher potential. The relationship between the corrosion current density and the open circuit potentials of the as-sputtered specimens after immersion in deaerated NaCl solution for 2 hours is shown in Figure 4.22. The plot obtained for the aluminium-copper alloys indicates that as the alloy copper content increases, the corrosion current density increases and the open circuit potential becomes more positive as well.

4.10 Discussion

4.10.1 Atomic force microscopy

Atomic force microscopy imaging of sputter-deposited superpure aluminium, Al-1.0at.%Cu, Al-5.0at.%Cu, Al-10at.%Cu and Al-30at.%Cu alloy revealed characteristic faceted textures. The height profiles of the resultant AFM images revealed that the

surface of the superpure aluminium presents higher roughness than the Al-Cu alloys as shown by the average roughness (R_a) and RMS roughness (R_q) values which is higher than that reported for copper-containing aluminium alloys. The AFM images obtained for the specimens confirm that grain refinement is achievable in sputtered deposited aluminium films with small amount of solute additions. The solute additions (copper), affects the grains by reducing grain size and thus reducing surface topography. The effect of copper solute addition on aluminium films is clearly evident. All measured aluminium-copper alloys shows markedly reduced levels of surface roughness compared with sputter-deposited superpure aluminium.

4.10.2 Open circuit potential and polarisation processes

The electrochemical potential of binary alloys is related to the thermodynamic equilibrium potentials of the two components of the alloy [284]. Hence, the electrochemical potential adopted by the binary alloy will be located between the potential values of the parent metals. The standard hydrogen electrode (SHE) potential for aluminium is -1.706V (SHE) and it is +0.34 (SHE) for copper, which is much more positive than aluminium. Therefore, thermodynamically, the addition of copper in the aluminium-copper alloys increased the open-circuit potential in the positive direction as shown by Figure 4.18 (b). Accordingly, the addition of copper to the sputtered aluminium deposits produced alloys which adopted open-circuit corrosion potentials that were positive compared to that of superpure aluminium but were negative with respect to that of pure copper. Thus, the potential-time measurements and polarisation behaviour revealed that percentage weight composition of aluminium-copper alloys influences the behaviour of the alloys in chloride environment with pitting potential increasing with increasing copper content of the alloys. While a stable potential value was observed for the superpure aluminium specimen, the copper-containing aluminium alloys behaved differently, since the open circuit potentials did not stabilise, but continued to oscillate, with the potential drift following a positive trend. However, the Al-30at.%Cu alloy behaved differently from the other aluminium alloys with moderate levels of copper content in that following a steep rise in potential (Figure 4.18 (b)), a period of rapid potential fluctuation was observed. These fluctuations in open circuit potential are usually attributed to the effect of localised corrosion such as pitting attack.

The corrosion behaviour of aluminium is highly dependent on the properties of the air-formed oxide film that forms on its surface. The Pourbaix diagram (see Figure 2.3) shows that aluminium exposed to de-ionised water of pH 4 to 7 would form protective barrier film of Al_2O_3, which reduces corrosion activity. Pourbaix reported that the quality of the oxide films varies notably in its degree of hydration and porosity even within the passive region. Extensive studies have been carried out on the protective properties of the air-formed films on aluminium surfaces [285-287]. Pits have been found to almost always initiate at some chemical or physical heterogeneity at the surface, such as inclusions, second phase particles, solute-segregated grain boundaries, flaws etc. Models for flaws are generally held to be associated with heterogeneity, either compositional or mechanical in the aluminium substrate. Wood et al [286, 288] observed that the pitting of aluminium is usually initiated at such flaws. When aluminium is immersed in an environment conducive to pitting attack, all flaws in the air-formed film can be considered as potential pit sites. The “residual” flaws which are associated with impurity segregates in the aluminium substrate tend to be predominantly cathodic in nature. The “mechanical” flaws on the other hand, possess a smaller, yet appreciable cathode-anode area ration and are considered to provide preferential sites for the immediate propagation of pits. Undermining of the passive film may occur if the film has pores in it which expose the aluminium substrate to the aggressive chloride solution. In such situations, the aluminium can dissolve both at the bottom of the pores and between the film and the metal which loosens the oxide by undermining and this eventually leads to its removal. The predicted effects of flaws [286] on the potential of air-formed films on aluminium substrate is consistent with the observed potential response of the superpure aluminium electrode immersed in deaerated 3.5 wt.% NaCl solution. Hence, this is definitive proof of flaw effects on the measured potential of air-formed oxide is consistent with the Wood Model.

The cathodic polarisation curves of the specimens (Figure 4.20) showed that copper acts to increase the cathodic kinetics. In superpure aluminium specimen, a diffusion control which is related to oxygen reduction as well as a second cathodic process involving hydrogen evolution is evident. The cathodic polarisation behaviour of copper-containing aluminium alloys revealed an increase in the cathodic current density as the copper content of the alloy is raised. This may be related to the increased rate of oxygen diffusion through the less protective oxide film formed on aluminium-copper alloys.

Mansfeld et al. [289] employed similar arguments to explain the difference in corrosion rates between aluminium alloys where none should be found in view of the fact that their corrosion reactions were under cathodic control. The authors proposed that differences in efficiency for oxygen reduction on individual aluminium alloys could also account for the difference in their corrosion rates.

An examination of the anodic polarisation behaviour of as-sputtered superpure aluminium and aluminium-copper alloys (Figure 4.21) revealed the presence of an extensive passive region in superpure aluminium and Al-1.0at.%Cu specimens. However, the higher the copper levels of the aluminium alloys, the lower the passive region observed in the polarisation curves. The Al-30at.%Cu specimen did not exhibit passive corrosion behaviour. The relatively smooth character of the polarisation curves for superpure aluminium and aluminium alloys (with low copper levels) in the passive region suggests there is much less metastable pit formation below the pitting potential, since "noise" in the passive region of the polarisation curves is usually interpreted physically as the formation of metastable pits that are subsequently repassivated [100].

The pitting potential of aluminium was found to increase as the copper content of aluminium alloy is raised with exception of the Al-30at.%Cu alloy where pitting occurred almost after polarisation. The effect is stronger for the first 1% copper addition, with the pitting potential becoming almost linear for higher copper contents with the pitting potential value being limited by solubility of copper in aluminium. This is due to the fact that at higher concentration the solubility of copper in aluminium is exceeded, and two different phases of aluminium system is formed which is composed of a solid solution of aluminium-copper with copper content changing with temperature but always less than 5.65 wt% copper [29] and the second phase will be the intermetallic $CuAl_2$. The results obtained in the present study were also observed for aluminium-copper alloys by Galvele et al. [29, 169]. The authors indicated that the addition of alloying elements to aluminium increases the pitting potential due to the fact that copper is enriched on the surface of incipient pits, resulting in faster hydrogen reduction kinetics than on pure aluminium surfaces. This consequently increases the dissolution kinetics by depolarisation of the hydrogen reduction reaction, which results in the observed increase in pitting potential of copper-containing aluminium alloys. The literature contains several reports of copper surface enrichment by corrosion of copper-

containing aluminium alloys [162, 290]. Many of these reports involve the phenomenon of deposition corrosion [290], which arises from the dissolution and redeposition of copper on a corroding aluminium alloy surface. Ramgopal and Frankel [171] also developed a clearer interpretation of the inhibiting effect of copper in Al-Cu solid solutions based on the measurement of the anodic polarisation response of artificial crevices using a decreasing potential scanning approach. Based on their results, copper increases the aluminium dissolution kinetics by increasing the exchange current density and the Tafel slope of the dissolution partial reaction. This increases the repassivation potential and reduces the dissolution kinetics producing the observed inhibiting effect.

It can be seen from Figure 4.21 that in deaerated sodium chloride solution the corrosion potential of the Al-1.0at.%Cu alloy was significantly shifted to more negative potential values compared with those in aerated solution (Figure 4.20). This phenomenon indicates that in aerated sodium chloride solution, oxygen reduction taking place on the Al-1.0at.%Cu alloy surface is the cathodic process determining the open circuit potential of the alloy. On the other hand, the open circuit potential of all other specimens changed far less as a result of the exclusion of air, revealing that reduction of dissolved oxygen is a slow process on the surfaces.

Sputter-deposited aluminium alloys have been found to exhibit dramatic increase in pitting potential [44, 57]. A few atomic percentage of metal solute will increase the pitting potential by around 200 mV and increases over 1 V are possible with higher amounts of alloying. Explanations for the improvement in pitting resistance conferred on aluminium by this non-equilibrium alloying have been offered based on influences on the composition and protectiveness or pH of zero charge of the passive film [291], the solubility of dissolved species in the pit solution [292], enrichment of the solute species at the active surface in a pit [293], and decreases in the pit dissolution kinetics [294]. On the other hand, studies conducted in the literature have found that microsegregation of copper and iron impurities at nodes in high purity aluminium was sufficient to increase the tendency for pitting corrosion at open circuit [291]. In reality, no pitting resistant alloy can be produced by alloying aluminium since a pitting potential higher than + 0.81 V would be necessary in aerated condition (in the presence of oxygen) [29]. However, the effect of copper on the pitting potential of copper-

containing aluminium alloys is of particular interest since it gives a clue for the possible mechanism of pitting.

4.11 Summary

In the present study, the effects of the alloying element copper on aluminium-copper solid solution alloys were investigated in order to elucidate the role of copper on localised corrosion of aluminium alloys. The following are key findings:

1. From open circuit corrosion potential measurements conducted in 3.5 wt% NaCl solution, it was found that sputter deposited aluminium alloys becomes progressively more active as the alloy copper content is increased.

2. Based on the pitting potentials obtained for the solid-solution aluminium-copper alloys, these alloys are less susceptible to pit initiation compared with aluminium in its pure state provided that the alloyed copper is retained in solid solution. This effect is evident in the present work with pitting potential increasing with copper content in aluminium-copper solid solution alloys.

3. The corrosion rates of aluminium-copper alloys containing up to 30% by weight copper were found to increase with increasing copper content indicating that the corrosion resistance of aluminium alloys will decrease with increasing copper content. This effect was attributed to galvanic cells created by formation of minute copper particles or films deposited onto the alloy surface as a result of corrosion.

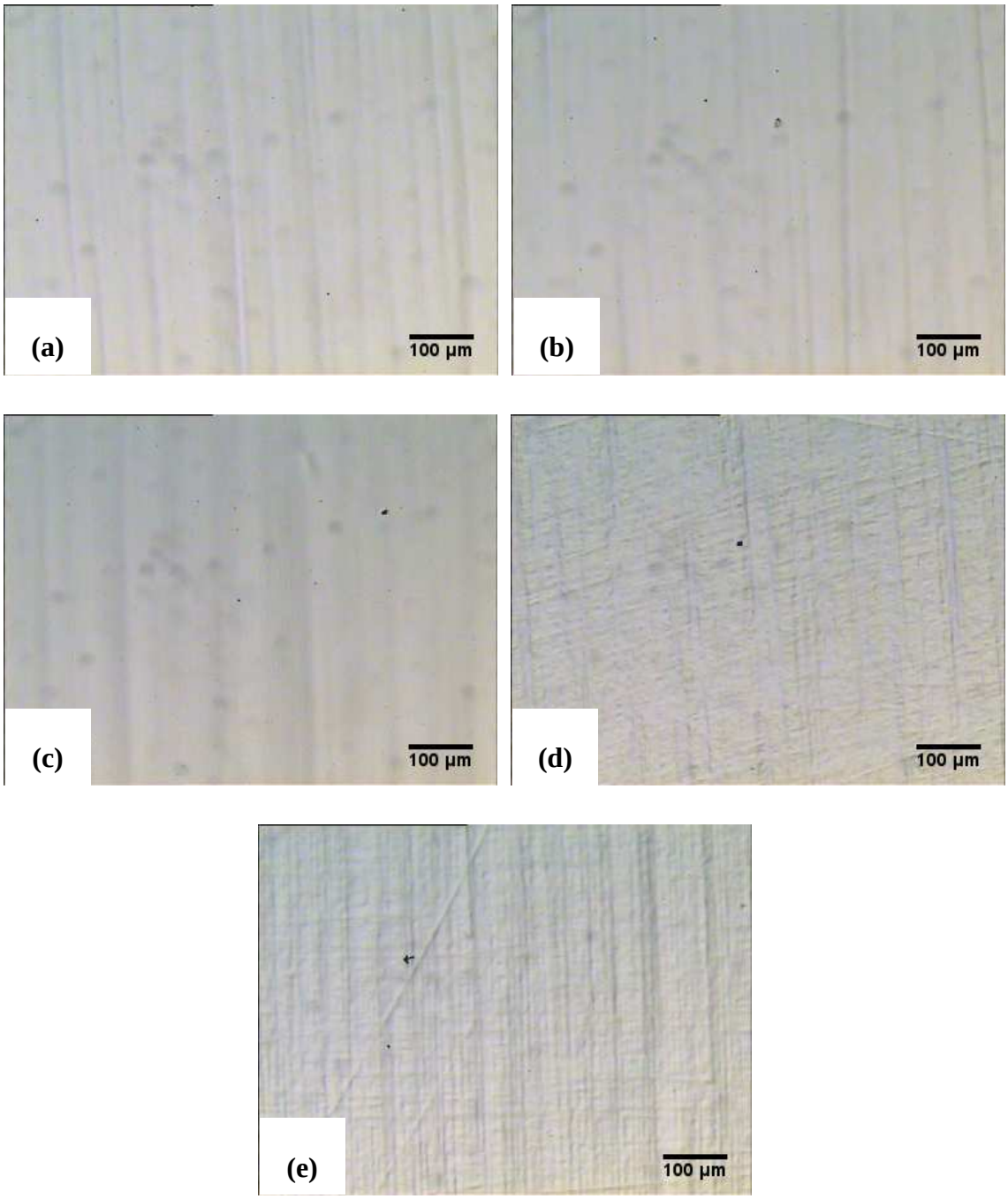

Figure 4.1 Optical micrographs of (a) superpure aluminium (b) Al-1.0at.%Cu (c) Al-5.0at.%Cu (d) Al-10at.%Cu and (e) Al-30at.%Cu alloy

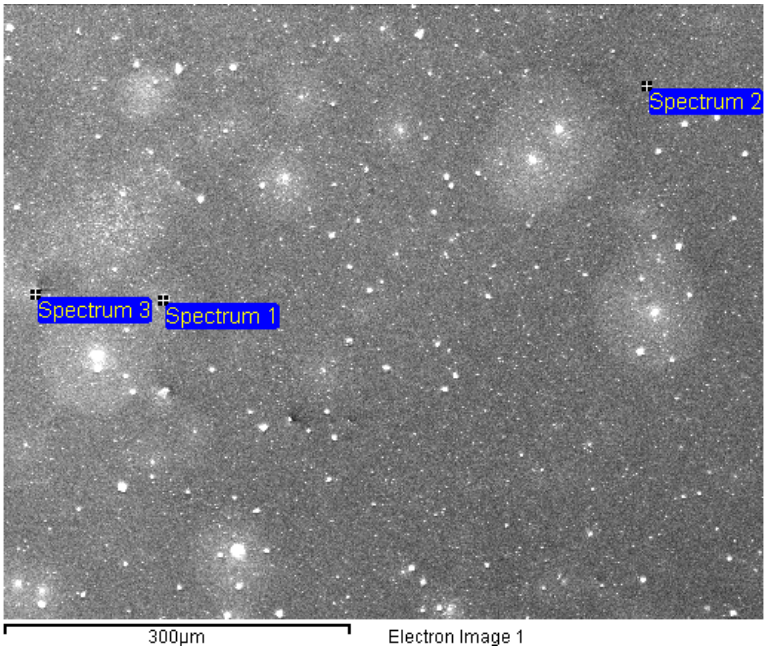

Figure 4.2 Scanning electron micrograph of as-sputtered superpure aluminium

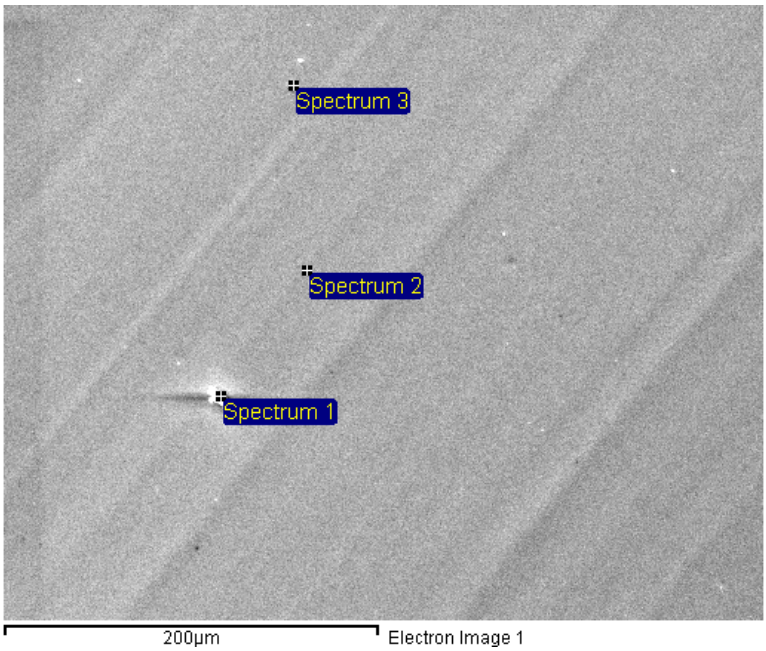

Figure 4.3 Scanning electron micrograph of as-sputtered Al-1.0at.%Cu alloy

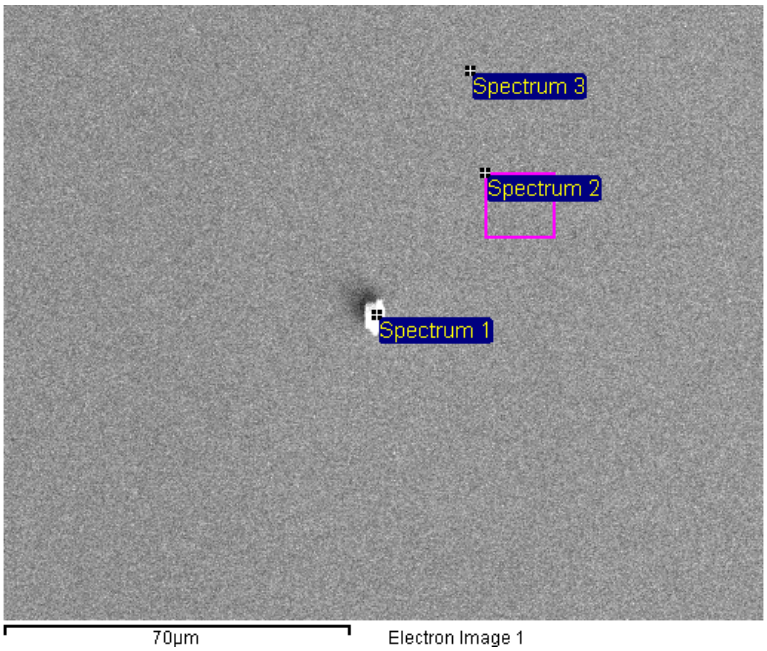

Figure 4.4 Scanning electron micrograph of as-sputtered Al-5.0at.%Cu alloy

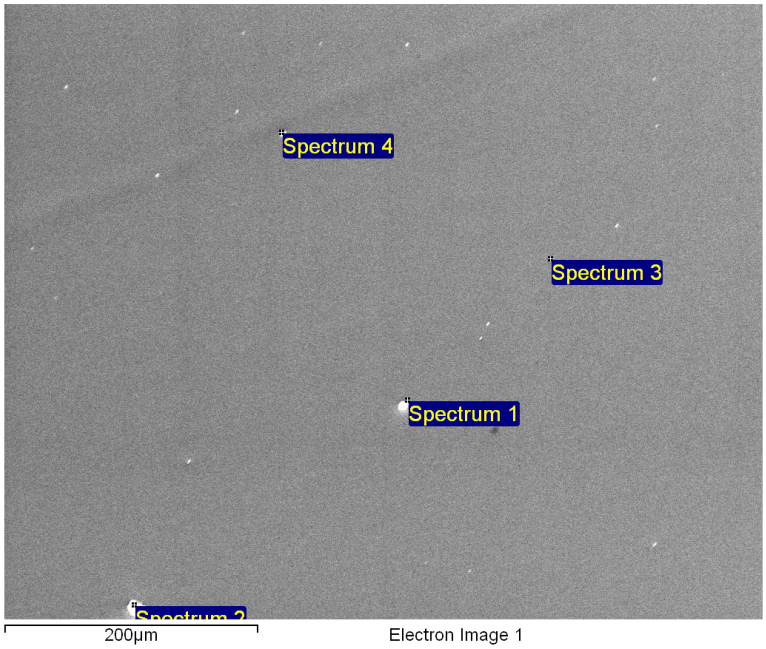

Figure 4.5 Scanning electron micrograph of as-sputtered Al-10at.%Cu alloy

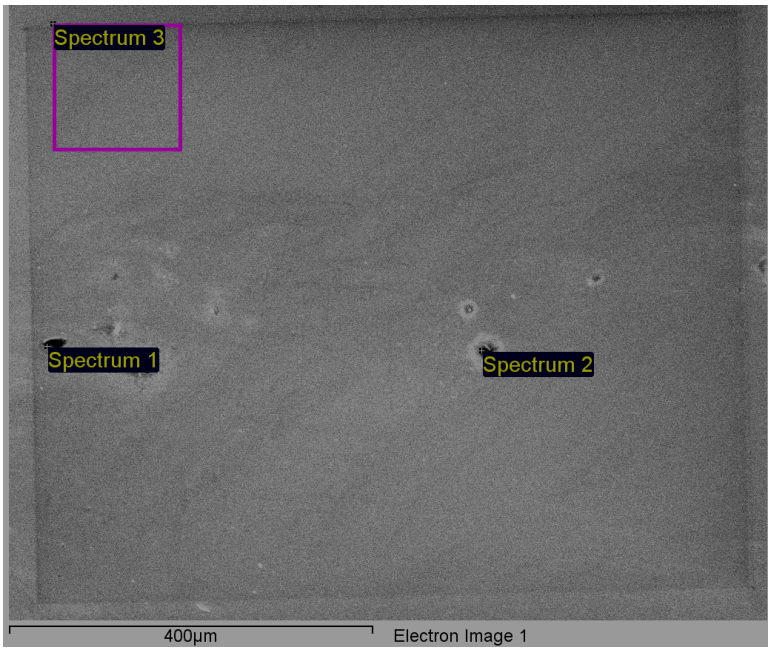

Figure 4.6 Scanning electron micrograph of as-sputtered Al-30at.%Cu alloy

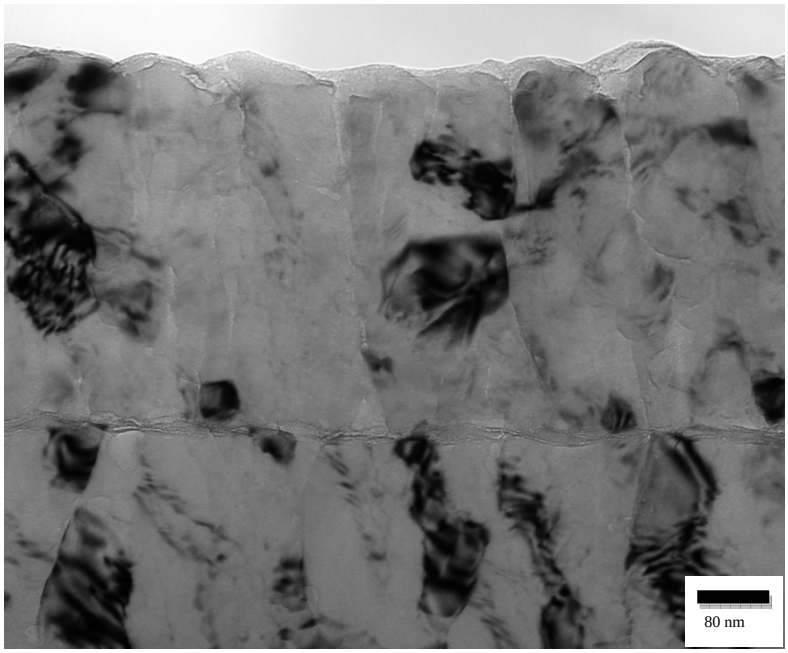

Figure 4.7 Transmission electron micrograph of superpure aluminium

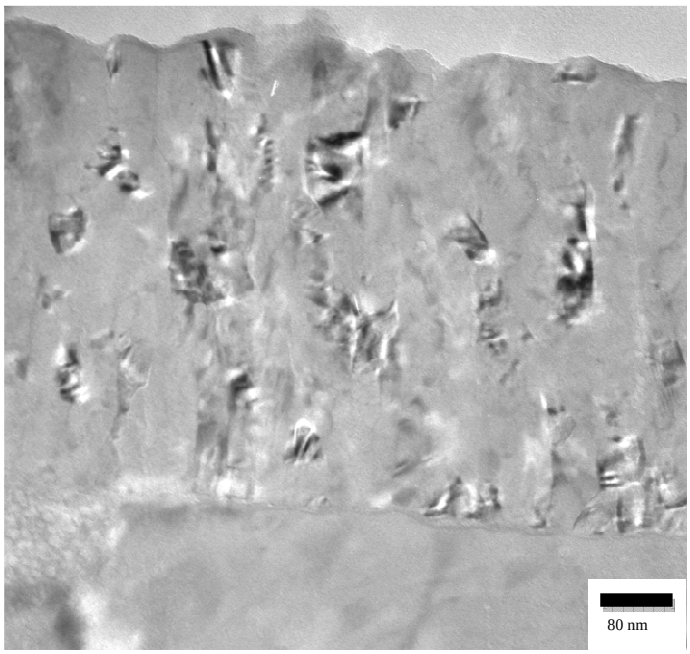

Figure 4.8 Transmission electron micrograph of the Al-1.0at.%Cu alloy

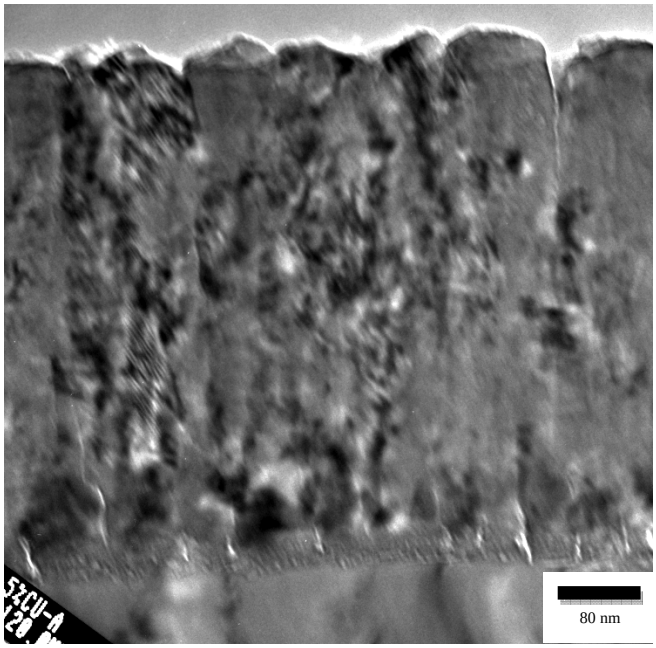

Figure 4.9 Transmission electron micrograph of the Al-5.0at.%Cu alloy

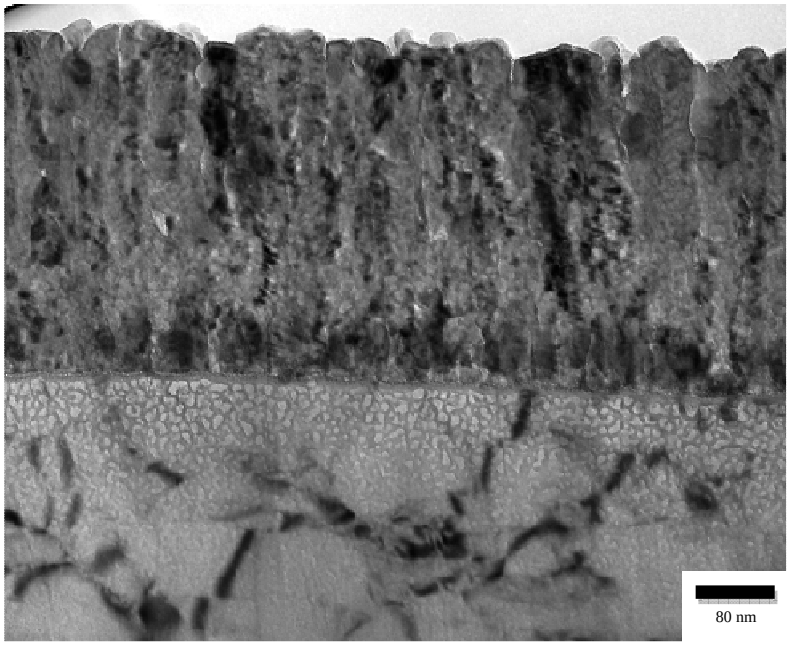

Figure 4.10 Transmission electron micrograph of the Al-10at.%Cu alloy

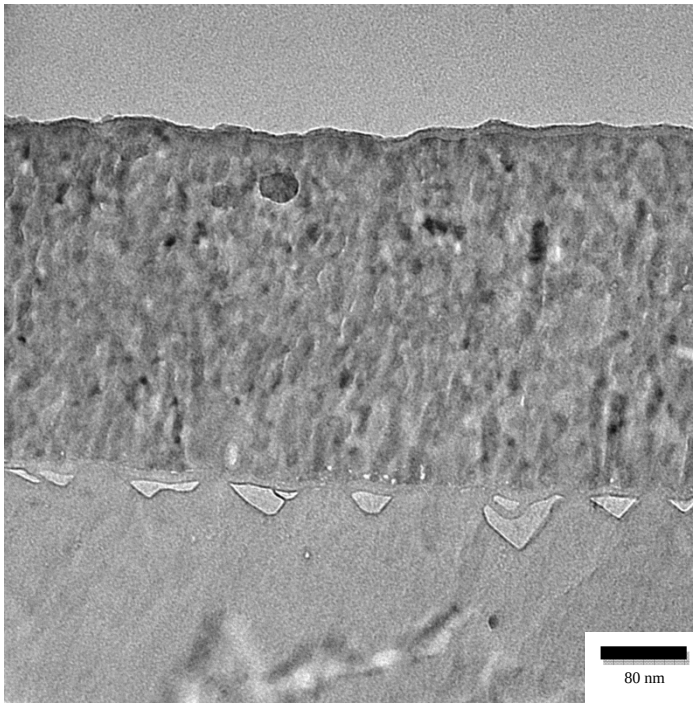

Figure 4.11 Transmission electron micrograph of the Al-30at.%Cu alloy

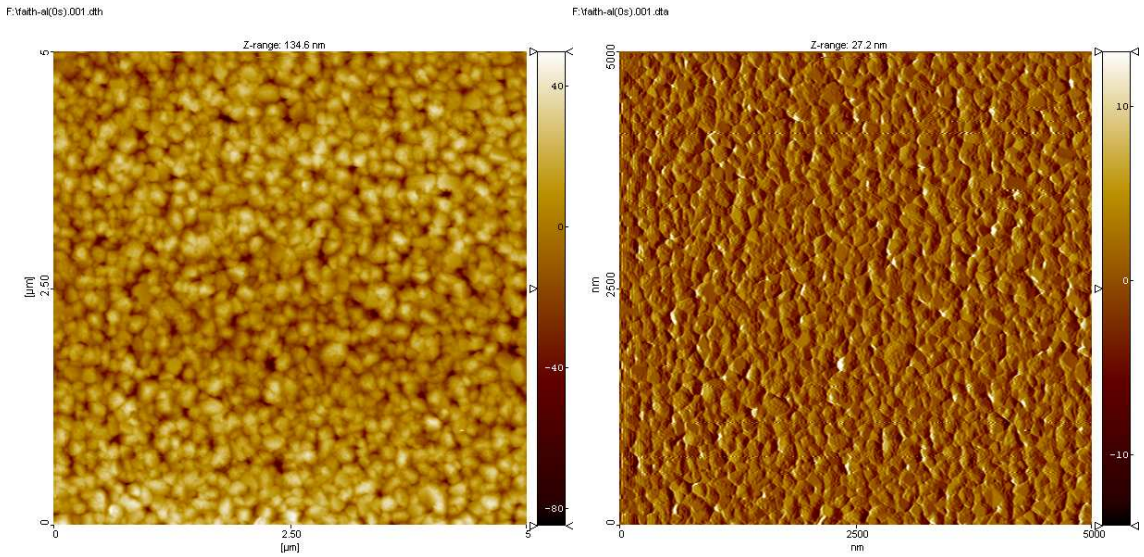

(a) **(b)**

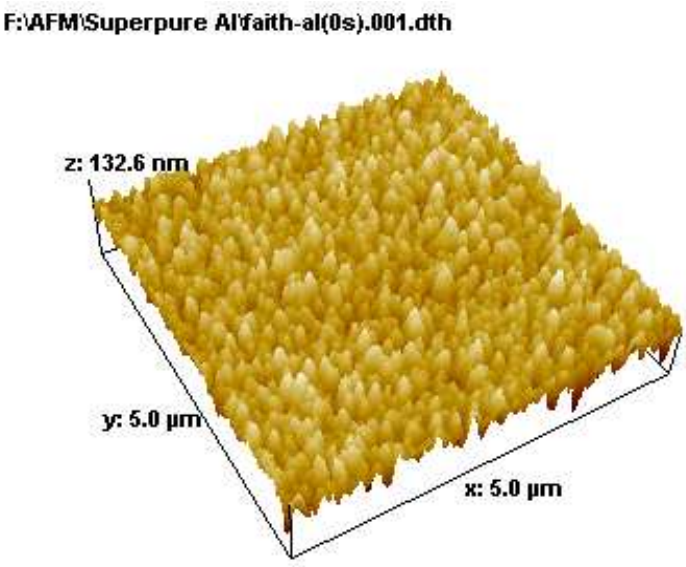

(c)

Figure 4.12 AFM images of the surface of a magnetron sputtered superpure aluminium; (a) height image; (b) 2-dimensional image; (c) 3-dimensional topographic image

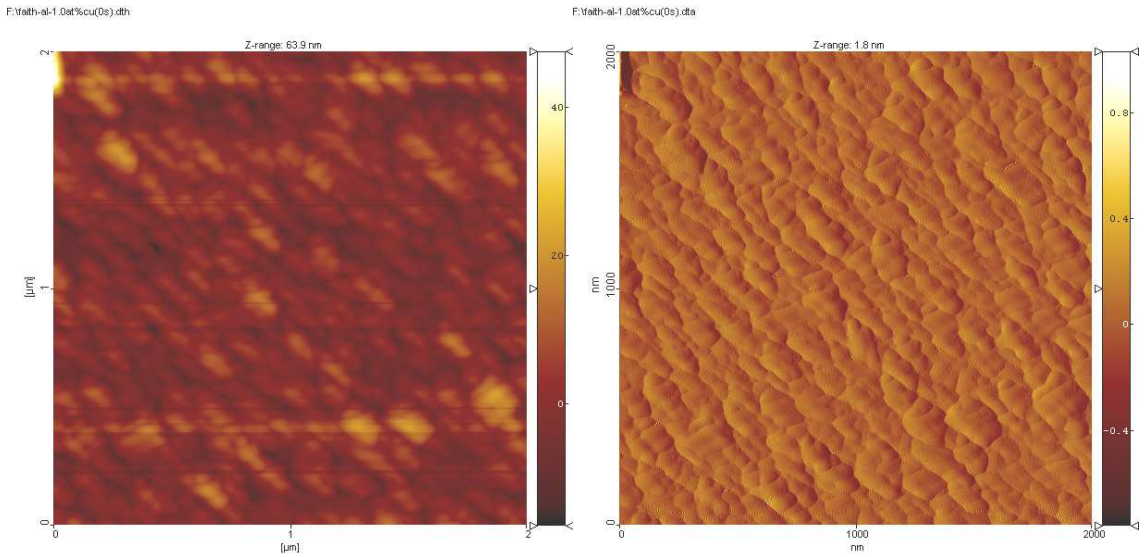

(a) **(b)**

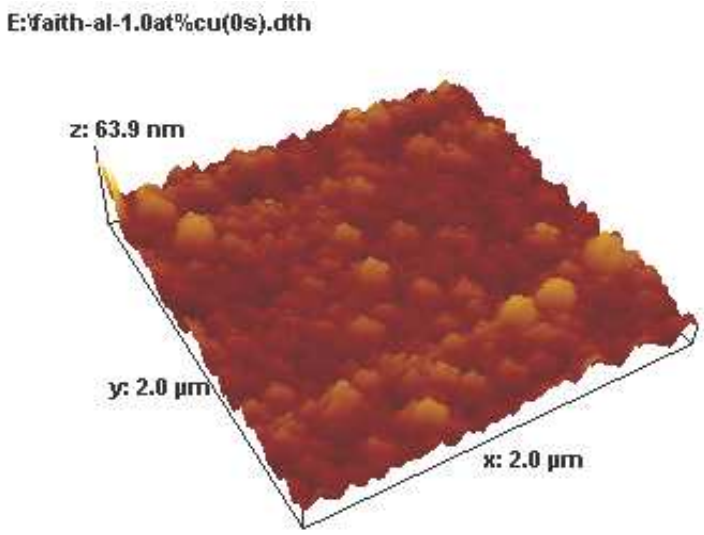

(c)

Figure 4.13 AFM images of the surface of a magnetron sputtered Al-1.0at.%Cu alloy; (a) height image; (b) 2-dimensional image; (c) 3-dimensional topographic image

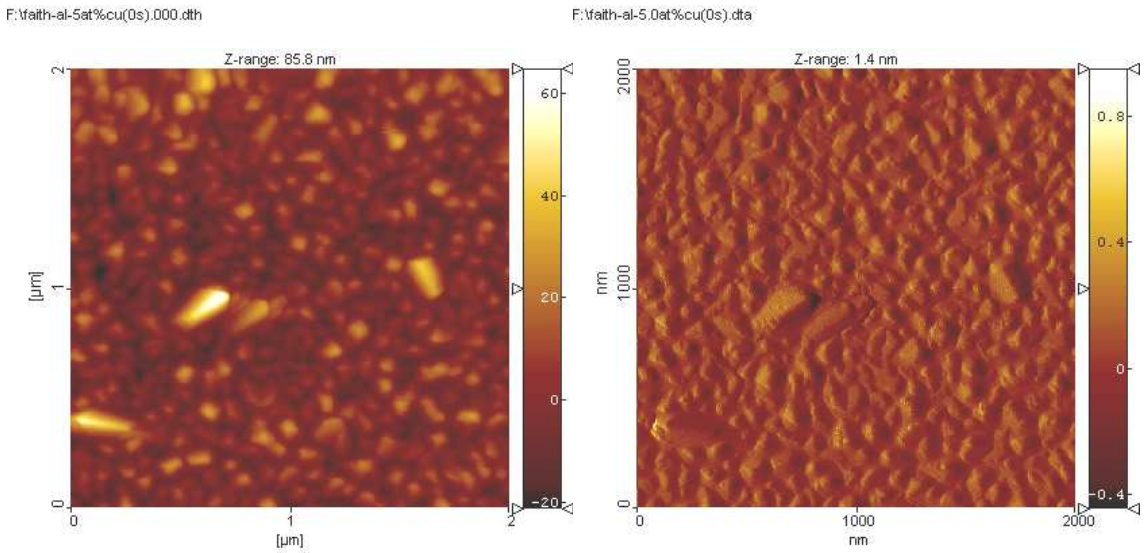

(a) **(b)**

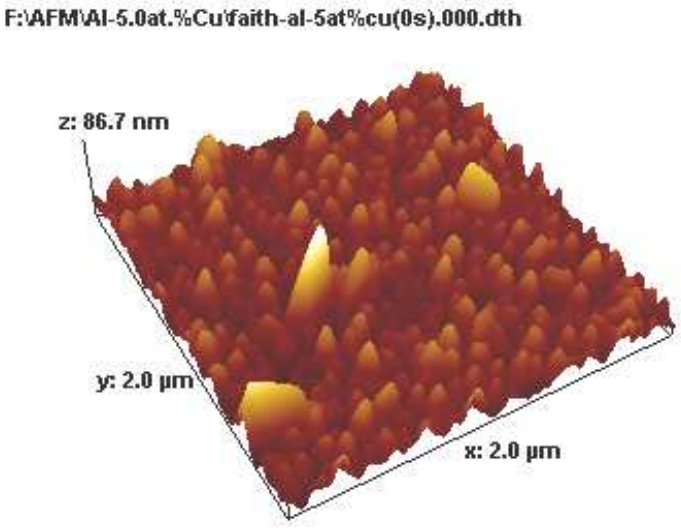

(c)

Figure 4.14 AFM images of the surface of a magnetron sputtered Al-5.0at.%Cu alloy; (a) height image; (b) 2-dimensional image; (c) 3-dimensional topographic image

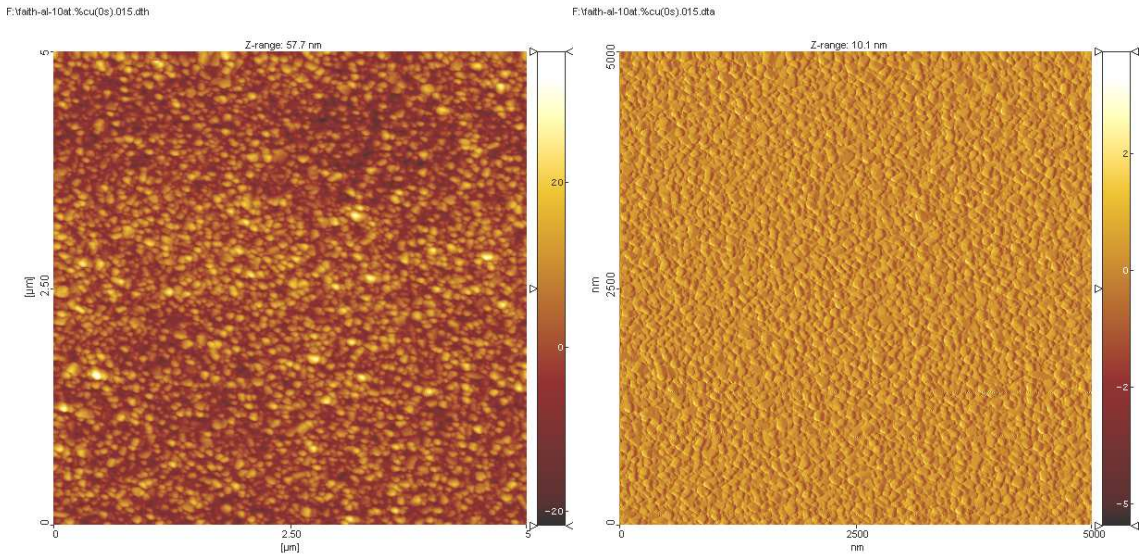

(a) **(b)**

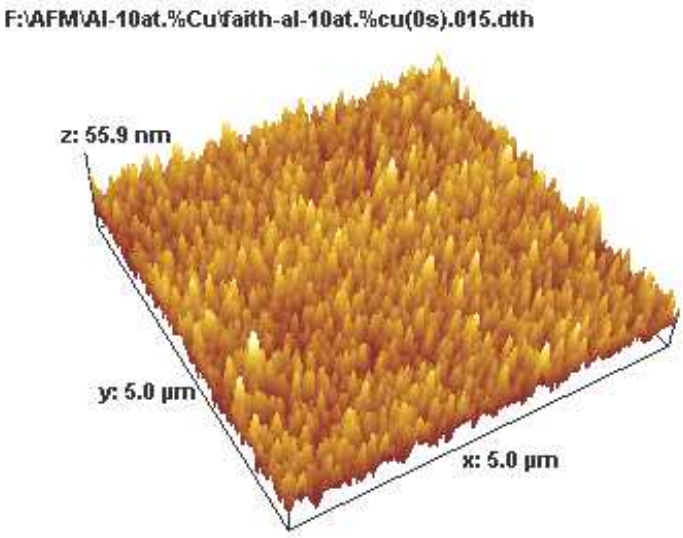

(c)

Figure 4.15 AFM images of the surface of a magnetron sputtered Al-10at.%Cu alloy; (a) height image; (b) 2-dimensional image; (c) 3-dimensional topographic image

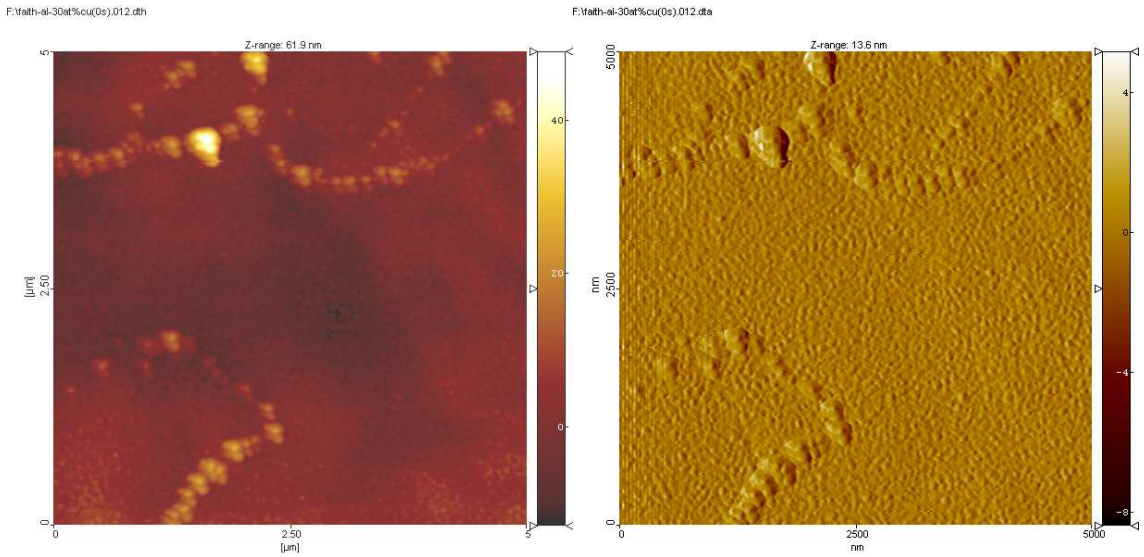

(a) **(b)**

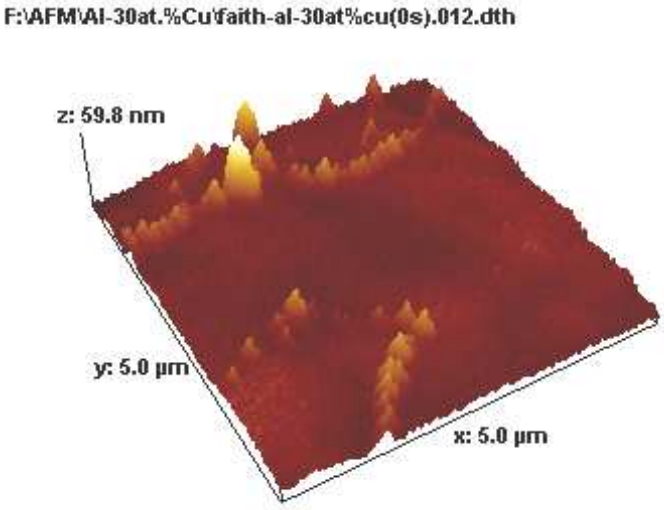

(c)

Figure 4.16 AFM images of the surface of a magnetron sputtered Al-30at.%Cu alloy; (a) height image; (b) 2-dimensional image; (c) 3-dimensional topographic image

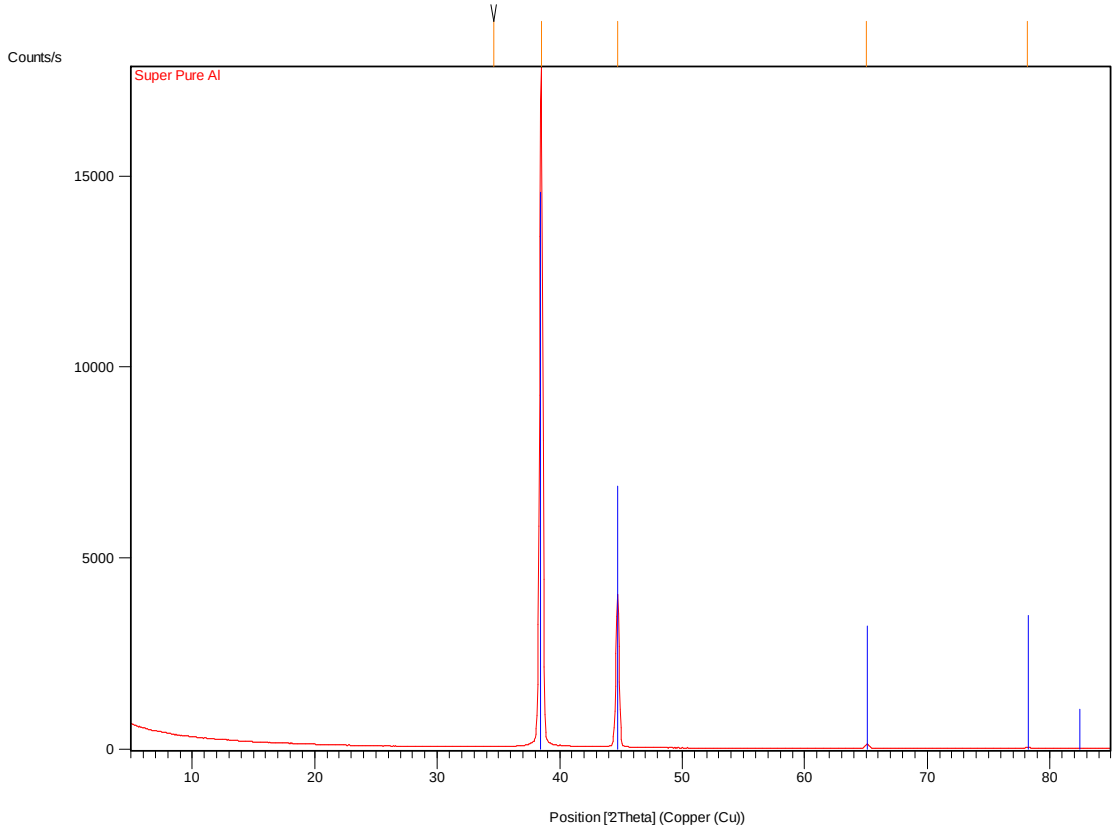

Figure 4.17 (a) XRD Spectrum of Superpure Aluminium

Pattern List:

Visible	Ref. Code	Compound Name	Displacement [°2Th.]	Scale Factor	Chemical Formula
*	00-004-0787	Aluminum, syn	0.000	0.795	Al

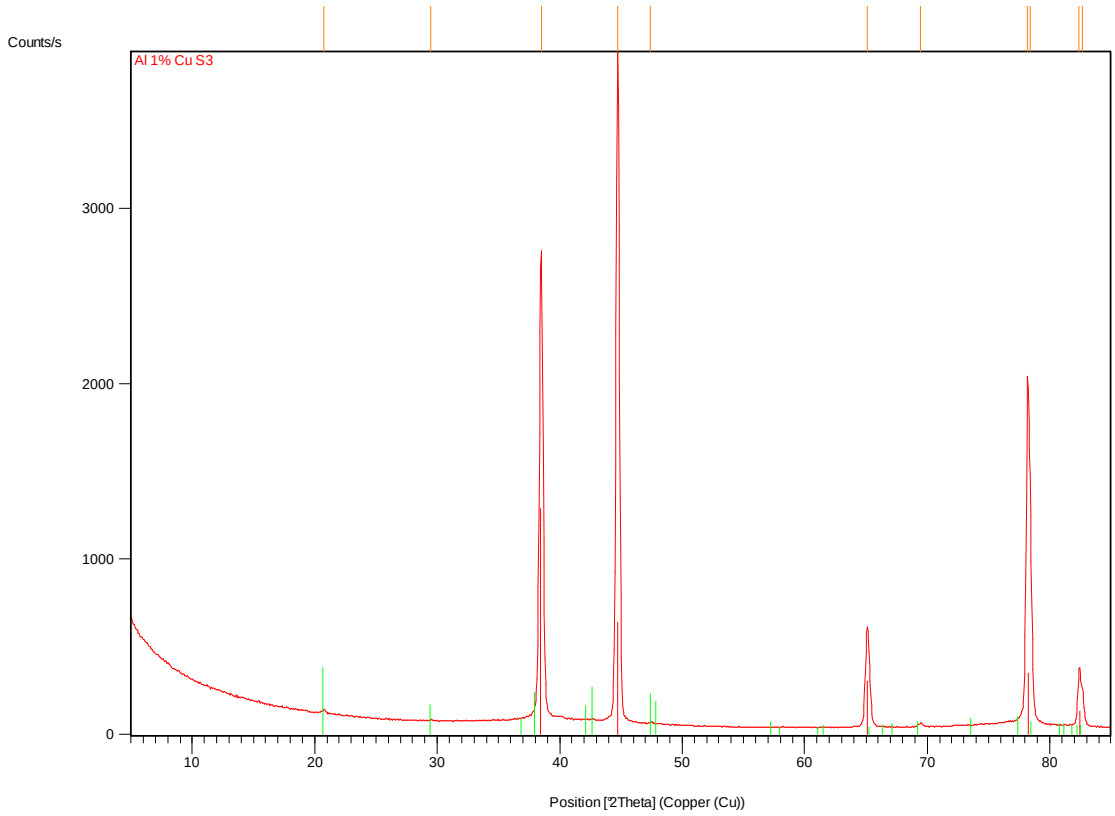

Figure 4.17 (b) XRD Spectrum of the Al-1.0at.%Cu alloy

Pattern List:

Visible	Ref. Code	Compound Name	Displacement [°2Th.]	Scale Factor	Chemical Formula
*	04-001-0564	Aluminum, syn	0.000	0.395	Al
*	04-001-0923	Khatyrkite, syn	0.000	0.016	Cu Al2

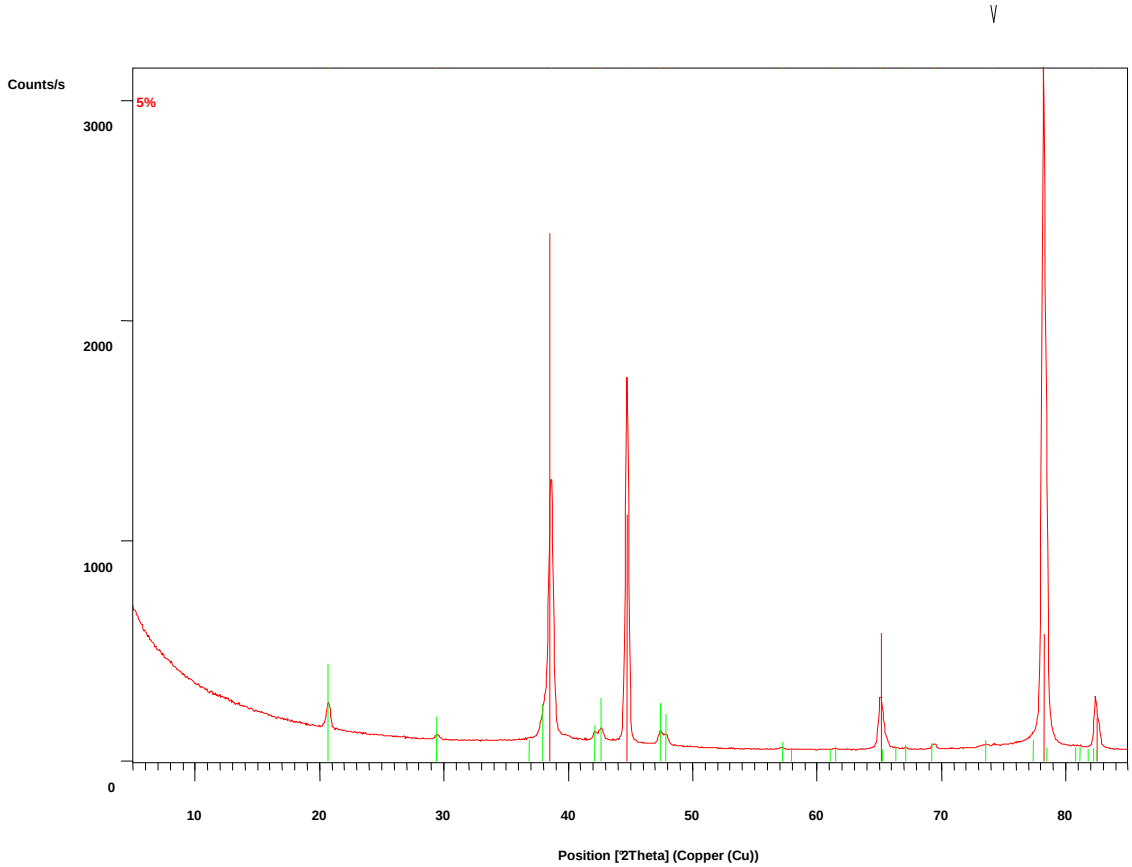

Figure 4.17 (c) XRD Spectrum of the Al-5.0at.%Cu alloy

Pattern List:

Visible	Ref. Code	Compound Name	Displacement [°2Th.]	Scale Factor	Chemical Formula
*	04-001-0564	Aluminum, syn	0.000	0.598	Al
*	04-001-0923	Khatyrkite, syn	0.000	0.044	Cu Al2

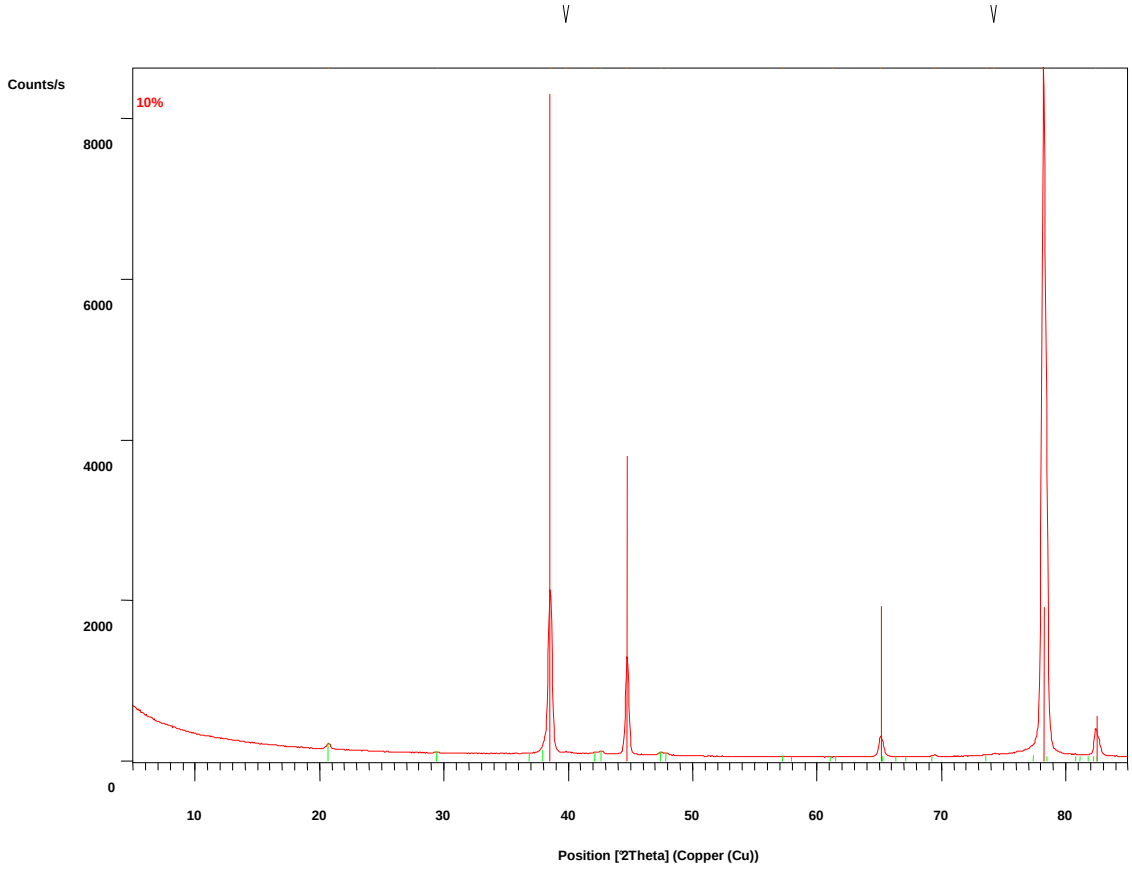

Figure 4.17 (d) XRD Spectrum of the Al-10at.%Cu alloy

Pattern List:

Visible	Ref. Code	Compound Name	Displacement [°2Th.]	Scale Factor	Chemical Formula
*	04-001-0564	Aluminum, syn	0.000	0.395	Al
*	04-001-0923	Khatyrkite, syn	0.000	0.016	Cu Al2

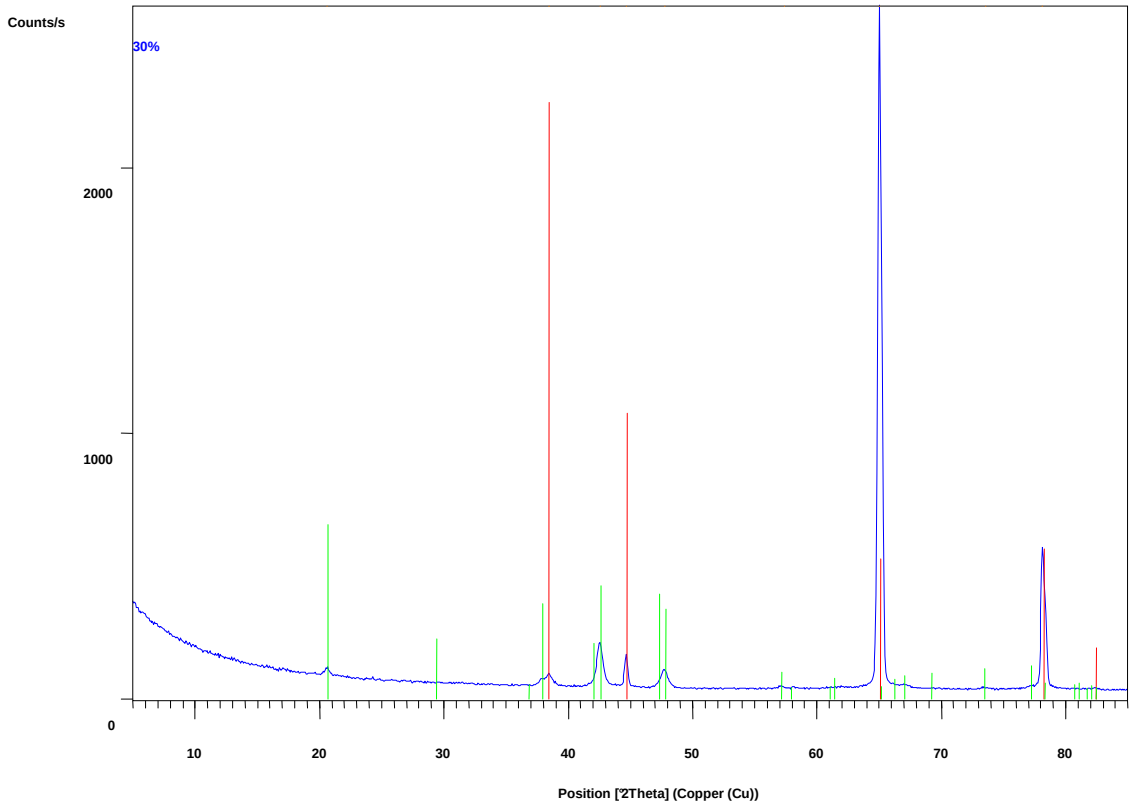

Figure 4.17 (e) XRD Spectrum of the Al-30at.%Cu alloy

Pattern List:

Visible	Ref. Code	Compound Name	Displacement [°2Th.]	Scale Factor	Chemical Formula
*	00-004-0787	Aluminum, syn	0.000	0.200	Al
*	04-007-0566	Khatyrkite, syn	0.000	0.036	Cu Al2

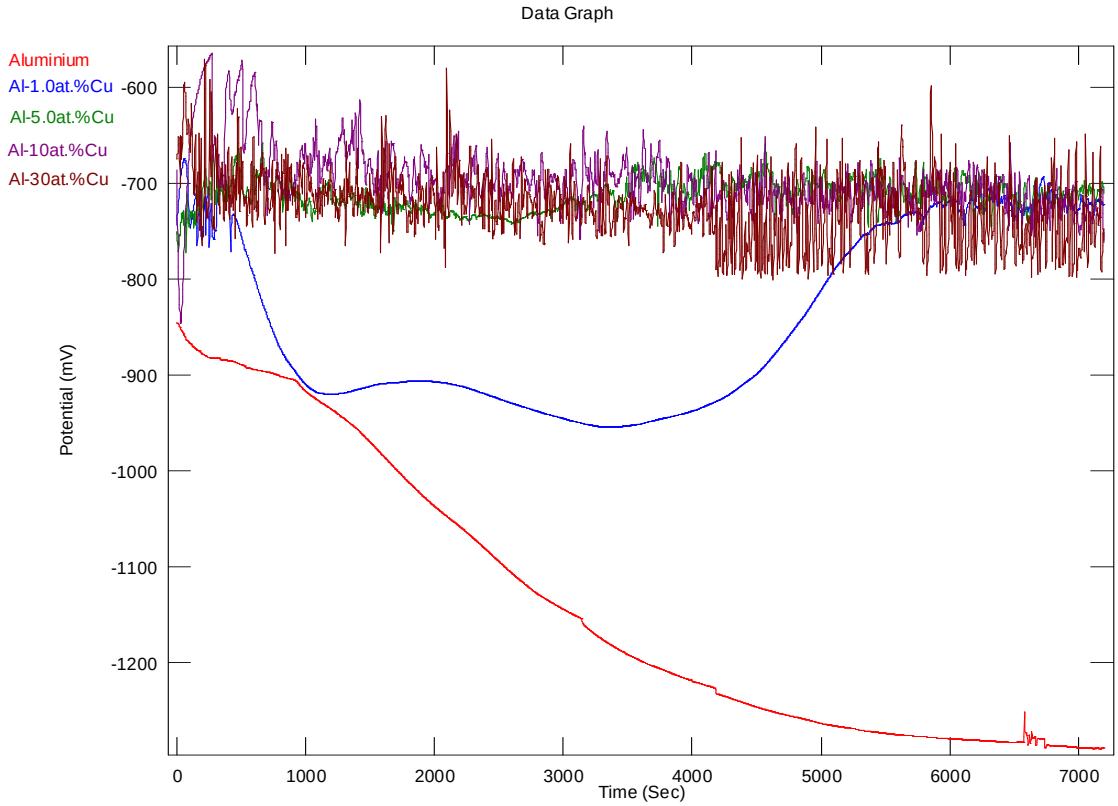

Figure 4.18 (a) Potential-time response of sputter-deposited superpure aluminium and model aluminium-copper alloys in 3.5% NaCl.

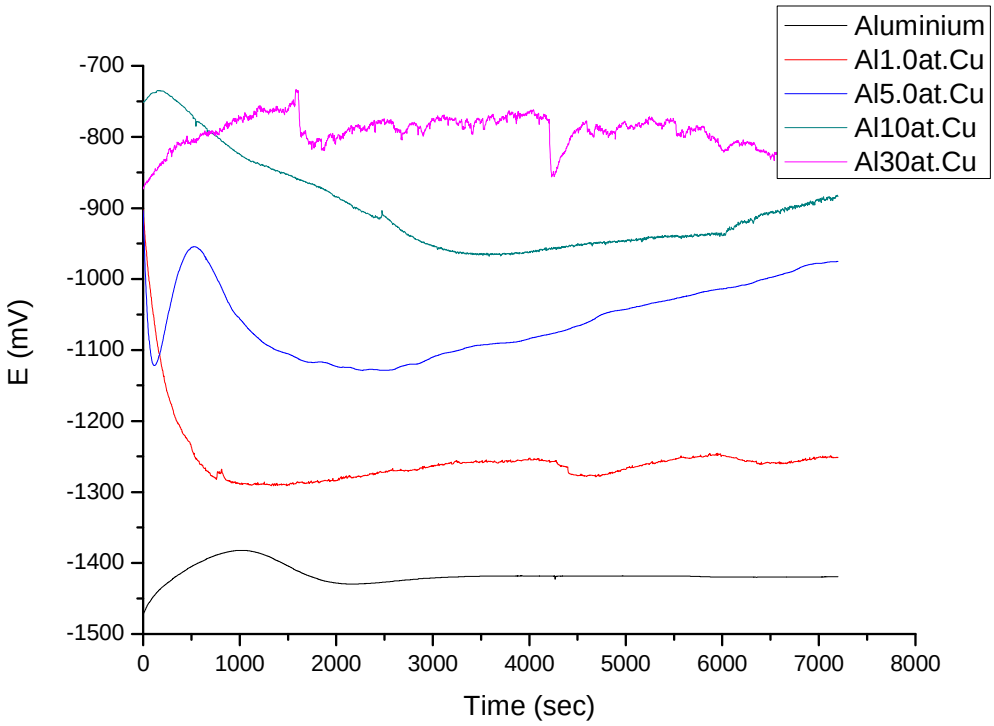

Figure 4.18 (b) Potential-time response of sputter-deposited superpure aluminium and model aluminium-copper alloys in deaerated 3.5% NaCl.

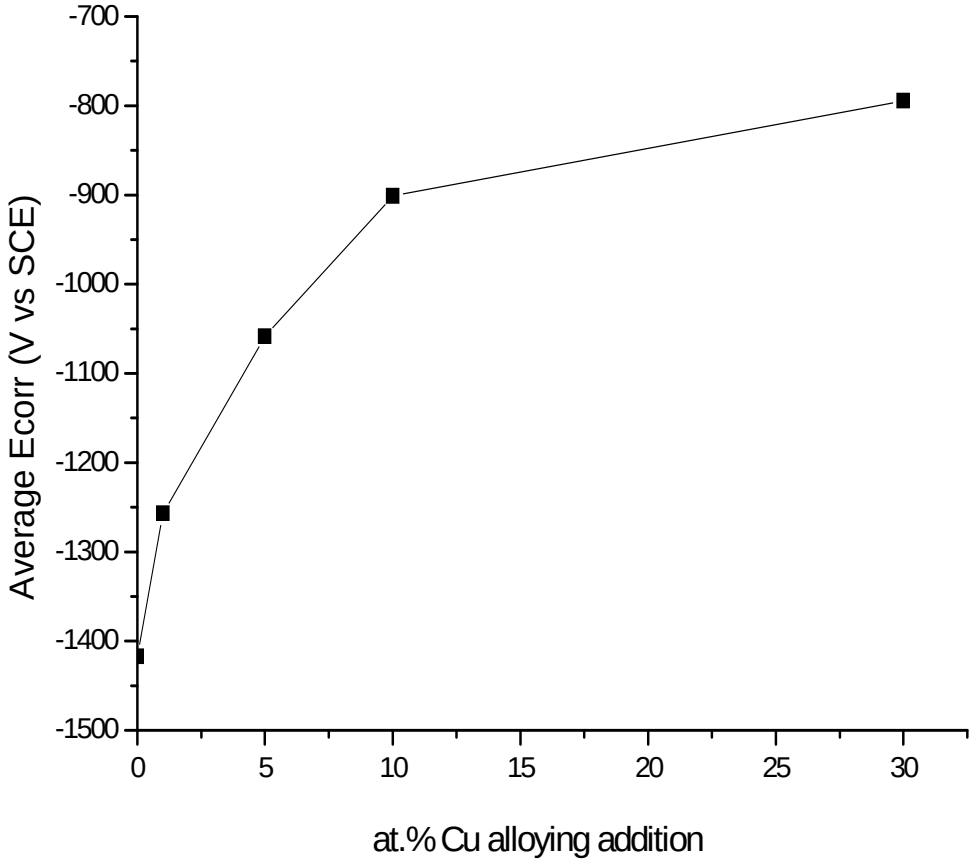

Figure 4.19 The relationship between average open-circuit potential and alloy composition for magnetron sputtered superpure aluminium and model aluminium-copper alloys, determined over 2 hours in 3.5 wt% NaCl solution.

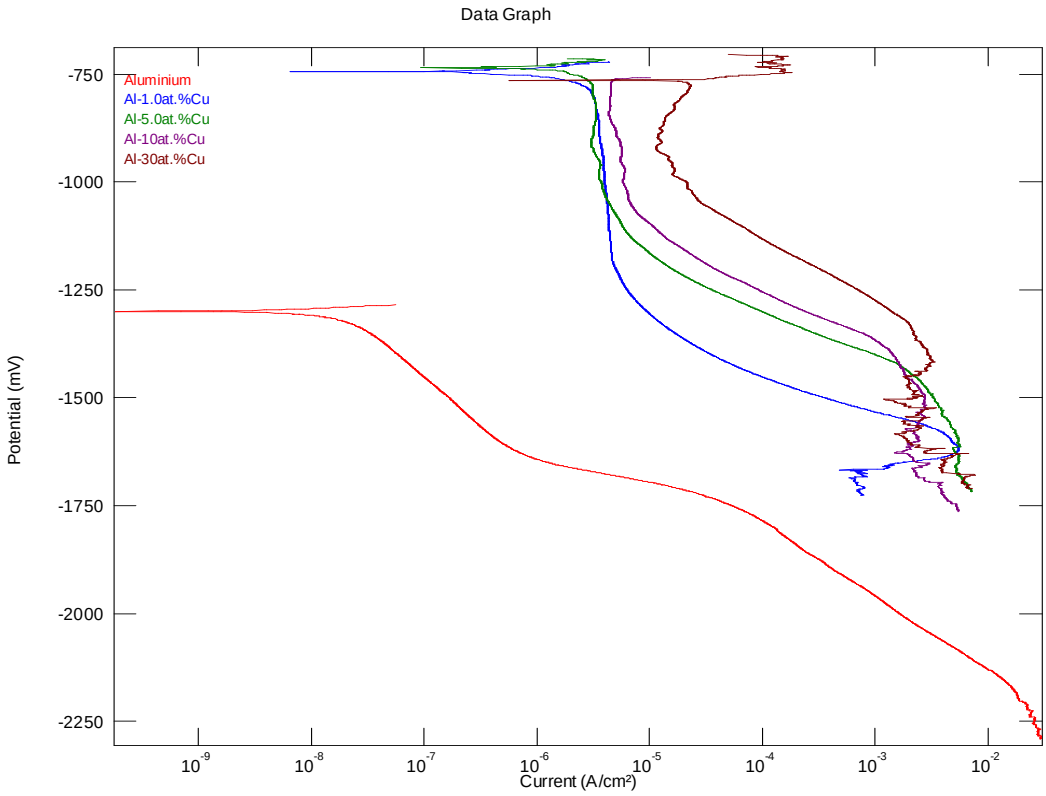

Figure 4.20 Cathodic polarisation behaviour of magnetron-sputtered superpure aluminium, Al-1.0at.%Cu, Al-5.0at.%Cu, Al-10at.%Cu and Al-30at.%Cu alloys in aerated 3.5 wt.% NaCl solution

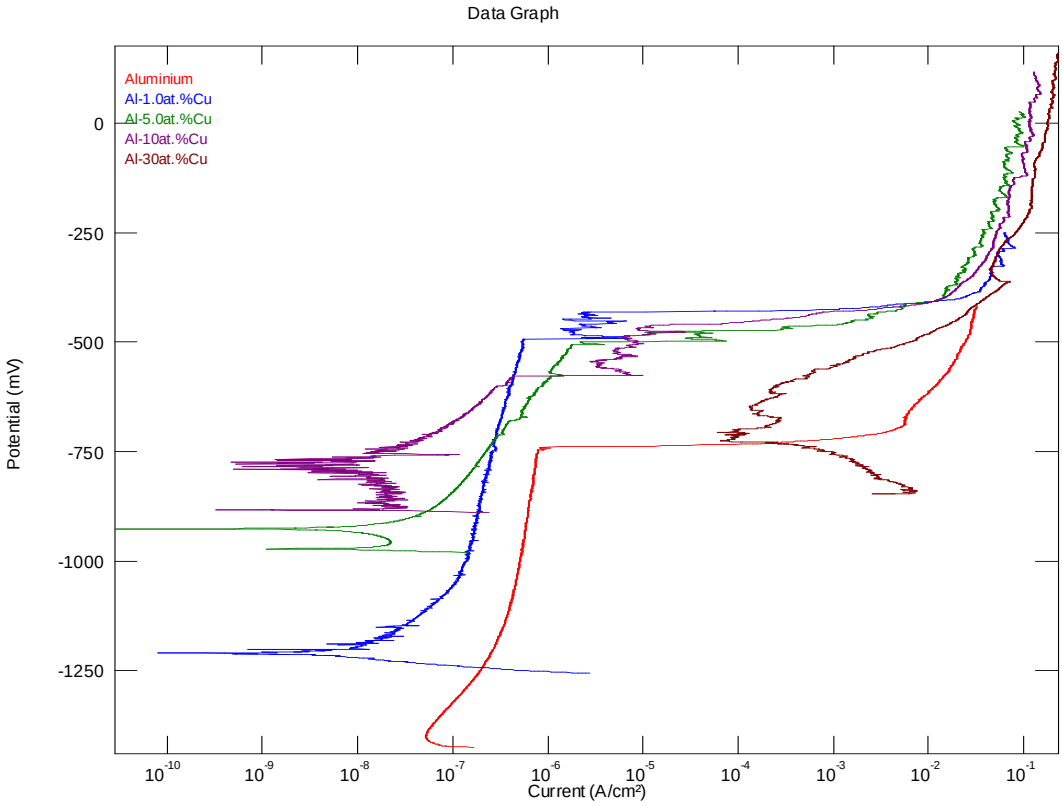

Figure 4.21 Anodic polarisation behaviour of magnetron-sputtered superpure aluminium, Al-1.0at.%Cu, Al-5.0at.%Cu, Al-10at.%Cu and Al-30at.%Cu alloys in aerated 3.5 wt.% NaCl solution.

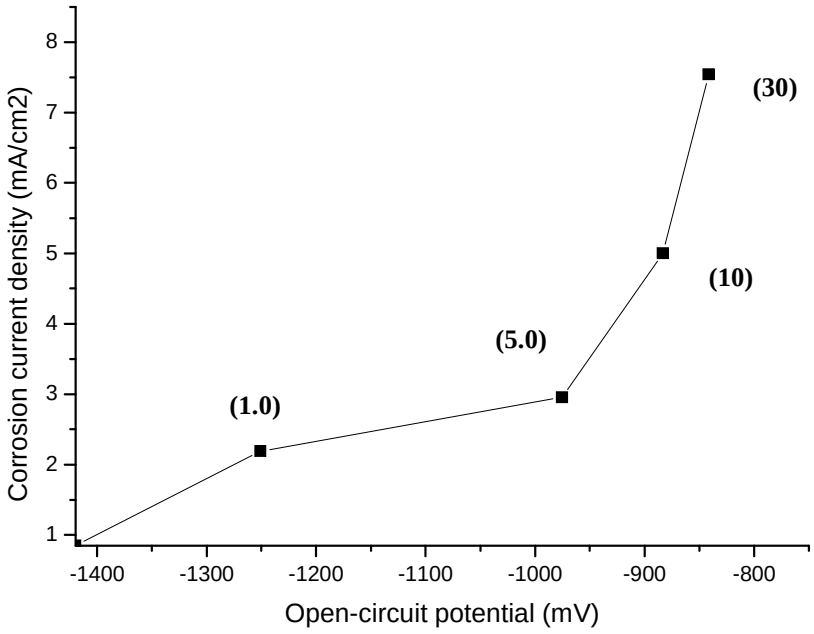

Figure 4.22 The relationship between corrosion current density and open-circuit corrosion potential for sputter-deposited Al-Cu alloys determined after 2 h immersion in deaerated NaCl solution. Atomic % copper content of each alloy is shown in brackets.

CHAPTER 5

5 ZIRCONIUM-BASED CONVERSION COATING ON ALUMINIUM AND ALUMINIUM-COPPER MODEL ALLOYS

5.1 Introduction

Commercially important aluminium alloys are usually alloyed with copper. These alloys have widespread applications, especially in the automotive and aerospace industry due to a good combination of cost, strength and light weight. Due to the high alloying element content, the fraction of intermetallic particles can be higher. These particles are electrochemically noble with respect to the aluminium matrix, and thus lead to local cathodic corrosion, thereby creating difficulties in surface finishing.

In many aqueous surface finishing procedures including conversion coatings, the presence of copper in the alloy substrate can be problematic. During conversion coating, the surface of copper-containing aluminium alloys become enriched with copper compounds, occasionally including metallic copper which are collectively referred to as "smut". Copper smut interferes with conversion coating formation and with bonding of subsequently applied adhesives and paint [295, 296]. As a result of this, any coating (such as conversion coating) may contain defects such as insufficient coverage and non-uniform deposition on or near the intermetallic particles present in the alloy substrate.

The push to replace chromium-based conversion coatings with environmentally-friendly conversion coatings that can provide similar levels of corrosion protection as CCCs has led to the development of a variety of conversion coating processes, with the resultant chemistry and performance having been widely reported. One such non-chromium formulation incorporates a zirconium salt, boric acid and a source of fluoride in the coating bath solution. This type of coating is a relatively recent development, and not much has been published about its morphology, composition and the influence of alloying elements on coating development on alloy substrates.

In the present study, morphological characterisation of zirconium-based conversion coatings on superpure aluminium and model binary aluminium-copper alloy is analysed

using several analytical tools. The aim of this study is to develop a better understanding of the role of alloy copper content in corrosion protection performance of zirconium-based conversion coating developed on superpure aluminium and aluminium-copper alloys with varying copper levels.

In this chapter, the surface morphology and composition of zirconium-based conversion coatings formed on magnetron-sputtered superpure aluminium and copper-based aluminium alloys were considered.

5.2 Composition and Characteristics of the Coating Electrolyte

The coating bath used in this study was prepared by dissolving 0.0014 M H_2ZrF_6, 5 g/l H_2BO_3, 10 g/l KNO_3 in deionised water and the bath chemistry was adjusted to a pH of 2.6 using approximately 0.4 ml HNO_3 [4N]. Specimens were immersed in the conversion coating bath for 30, 60, 180, 300 or 600 seconds. After coating, specimens were rinsed with deionised water and dried with cool air stream before any further surface testing. Treated specimens were stored in a desiccator in order to minimise aging effects.

5.3 Coating Development

In order to examine the initial stages of coating growth, the potential of selected specimens was measured initially in the conversion solution. The deposition of zirconium conversion coating was studied by monitoring the open-circuit potential of superpure aluminium in the zirconium-based bath as a function of immersion time as shown in Figure 5.1. For the as-sputtered superpure aluminium specimen, the OCP was initially approximately -1750 mV (SCE) within the first few seconds of immersion in the zirconium bath solution. The OCP then increased from -1750 mV (SCE) to a maximum value of 169.4 mV (SCE) (A→B) after 25 s of immersion. After the peak value, the potential then decreased gradually to attain a steady value of 110.65 mV (SCE) after 60 s of immersion (B→C). Finally, the OCP was stable for the longer immersion times except for the sudden peak (C→D) observed after 110 s of immersion in the conversion bath. Based on the curve, the surface alumina was immediately thinned to expose the aluminium substrate as soon as the specimen was immersed into the zirconium bath resulting in the gradual formation of conversion film on the

specimen. At stage (B→C), the conversion film formed was improved further until the dynamic balance of film dissolution and formation was established. As a result, the OCP nearly kept a steady value with increased times of immersion.

5.3.1 Morphologies of coatings

In order to reveal the surface morphology and to quantify the thickness of the coatings formed by immersion of the specimens for various times in the conversion treatment solution, transmission electron microscopy (TEM) and atomic force microscopy (AFM) analytical techniques have been employed to examine the coatings developed. A study of the formation of zirconium-based conversion coatings on superpure aluminium and copper-containing aluminium alloys, with specific interest in the influence of immersion time on the rate of coating development has been carried out. Relatively short immersion times of 30 s and 60 s were employed to enable focus on the initial development of coatings and to gain insight into the relationship between the preferred sites for coating development.

5.3.1.1 Coatings developed on superpure aluminium

5.3.1.1.1 Surface characterisation by transmission electron microscopy

The influence of conversion time on the thickness of the formed layer was studied by means of transmission electron microscopy. The conversion film is essentially amorphous. Figure 5.2 (a) – (e) shows the transmission electron micrographs of the superpure aluminium specimens after sputter deposition and conversion treatment in zirconium-based conversion coating. The micrograph of the as-sputtered specimen, Figure 4.7, shows that the thickness of the sputtered layer is 437.5 ± 12.5 nm. Figure 5.2 (a) shows a TEM cross-section of the superpure aluminium specimen after conversion treatment for 30 s. The transmission electron micrograph reveals a limited coating growth and the total sputtered layer consumed was 25.0 nm. In Figure 5.2 (b), the transmission electron micrograph shows that the conversion coating thickness on the superpure aluminium substrate (after 60 s of immersion) is uniform. After 180 s of immersion in the conversion solution, (Figure 5.2 (c)) a uniform coating thickness of approximately 112.5 nm was observed. The total sputtered substrates consumed in the conversion process are shown graphically in Figure 5.3 (a). It can be seen from the

graph that the thinning of the aluminium substrate is fastest (0.83 nm s^{-1}) in the first 30 s of immersion, followed by slower rates of thinning (between (0.31 – 0.08 nm s^{-1}) for longer time of immersion in the conversion bath. Thus, it is evident that the longer the specimens were immersed in the conversion bath solution, the greater the aluminium substrate consumed in forming the conversion coating on the aluminium specimens. The coating thickens rapidly within the first 30 s of immersion at a rate of 1.46 nm s^{-1} as shown in Figure 5.3 (b).

5.3.1.1.2 Surface characterisation by atomic force microscopy

AFM images of the coatings formed on superpure aluminium substrates after immersion in the conversion coating solutions for 30, 60, 180, 300 and 600 s are displayed in Figures 5.4 – 5.8. The roughness of coatings formed at relatively short immersion times are less than those formed at longer time of immersion. Since the aluminium substrate is uneven and the conversion coating film is too thin to cover the roughness of the superpure aluminium substrate, the topography of the specimen reflects the underlying roughness in the AFM images. After 60 s (Figure 5.5) of immersion in zirconium-based conversion bath solution, some nodules were observed on the surface of the aluminium specimen. Larger nodules are seen on the surfaces treated for longer immersion times than the nodules formed on the surfaces treated for lower time of immersion. The coated surfaces became relatively rough as a result of the formation of the conversion coatings on the faceted surfaces. The surface roughness increased considerably as a result of longer time of immersion in the bath solution as shown by the arithmetic mean roughness (R_a) and RMS roughness (R_q) values reported in Table 5.1. However, after an increased time of immersion of 600 s, the AFM image (Figure 5.8) disclosed regions of the surface from which most of the original coating material had been lost and adjacent regions with original coating material still present, hence the reduction in the roughness parameters.

Table 5.1 Roughness parameters of the superpure aluminium specimens calculated from whole three-dimensional data sets.

Time of immersion	Arithmetic mean roughness (R_a)	RMS roughness (R_q)
0 s	11.36 nm	14.47 nm
30 s	15.00 nm	19.50 nm
60 s	24.40 nm	34.90 nm
180 s	25.10 nm	36.80 nm
300 s	46.20 nm	66.10 nm
600 s	9.14 nm	13.00 nm

5.3.1.2 Coatings developed on the Al-1.0at.%Cu alloy

5.3.1.2.1 Surface characterisation by transmission electron microscopy

Figures 5.9 (a) – (e) display the transmission electron micrographs of the ultramicrotomed sections of the coating developed on Al-1.0at.%Cu substrate after immersion for 30 – 600 s in the conversion coating bath. The micrographs revealed the sputtered deposited substrate and growth of the coating with increasing time of conversion treatments. The average thickness of the sputter deposited Al-1.0at.%Cu alloy (Figure 4.8) is 437.5 ± 6.2 nm. Figures 5.9 (a) - (e) reveals progressive loss of the alloy substrate with increasing time of immersion in comparison with the initial alloy. The relationship between the total sputtered substrate consumed with immersion time in the conversion treatment process is shown in Figure 5.10 (a). The loss of the alloy substrate is fastest (1.25 nm s^{-1}) in the first 60 s of immersion, during which about 56.3 nm of the alloy was consumed. The rate then reduces to an approximately constant value of 0.21 nm s^{-1} between 60 and 300 s. This later reduces to approximately 0.13 nm s^{-1} between 300 and 600 s, the longest immersion time. The coating correspondingly

thickens rapidly in the first 30 s, forming a layer of thickness about 25 nm (Figure 5.10 (b)) at an average rate of 0.83 nm s^{-1}. Thereafter, the coating growth rate slows substantially, with a thickness of 112.5 nm achieved at 600 s, at an average rate of 0.13 nm s^{-1}. It is evident from the TEM results that the longer the specimens were immersed in the zirconium bath, the greater the loss of aluminium substrate consumed in the growth of the conversion coating.

5.3.1.2.2 Surface characterisation by atomic force microscopy

Figures 5.11 – 5.15 show the typical AFM images of the conversion coated Al-1.0at.%Cu substrates after immersion in the zirconium-based conversion coating baths for 30, 60, 180, 300 and 600 s. The roughness of coatings formed at relatively short immersion times are less than those formed at longer time of immersion. After 30 s (Figure 5.11) of immersion in zirconium-based conversion bath solution, some nodules were observed on the alloy surface. These nodules increased with increasing treatment times. The coated surfaces became relatively rough as a result of the formation of conversion coatings. The surface roughness increased slightly with immersion time in the first 60 s of treatment, but at longer immersion times, the surface roughness reduces as shown by the arithmetic mean roughness (R_a) and RMS roughness (R_q) values reported in Table 5.2. The smaller RMS roughness values suggest the smoothness of the coatings formed on the alloy surface. These results confirm the results obtained from the TEM characterisation which revealed that coating thickens with increasing time of treatment.

Table 5.2 Roughness parameters of the Al-1.0at.%Cu alloy calculated from whole three-dimensional data sets.

Time of immersion	Arithmetic mean roughness (R_a)	RMS roughness (R_q)
0 s	4.24 nm	5.47 nm
30 s	7.89 nm	11.50 nm
60 s	15.30 nm	22.70 nm
180 s	13.50 nm	19.60 nm
300 s	6.73 nm	9.03 nm
600 s	7.78 nm	9.85 nm

5.3.1.3 Coatings developed on the Al-5.0at.%Cu alloy

5.3.1.3.1 Surface characterisation by transmission electron microscopy

Transmission electron micrographs reveal thinning of the sputter-deposited Al-5.0at.%Cu alloy and growth of the coating with increasing treatment times in zirconium-based conversion treatment bath solution (Figures 5.16 (a) – (e)). The average thickness of the sputter deposited Al-5.0at.%Cu alloy (Figure 4.9) is 487.5 ± 6.25 nm. The loss of the alloy substrate is fastest (0.42 nm s^{-1}) in the period from 30 s to 60 s of treatment in the conversion coating bath, followed by a slower, approximately constant rate of thinning of 0.16 nm s^{-1} after 180 and 300 s time of immersion (Figure 5.17 (a)). The coating correspondingly thickens rapidly in the first 60 s, forming a layer of thickness about 25 nm (Figure 5.17 (b)) at an average rate of 0.42 nm s^{-1}. Thereafter, the coating growth rate slows substantially, with a thickness of 62.5 nm achieved at 180 s, at an average of about 0.16 nm s^{-1}. However, at longer times of immersion the coatings are greatly reduced in thickness as shown by Figure 5.17 (b).

5.3.1.3.2 Surface characterisation by atomic force microscopy

The AFM images shown in Figures 5.18 – 5.22 correspond to exposure times of 30 s, 60, 180, 300 and 600 s in the conversion bath solution respectively. The surface morphology of the conversion treated surfaces were observed and characterised by roughness analysis in order to understand the effect of longer treatment times on the Al-5.0at.%Cu alloy. The immersion in the zirconium-based bath solution for 30 s (Figure 5.18) leads to some nodules being observed on the alloy surface. These nodules increased with increasing treatment times. When the duration of the conversion treatment process was increased to 60 s, some isolated and oval-shaped deposits are observed on the surface (Figure 5.19). These deposits can be attributed to the precipitation of zirconium hydroxide/oxide. A further prolonging of immersion of alloy substrate in the conversion bath solution for up to 180 s causes the formation of clusters of nodules on the surface of the treated alloy as observed in the topographic image of Figure 5.20. Hence, after 180 s of immersion the conversion coating bath, several layers of spherical particles which coalesce were observed.

The surfaces morphology of the coated surfaces were observed and characterised by roughness analysis. The roughness values of the untreated and treated specimens displayed in Table 5.3 shows the increase in surface roughness with increasing time of immersion. This increase in surface roughness is as a result of the formation of conversion coatings. The surface roughness reduce slightly after 60 s of treatment, but at longer immersion times (with the exception of specimen treated for 600 s), the surface roughness increases as shown by the arithmetic mean roughness (R_a) and RMS roughness (R_q) values reported in Table 5.3.

Table 5.3 Roughness parameter of the Al-5.0at.%Cu alloy calculated from whole three-dimensional data sets.

Time of immersion	Arithmetic mean roughness (R_a)	RMS roughness (R_q)
0 s	7.36 nm	9.65 nm
30 s	11.60 nm	15.90 nm
60 s	8.40 nm	11.30 nm
180 s	11.60 nm	17.80 nm
300 s	14.00 nm	18.50 nm
600 s	6.55 nm	8.96 nm

5.3.1.4 Coatings developed on the Al-10at.%Cu alloy

5.3.1.4.1 Surface characterisation by transmission electron microscopy

Transmission electron micrographs reveal thinning of the sputter-deposited Al-10at.%Cu alloy and growth of the coating with increasing treatment times in zirconium-based conversion treatment bath solution. The transmission electron micrographs reveal the sputtered deposited substrate and growth of the coating with increasing time of conversion treatments (Figures. 5.23 (a) - (e)). The thickness of the as-sputtered Al-10at.%Cu alloy (Figure 4.10) is 362.5 ± 6.25 nm. Figures 5.23 (a) - (e) reveals progressive loss of the alloy substrate with increasing time of immersion in comparison with the initial alloy shown in Figure 4.10. The loss of the alloy substrate is fastest (0.58 nm s^{-1}) in the first 30 s of immersion, during which about 17.5 nm of the alloy was consumed (Figure 5.24 (a)). The rate then reduces to 0.5 nm s^{-1} after the first 60 s of treatment time. This rate later reduces to 0.04 nm s^{-1} between 180 and 300 s after which, increasing the treatment time has no effect on the matrix consumed. The coating formed on the alloy substrate correspondingly thickens rapidly in the first 30 s, forming a layer

of thickness about 20 nm (Figure 5.24 (b)) at an average rate of 0.67 nm s^{-1}. Thereafter, the coating growth rate slows substantially, with a thickness of 40 nm achieved at 300 s, at an average of about 0.04 nm s^{-1}, after which any increase in the immersion time has no effect on the coating thickness. It is evident from the TEM results that the longer the specimens were immersed in the zirconium bath, the greater the loss of aluminium substrate consumed in the growth of the conversion coating.

5.3.1.4.2 Surface characterisation by atomic force microscopy

The AFM topographic images of the Al-10at.%Cu alloy after immersion in zirconium-based conversion coating solution is shown in Figures (5.25) – (5.29). Increasing the time of immersion in the conversion solution (60 s and above) give rise to the formation of nodules which increases as the treatment time of the alloys increases. Finally, after 300 s (Figure 5.28) and 600 s (Figure 5.29) of exposure to the zirconium-based conversion bath, the coating formed on the Al-10at.%Cu alloy surface consists of appreciable clusters of nodules.

The roughness values of the untreated and treated specimens displayed in Table 5.4 shows an increase in surface roughness with increasing time of immersion. This increase in surface roughness is as a result of the formation of conversion coatings. The surface roughness values between 60 s and 300 s of immersion is almost constant, while at longer immersion times (600 s), the surface roughness increases as shown by the arithmetic mean roughness (R_a) and RMS roughness (R_q) values reported in Table 5.4.

Table 5.4 Roughness parameter of the Al-10at.%Cu alloy calculated from whole three-dimensional data sets.

Time of immersion	Arithmetic mean roughness (R_a)	RMS roughness (R_q)
0 s	5.30 nm	6.62 nm
30 s	7.27 nm	9.46 nm
60 s	15.00 nm	23.10 nm
180 s	15.50 nm	23.90 nm
300 s	15.60 nm	27.20 nm
600 s	23.60 nm	35.30 nm

5.3.1.5 Coatings developed on the Al-30at.%Cu alloy

5.3.1.5.1 Surface characterisation by transmission electron microscopy

Figures 5.30 (a) – (e) show transmission electron micrographs of the Al-30at.%Cu alloy specimens after sputter deposition and immersion in the zirconium-based bath. The comparison of the as-sputtered specimen with the specimens treated in the zirconium bath shows a progressive loss of aluminium substrate with increasing immersion time. The micrograph of the as-sputtered specimen (Figure 4.11) reveals the thickness of the alloy is 337.5 ± 12.5 nm. Similar to the previous trend, Figure 5.31 (a) shows that the loss of alloy substrate is fastest in the first 30 s of immersion (0.83 nm s^{-1}), followed by a slower rate of loss of substrate (0.52 nm s^{-1}), after which the conversion treatment of the Al-30at.%Cu alloy then proceeded at a relatively constant rate of 0.03 nms^{-1} after 180 s of treatment time. With the Al-30at.%Cu alloy, a thin zirconium-based coating forms initially, leading to enrichment of copper in the alloy immediately beneath the coating for longer time of immersion (Figure 5.30 (c) - (e)). Similar to the trend in the Al-10at.%Cu alloy, the coating thickens rapidly in the first 30 s of immersion, forming a

layer of thickness about 18.75 nm (Figure 5.31 (b)) at an average rate of 0.63 nm s^{-1}. Thereafter, the coating growth slows substantially, with a thickness of 43.75 nm achieved at 180 s, at an average rate of about 0.03 nm s^{-1} and Figure 5.31 (b) also revealed that any further increase in the immersion time has no effect on the coating thickness.

5.3.1.5.2 Surface characterisation by atomic force microscopy

The AFM images shown in Figures 5.32 – 5.36 correspond to exposure times of 30, 60, 180, 300 and 600 s in the conversion bath solution respectively. After 60 s (Figure 5.33) of immersion in zirconium-based conversion bath solution, some clusters of nodules were observed on the alloy surface. The coatings formed on the alloy surfaces are non-uniform. The surface of coated Al-30at.%Cu specimens treated in the zirconium-based conversion bath solutions were characterised by roughness analysis of 5 × 5 μm^2 images, and the values of the arithmetic mean roughness (R_a) and RMS roughness (R_q) are shown in Table 5.5. The surface roughness increased slightly with immersion time in the first 60 s of treatment but, at longer immersion times, the surface roughness reduces as shown by the arithmetic mean roughness (R_a) and RMS roughness (R_q) values reported in Table 5.5.

Table 5.5 Roughness parameter of the Al-30at.%Cu alloy calculated from whole three-dimensional data sets.

Time of immersion	Arithmetic mean roughness (R_a)	RMS roughness (R_q)
0 s	4.06 nm	5.47 nm
30 s	13.30 nm	19.10 nm
60 s	15.00 nm	28.20 nm
180 s	14.10 nm	23.40 nm
300 s	14.70 nm	24.50 nm
600 s	15.70 nm	20.90 nm

5.3.2 Composition and structure of zirconium-based conversion coatings

The characterisation of zirconium-based conversion coating in terms of composition, chemistry and structure as a function of immersion time in aqueous conversion bath is important to provide further understanding of the nature of the resultant protection given to the substrate, and the mechanism of such protection. In this section, the characterisation of zirconium-based conversion coating was performed by (FEG-SEM) equipped with an EDX analytical system, Rutherford backscattering spectroscopy (RBS) and Nuclear reaction analyses. The structure of the coating formed on selected aluminium-copper specimens was also probed by glow discharge optical emission spectroscopy (GDOES).

5.3.2.1 Composition and structure of coatings formed on superpure aluminium specimens

5.3.2.1.1 Elemental analyses

The surface morphology and chemistry of the untreated and treated specimens after immersion in zirconium-based was studied using the field emission gun scanning electron microscope (FEGSEM). Compositional analyses of the zirconium-based conversion coating were carried out on aluminium specimens using the FEGSEM equipped with an energy dispersive X-ray spectroscopy analytical system. Energy dispersive X-ray analyses were carried out at an accelerating voltage of 20 kV. Figure 5.37 show the scanning electron micrographs of zirconium-based conversion layer, formed on superpure aluminium substrates, treated for 30, 60, 180, 300 and 600 s. After 30 s to 180 s, the scanning electron micrographs show that the coating has started to deposit on the substrate (Figures 5.37 (a)), but the morphology of the coating was only clearly evident after immersion times for 300 s to 600 s (Figures 5.37 (d) - (e)). The scanning electron micrographs reveal systematically the presence of small cavities. These cavities were attributed to the porous nature of the conversion layer formed. The zirconium-based conversion coatings exhibit a slight “mud-crack” morphology which is more visible in specimen treated for 600 s. Fine zirconium-rich nodules where observed on the surface of the conversion coated superpure specimen after immersion in the zirconium bath. The EDX analyses (in wt.%) for each treatment time investigated are reported in Table 5.6. The EDX zirconium peaks for specimens treated below 180 s were weak and become more intense as the treatment time increased.

Table 5.6 EDX analyses of superpure aluminium before and after treatment in zirconium bath

Time of immersion	Al	O	Zr	F
0 s	98.39	1.61	-	-
30 s	95.10	4.17	0.48	0.26
60 s	91.38	5.32	2.79	0.50
180 s	79.21	13.12	5.99	1.68
300 s	71.84	11.82	14.58	1.76
600 s	69.91	12.51	17.58	-

5.3.2.1.2 RBS analyses

The growth of the zirconium-based conversion coating was examined on superpure aluminium specimens using Rutherford backscattering spectroscopy. The RBS spectra of the superpure aluminium specimens as a function of immersion time are shown in Figures 5.38 (a) - (f). The presence of the conversion coating on the superpure aluminium specimens was indicated by the detection of the elements oxygen (O), zirconium (Zr) and aluminium (Al) as shown in the diagrams. The shapes of the O and Zr peaks suggest that the oxide was of variable thickness across the specimen surface, an interpretation supported by the TEM, which shows regions of thin oxide and regions of thicker growth. It can be seen that both Zr and O peaks increased in width with increasing immersion time, indicating the growth of zirconium oxide on the specimen surface. The RBS spectrum after 30 s treatment time (Figure 5.38 (b)) is similar to those observed for as-sputtered specimen (Figure 5.38 (a)), indicating that little or no conversion coating was formed on the specimen after 30 s immersion time. Comparison of the RBS spectra after 60 s, 180 s, 300 s and 600 s of treatment time (Figures 5.38 (c)

- (f)) revealed that the Zr and oxygen peaks become wider with increasing time of treatment, suggesting that thicker oxide was formed as treatment times increases. This is in agreement with EDX analysis which shows strong peaks of Zr as treatment time increases. Figure 5.38 (g) revealed that zirconium content of the coating increases with increase in treatment time. The thickness is obtained from RBS analyses of conversion layers treated for 60 s, 180 s, 300 s, and 600 s and the zirconium contents are 66.41 × 10^{15}, 143.63 × 10^{15}, 248.26 × 10^{15} and 323.18 × 10^{15} atms/cm^2 respectively.

5.3.2.2 Composition and structure of coatings formed on the Al-1.0at.%Cu alloys

5.3.2.2.1 Elemental analyses

The morphologies of the treated Al-1.0at.%Cu aluminium alloy are shown in Figure 5.39. The initiation and development of conversion film was related with the corrosion behaviours of aluminium-copper alloys. The SEM images show steps in the formation of the conversion coating on the substrates with immersion time. The results indicate that the surface coverage of the conversion coating, after 60 s immersion in the conversion bath solution was low. However, at longer time of immersion (Figures 5.39 (c) – (e)), the surface coverage is relatively better but still relatively non-uniform as shown in Figures 5.39 (d) to (e). The zirconium-based conversion coatings formed on the Al-1.0at.%Cu specimens after longer immersion times (180 – 600 s) exhibited a "mud-crack" morphology which is more visible in specimen treated for 600 s. The EDX analyses integrated over different points of interest (specified as spectrum in the scanning electron micrographs) are reported in Table 5.7. The EDX zirconium (Zr) peaks for specimens treated for shorter times were weak and became more intense as the treatment time increases as seen from the Zr weight percentage concentration which increases from 1.23 wt.% to 11.08 wt.% after 300 s of immersion in the zirconium-based treatment bath solution. However, this values later reduces to 7.08 wt.% after 600 s of immersion. This decrease in the Zr peaks for the longest time of immersion most likely arise from regions of the surface from which most of the original coating material had been lost.

Table 5.7 EDX analyses (wt.%) of the Al-1.0at.%Cu alloy before and after treatment in zirconium bath

Time of immersion	Al	O	Zr	F	Cu
0 s	90.85	7.70	-	-	1.38
30 s	94.89	2.81	1.23	0.20	0.87
60 s	93.15	3.34	2.25	0.55	0.71
180 s	85.72	6.67	5.35	1.54	0.72
300 s	86.97	9.68	11.08	-	0.68
600 s	83.77	8.53	7.08	-	0.62

5.3.2.3 Composition and structure of coatings formed on the Al-5.0at.%Cu alloys

5.3.2.3.1 Elemental analyses

Figure 5.39 shows the surface morphology of the Al-5.0at.%Cu alloy after immersion in zirconium bath for 30 s, 60 s, 180 s, 300 s and 600 s. After the initial 60 s of immersion, the scanning electron micrographs show that the coating has started to deposit on the substrate (Figures 5.40 (a) and (b)). However, the morphology of the coating was only clearly evident after immersion times for 180 s to 600 s (Figures 5.40 (c) - (e)). The zirconium-based conversion coatings formed on the Al-5.0at.%Cu alloys after longer immersion times exhibited “mud-crack” morphology with some clusters of nodules rich in zirconium. Figures 5.40 (d) and 5.40 (e) show the presence of Zr-rich nodules over a large area of the Al-5.0at.%Cu alloy after 300 s and 600 s of immersion in the zirconium bath. In order to investigate the composition of the film, some EDX point analyses were carried out. The EDX analyses (in wt.%) for each treatment time investigated are given in Table 5.8. The strong peaks of zirconium and aluminium for

longer times of immersion, implies a mixed oxide layer. The fluoride concentration in the coating remained low even for the films of highest zirconium content. This suggests that zirconium is mostly in an oxide or oxyhydroxide form rather than fluoride [233].

Table 5.8 EDX analyses (wt.%) of the Al-5.0at.%Cu alloy before and after treatment in zirconium bath

Time of immersion	Al	O	Zr	F	Cu
0 s	90.70	5.63	-	-	3.67
30 s	88.61	5.75	2.12	0.82	2.70
60 s	90.18	4.83	1.61	0.69	2.69
180 s	84.43	6.11	6.66	-	2.80
300 s	79.46	9.50	8.04	-	3.00
600 s	80.92	8.02	5.45	2.88	2.73

5.3.2.4 Composition and structure of coatings formed on the Al-10at.%Cu alloys

5.3.2.4.1 Elemental analyses

Figure 5.41 shows the scanning electron micrographs of zirconium-based conversion layers, formed on the Al-10at.%Cu alloys after immersion in zirconium-containing bath for 30 s, 60 s, 180 s, 300 s and 600 s. The scanning electron micrographs (taken at low magnifications) show small white particles distributed on the surface of the specimens, which when closely examined are found to be spherical particles rich in zirconium (see EDX analyses). After immersion in the zirconium bath for 60 s and longer, the zirconium-rich spherical nodules observed on the surface of the alloy increase. With the

increase of the treatment time to 180 s as shown in Figure 5.41 (c), the Al-10at.%Cu alloy was completely covered with the conversion coating with minimal 'mud cracks' (due to drying) observed on the surface of the alloy. After 600 s of immersion in the conversion treatment solution (Figure 5.41 (d)), there were no significant changes to the surface morphology. The EDX analyses (in wt.%) for each treatment time investigated are given in Table 5.9. The peaks detected for copper in some of the spectra are most likely as a result of the incorporation of copper into the conversion layer.

Table 5.9 EDX analyses (wt.%) of the Al-10at.%Cu alloy before and after treatment in zirconium bath

Time of immersion	Al	O	Zr	F	Cu
0 s	91.15	2.75	-	-	6.10
30 s	89.30	5.51	0.98	0.92	3.29
60 s	87.41	6.73	1.91	0.90	3.04
180 s	82.99	9.47	4.02	-	3.52
300 s	83.62	9.81	2.57	-	4.01
600 s	81.37	10.63	6.58	-	1.42

5.3.2.4.2 RBS analysis

RBS was used to study the difference in the thicknesses of the conversion coatings deposited on the Al-10at.%Cu alloy at different immersion times. RBS spectra for Al-10at.%Cu specimens are shown in Figures 5.42 (a) – (f) as a function of increasing immersion time. The main features of the spectra are Al, Cu, Zr and O steps at Channels 279, 388, and 187 respectively. The Zr region displayed a consistent increase in the

level of incorporated Zr with increased immersion time, consistent with the development of a heavier coating. Although the change in the O peak was small, there was a trend of increasing width with increasing processing time. This indicates an increase in oxide thickness. The shape of the oxygen peak was similar for all Al-10at.%Cu alloy specimens indicating that the variation in oxide thickness was consistent. The similarities in the shapes of the Zr and O peaks suggest that Zr was evenly distributed throughout the oxide (Figures 5.42). The efficiency of the conversion treated Al-10at.%Cu alloy was determined by measurements of the zirconium contents of coatings by RBS, which were compared with the loss of the alloy substrate, from TEM. The Zr peaks had a greater peak height for the longer immersion times, indicating that Zr deposition was greater with longer immersion time.

5.3.2.5 Composition and structure of coatings formed on the Al-30at.%Cu alloys

5.3.2.5.1 Elemental analyses

Figure 5.43 shows the scanning electron micrographs of the Al-30at.%Cu alloys after immersion in zirconium-containing bath for 30 s, 60 s, 180 s, 300 s and 600 s. The surface coverage of the conversion coatings formed after 30 s immersion (Figure 5.43 (a)) in the conversion bath solution was low since the array of grooves observed by AFM is still visible. Immersion for 60 s in the conversion bath (Figure 5.43 (b)) gave a better coverage of the conversion film compared with 30 s; however, the film formation was still relatively non-uniform. The alloy surface exhibited discrete islands of deposit, evident as light grey regions on the low magnification micrograph for specimens treated for 180 s (Figure 5.43 (c)). With increase of the treatment time to 300 s and above as shown in Figure 5.43 (d) and (e), the Al-30at.%Cu alloy surface revealed spherical regions (seen as light spherical regions). These regions likely nucleated primarily from the intermetallic particles in the alloy matrix, which XRD results revealed as Al_2Cu. Some EDX point and area analyses were carried out on the treated specimens in order to investigate the composition and influence of time of immersion on the coatings formed. The EDX analyses (in wt.%) for each treatment time investigated are given in Table 5.10. The strong peaks of zirconium and aluminium were observed for longer times of immersion, and this implies that the coatings formed on the Al-30at.%Cu alloy comprised of a mixed oxide layer.

Table 5.10 EDX analyses (wt.%) of the Al-30at.%Cu alloy before and after treatment in zirconium bath

Time of immersion	Al	O	Zr	F	Cu
0 s	79.58		-	-	20.42
30 s	81.62	4.47	1.91	0.19	11.81
60 s	80.04	5.26	1.67	1.08	11.95
180 s	81.64	6.64	2.37	1.05	8.30
300 s	76.59	8.99	3.82	2.15	8.45
600 s	76.00	8.52	6.84	2.81	5.84

5.3.2.5.2 RBS analyses

The RBS analyses of the Al-30at.%Cu alloy specimens after different immersion times are shown in Figures 5.44 (a) - (f). The presence of the conversion coating on the Al-30at.%Cu alloy was indicated by the detection of elements O, Zr, Al and Cu (Figures 5.44 (a) - (f)). The width of the peaks is a function of coating thickness. The main features of the spectra are Al, Cu, Zr, and O steps at channel 279, 410, 439, and 172, respectively. As anticipated, the position of the leading edge of the peak, about 439, indicates zirconium at the surface of the specimen. The Zr region displayed a consistent increase in the level of incorporated Zr with increased immersion time, associated with development of a coating of increasing thickness. The shape of the oxygen peak was similar for all the specimens indicating that the variation in oxide thickness was consistent. The shapes of the O and Zr peaks suggest that the oxide was of variable thickness across the alloy surface. The Zr peaks had a greater peak height for longer immersion times, indicating that Zr deposition was greater when the specimens were immersed longer in the conversion coating bath.

5.3.2.6 NRA and RBS analyses

Nuclear reaction analyses were carried out on the conversion coated superpure aluminium and Al-30at.%Cu alloy specimens, utilising coatings developed on specimen for 30 s, 60 s, 180 s, 300 s and 600 s. The results obtained are displayed in Figure 5.45 Such analyses quantify the amount of oxygen in the conversion coating layer. It is evident that with increase of conversion treatment time, the oxygen content increased as the coating thickened. The RBS spectra revealed similar features for both the superpure aluminium specimens and the Al-30at.%Cu alloy specimens after different coating times, with the peaks for the coating elements zirconium and oxygen varying according to the thickness of the conversion coating developed on the specimens.

From the RBS and nuclear reaction analyses, the ratio of the oxygen atoms in the coating to zirconium atoms with immersion time is shown in Figure 5.46. It is evident that at relatively short conversion treatment times, the ratio of oxygen to zirconium is 3:1, with a suggested coating composition of $ZrO_2.H_2O$. After 180 s conversion treatment time, the ratio of oxygen to zirconium is 4:1, with a suggested coating composition of $ZrO_2.2H_2O$, which indicates an increase in oxygen content, probably due to an increase in the thickness of the conversion coating formed on the specimens after prolonged immersion in the conversion bath. Therefore, the overall suggested composition of the coating is $ZrO_2.nH_2O$ (where n = 1 for relatively short immersion times and, n = 2 for prolonged times of immersion in the conversion treatment bath).

RBS also detected the presence of aluminium in the conversion coating. The ratio of zirconium to aluminium is listed in Table 5.11. Some contributions to the aluminium signal for the coating analysed by RBS may result from the roughness of surface as evident from the AFM results, or through limited coating thickness in certain areas, with the alloy substrate being detected. Therefore, the amount of aluminium in the conversion coating developed on the specimen cannot be clearly quantified by RBS analyses.

Concerning interfacial enrichment of copper in the Al-30at.%Cu alloy, RBS analyses did not clearly identify the presence of such a layer due to the relatively thin nature of the conversion coating, and the relatively thin nature of the copper enriched layer. Furthermore, RBS analyses did not detect the presence of a residual alumina layer on

the conversion coated superpure aluminium specimens, again, due to the relatively low thickness of the residual alumina film.

Table 5.11 The ratio of zirconium to aluminium in the zirconium conversion coating.

	Immersion time (s)					
Ratio of zirconium to aluminium		30	60	180	300	600
	Superpure aluminium	0.00	0.22	1.04	0.79	0.63
	Al-30at.%Cu alloy	0.25	2.75	2.00	1.55	0.87

5.3.2.7 GDOES depth profiling analysis of Al-Cu model binary alloys

Depth profiles of the chemical composition of the treated surfaces were obtained by glow discharge optical emission spectroscopy (GDOES). Representative examples are shown using the spectra for Al-1.0at.%Cu, Al-10at.%Cu and Al-30at.%Cu alloys in the as-sputtered and conversion treated condition.

5.3.2.7.1 Depth profiles of the Al-1.0at.%Cu alloy

The GDOES depth profile for the as-sputtered and conversion treated Al-1.0at.%Cu alloy are shown in Figures 5.47 (a). Depth profile of the composition of the as-sputtered alloy revealed a brief initial silicon (Si) signal (which is likely due to surface enrichment of impurities during electropolishing of high-purity aluminium substrates) which decayed after a second of sputtering. Surface oxygen in the alloy substrate started decaying after a couple of seconds of sputtering. Figures 5.47 (b) to 5.47 (e) show the GDOES intensity spectra as a function of sputtering time for Al-1.0at.%Cu specimen following immersion in the zirconium-based conversion solution for 30 s, 180 s, 300 s and 600 s respectively. However, a peak was evident for copper due to enrichment of copper near the alloy/electropolished matrix interface (i.e. interface between the magnetron sputtered alloy and the initial electropolished superpure aluminium substrate used). Notably, any peak due to enrichment of copper in the region of the alloy/coating

interface was not resolved from the profile of copper in the alloy. The coating also contained zirconium species (derived from the constituents of the conversion coating solution) concentrated in the surface region.

5.3.2.7.2 Depth profiles of the Al-10at.%Cu alloy

The GDOES depth profile for the magnetron-sputtered Al-10at.%Cu alloy, shown in Figure 5.48 (a), revealed a three-layered structure of Al-Cu substrate with a thin film containing oxygen species, suggesting a thin oxide film on the specimen in the as-sputtered condition. By inspection of the profiles for the treated alloys, interesting features are observed in the Al, Cu, O and Zr peaks displayed in Figure 5.48 (b) to 5.48 (e). An extensive plateau region associated with the conversion coating is distinguished clearly in the Al profile. As sputtering continues and as the aluminium substrate is exposed, the intensity of Al signal increases rapidly and reaches a steady, maximum value. According to Shimizu et al [297], the sharp increase in the Al signal intensity is due to the increased yield of the sputtered Al atoms associated with the higher sputtering rate of the aluminium substrate than the surface film or coating. With reference to the copper signal, a thin layer highly enriched in Cu is observed in the alloy substrate immediately beneath the conversion coating after longer times of immersion in the conversion bath solution. For the alloy treated for 300 s (Figure 5.48 (d)), the copper enriched layer persists a significant distance into the metal, corresponding to about 10 s of sputtering time. Zirconium was also enriched near the surface of the oxide, and for 180 s and longer times of immersion, copper was incorporated into the coatings; this result was also corroborated by the RBS spectra of the alloy after longer treatment times. A significant increase in the intensity of the oxide of this element was also observed near the oxide-metal interface. Similar GDOES profiles were observed for specimens immersed for 300 and 600 s in the zirconium-based conversion solution.

5.3.2.7.3 Depth profiles of the Al-30at.%Cu alloy

Figures 5.49 (a) – (e) show depth profiles from conversion coatings obtained by immersion of the Al-30at.%Cu alloys in the zirconium-containing conversion treatment solution. The depth profiles revealed a substantial difference in the surface composition for the as-sputtered alloy and for specimens treated for shorter and longer times of

immersion in conversion bath solution. The GDOES depth profile analysis for the as-sputtered alloy (Figure 5.49 (a)), revealed a high aluminium and copper intensities; and a comparably minimal oxide layer. By inspection of the profiles for the treated specimens, the phase boundary between the oxide and metal alloy is deduced to correspond to about 6 s of sputtering. With regard to the copper signal, a thin layer enriched in copper is observed in the alloy substrate immediately beneath the conversion coatings formed. The copper enriched layer also persists a significant distance into the alloy corresponding to a range between 8 - 10 s of sputtering time depending on the treatment times. A bimodal distribution of copper most likely associated with copper oxide, were observed to be incorporated into the coatings for all treatment times. Finally, consideration is given to the zirconium profiles, where no significant differences are observed for the coatings formed during the various treatment times. The signal intensity of zirconium is high at the surface, and decreases rapidly with depth in the near-surface regions.

5.4 Discussion

5.4.1 Mechanism of coating growth

The formation and growth of zirconium-based conversion coating is influenced by complex microstructures of high strength aluminium alloy substrates. This results in a coating whose thickness and composition varies across the alloy surface. The results obtained in this study revealed that the growth of the zirconium-based conversion coating on superpure aluminium (where the preferred cathodic sites are predominantly small) proceeds in a relatively uniform manner, with the occasional presence of holes in the aluminium surface where the conversion coating is absent after 30 s of immersion in the aqueous bath solution. According to Shimizu et al [269, 297], the observed non-uniformity of the coating developed after relatively short immersion time in the conversion bath is strongly dependent on the crystallographic orientation of the substrate which are residual flaw sites and this in turn, is related to the preferential deposition of the conversion coating over the pre-existing metal ridges rather than over the general aluminium surface. The growth of conversion coating on superpure aluminium is explained on the basis that the deposition of the coatings occurs by electron tunnelling through a thinned, residual alumina film which is always present on

the surface of aluminium. For superpure aluminium with relatively few impurity segregates, sites of ready electron conduction are in relatively short supply, hence, the chemical reaction of fluoride species with thin alumina film results in an aluminium film of reduced thickness and this enables electron tunnelling. Film formation on aluminium substrates occurs by interaction of the fluorozirconate with alumina at the surface of the aluminium substrate according to the reaction:

$$H_2ZrF_6 + 2Al_2O_3 \rightarrow 4AlOF + ZrOF_2 + H_2O \quad (5.1)$$

The anodic dissolution of aluminium occurs through formation of an anodic aluminium oxide film and its subsequent dissolution by fluoride species in the conversion bath. Anodic dissolution takes place at different locations on the aluminium substrate according to:

$$Al \rightarrow Al^{3+} + 3e^- \quad (5.2)$$

The rate of growth of alumina film depends on the rate of chemical dissolution of the oxide by fluoride species. Hence, during the coating formation, the main process is the reduction of oxygen,

$$O_2 + 2H_2O + 4e^- \rightarrow 4OH^- \quad (5.3)$$

The coating developed at cathodic sites, spreads over the surface of the aluminium, thus hindering the anodic process until it is stifled.

Hence, the zirconium-based conversion coating development on superpure aluminium is suggested by the anodic dissolution of aluminium substrate at anodic sites and the cathodic deposition of zirconium species at cathodic sites. The cathodic sites are derived from flaws generated by impurity segregates in the aluminium substrate. The conversion coating is assumed to form by the precipitation of zirconium oxide due to an increase in pH (hydrogen evolution at cathodic sites leads to a local increase in pH) of the bath solution at the metal oxide/liquid interface. The solubility of the coating compound decreases when the pH increases, resulting in precipitation of coating material. The principal assumption of this model is that the natural alumina covering the aluminium surface is not completely removed by chemical dissolution but rather thinned until appreciable tunnelling of the electrons becomes possible. Clearly, the coating does not develop in a similar manner to Cr_2O_3 or $CrPO_4$ coating since ZrO_2 type

material can only be produced by interfacial pH changes [35]. Furneaux et al [298] provided some insight into the locations of anodic and cathodic reactions, as well as the mode of coating growth on aluminium substrates. The authors suggested fine pathways, observed electronoptically to penetrate the coatings to the substrate, through the initial gel-like material which becomes more compact with time, probably provide routes for solution access to the metal. There, anodic dissolution may occur and cathodic activity rapidly results in the production of conversion coating material, which plugs the original pathway. The positions of active sites probably fluctuate, depending on the opening up of new pathways by the complexing action of the fluoride species and subsequent plugging by deposited material. As the conversion coating thickens, more permanent pathways extend much of the way from the bulk solution towards the substrate, but fine pathways, appearing as 'crow's feet', still provide the means of access for solution species to the metal. However, the production of progressively greater quantities of relatively less reactive coating material probably restricts solution access to the metal and thus rapidly limits coating growth.

The conversion coating developed on copper-containing aluminium alloys exhibits a different morphology and composition on the matrix and intermetallics due to their heterogeneous microstructure. For these aluminium alloys, the alloying elements present in the alloy contribute to compositional variation in the alloy surface and the generation of cathodic and anodic sites. From the X-ray diffraction patterns of the as-sputtered aluminium-copper alloys (section 4.6), we have established the presence of tetragonal Al_2Cu intermetallic compound in magnetron-sputtered aluminium-copper alloys used in this study. The combination of cathodic Al_2Cu precipitates and the more anodic aluminium matrix constitutes a galvanic couple which leads to an electrochemical dissolution of the matrix material during conversion treatment. For aluminium-copper alloys, the oxygen reduction (equation 5.3) occurs predominantly on the intermetallic particles. At the outset, the corresponding anodic reaction is the anodic etching and thinning of the aluminium matrix. Owing to the large ratio of anode to cathode, the rate of matrix etching per unit area is very small and this causes the interfacial pH to increase locally. This local alkalinity thus created around the intermetallic particles by virtue of equation 5.3 will favour the following chemical and electrochemical reactions and this leads to the precipitation of ZrO_2 [299] since the

solubility of the coating compound decreases when the pH increases, resulting in precipitation of coating material.

$$Zr^{4+} + H_2O \rightarrow ZrO^{2+} + 2H^{+} \quad (5.4)$$

$$ZrO^{2+} + H_2O \rightarrow ZrO_2 + 2H^{+} \quad (5.5)$$

These observations are consistent with the surface chemistry found by our EDX and GDOES results. The rate of coating deposition is greater over the matrix, followed by copper-containing intermetallic phases which are noble compared to the matrix. The alkaline environment created around the Cu-rich intermetallics may also cause the selective dissolution of the aluminium component of the intermetallics which leads to enrichment of copper in the layer just beneath the conversion layers and this subsequently leads to incorporating of copper into the coating, following sufficient enrichment of the alloy.

5.4.2 Effect of immersion time on coating development

The time-dependent OCP of the superpure aluminium specimen immersed in zirconium-based conversion bath is revealed in Figure 5.1. The initial increase in potential observed, is as a result of surface activation where dissolution of aluminium occurred simultaneously with the evolution of hydrogen. An important aspect suggested is that such an increase in potential drives local thickening of the alumina oxide in regions which are not covered with the conversion coating deposit. As a result, the thickened alumina oxide renders the tunnelling of electrons negligibly small, or insignificant, such that deposition by electron tunnelling is absent at the anodic sites. The process of coating growth involves three stages. The dissolution of surface oxide of the metals occurs at first stage. The surface film consisting of oxides and hydroxides were dissolved in the acidic zirconium bath as a result of the fluoride species. At the second stage, the initiation and growth of zirconium-based conversion coatings occurred while at the final stage, there was an improvement of conversion coating formed. The coating improved gradually until the dynamic balance of oxide dissolution and coating formation was established and the conversion coating was thus formed completely. The first and second stages were observed during the initial 30 s of immersion in the conversion bath solution. The RBS results also confirm that there is an induction period

where there is little zirconium deposition, followed by prolonged immersion times where the zirconium layer develops. The presence of the conversion coating on the aluminium matrix and model aluminium-copper binary alloys was indicated by the detection of the elements oxygen, zirconium, and aluminium which were labelled in the various RBS spectra for different treatment times. The depth profile of an element is given by the distribution at channel numbers below the elemental position that indicates where the element would fall if it was at the surface of the specimen [35]. The thickness of the zirconium content in the conversion layer increases with increase in treatment time. Furthermore, EDX analysis of several specimens have shown that the longer pre-treatment time, the higher the zirconium content in the conversion coating layer. A substantial fraction of aluminium was detected during EDX analysis. This is due to the fact that the size of the sputter deposits was small compared to the interaction depth of the probe beam and this is as a result of the electron beam penetrating through the sputtered layer to the underlying aluminium substrate. The change of the zirconium content on the different coated surfaces indicated that the longer the treatment time in the conversion bath solution, the thicker the coatings under the same deposition conditions.

5.4.3 Influence of copper alloying element

The formation of the zirconium-based conversion coating on Al-1.0at.%Cu, Al-5.0at.%Cu, Al-10at.%Cu and Al-30at.%Cu alloys follows the pattern found by some authors in previous studies of conversion coating growth on binary aluminium alloys [228, 230]. The initial coating growth developed with oxidation of aluminium only, while copper enriches in the alloy. However, for high copper content alloys, copper is eventually incorporated into the coating and the coating thickness then reduces over the general surface of the specimen, with the coating subsequently formed on the alloys being relatively thin. For the Al-1.0at.%Cu alloy, the initial coatings is similar to those formed on the superpure aluminium but with a slower rate of coating growth as shown in Figure 5.10 (b). With the higher copper content alloys (Al-5.0at.%Cu, Al-10at.%Cu and Al-30at.%Cu), a thin zirconium-based conversion coating forms initially, leading to enrichment of copper in the alloy immediately beneath the coating. The enrichment will occur with oxidation of no more than a few nanometres of alloy, with a significant contribution being made by the formation of the air-formed oxide. From the GDOES

results obtained for Al-10at.%Cu and Al-30at.%Cu alloys, copper is incorporated into the coating at a relatively early stage in the coating process. These observations confirms the data suggested in the literature that second phase particle such as Al_2Cu may be considered as highly alloyed aluminium matrix, since to some extent it behaves in a similar manner as the matrix of the matrix after enrichment to the steady level [153]. This explains the small thickness of the coatings formed on high copper-content alloys and the incorporation of copper into the coatings during short immersion times.

5.4.4 Coating composition and structure

The results of this study show that the zirconium-based conversion layers formed on superpure aluminium and aluminium-copper model binary alloys exhibit different morphologies. TEM and RBS images reveal that the coating is much thicker on the superpure aluminium matrix than on the alloy matrixes. The EDX point and area analyses of the conversion coatings formed on the superpure aluminium substrates indicates that the zirconium-based conversion coating is composed of zirconium, oxygen as well as a small amount of fluorine.

Nuclear reaction analyses determined the composition level of oxygen (a major component of the coating) conversion coating layer. The conversion coating has oxygen to zirconium ratio of 3:1 at relatively short immersion times up to 60 s. This fits a $ZrO_2.H_2O$ compositional model. However, with prolonged immersion times, the oxygen to zirconium ratio revealed an enhanced concentration for oxygen, suggesting a compositional model of $ZrO_2.2H_2O$. This satisfies an overall composition of $ZrO_2.nH_2O$, where n equals 1 or 2 for shorter or prolonged immersion times respectively.

The GDOES measurements indicated further that the oxide layer formed on the matrix consisted of mixed oxides of zirconium, and aluminium. These observations for the zirconium-based conversion coating are consistent with previous X-ray photoelectron spectroscopy (XPS), Auger electron spectroscopy (AES) and secondary ion mass spectrometry (SIMS) measurements [199, 231, 233, 300] except for the fact that the detector of the GDOES machine used in the present study is not capable of resolving the chemical identity of the oxides nor is it possible for it to detect the presence of hydrogen efficiently as XPS measurements. Hence, it is not possible to eliminate the possibility

that hydroxides are present in the coatings. In addition GDOES does not give any information about the lateral distribution and heterogeneity of the conversion coating, which is in fact highly heterogeneous, as revealed by electron microscopy.

The XPS, AES and SIMS results in the literature reveal that zirconium is always present in its dioxide form ZrO_2, and some hydroxy-oxide or hydroxyfluoride may also be present depending on the composition of the conversion bath [233]. From in-depth elemental profiles through the resultant zirconium conversion coatings formed aluminium and aluminium alloys, the conversion coatings have been considered to be multi-layered, with Al_2O_3 adjacent to the aluminium surface, a Zr/O/F containing outer layer and ZrO_2 sandwiched between the previous layers [35]. Zirconium, aluminium, oxygen and fluorine are the main constituents of the conversion film, with zirconium accounting for about 36% of the total weight [51].

Schram et al. [231] used AES, SIMS and XPS to studied the composition of a commercial zirconium-based conversion bath Alodine 4830/4831 (which contains mainly a fluorinated zirconium salt and a water soluble polymer) . They found that zirconium-based conversion coating consists of a two-layered structure, in which the inner region (close to the metal interface) contains only Al and O, while the outer region (closer to the outer surface) contains a fluorinated zirconium compound and probably a polymeric compound that is concentrated towards the outer surface of the coating.

In order to characterise the structure and chemical composition of zirconium-based conversion coating, Newhard Jr. et al. [300], used AES and XPS complimentary analytical techniques. The Auger electron spectroscopy measurements of these conversion coatings revealed the presence of both zirconium and fluorine in the coating layer. XPS depth profiling indicated that the layer of coating is built up of three sublayers: near the metal interface Al_2O_3, above a layer of ZrO_2 and on top a mixture of zirconium (Zr), oxygen (O) and fluorine (F).

In the present study, the resulting analyses of the zirconium-based conversion coatings are dependent on the complementary surface analytical techniques employed. RBS, EDX and GDOES analyses disclosed the presence of zirconium and oxygen species and in some cases, fluorine species. RBS and GDOES results also suggest the presence of aluminium species in the coating material. It is apparent that some of the aluminium

signals detected by RBS could be due to the aluminium substrate; hence the exact quantity of aluminium in the conversion coatings is not clearly identified by this technique.

The EDX and RBS analyses of the coatings formed on copper-containing aluminium alloys also revealed the presence of copper species in the conversion coating. The presence of copper species in the coating detected by RBS is likely due to the exposure of coarse second phase intermetallic particles present in the near-surface regions or due to the incorporation of copper species into the coating after prolonged immersion time.

Fluoride species were detected in some of the coating using EDX and RBS technique but not by GDOES since the GDOES technique used in the present work is not capable of resolving the chemical identity of fluoride species since the depth profiling analysis of the coatings was carried out in low pressure argon and not neon which is capable of detecting fluoride species.

Further investigation will be needed in order to determine the level of corrosion protection provided by the zirconium-based conversion coatings formed on aluminium and aluminium alloys and the effect of alloy composition on the protection of zirconium-based conversion coating as a possible alternative to chromium-based conversion coatings. In the following chapter, an assessment of the effectiveness of the protection offered by zirconium-based conversion coatings on aluminium and aluminium-copper alloys are considered.

5.5 Summary

In this study, zirconium-based conversion coatings formed on aluminium and aluminium-copper binary alloys was characterised using AFM, TEM, RBS, SEM-EDX and GDOES complementary surface analytical techniques. The following are key findings:

1. The zirconium-based conversion layer formed on the surface of aluminium is somewhat homogenous while on aluminium-copper alloys, it is in most cases heterogeneous.

2. The presence of the conversion coating on the aluminium matrix and model aluminium-copper binary alloys was indicated by the detection of the elements oxygen, zirconium, and aluminium which were labelled in the various RBS spectra for different treatment times.

3. The zirconium-based conversion coating developed on the specimens is composed of a likely outer layer of $ZrO_2.nH_2O$ with hydrated aluminium oxide adjacent to the metal/coating interface.

4. Increasing the immersion time resulted in an increase in coating thickness for aluminium substrates but little change in coating thickness occurred for aluminium-copper model alloys after prolonged immersion in the conversion bath solution.

5. The zirconium-based conversion coating on the matrix exhibits a typical mud-crack morphology which likely occurred due to exposure to vacuum which rapidly dehydrate the conversion coatings during FEGSEM analysis.

6. In high copper-content aluminium alloys, the initial coating growth developed with oxidation of aluminium only, while copper enriches in the alloy. However, copper is eventually incorporated into the coating and the coating thickness then reduces over the general surface of the specimen, with the coating subsequently formed on the alloys being relatively thin.

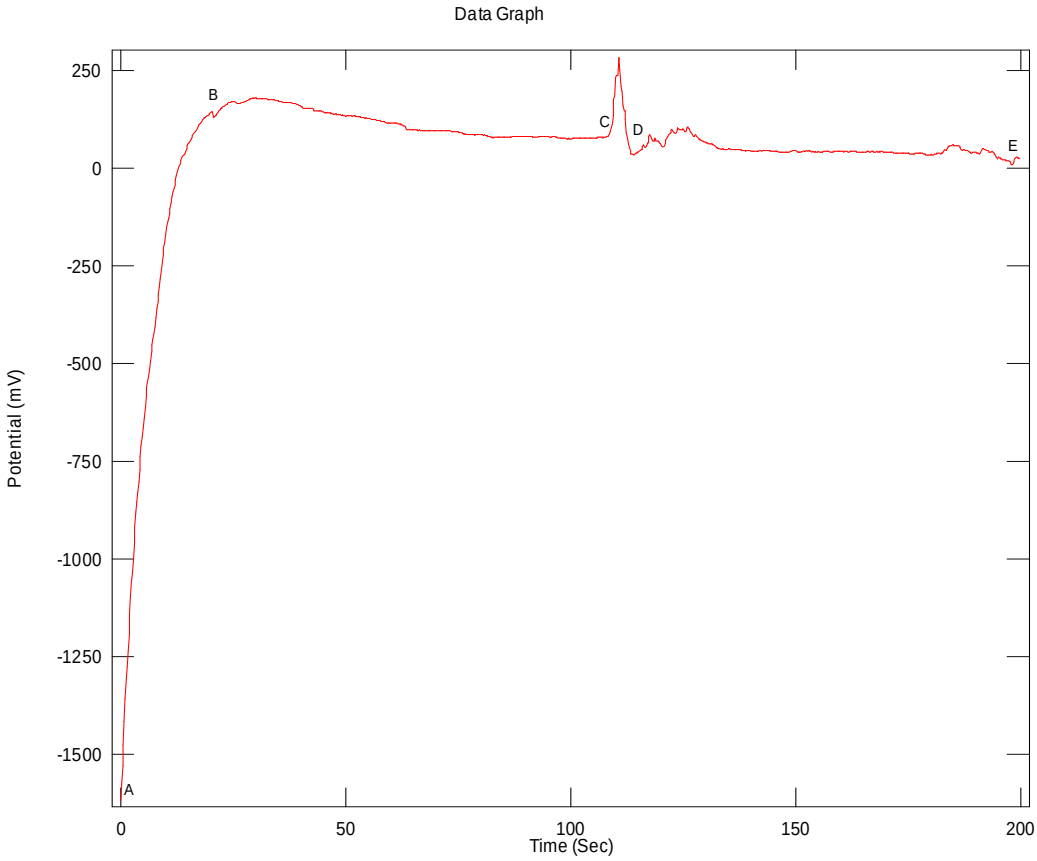

Figure 5.1 Potentiodynamic curve of superpure aluminium in zirconium conversion bath.

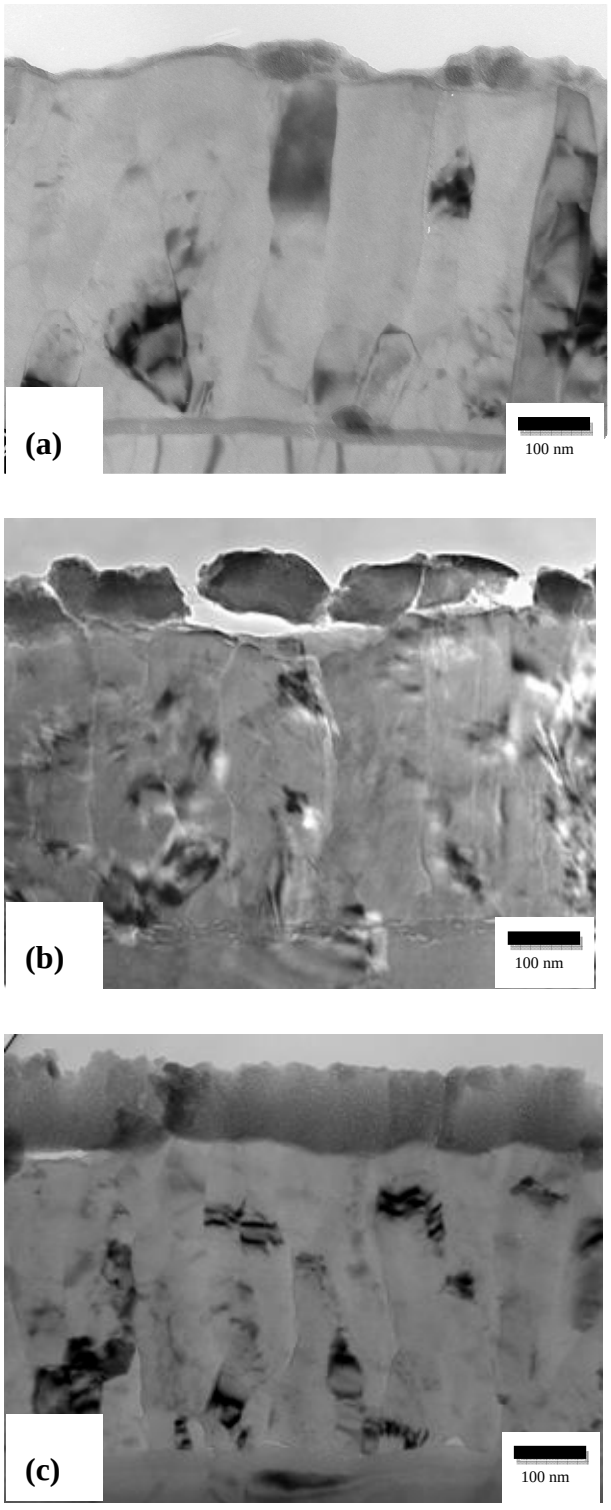

Figure 5.2 Transmission electron micrographs of ultramicrotomed sections of superpure aluminium specimens following sputter deposition and conversion treatment in zirconium-based conversion bath for (a) 30 s, (b) 60 s and (c) 180 s.

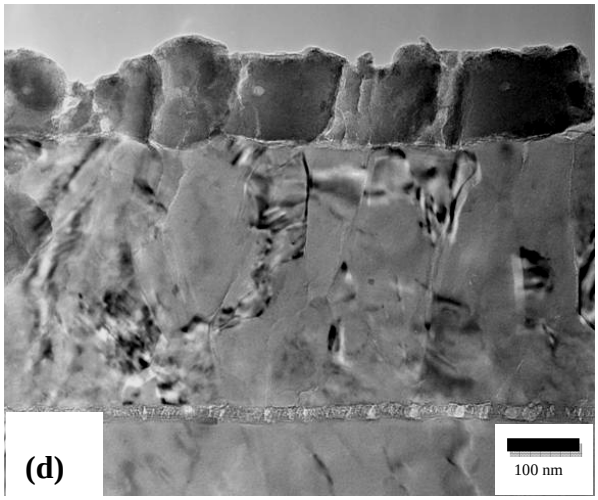

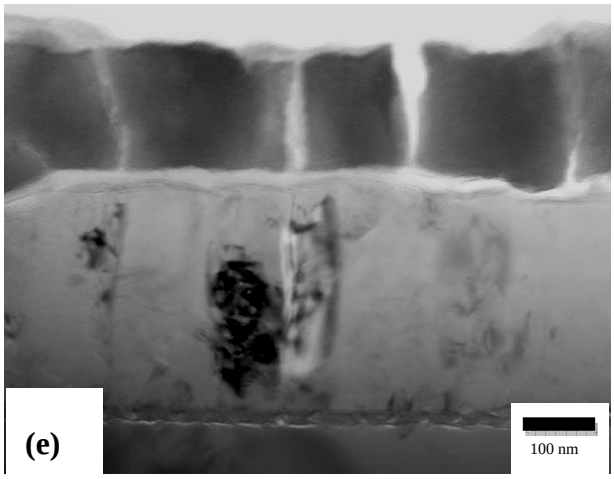

Figure 5.2 Transmission electron micrographs of ultramicrotomed sections of superpure aluminium specimens following sputter deposition and conversion treatment in zirconium-based conversion bath for (d) 300 s and (e) 600 s.

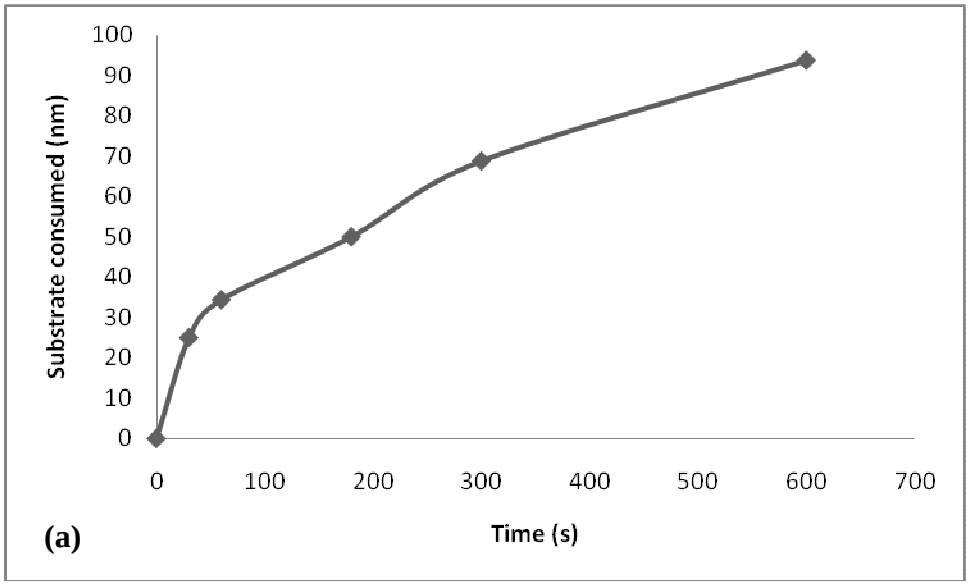

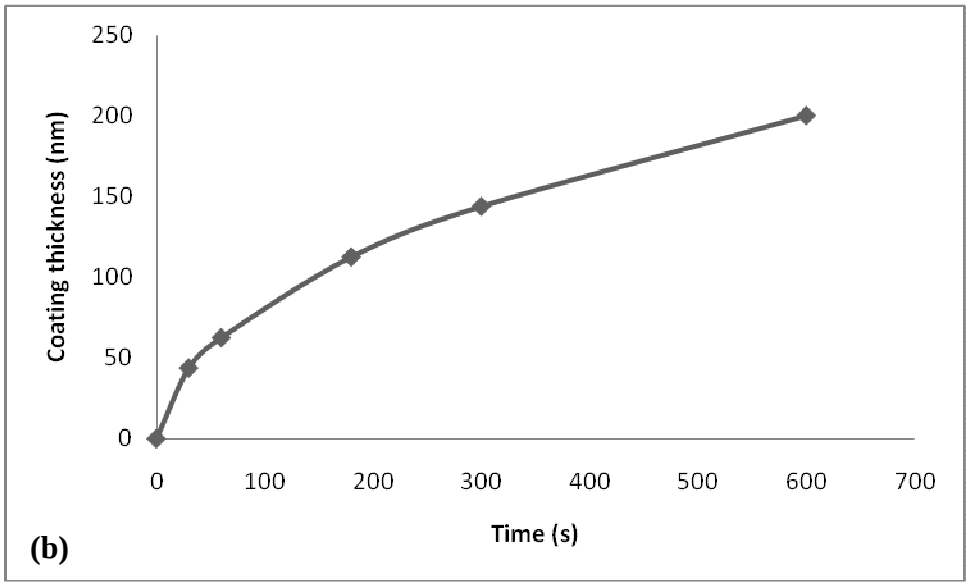

Figure 5.3 Loss of substrate thickness (a) and thickness of conversion coatings (b), determined from transmission electron micrographs for the superpure aluminium surface after zirconium-based conversion treatments.

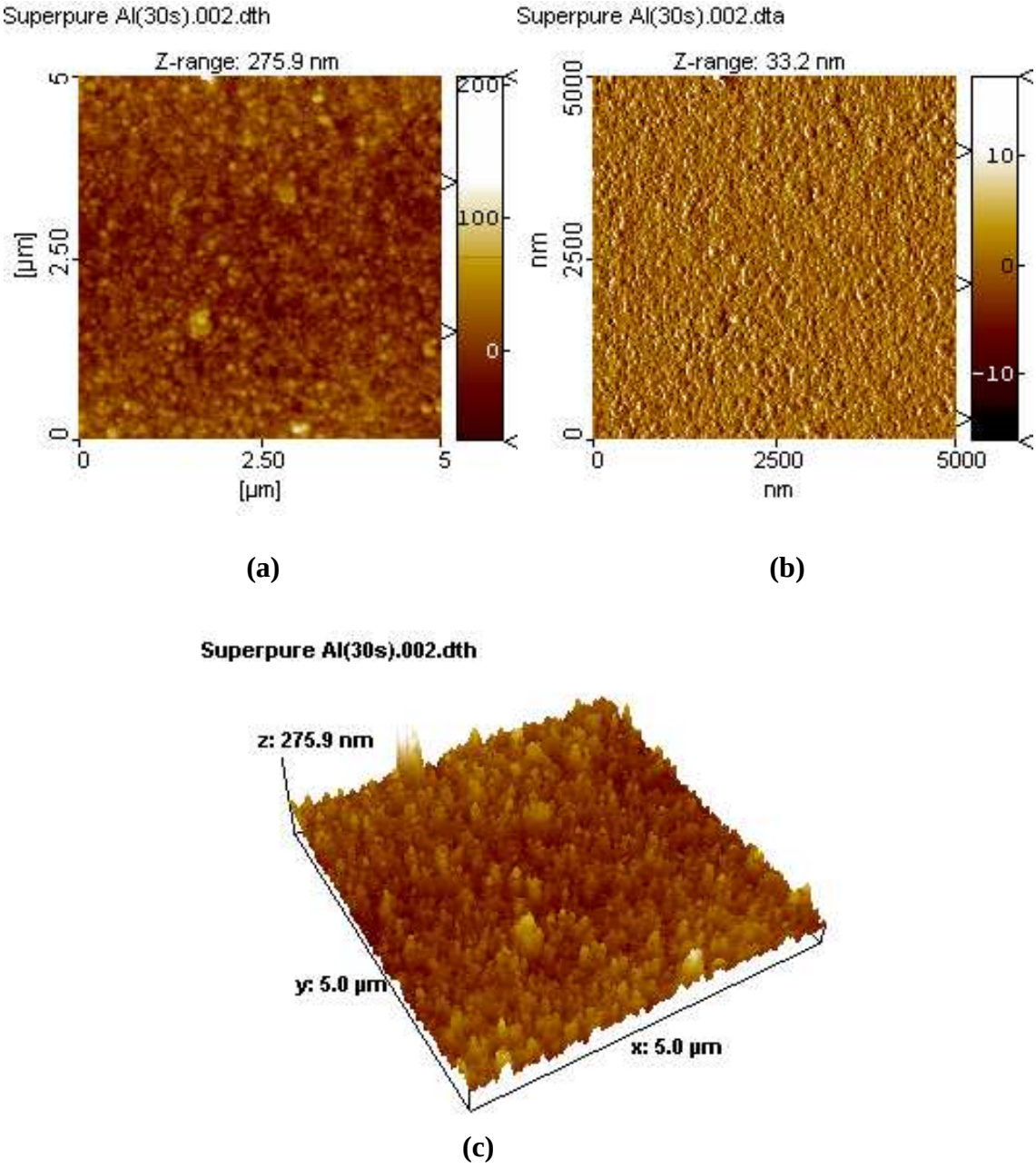

Figure 5.4 AFM images of the coating development on the superpure aluminium surface after immersion for 30 s; (a) height image; (b) 2-dimensional image; (c) 3-dimensional topographic image

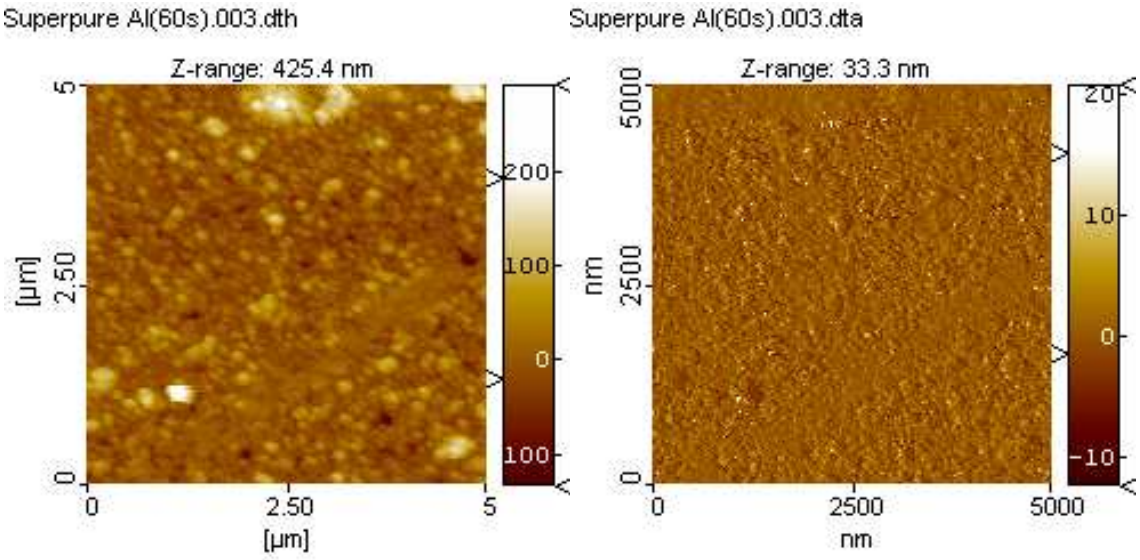

(a) **(b)**

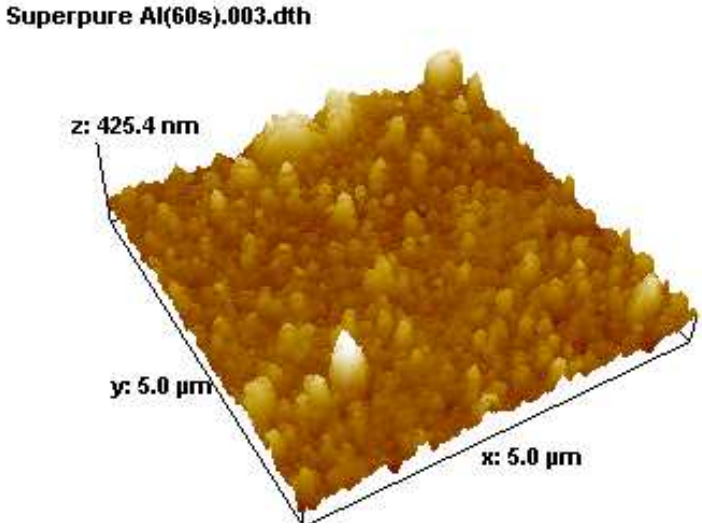

(c)

Figure 5.5 AFM images of the coating development on the superpure aluminium surface after immersion for 60 s; (a) height image; (b) 2-dimensional image; (c) 3-dimensional topographic image

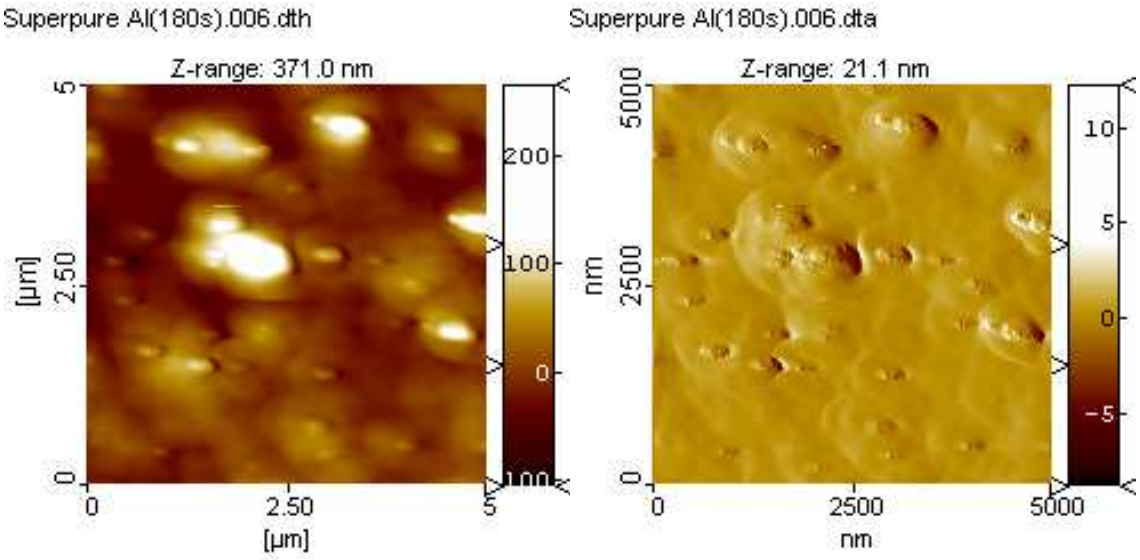

(a) **(b)**

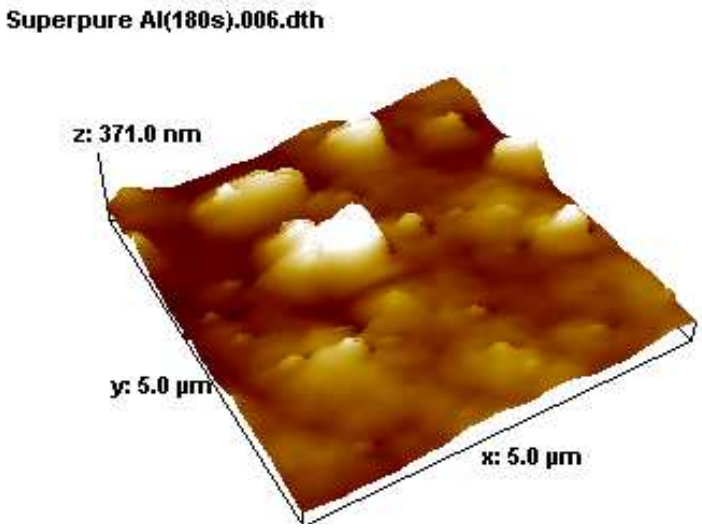

(c)

Figure 5.6 AFM images of the coating development on the superpure aluminium surface after immersion for 180 s; (a) height image; (b) 2-dimensional image; (c) 3-dimensional topographic image

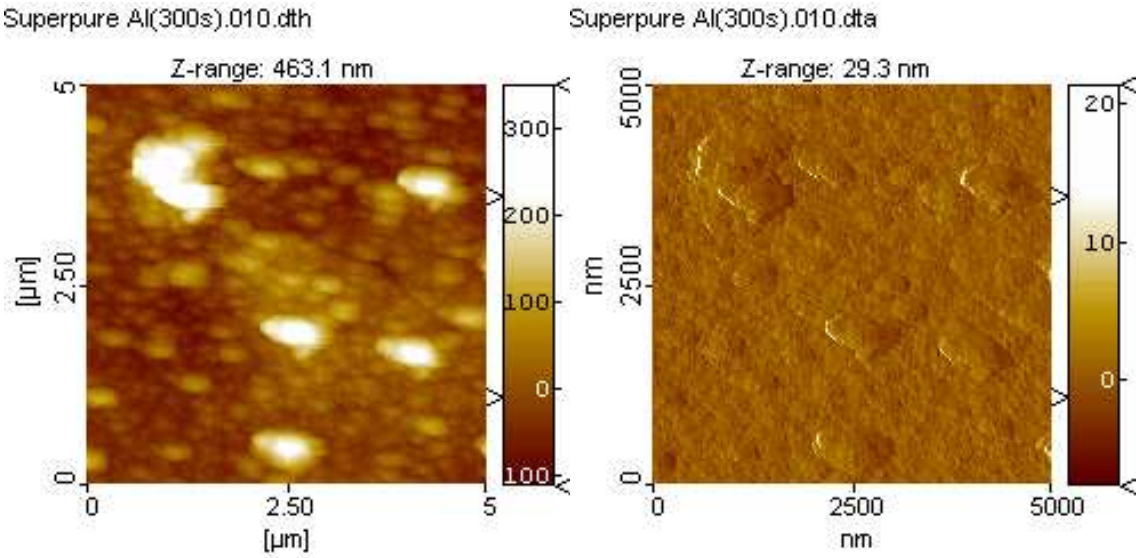

(a) **(b)**

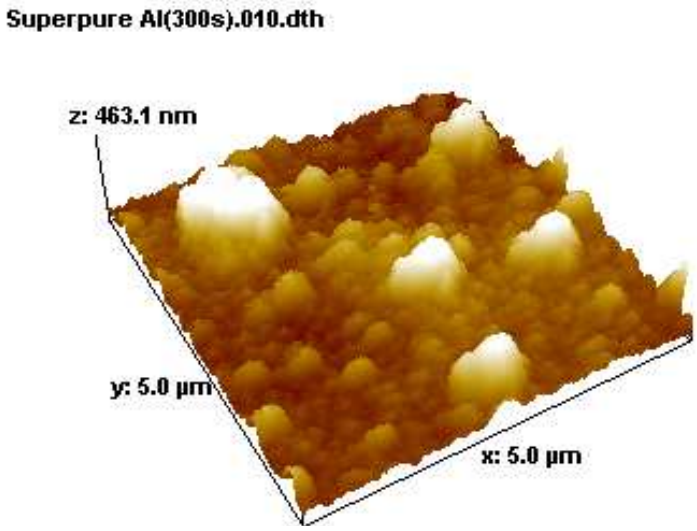

(c)

Figure 5.7 AFM images of the coating development on the superpure aluminium surface after immersion for 300 s; (a) height image; (b) 2-dimensional image; (c) 3-dimensional topographic image.

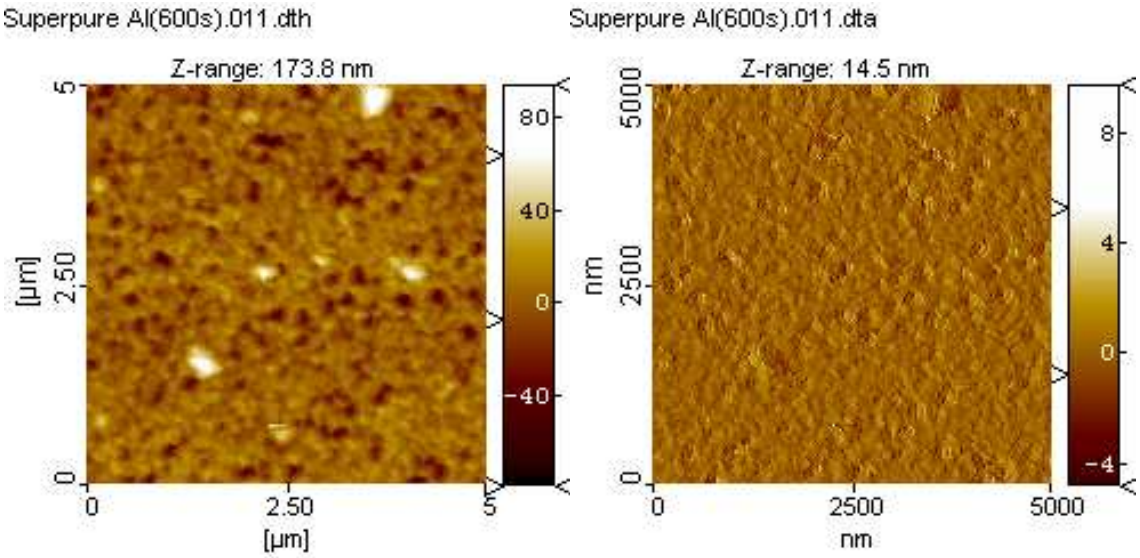

(a) **(b)**

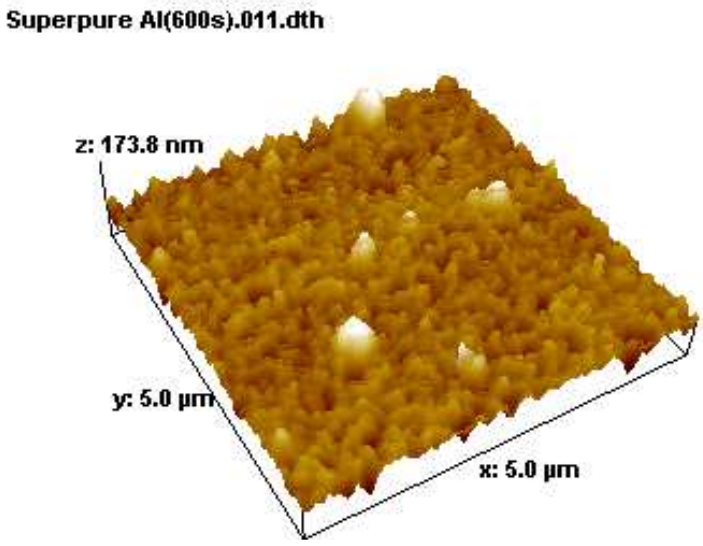

(c)

Figure 5.8 AFM images of the coating development on the superpure aluminium surface after immersion for 600 s; (a) height image; (b) 2-dimensional image; (c) 3-dimensional topographic image.

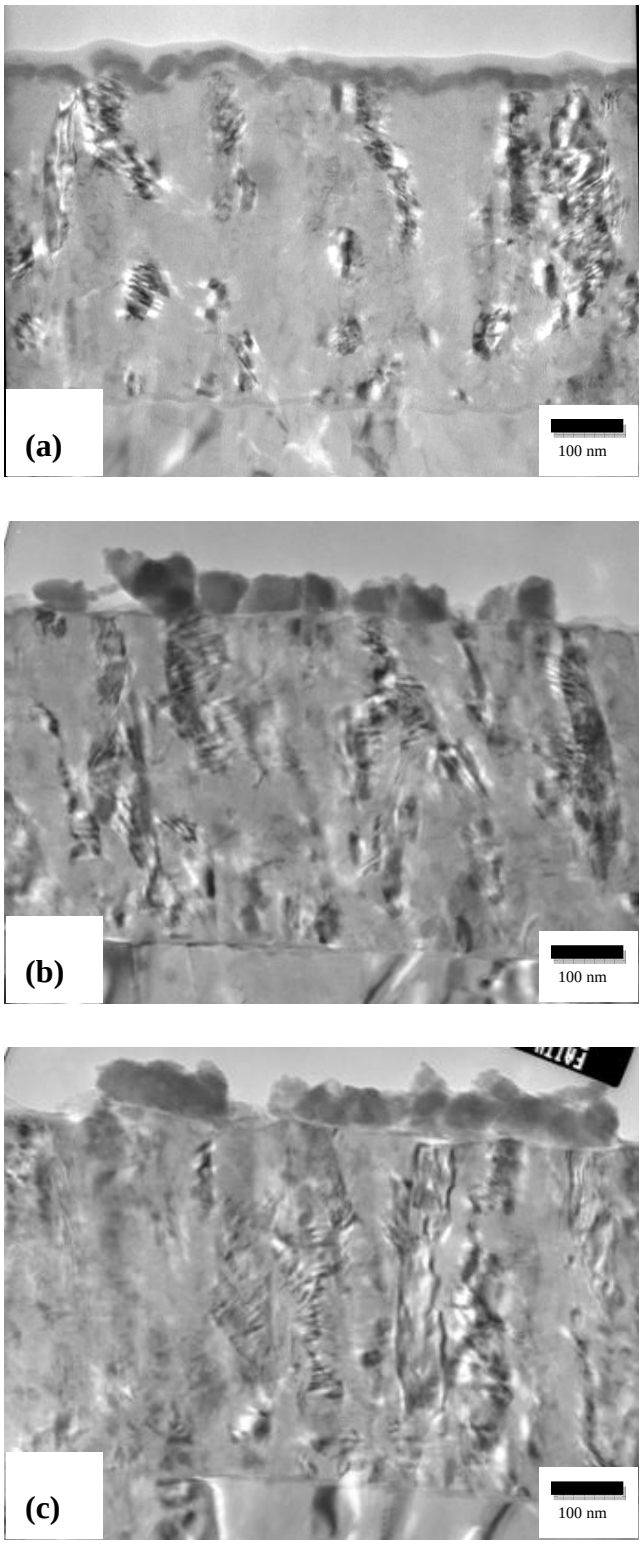

Figure 5.9 Transmission electron micrographs of ultramicrotomed sections of Al-1.0at.%Cu alloy following sputter deposition and conversion treatment in zirconium-based conversion bath for (a) 30 s, (b) 60 s and (c) 180 s.

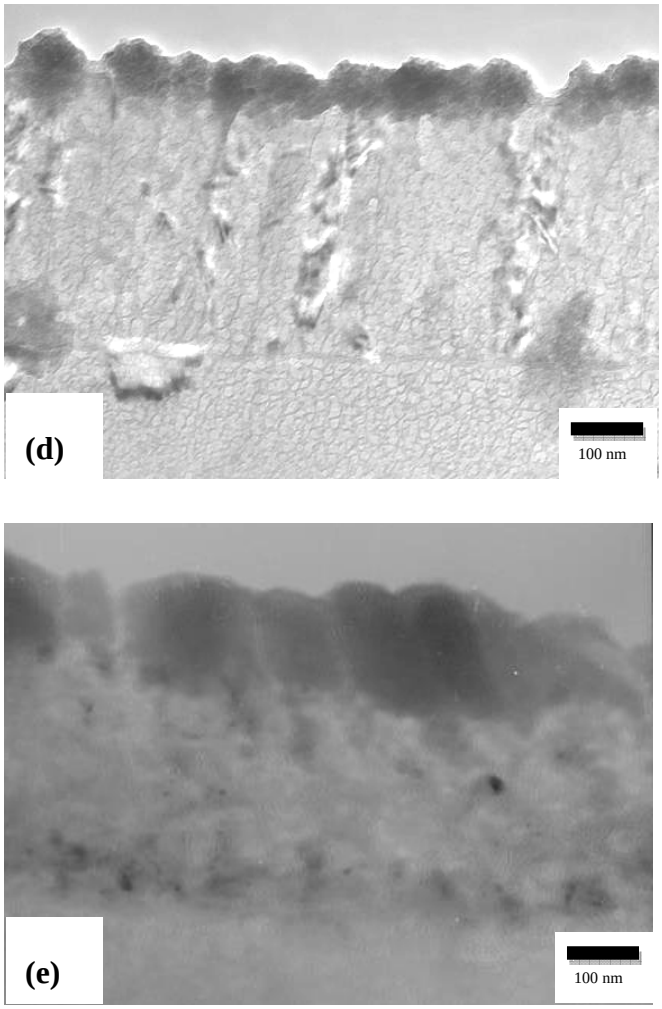

Figure 5.9 Transmission electron micrographs of ultramicrotomed sections of Al-1.0at.%Cu alloy following sputter deposition and conversion treatment in zirconium-based conversion bath for (d) 300 s and (e) 600 s.

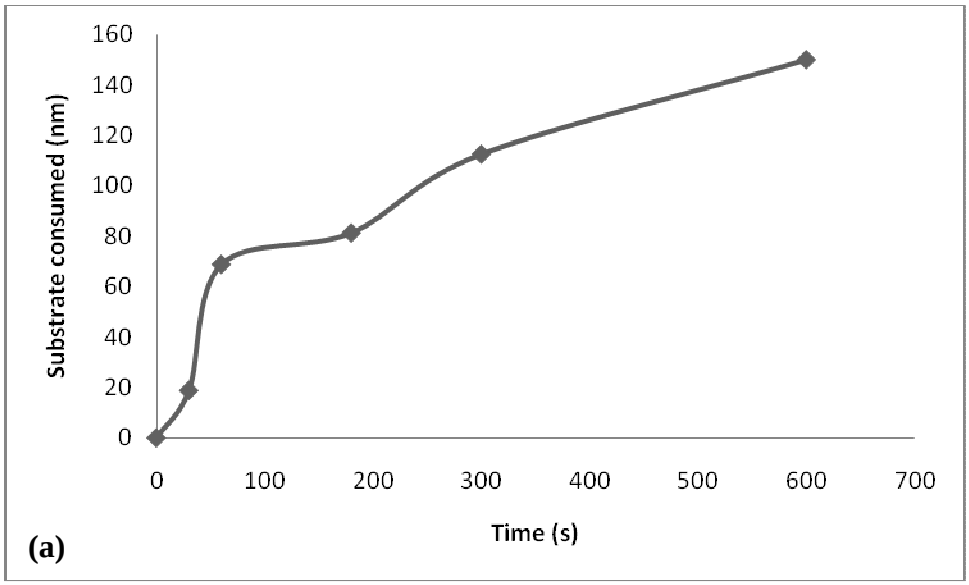

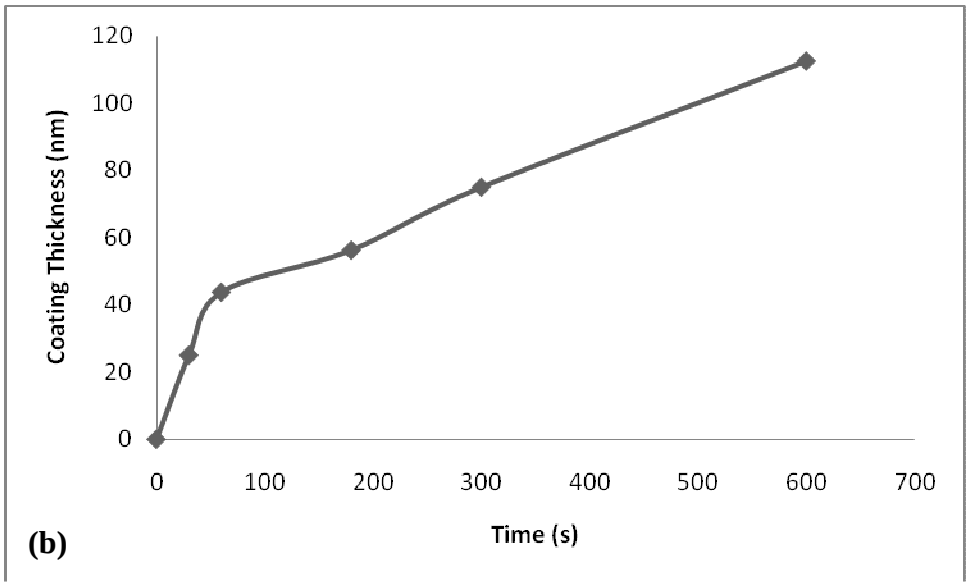

Figure 5.10 Loss of substrate thickness (a) and thickness of conversion coatings (b), determined from transmission electron micrographs for the Al-1.0at.%Cu alloy after zirconium-based conversion treatments.

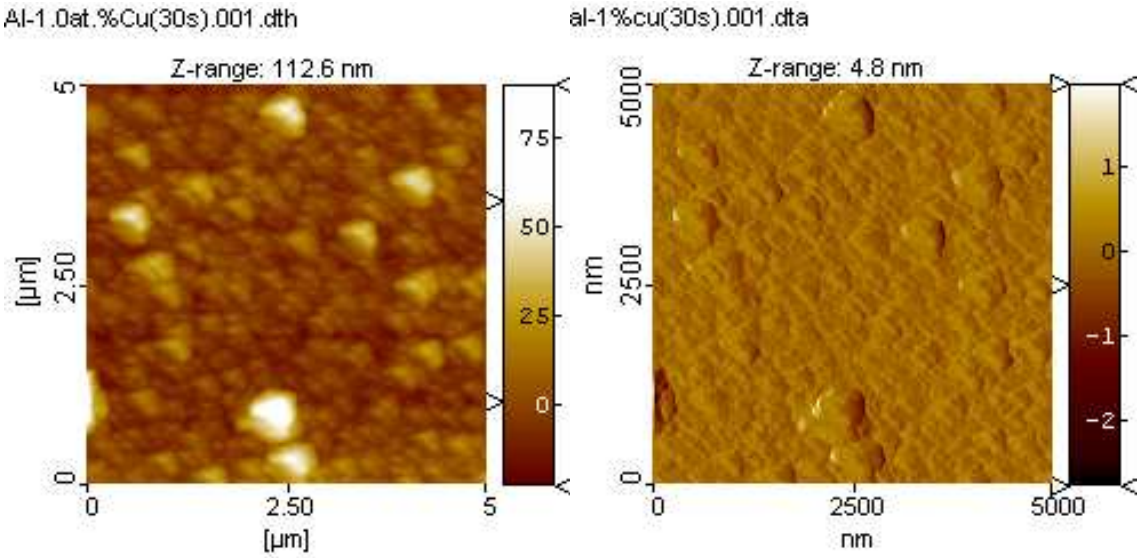

(a) **(b)**

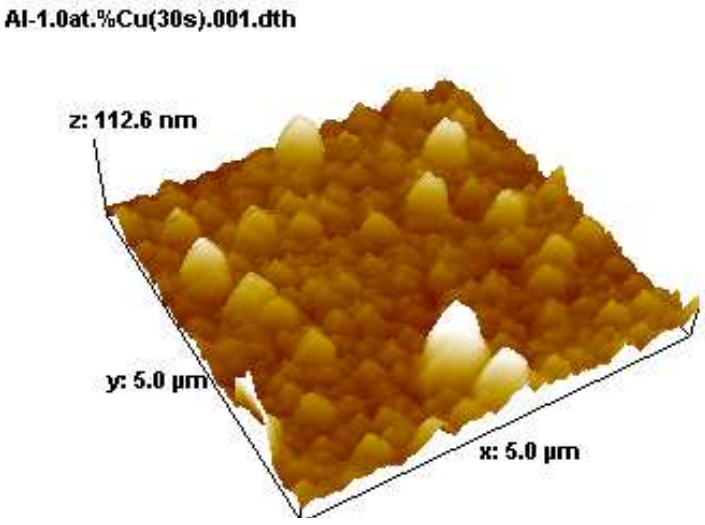

(c)

Figure 5.11 AFM images of the coating development on the Al-1.0at.%Cu alloy surface after immersion for 30 s; (a) height image; (b) 2-dimensional image; (c) 3-dimensional topographic image.

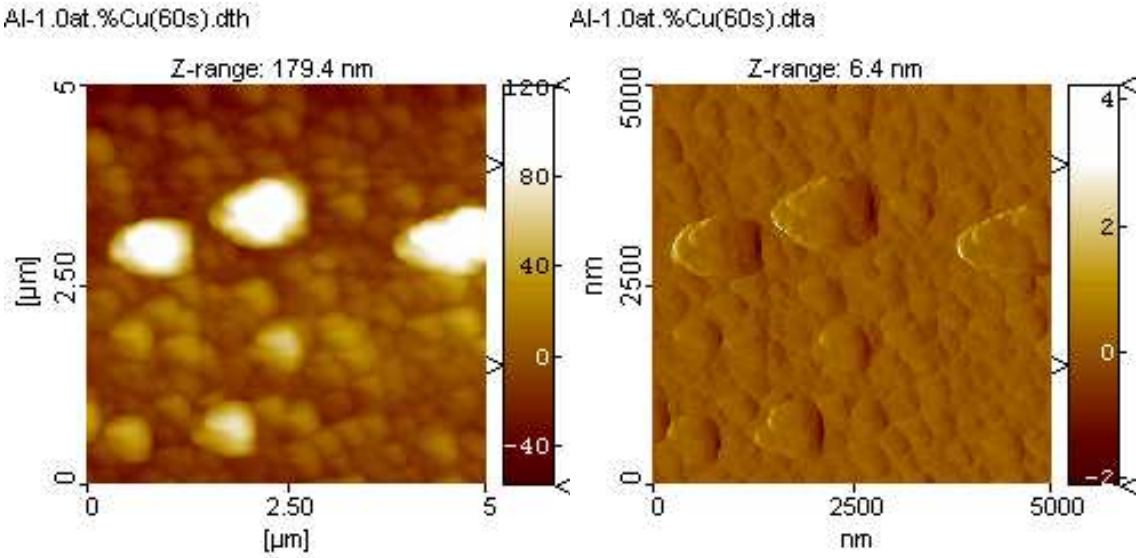

(a) **(b)**

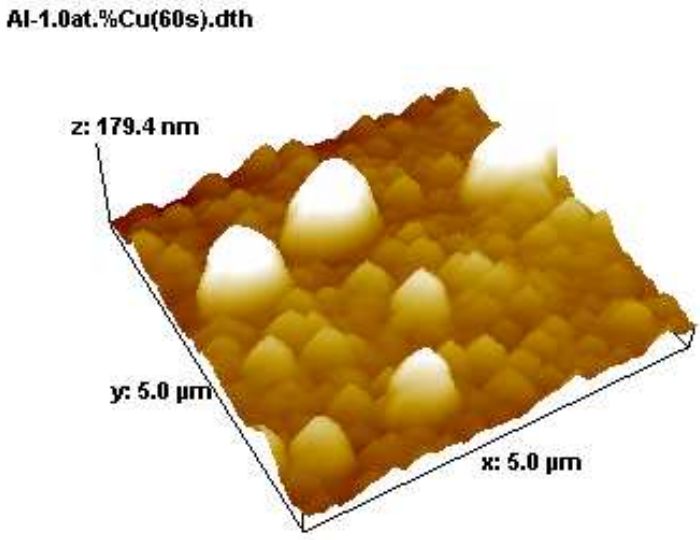

(c)

Figure 5.12 AFM images of the coating development on the Al-1.0at.%Cu alloy surface after immersion for 60 s; (a) height image; (b) 2-dimensional image; (c) 3-dimensional topographic image.

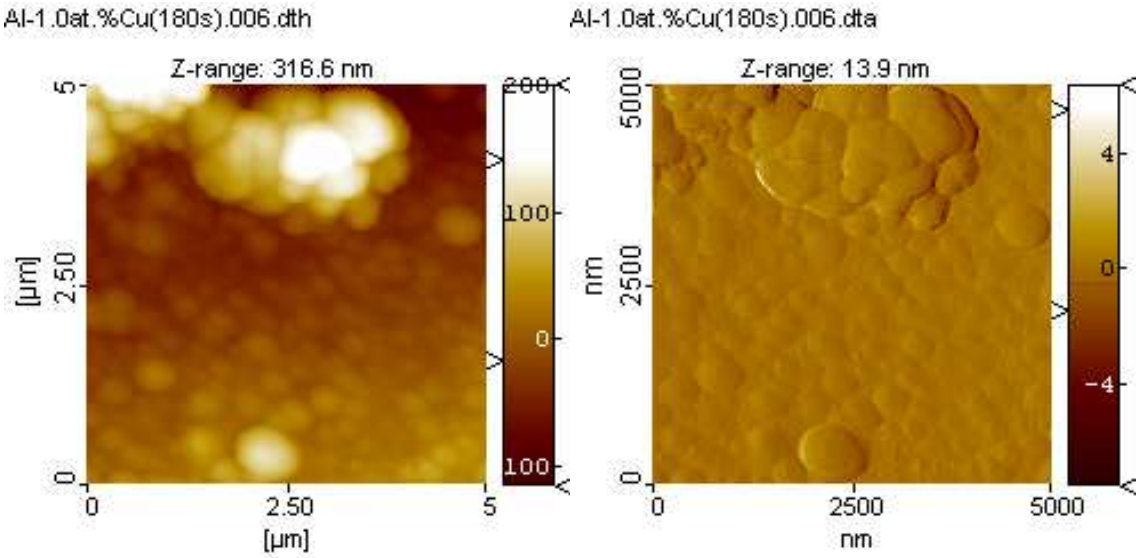

(a) **(b)**

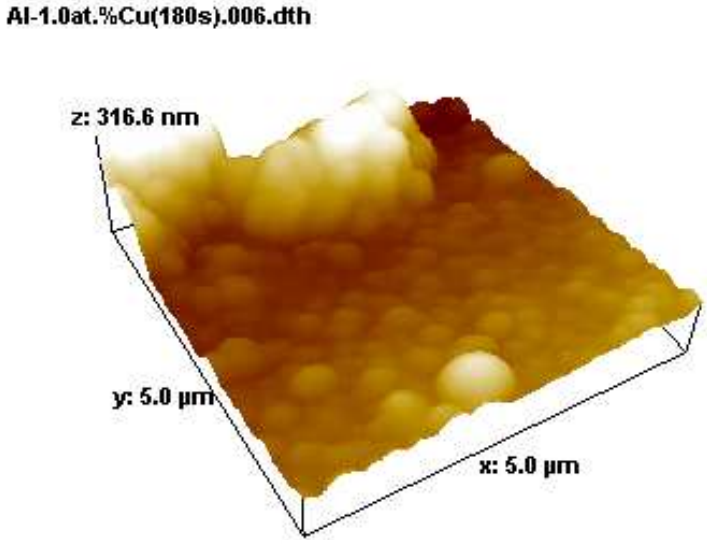

(c)

Figure 5.13 AFM images of the coating development on the Al-1.0at.%Cu alloy surface after immersion for 180 s; (a) height image; (b) 2-dimensional image; (c) 3-dimensional topographic image.

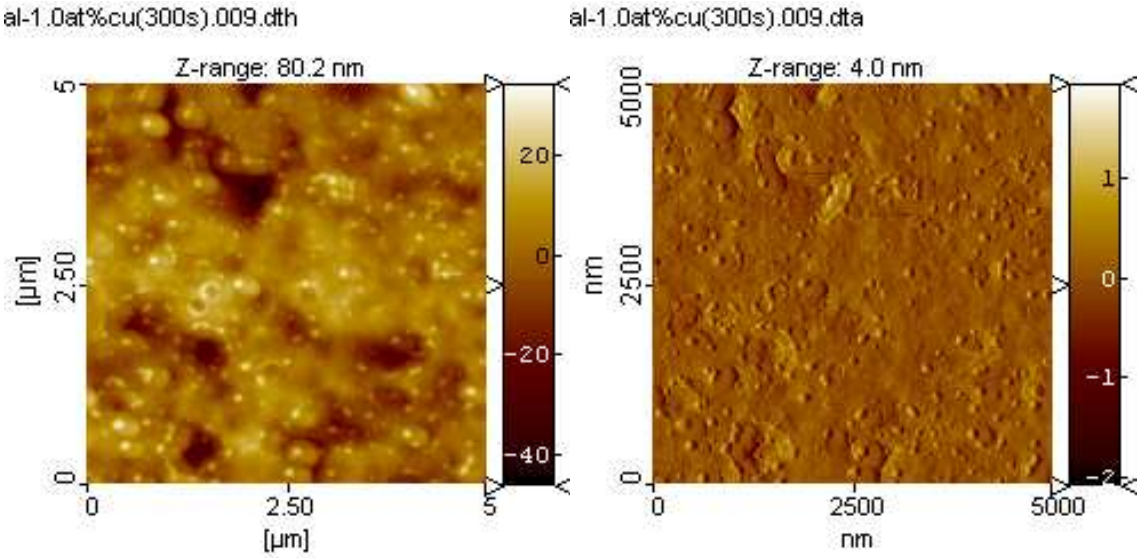

(a) **(b)**

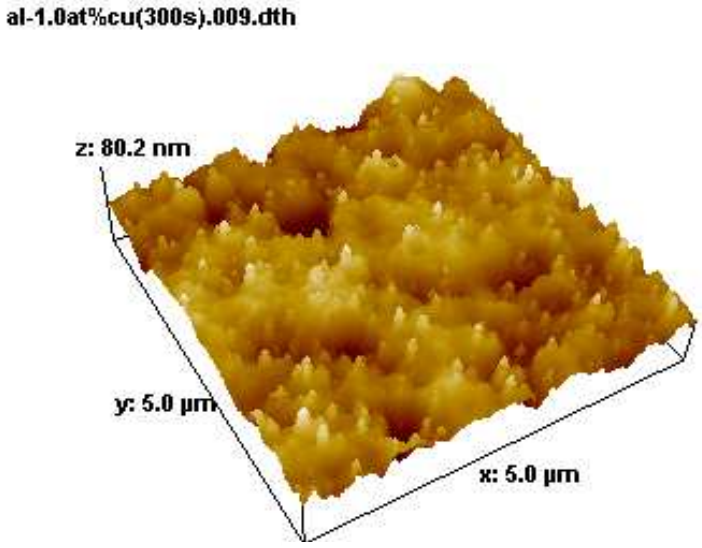

(c)

Figure 5.14 AFM images of the coating development on the Al-1.0at.%Cu alloy surface after immersion for 300 s; (a) height image; (b) 2-dimensional image; (c) 3-dimensional topographic image.

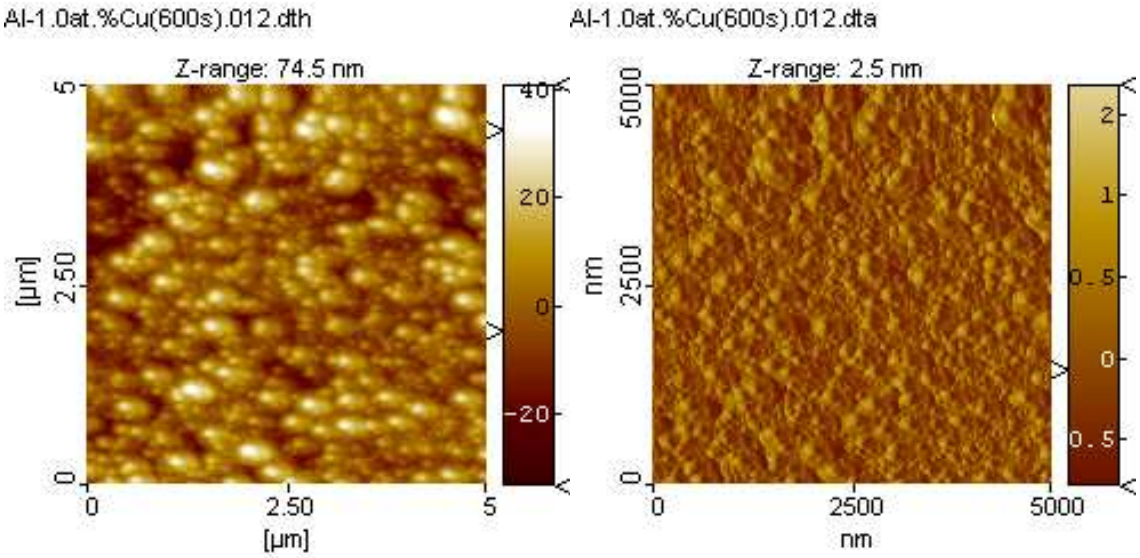

(a) **(b)**

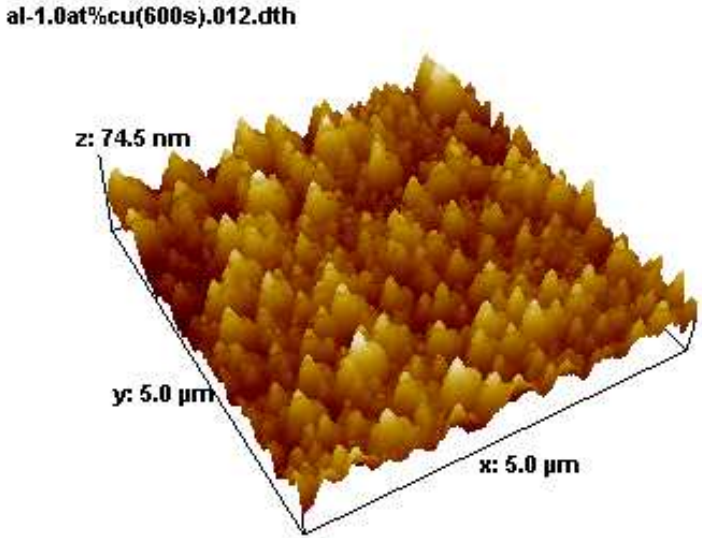

(c)

Figure 5.15 AFM images of the coating development on the Al-1.0at.%Cu alloy surface after immersion for 600 s; (a) height image; (b) 2-dimensional image; (c) 3-dimensional topographic image.

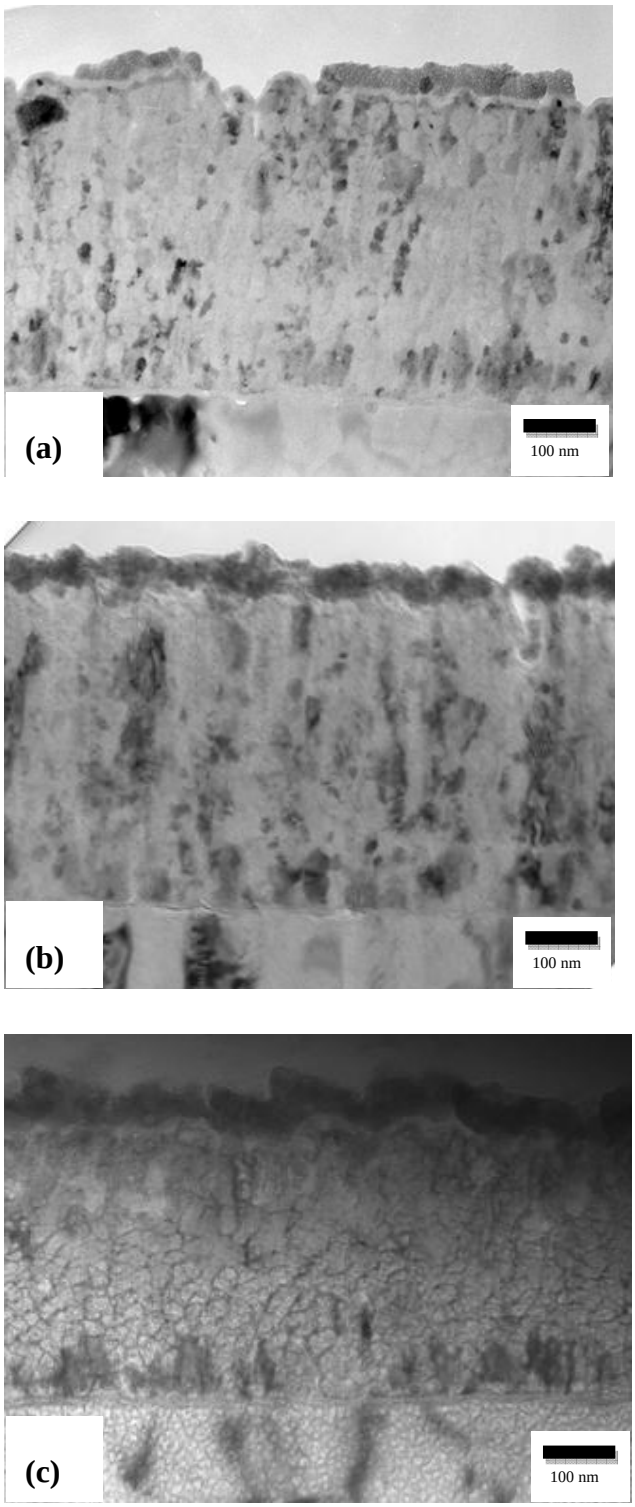

Figure 5.16 Transmission electron micrographs of ultramicrotomed sections of Al-5.0at.%Cu alloy following sputter deposition and conversion treatment in zirconium-based conversion bath for (a) 30 s, (b) 60 s and (c) 180 s.

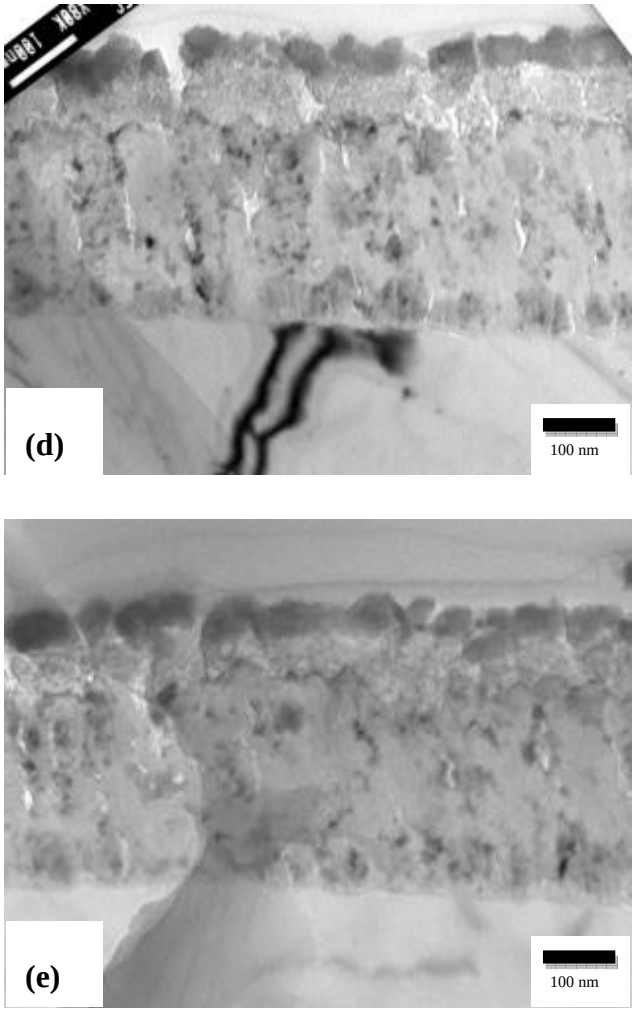

Figure 5.16 Transmission electron micrographs of ultramicrotomed sections of Al-5.0at.%Cu alloy following sputter deposition and conversion treatment in zirconium-based conversion bath for (d) 300 s and (e) 600 s.

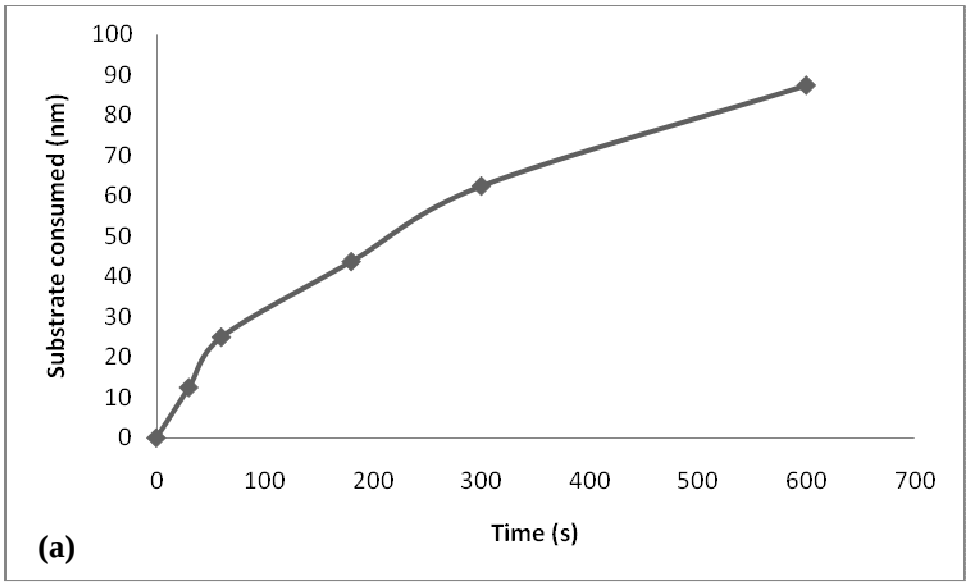

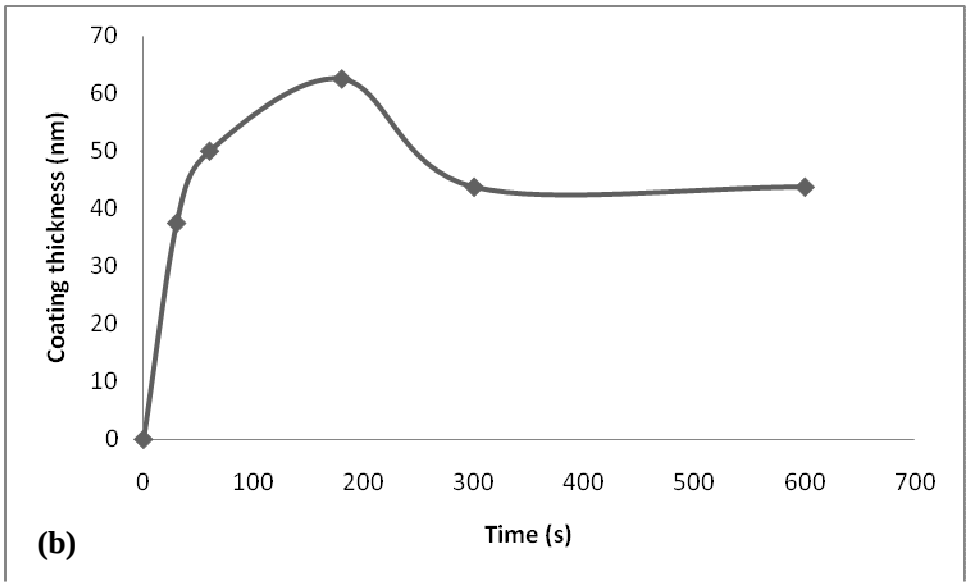

Figure 5.17 Loss of substrate thickness (a) and thickness of conversion coatings (b), determined from transmission electron micrographs for the Al-5.0at.%Cu alloy after zirconium-based conversion treatments.

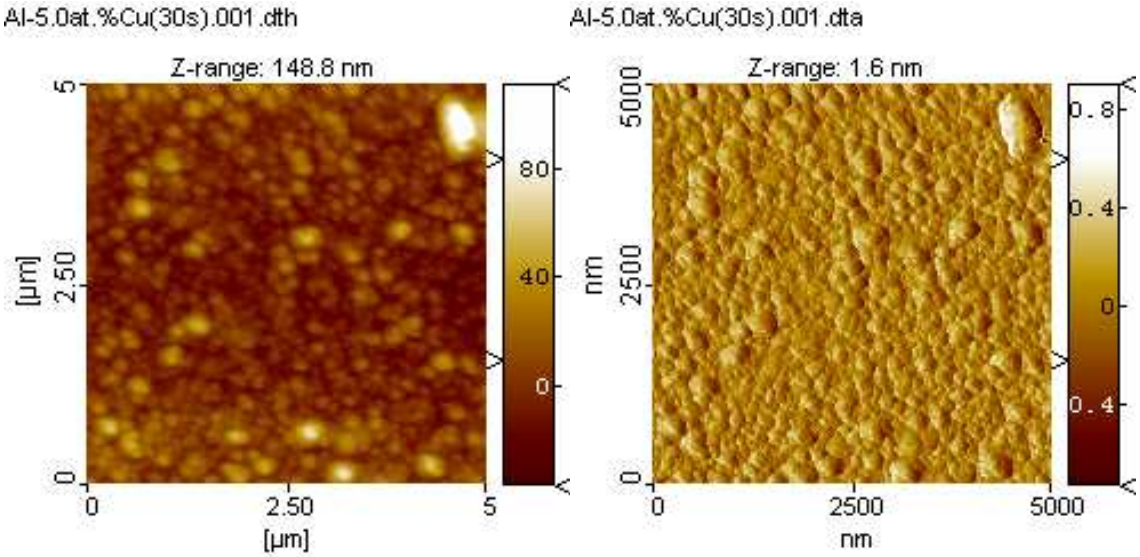

(a) **(b)**

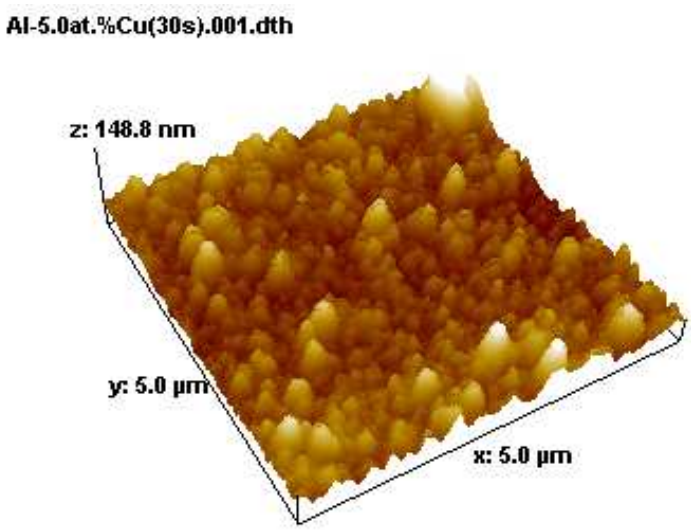

(c)

Figure 5.18 AFM images of the coating development on the Al-5.0at.%Cu alloy surface after immersion for 30 s; (a) height image; (b) 2-dimensional image; (c) 3-dimensional topographic image.

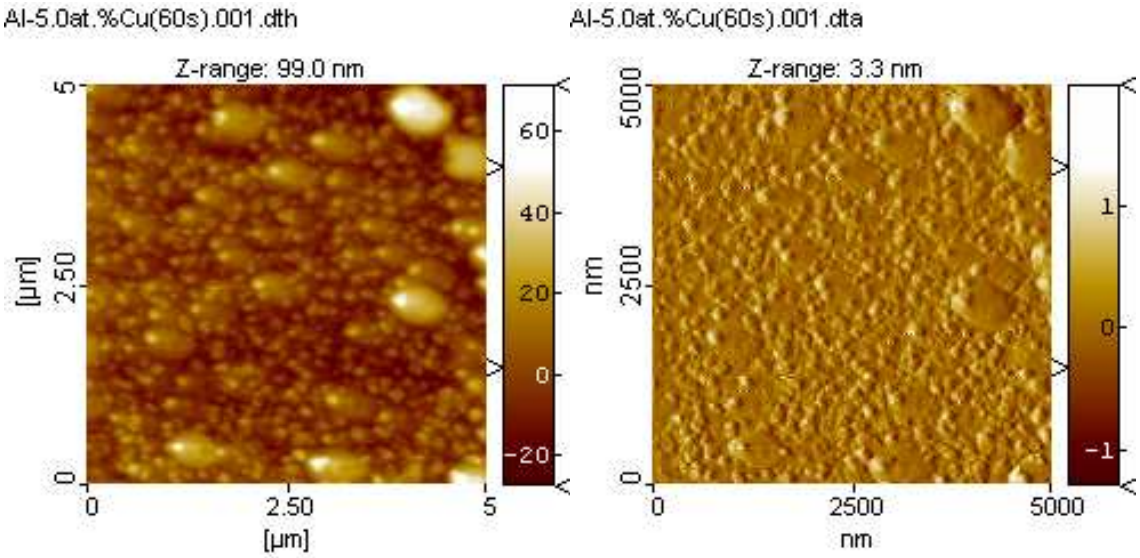

(a) **(b)**

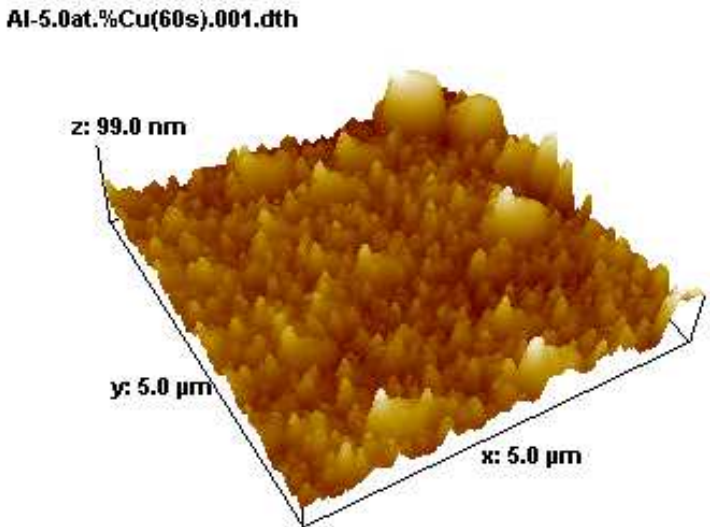

(c)

Figure 5.19 AFM images of the coating development on the Al-5.0at.%Cu alloy surface after immersion for 60 s; (a) height image; (b) 2-dimensional image; (c) 3-dimensional topographic image.

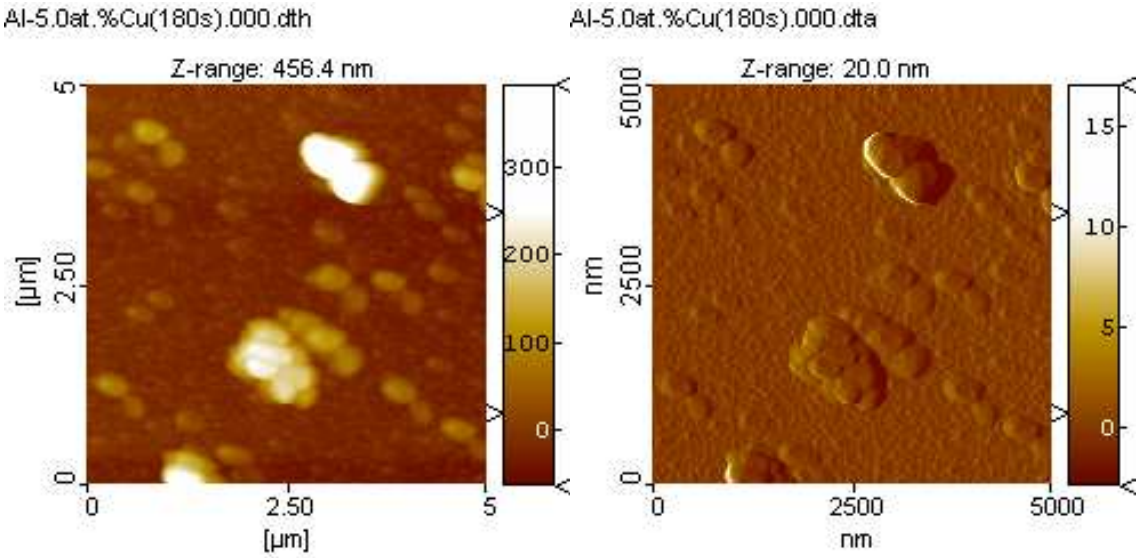

(a) **(b)**

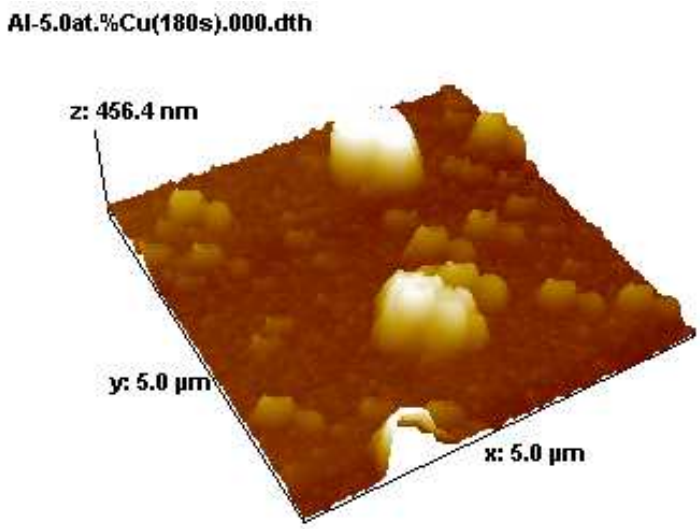

(c)

Figure 5.20 AFM images of the coating development on the Al-5.0at.%Cu alloy surface after immersion for 180 s; (a) height image; (b) 2-dimensional image; (c) 3-dimensional topographic image.

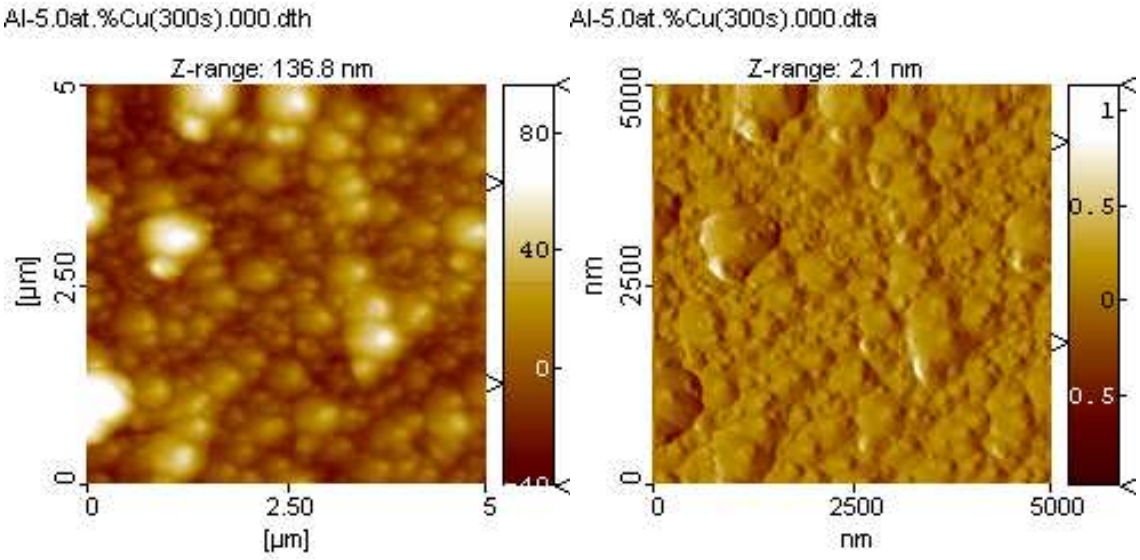

(a) **(b)**

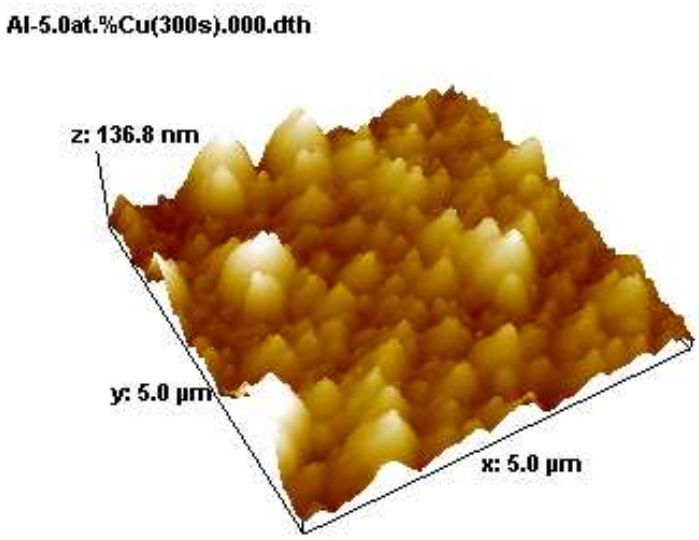

(c)

Figure 5.21 AFM images of the coating development on the Al-5.0at.%Cu alloy surface after immersion for 300 s; (a) height image; (b) 2-dimensional image; (c) 3-dimensional topographic image.

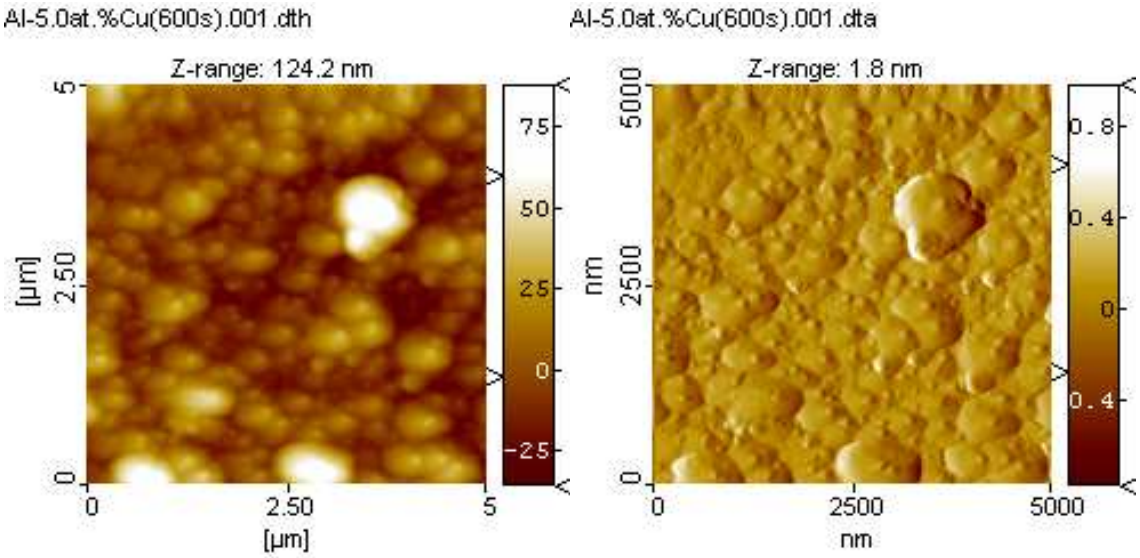

(a) **(b)**

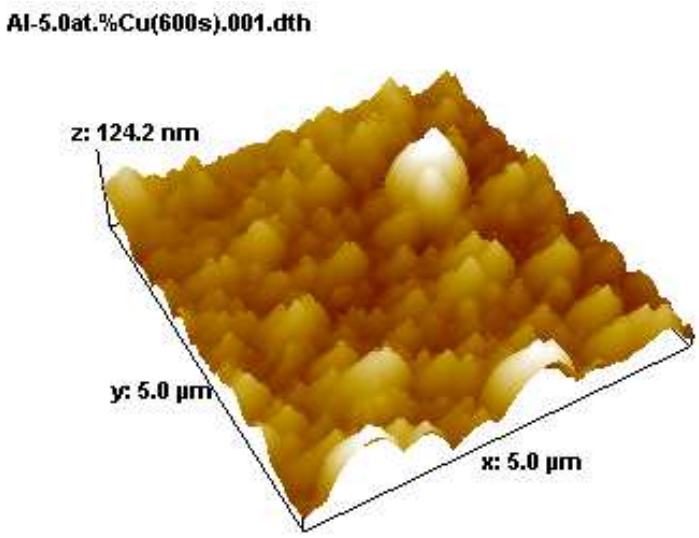

(c)

Figure 5.22 AFM images of the coating development on the Al-5.0at.%Cu alloy surface after immersion for 600 s; (a) height image; (b) 2-dimensional image; (c) 3-dimensional topographic image.

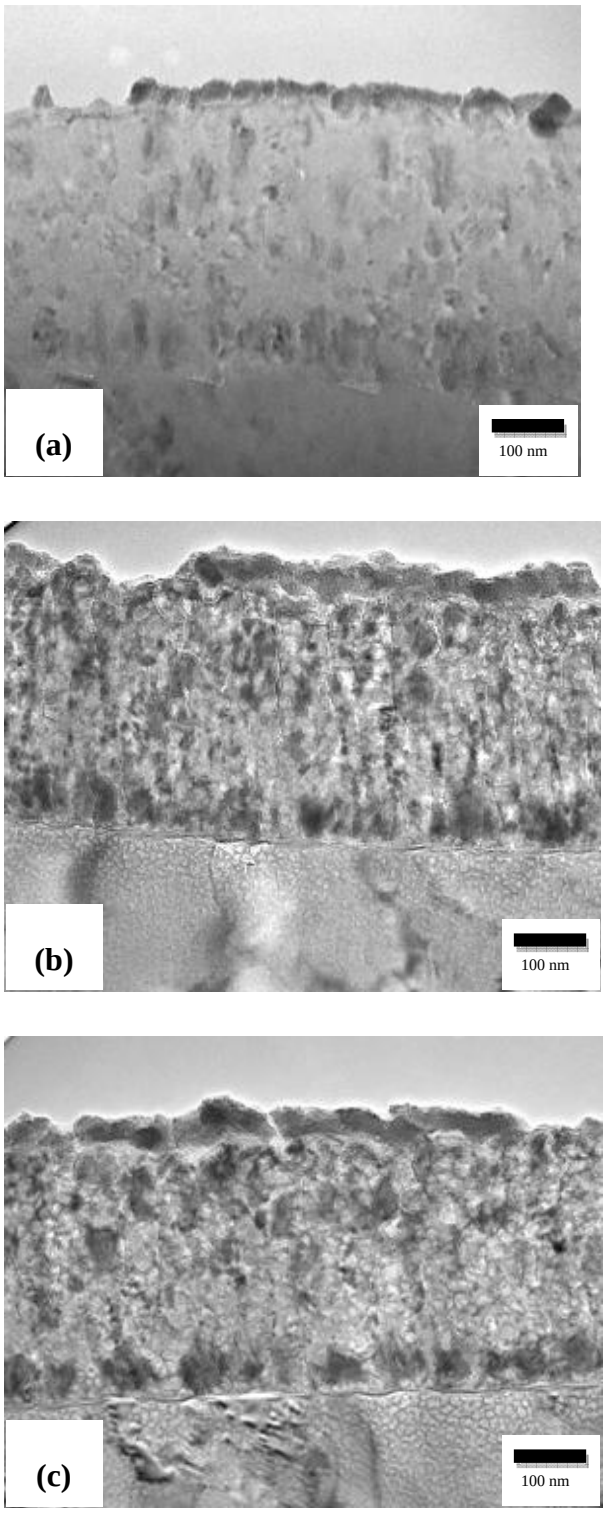

Figure 5.23 Transmission electron micrographs of ultramicrotomed sections of Al-10at.%Cu alloy following sputter deposition and conversion treatment in zirconium-based conversion bath for (a) 30 s, (b) 60 s and (c) 180 s.

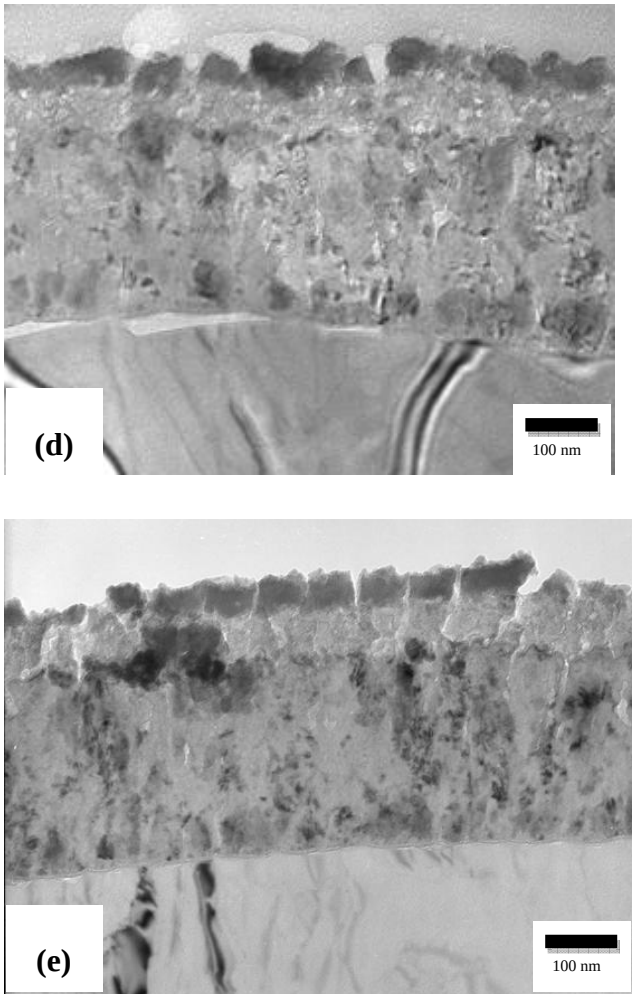

Figure 5.23 Transmission electron micrographs of ultramicrotomed sections of Al-10at.%Cu alloy following sputter deposition and conversion treatment in zirconium-based conversion bath for (d) 300 s and (e) 600 s.

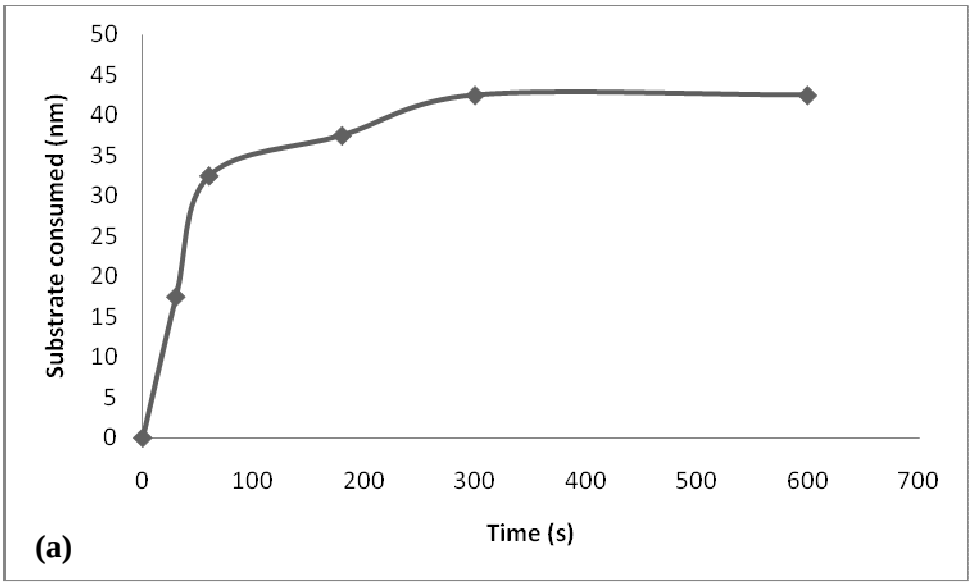

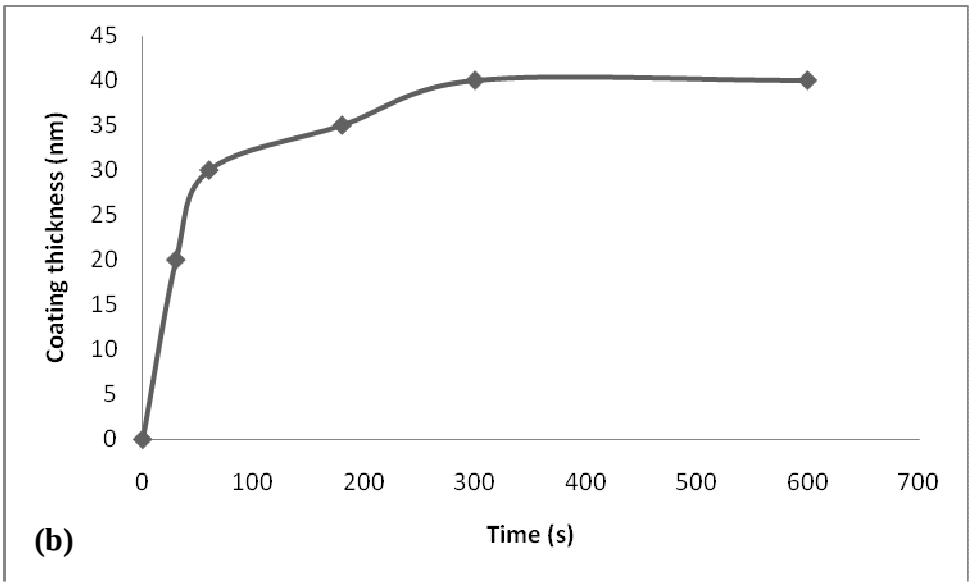

Figure 5.24 Loss of substrate thickness (a) and thickness of conversion coatings (b), determined from transmission electron micrographs for the Al-10at.%Cu alloy after zirconium-based conversion treatments.

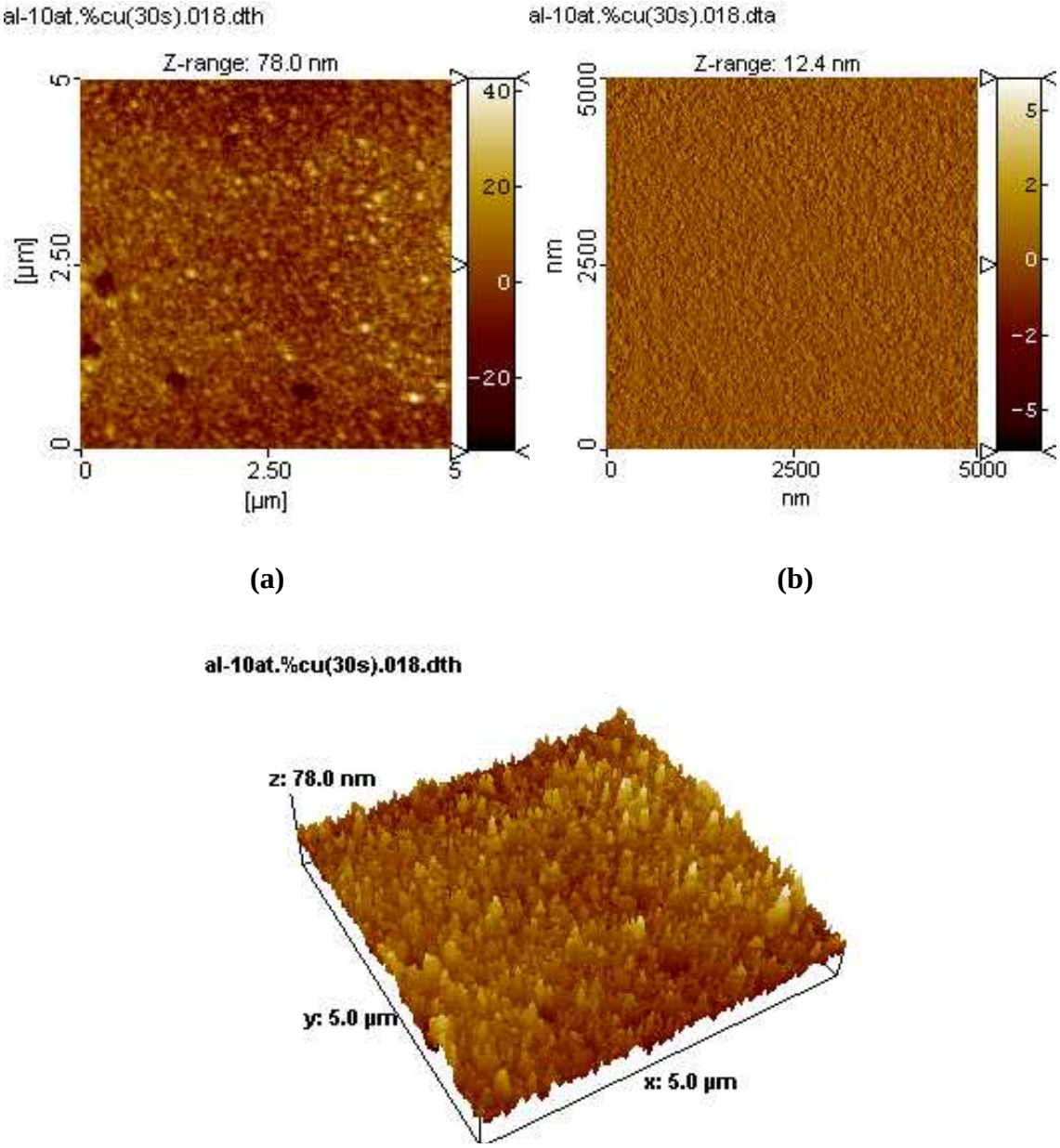

Figure 5.25 AFM images of the coating development on the Al-10at.%Cu alloy surface after immersion for 30 s; (a) height image; (b) 2-dimensional image; (c) 3-dimensional topographic image.

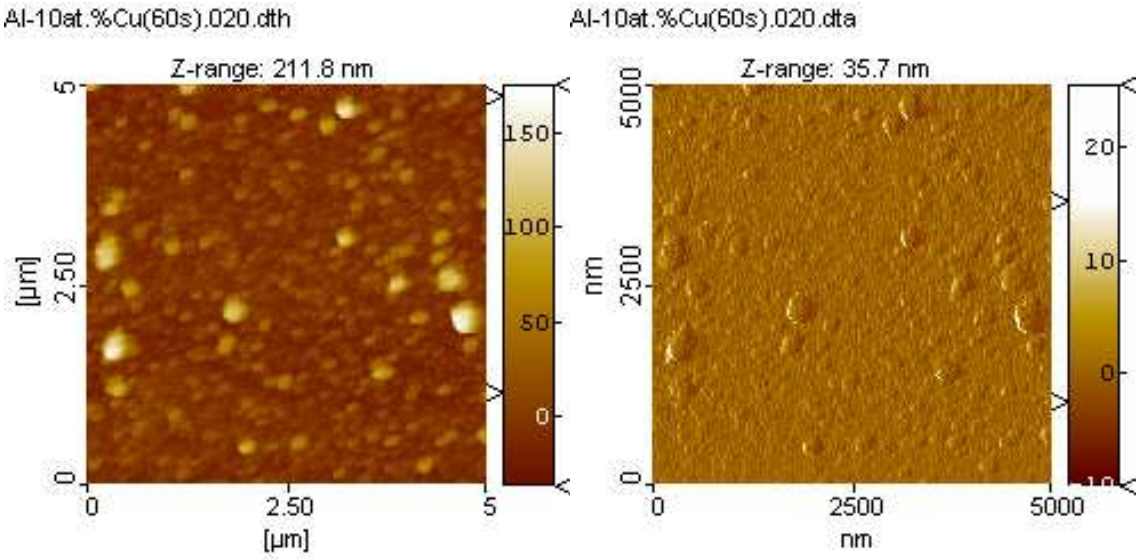

(a) **(b)**

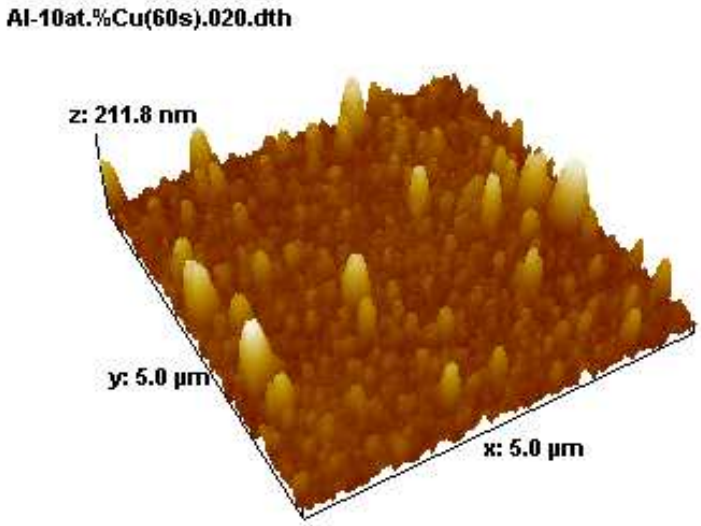

(c)

Figure 5.26 AFM images of the coating development on the Al-10at.%Cu surface alloy after immersion for 60 s; (a) height image; (b) 2-dimensional image; (c) 3-dimensional topographic image.

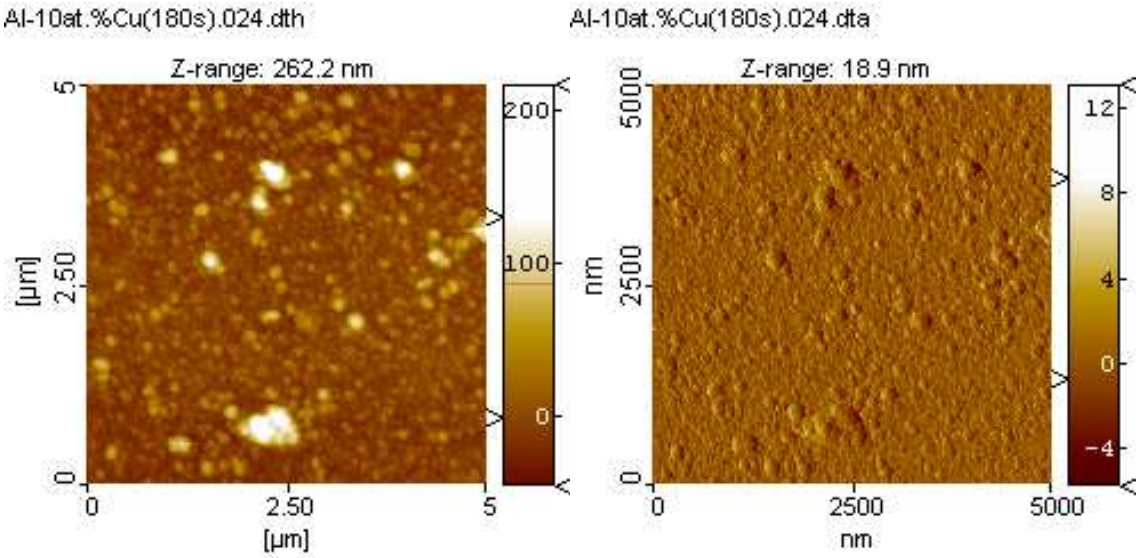

(a) **(b)**

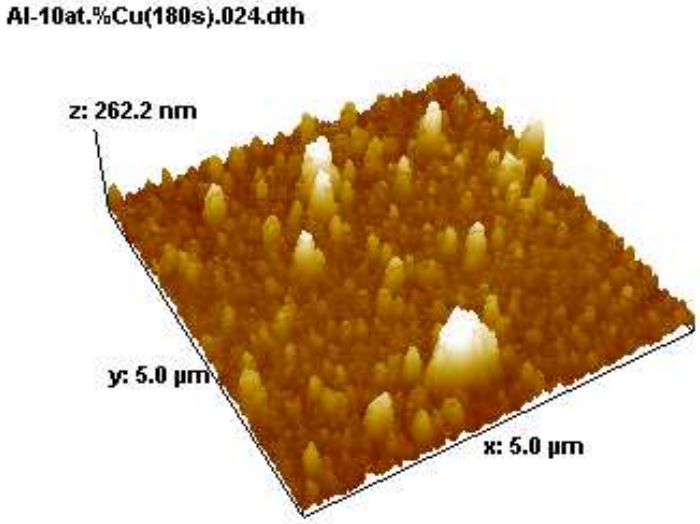

(c)

Figure 5.27 AFM images of the coating development on the Al-10at.%Cu alloy surface after immersion for 180 s; (a) height image; (b) 2-dimensional image; (c) 3-dimensional topographic image.

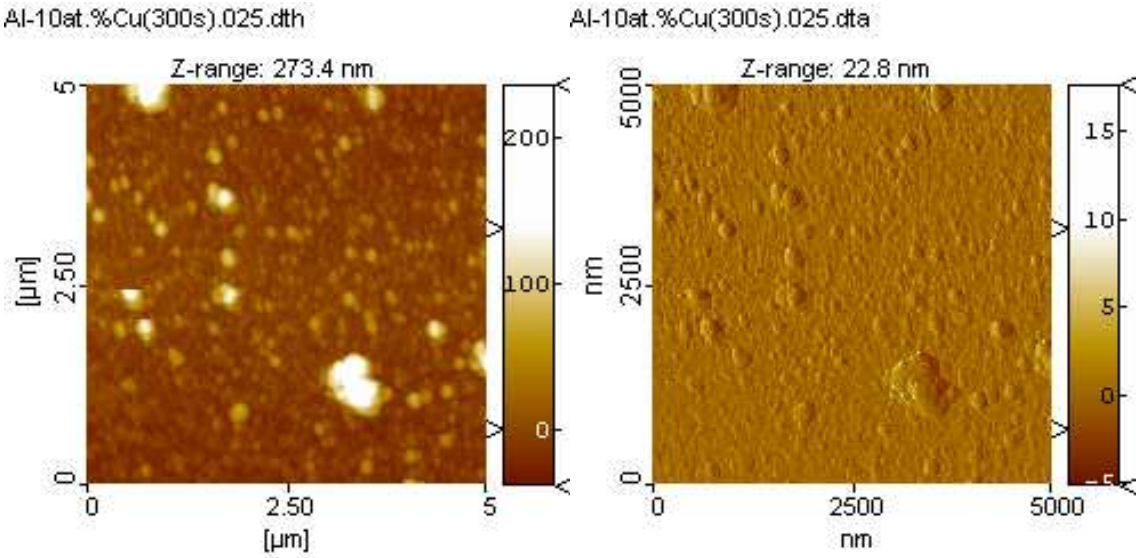

(a) **(b)**

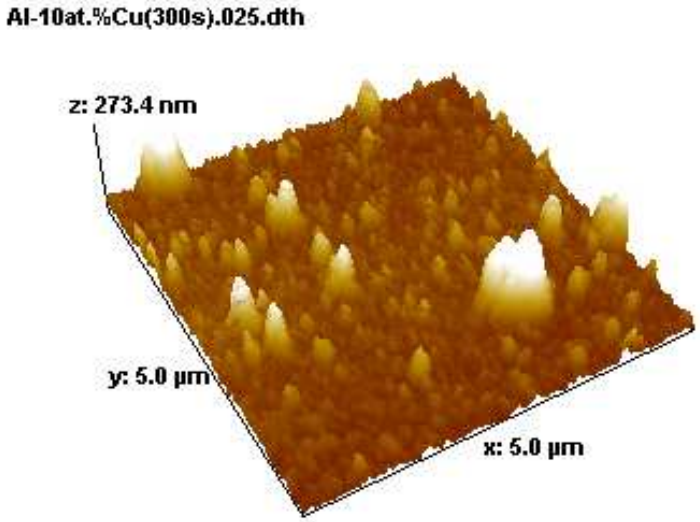

(c)

Figure 5.28 AFM images of the coating development on the Al-10at.%Cu alloy surface after immersion for 300 s; (a) height image; (b) 2-dimensional image; (c) 3-dimensional topographic image.

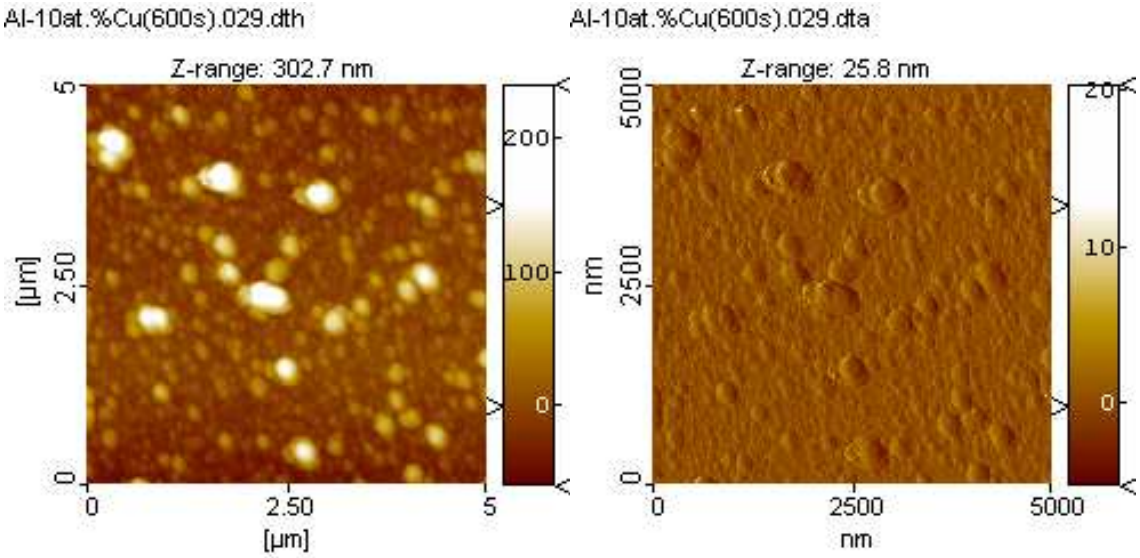

(a) **(b)**

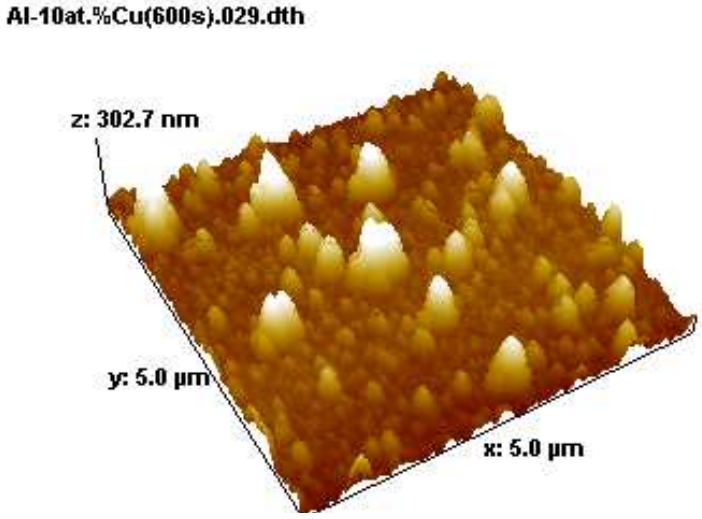

(c)

Figure 5.29 AFM images of the coating development on the Al-10at.%Cu alloy surface after immersion for 600 s; (a) height image; (b) 2-dimensional image; (c) 3-dimensional topographic image.

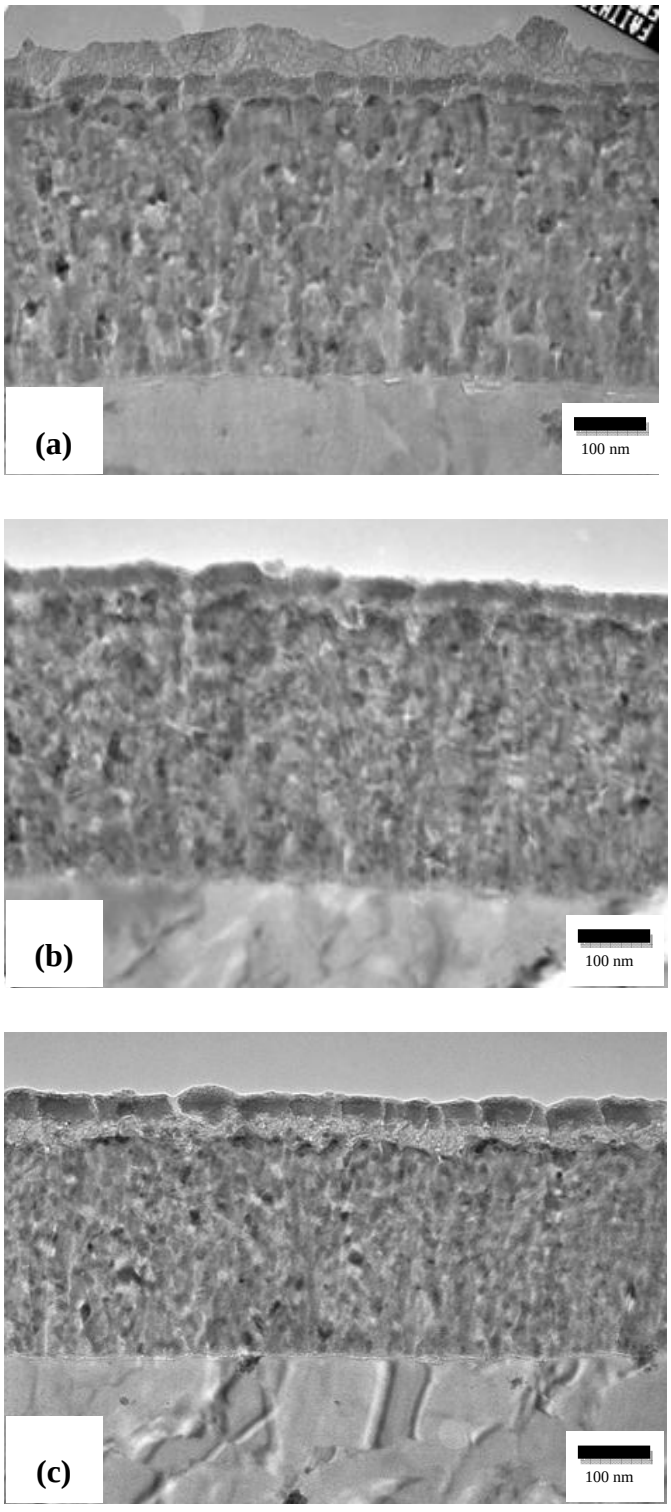

Figure 5.30 Transmission electron micrographs of ultramicrotomed sections of Al-30at.%Cu alloy following sputter deposition and conversion treatment in zirconium-based conversion bath for (a) 30 s, (b) 60 s, and (c) 180 s.

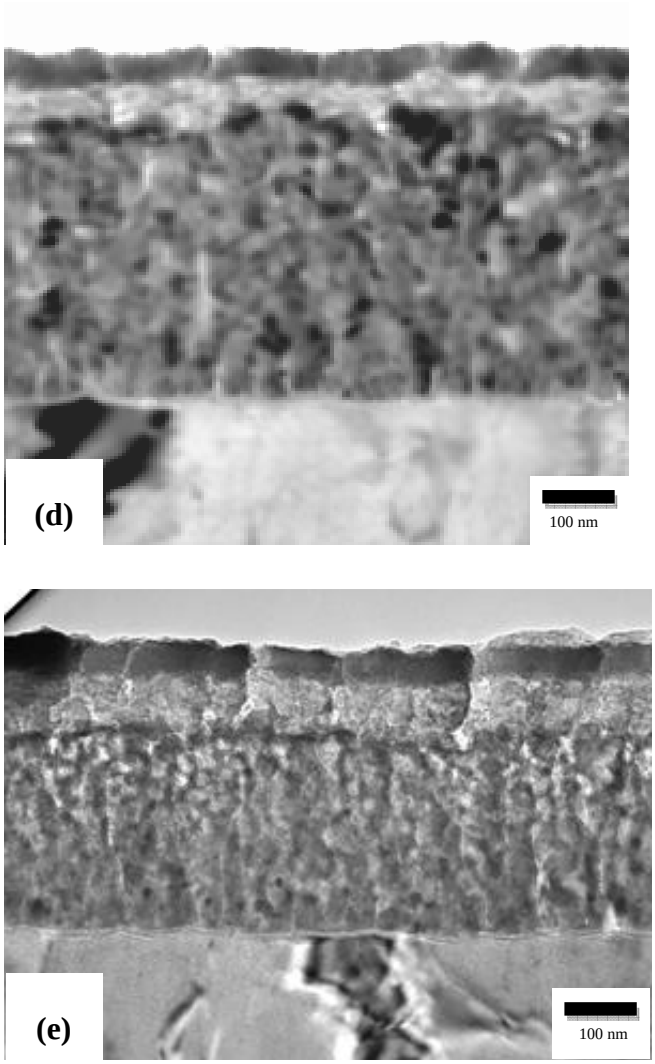

Figure 5.30 Transmission electron micrographs of ultramicrotomed sections of Al-30at.%Cu alloy following sputter deposition and conversion treatment in zirconium-based conversion bath for (d) 300 s and (e) 600 s.

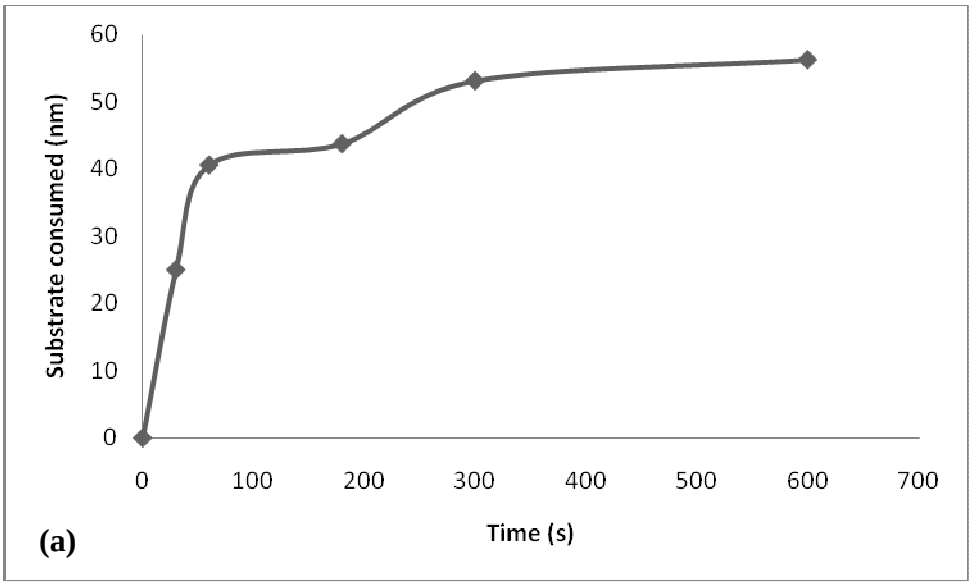

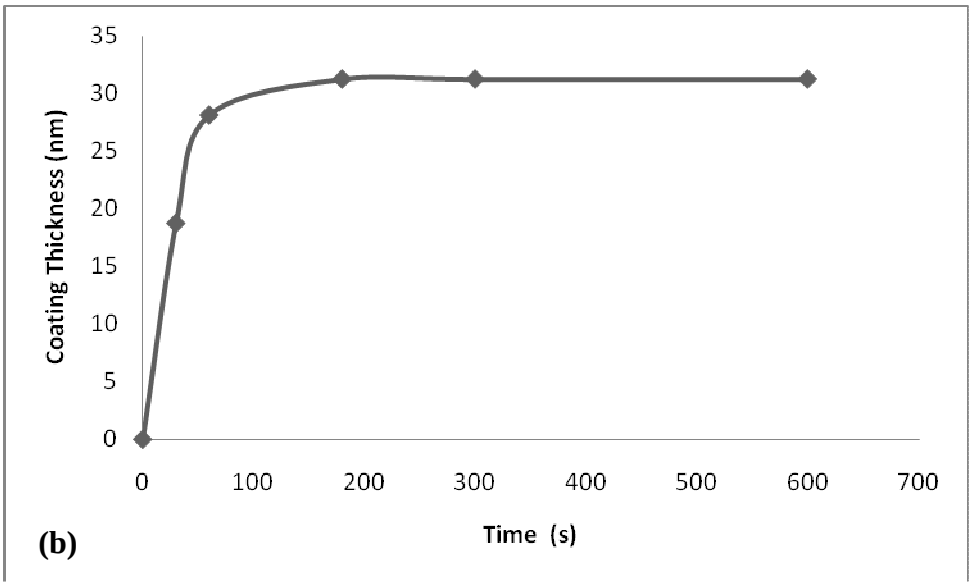

Figure 5.31 Loss of substrate thickness (a) and thickness of conversion coatings (b), determined from transmission electron micrographs for the Al-30at.%Cu alloy after zirconium-based conversion treatments.

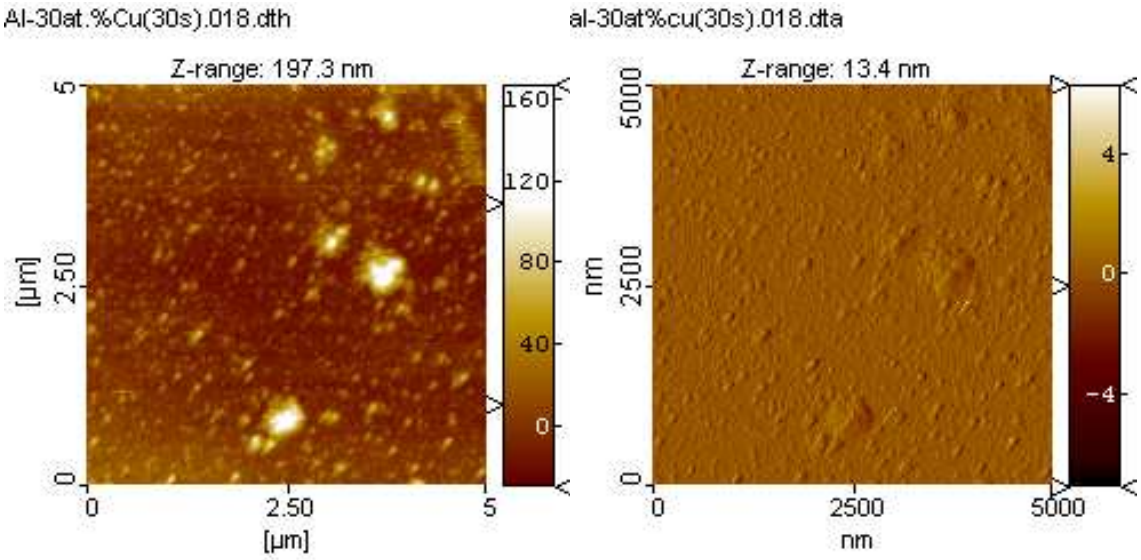

(a) **(b)**

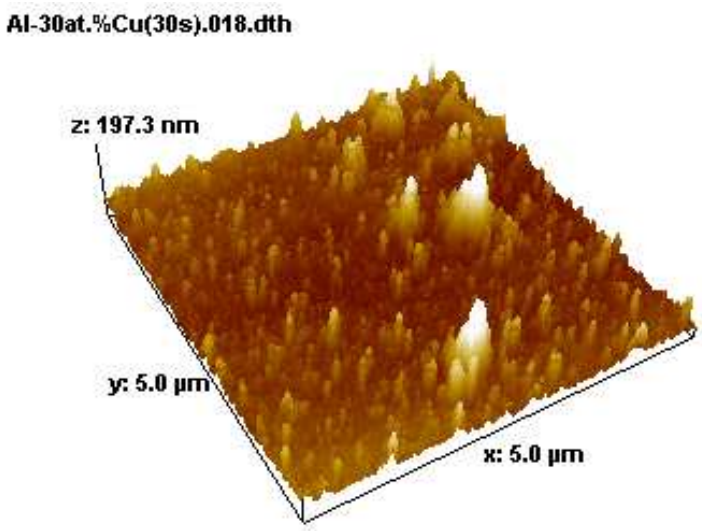

(c)

Figure 5.32 AFM images of the coating development on the Al-30at.%Cu alloy surface after immersion for 30 s; (a) height image; (b) 2-dimensional image; (c) 3-dimensional topographic image.

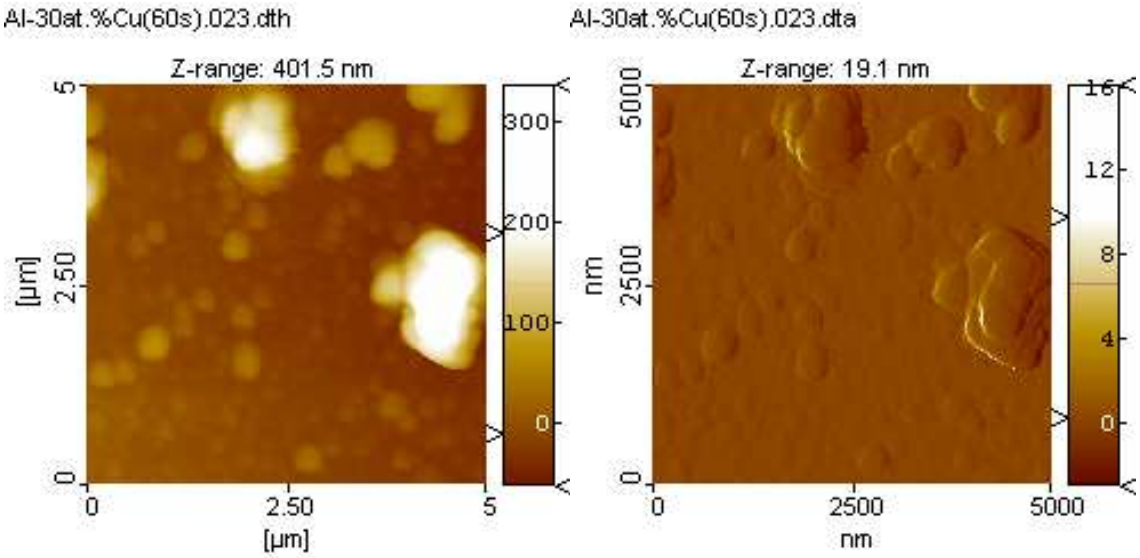

(a) **(b)**

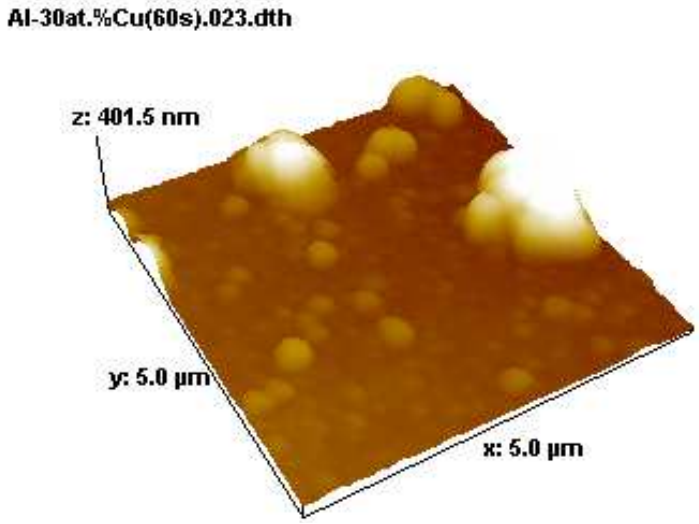

(c)

Figure 5.33 AFM images of the coating development on the Al-30at.%Cu alloy surface after immersion for 60 s; (a) height image; (b) 2-dimensional image; (c) 3-dimensional topographic image.

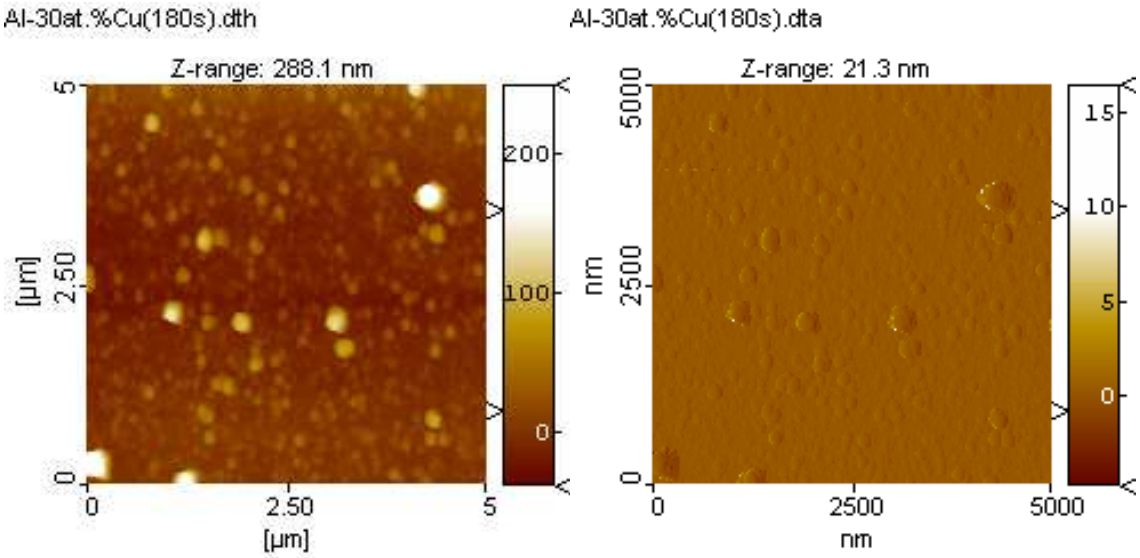

(a) **(b)**

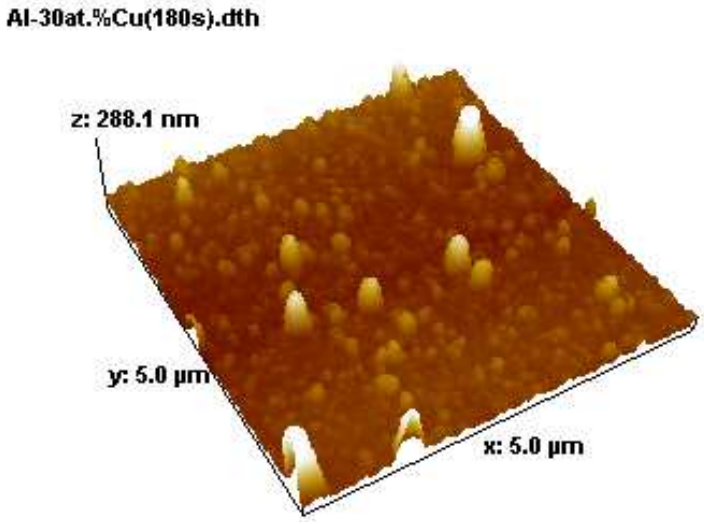

(c)

Figure 5.34 AFM images of the coating development on the Al-30at.%Cu alloy surface after immersion for 180 s; (a) height image; (b) 2-dimensional image; (c) 3-dimensional topographic image.

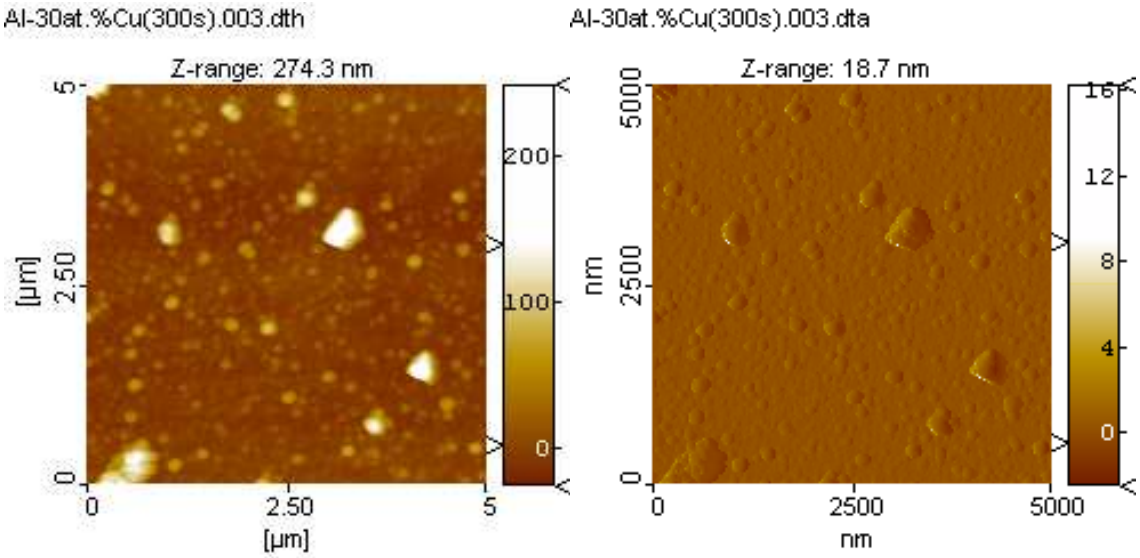

(a) **(b)**

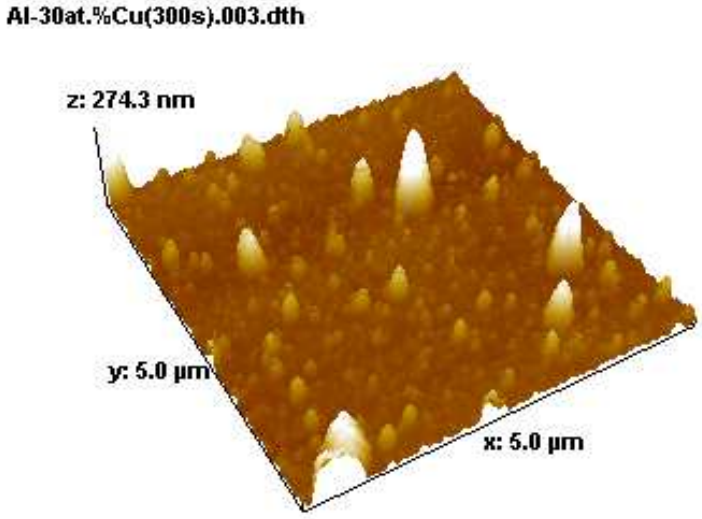

(c)

Figure 5.35 AFM images of the coating development on the Al-30at.%Cu alloy surface after immersion for 300 s; (a) height image; (b) 2-dimensional image; (c) 3-dimensional topographic image.

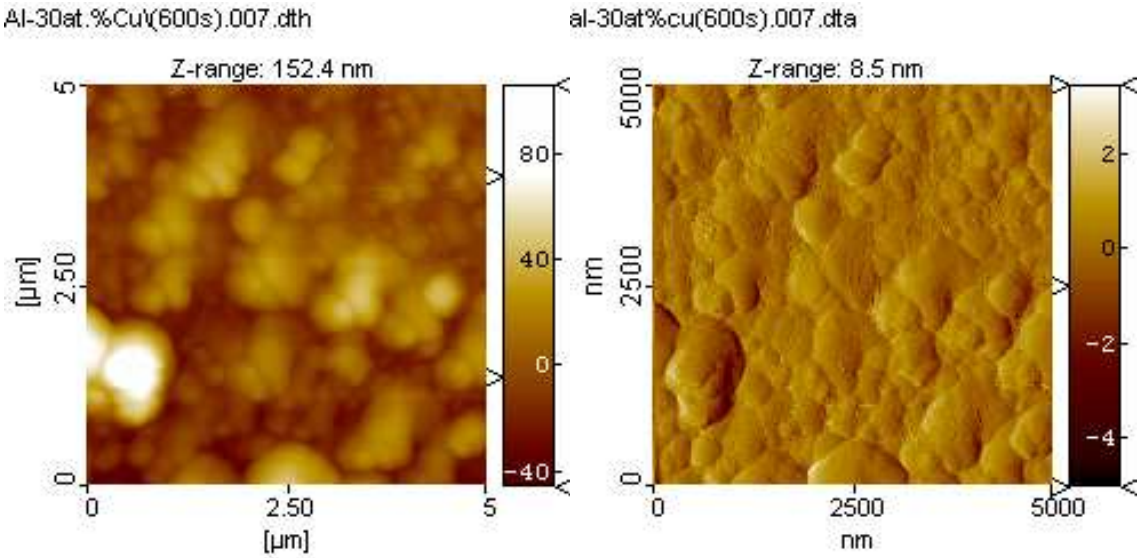

(a) **(b)**

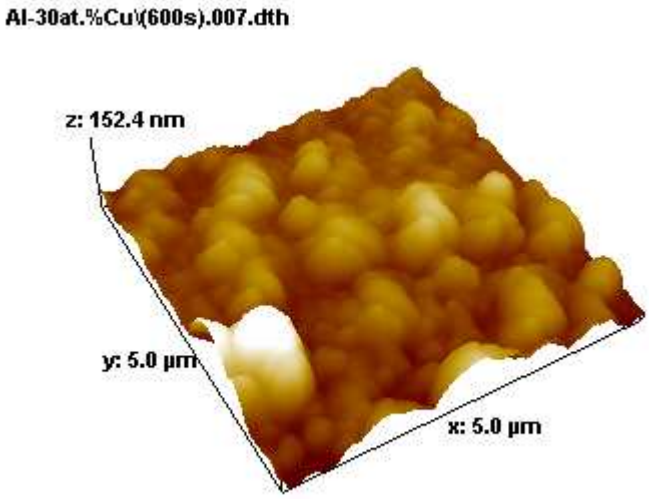

(c)

Figure 5.36 AFM images of the coating development on the Al-30at.%Cu alloy surface after immersion for 600 s; (a) height image; (b) 2-dimensional image; (c) 3-dimensional topographic image.

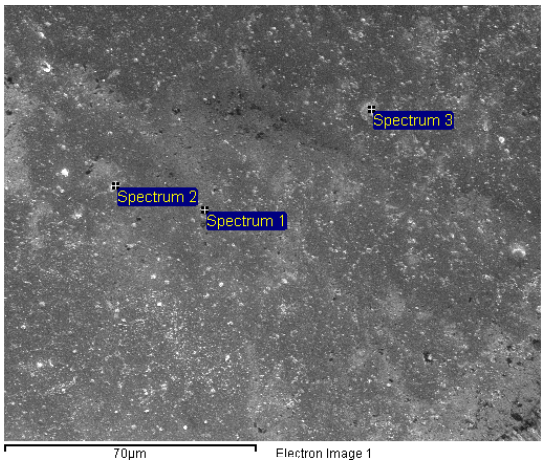

(a)

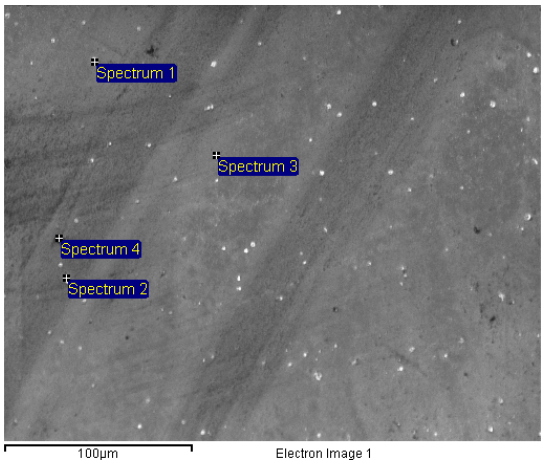

(b)

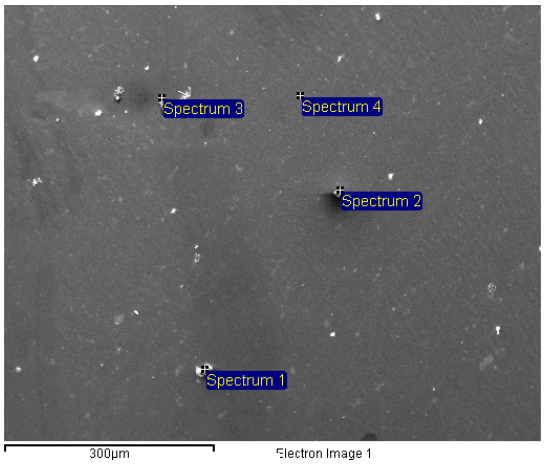

(c)

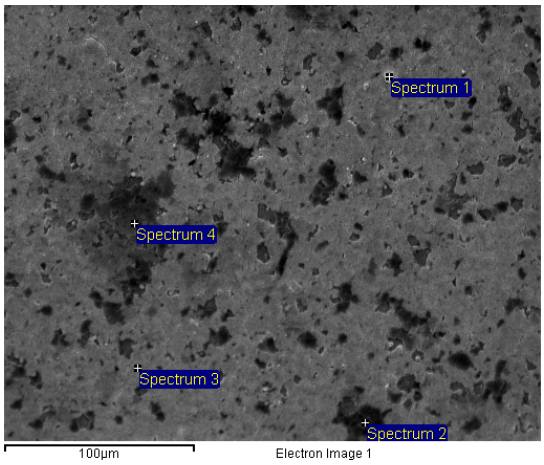

(d)

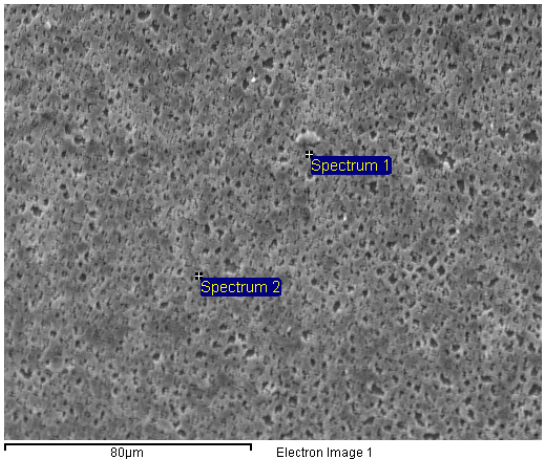

(e)

Figure 5.37 Scanning electron micrographs of superpure aluminium after (a) 30 s (b) 60 s (c) 180 s (d) 300 s and (e) 600 s immersion in the zirconium-based conversion bath.

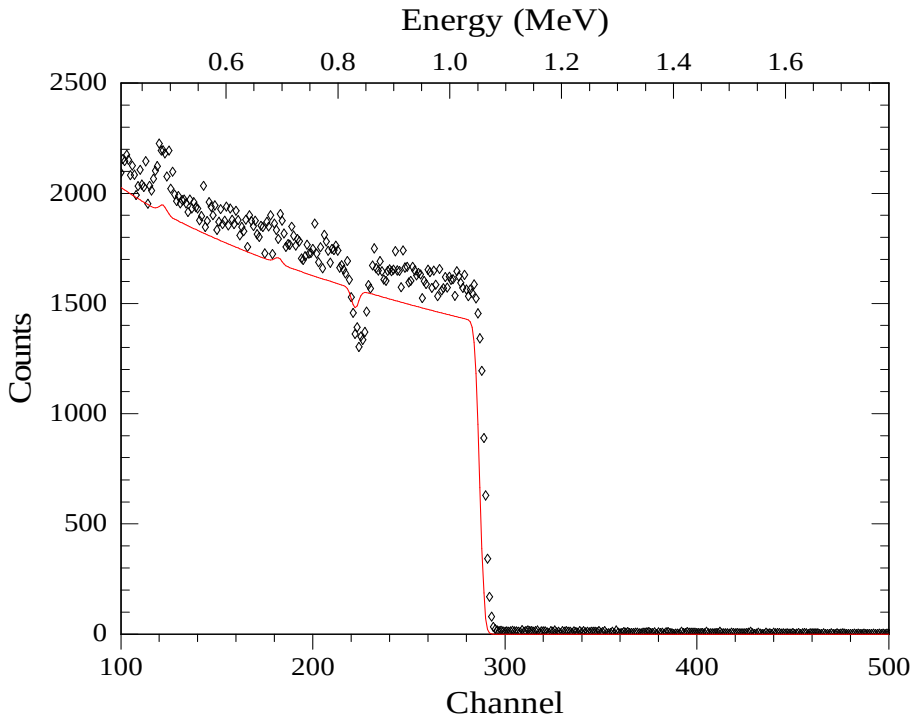

(a)

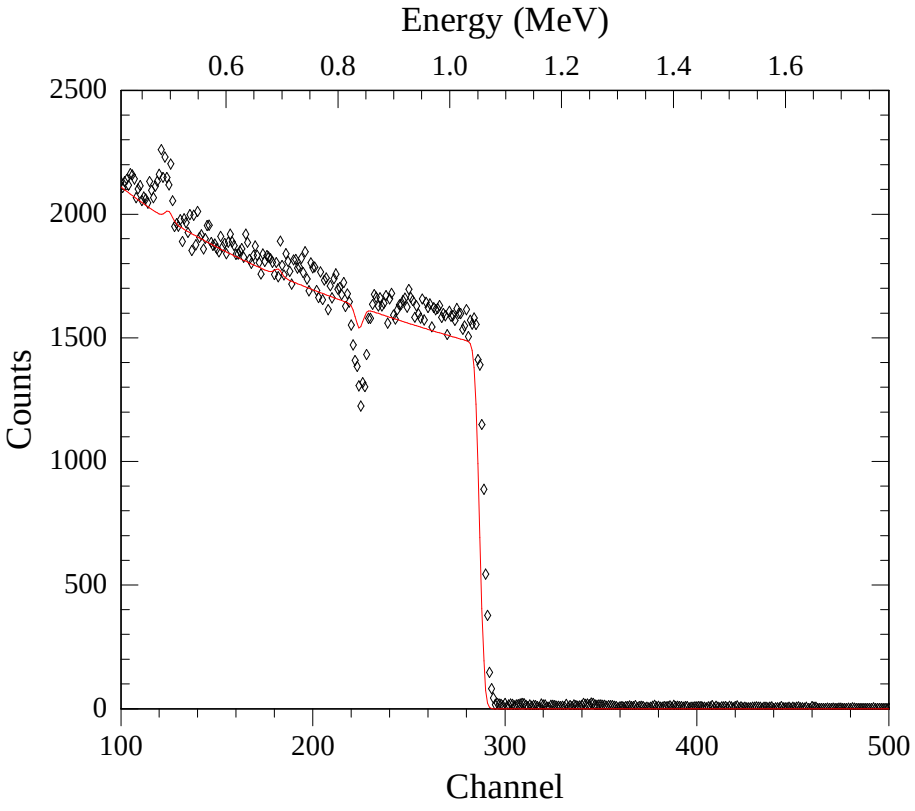

(b)

Figure 5.38 The RBS spectra of superpure aluminium after (a) 0 s and (b) 30 s immersion in Zr-based conversion coating bath.

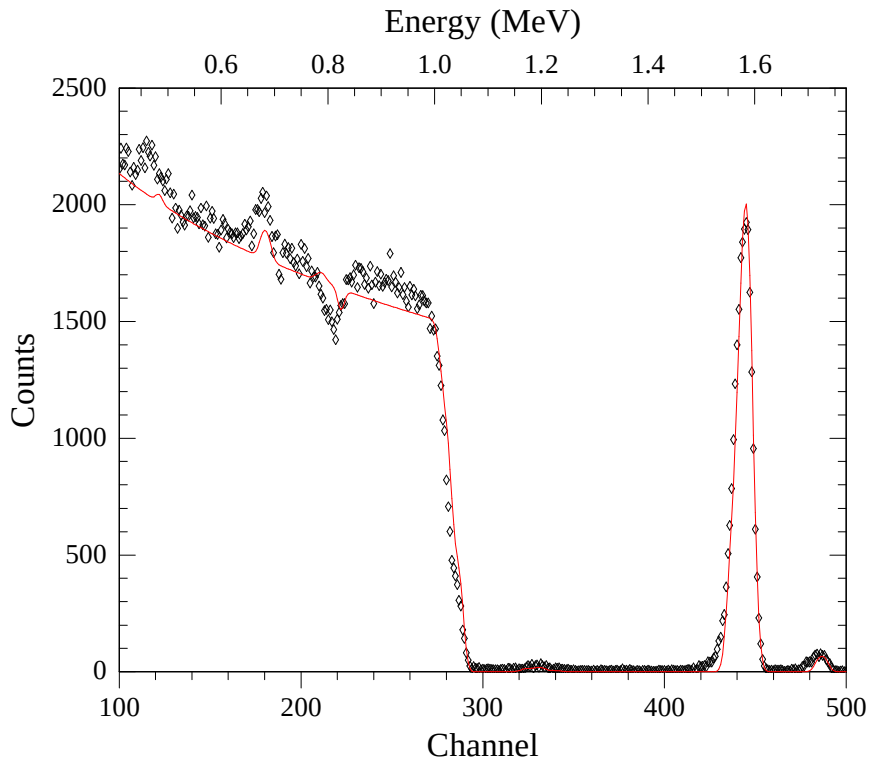

(c)

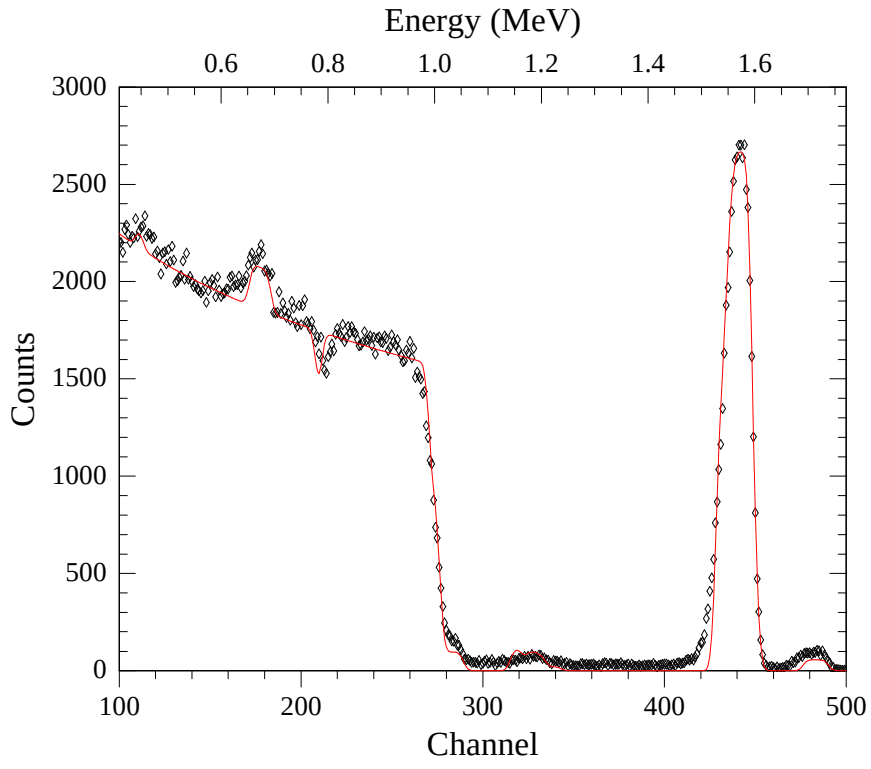

(d)

Figure 5.38 The RBS spectra of superpure aluminium after (c) 60 s and (d) 180 s immersion in Zr-based conversion coating bath.

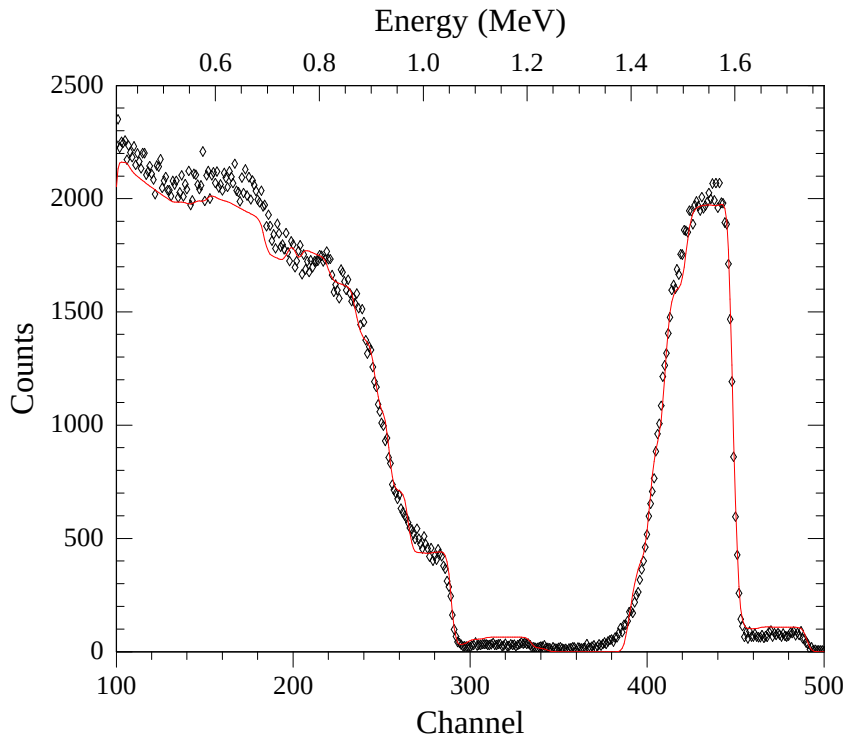

(e)

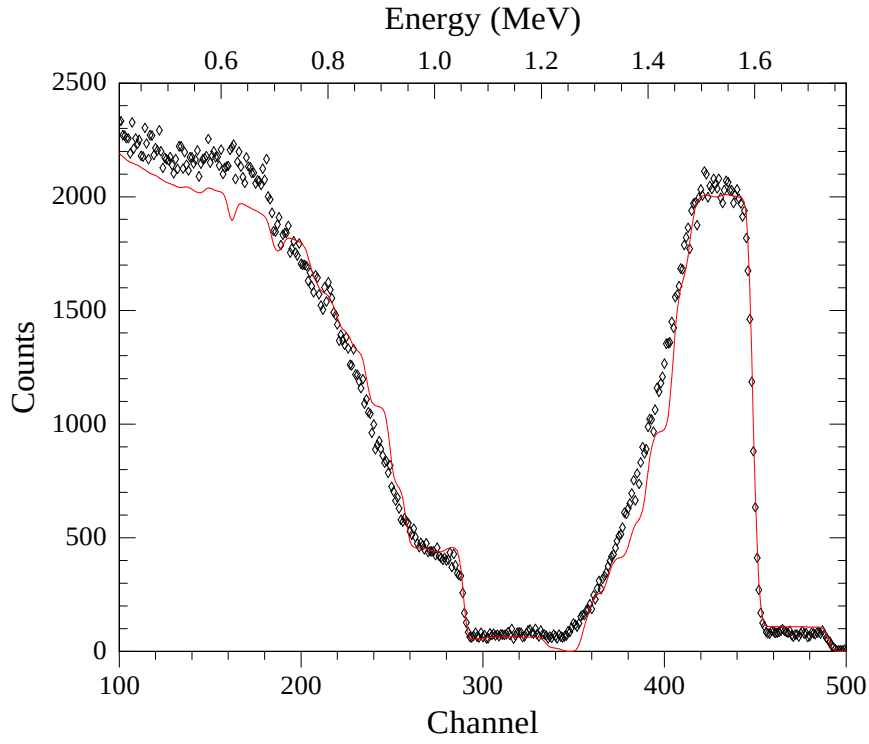

(f)

Figure 5.38 The RBS spectra of superpure aluminium after (e) 300 s and (f) 600 s immersion in Zr-based conversion coating bath.

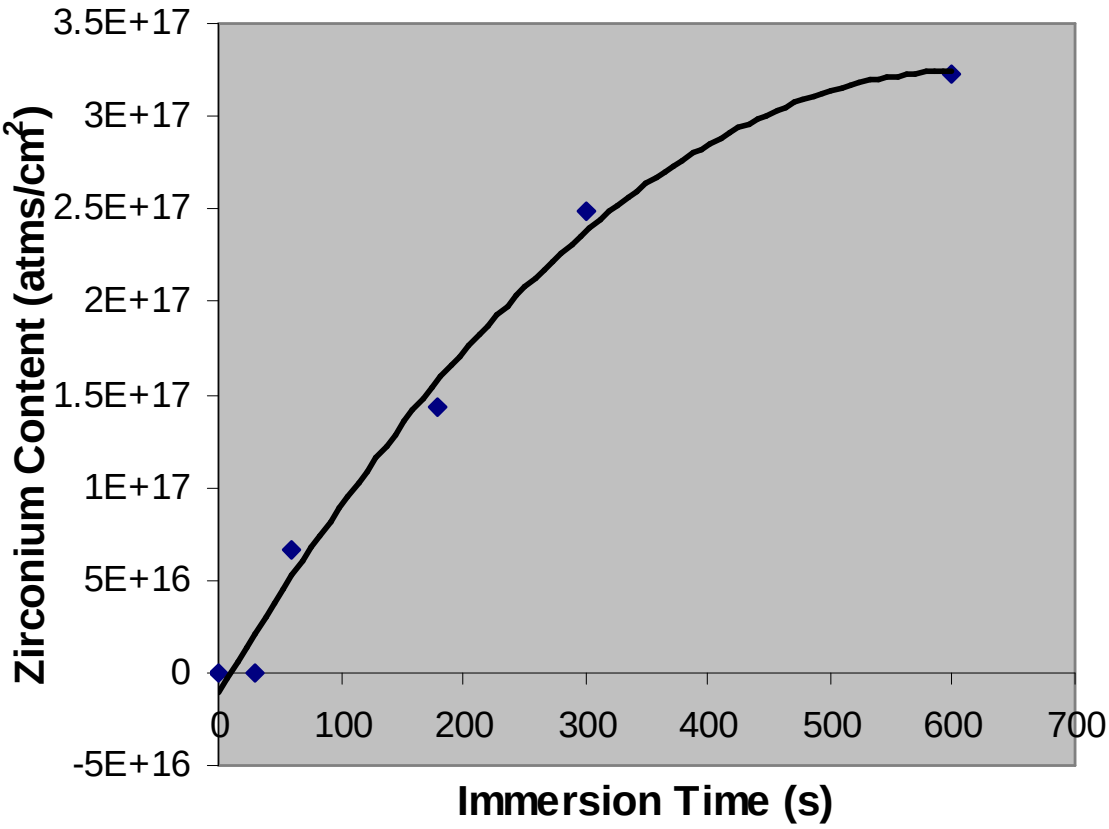

Figure 5.38 (g) Zirconium atoms in the coatings formed after immersion in zirconium bath.

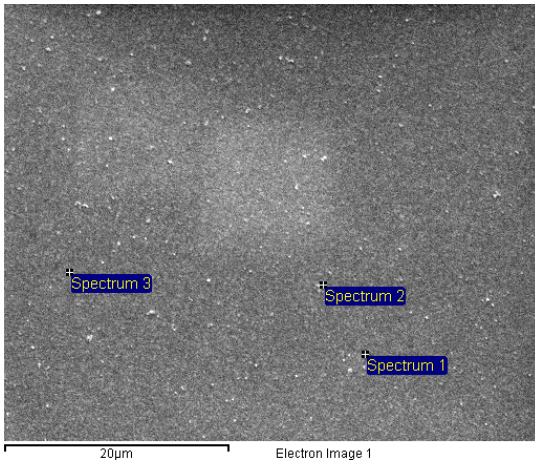

(a)

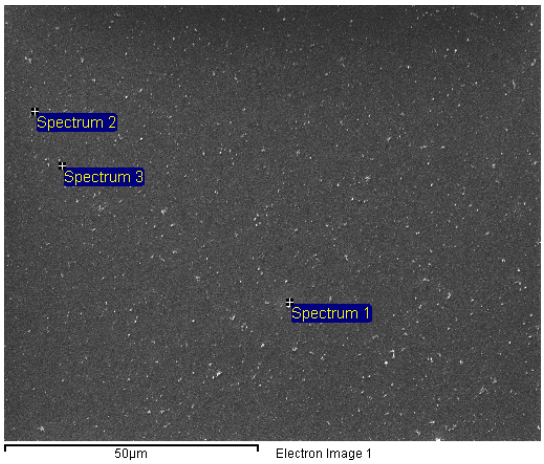

(b)

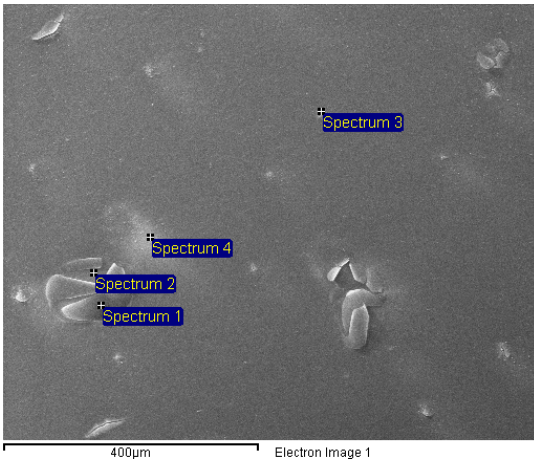

(c)

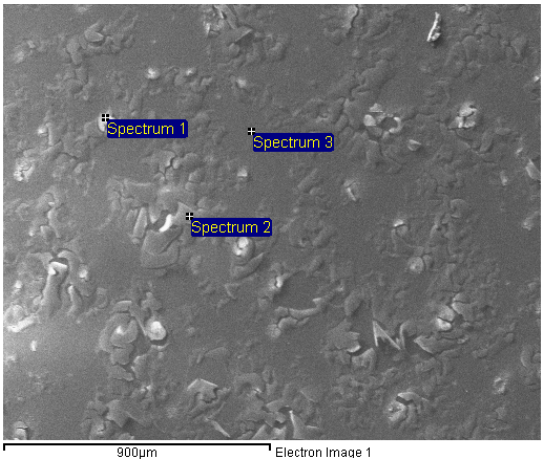

(d)

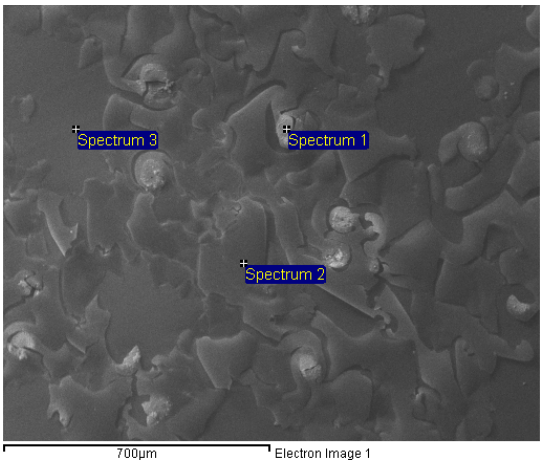

(e)

Figure 5.39 Scanning electron micrographs of Al-1.0at.%Cu alloy after (a) 30 s, (b) 60s, (c) 180 s, (d) 300 s and (e) 600 s immersion in the zirconium-based conversion bath.

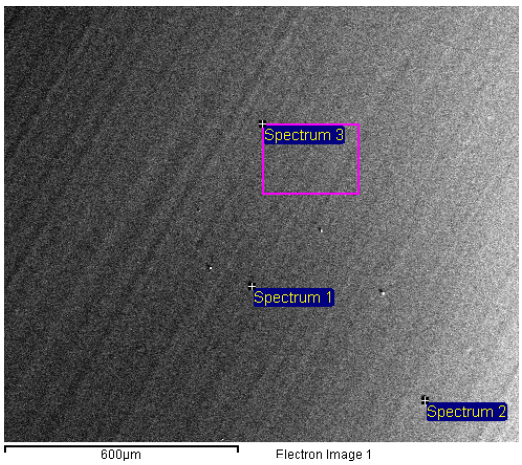

(a)

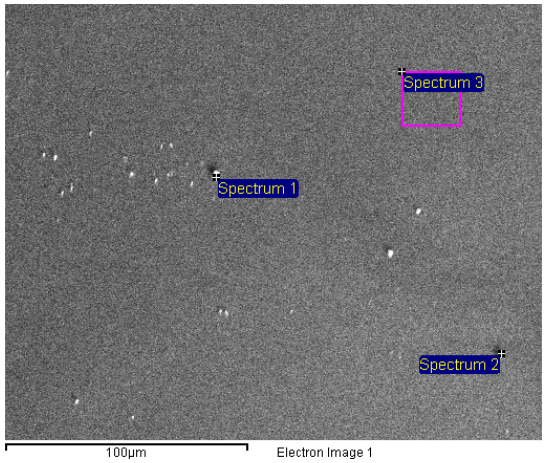

(b)

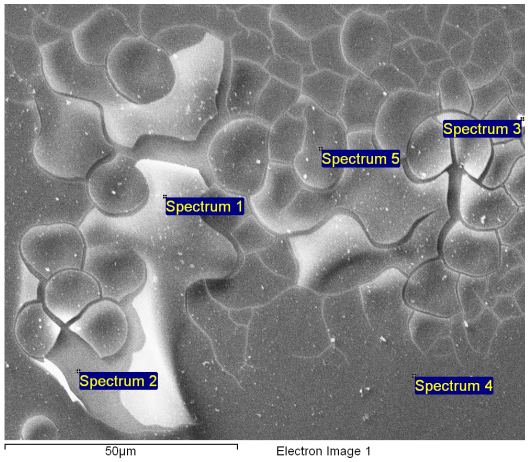

(c)

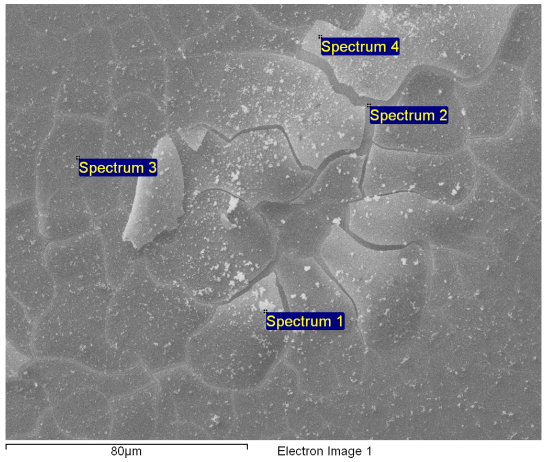

(d)

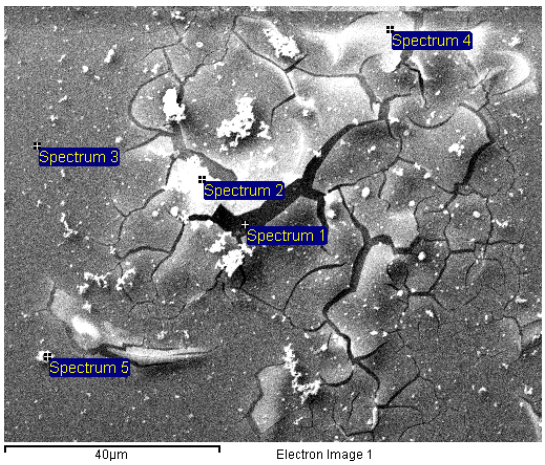

(e)

Figure 5.40 Scanning electron micrographs of Al-5.0at.%Cu alloy after (a) 30 s (b) 60 s (c) 180 s (d) 300 s and (e) 600 s immersion in the zirconium-based conversion bath.

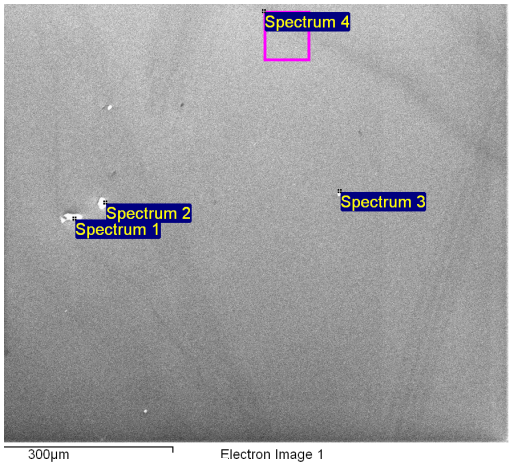

(a)

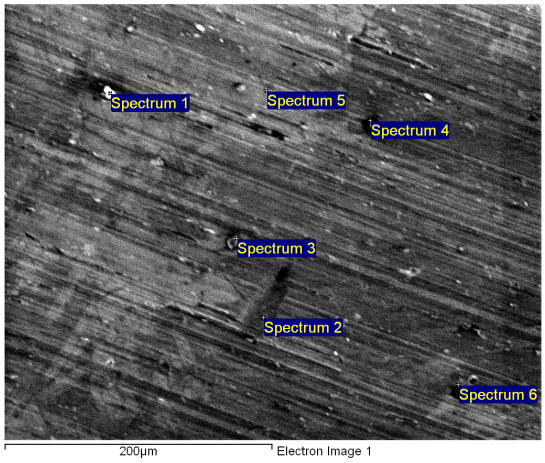

(b)

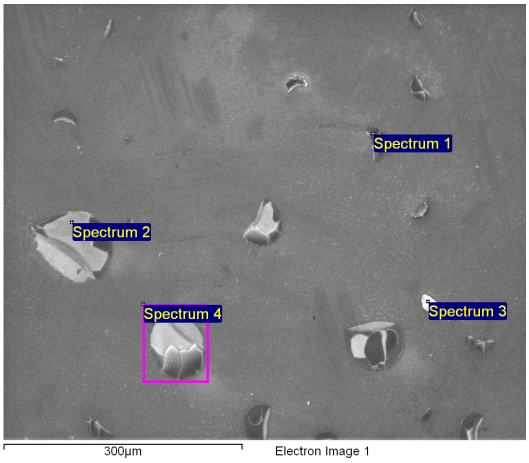

(c)

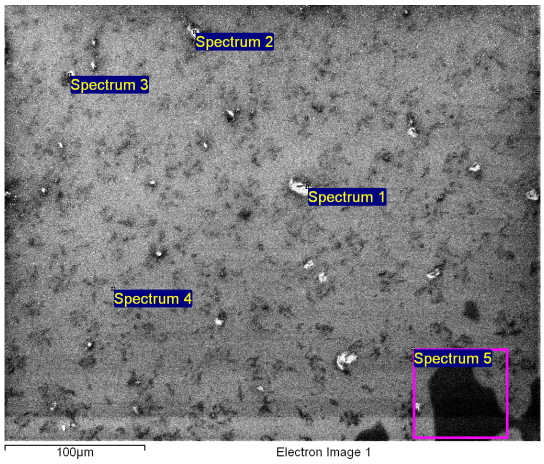

(d)

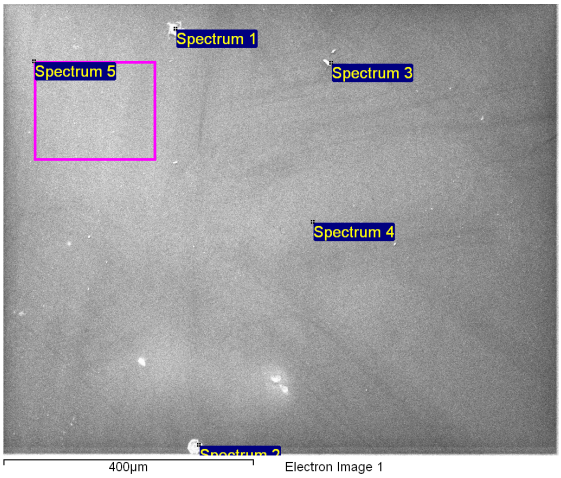

(e)

Figure 5.41 Scanning electron micrographs of Al-10at.%Cu alloy after (a) 30 s (b) 60 s (c) 180 s (d) 300 s and (e) 600 s immersion in the zirconium-based conversion bath.

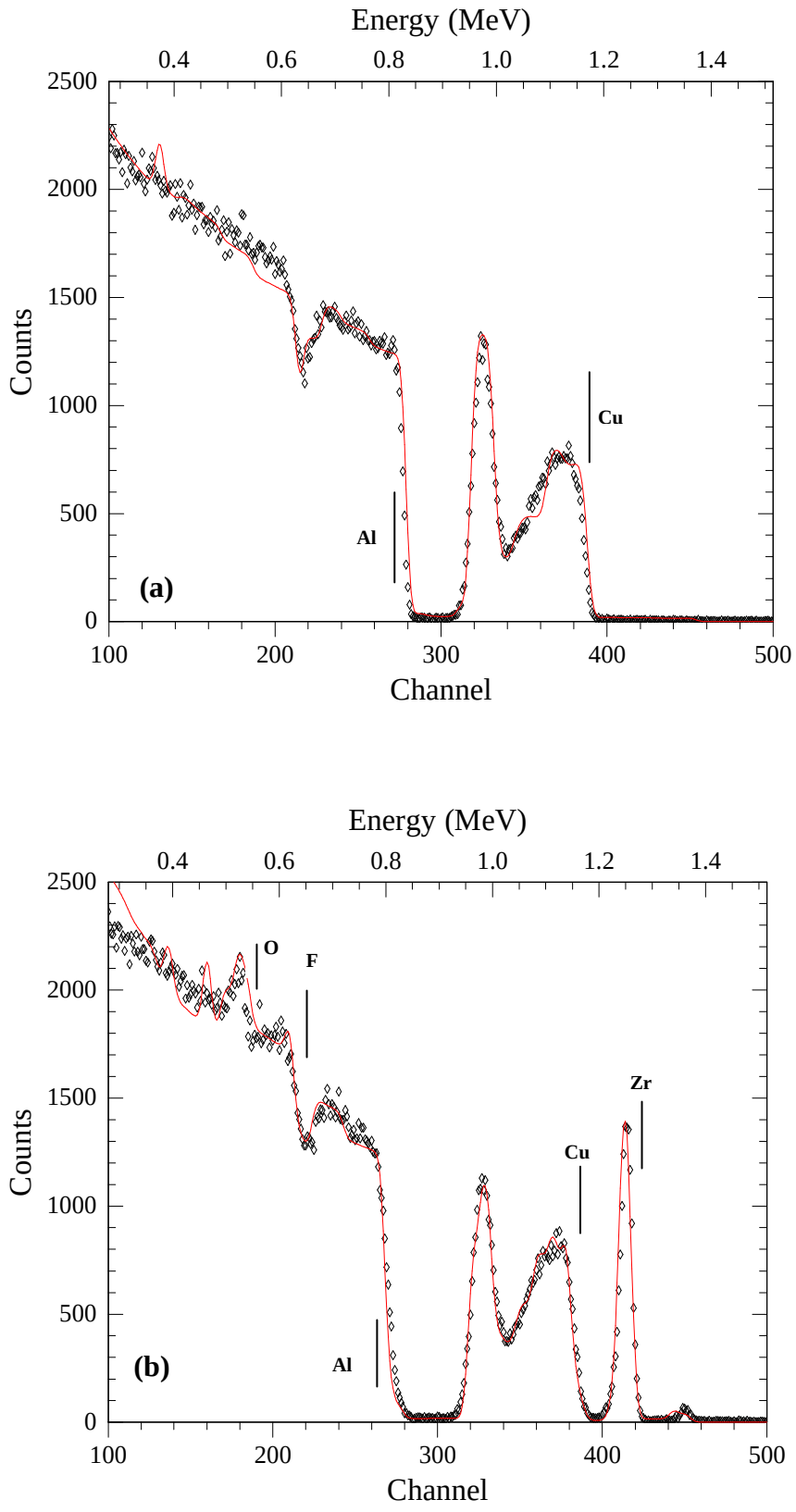

Figure 5.42 RBS Spectra of Al-10at.%Cu alloy after (a) 0 s and (b) 30 s immersion in zirconium-based conversion coating bath. The bars indicate energies corresponding to Al, Cu, Zr, F and O at the surface.

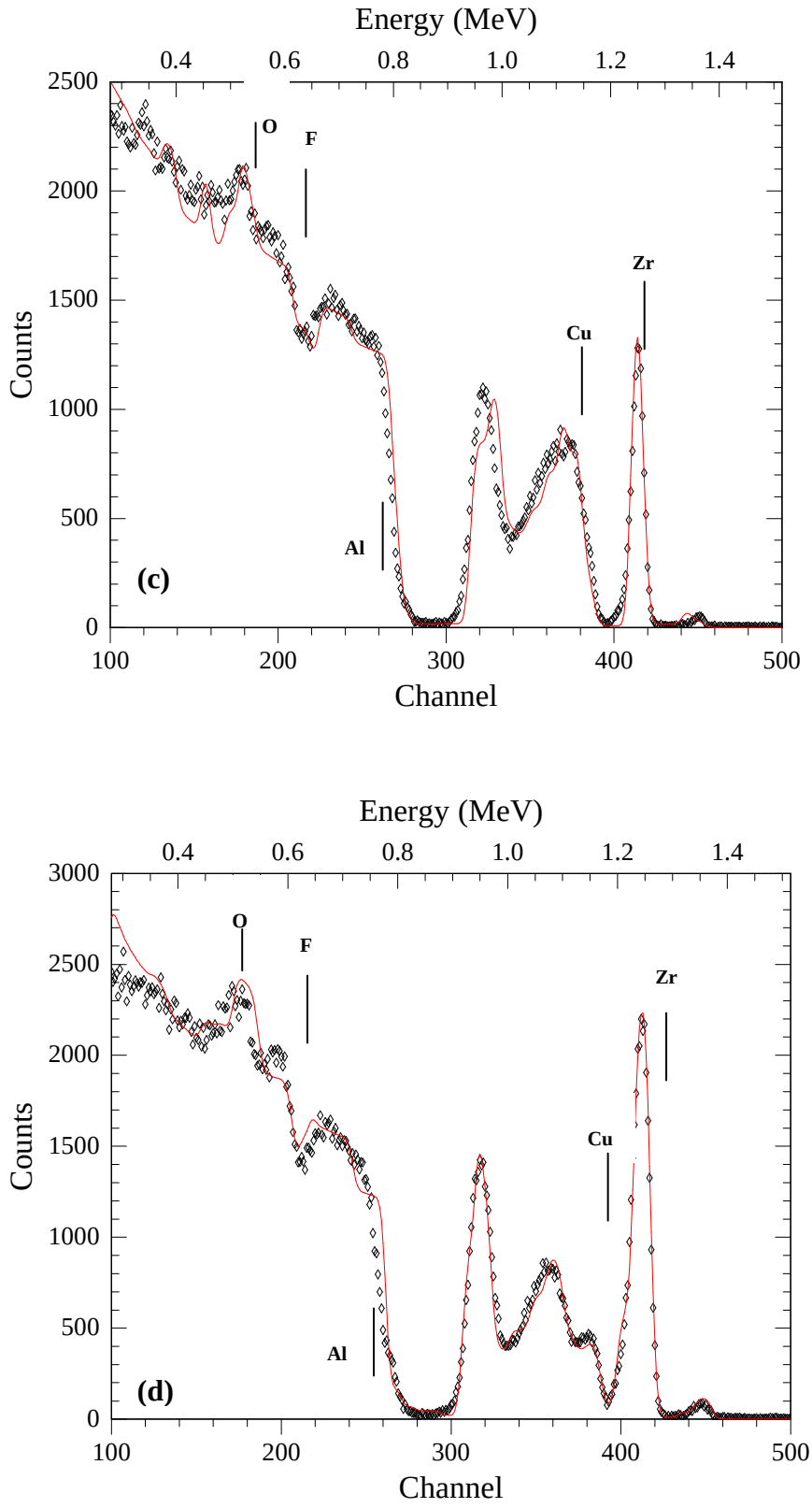

Figure 5.42 RBS Spectra of Al-10at.%Cu alloy after (c) 60 s (d) and 180 s immersion in zirconium-based conversion coating bath. The bars indicate energies corresponding to Al, Cu, Zr, F and O at the surface.

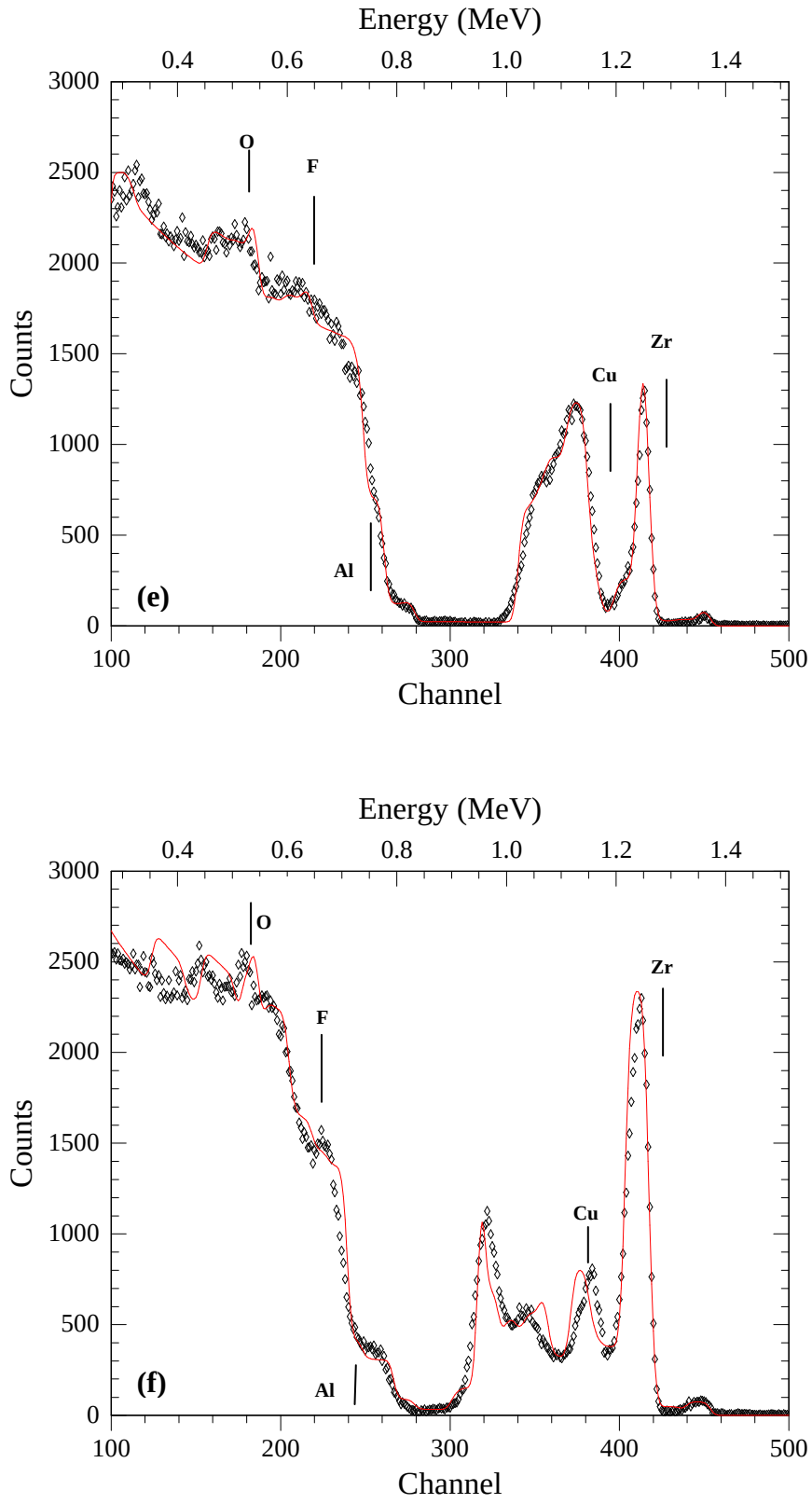

Figure 5.42 RBS Spectra of Al-10at.%Cu alloy after (e) 300 s and (f) 600 s immersion in zirconium-based conversion coating bath. The bars indicate energies corresponding to Al, Cu, Zr, F and O at the surface.

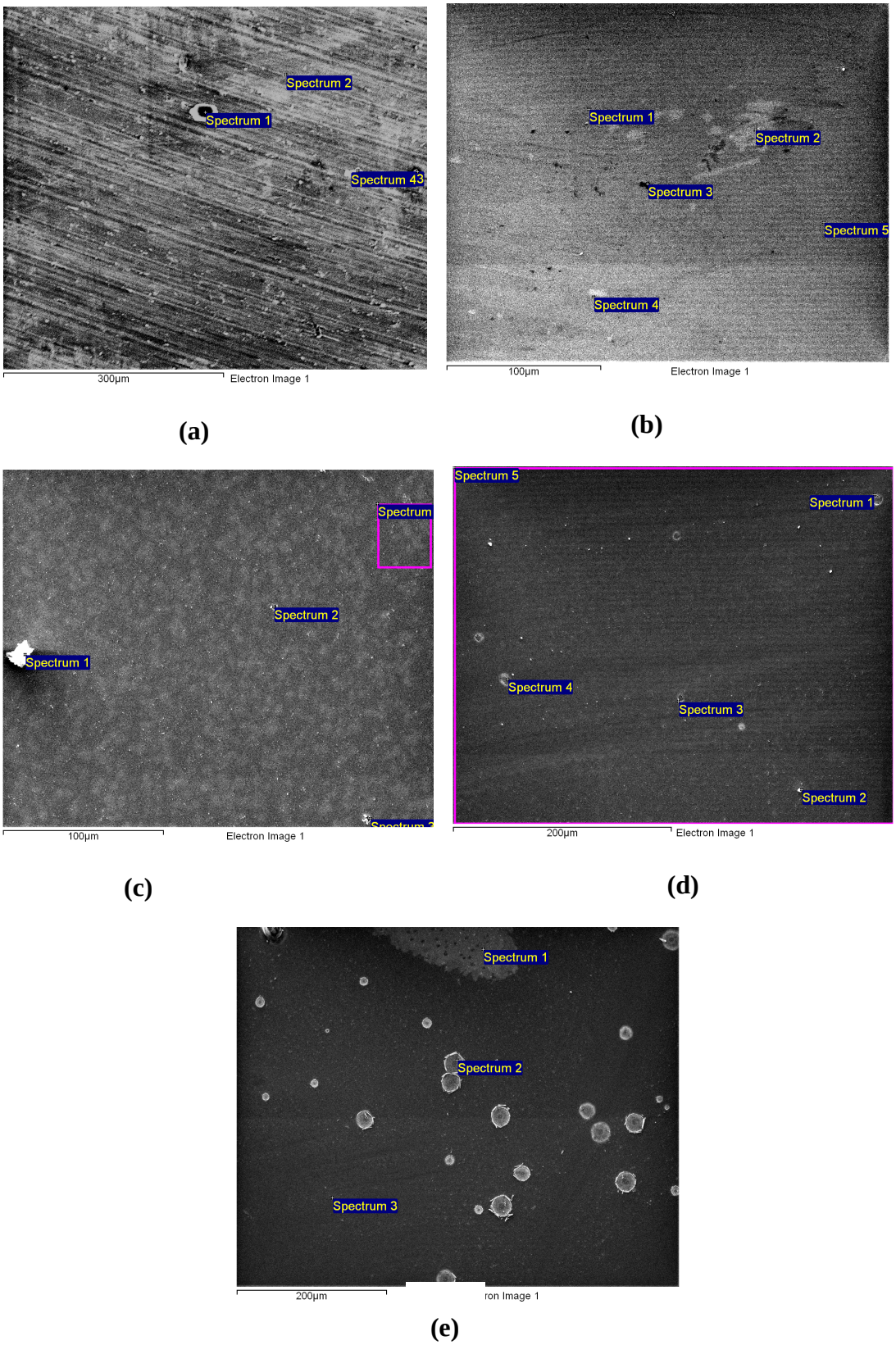

Figure 5.43 Scanning electron micrographs of Al-30at.%Cu alloy after (a) 30 s (b) 60 s (c) 180 s (d) 300 s and (e) 600 s immersion in the zirconium-based conversion bath.

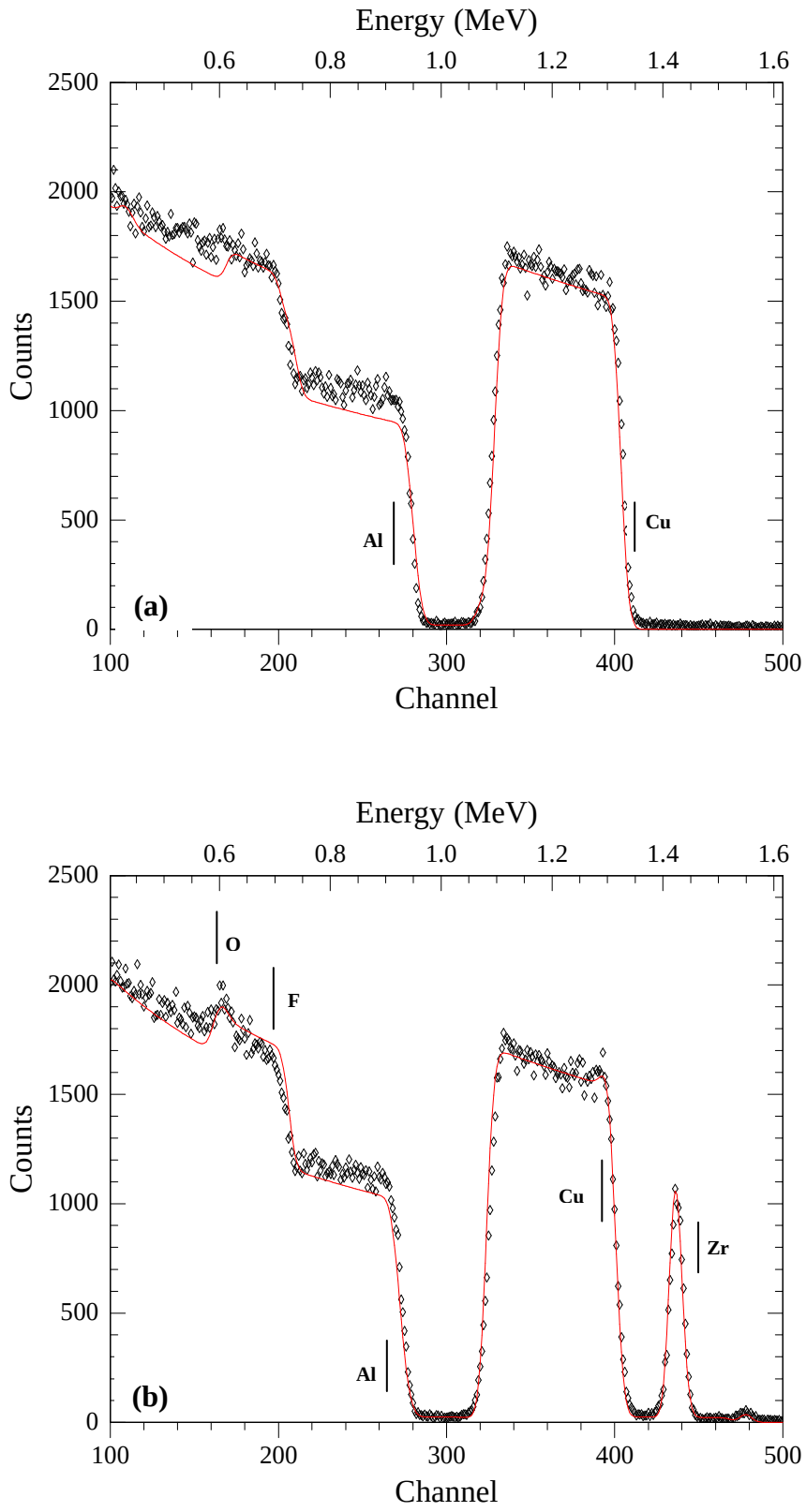

Figure 5.44 RBS Spectra of Al-30at.%Cu alloy after (a) 0 s and (b) 30 s immersion in zirconium-based conversion coating bath. The bars indicate energies corresponding to Al, Cu, Zr, F and O at the surface.

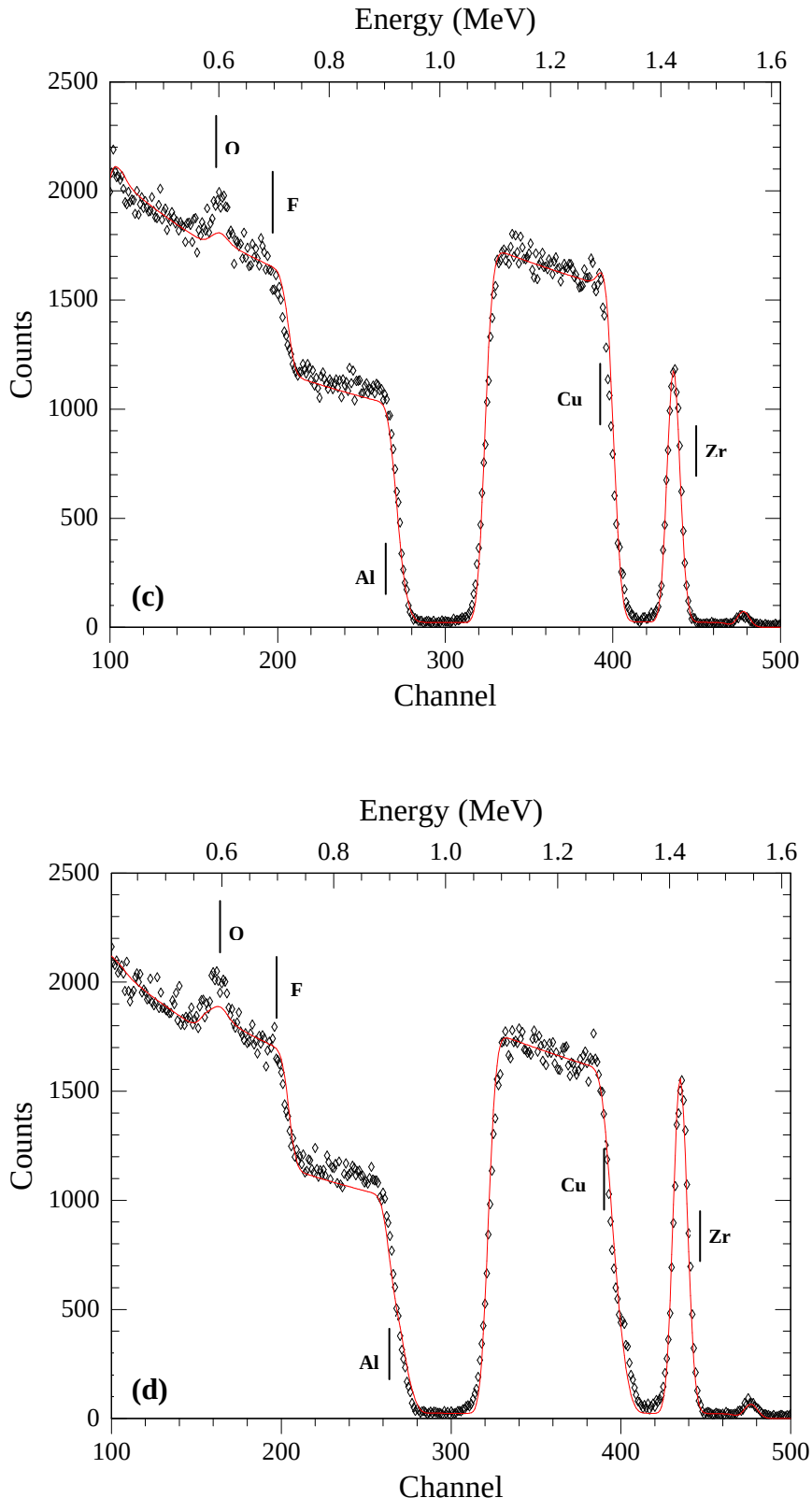

Figure 5.44 RBS Spectra of Al-30at.%Cu alloy after (c) 60 s and (d) 180 s immersion in zirconium-based conversion coating bath. The bars indicate energies corresponding to Al, Cu, Zr, F and O at the surface.

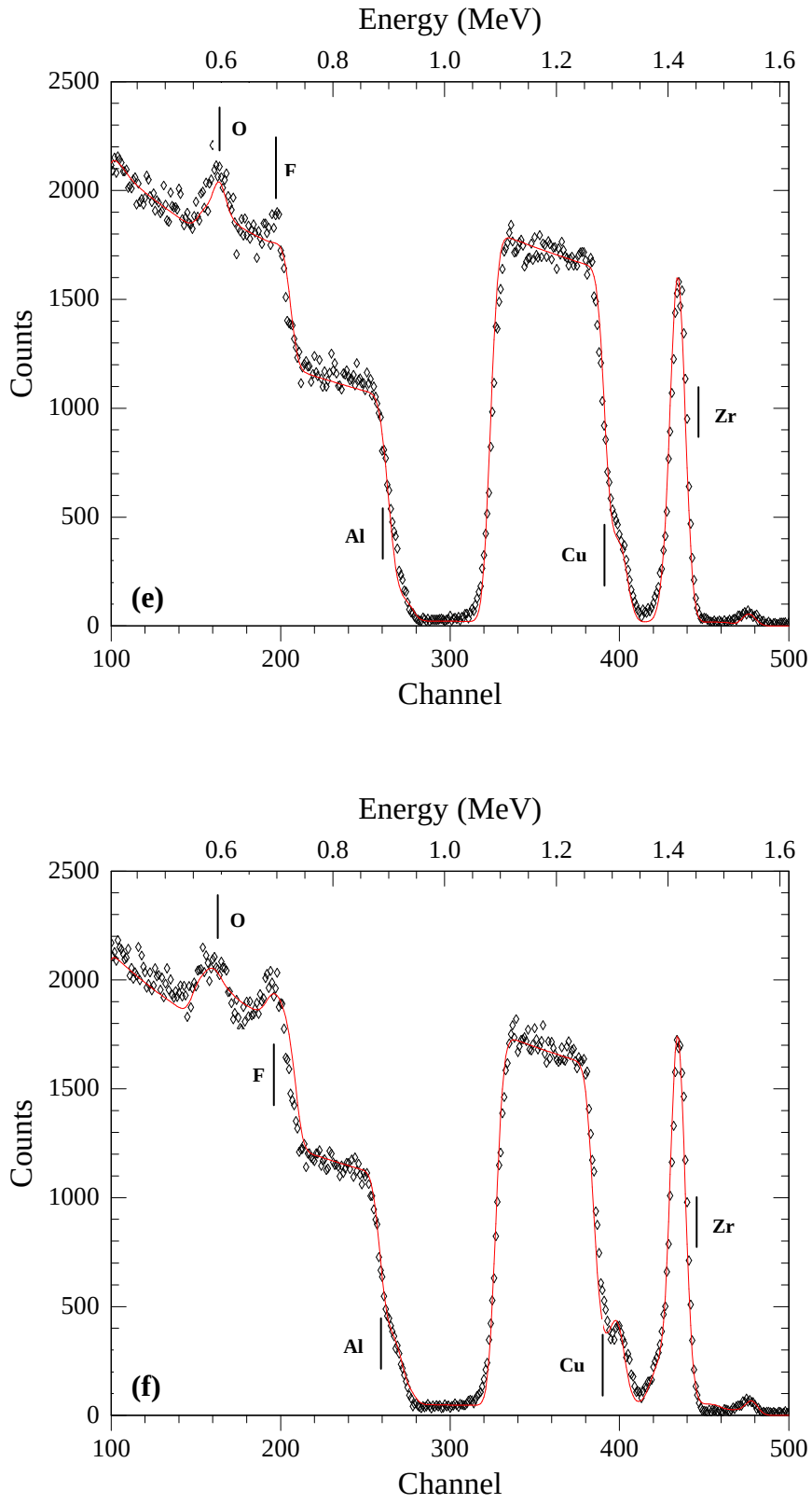

Figure 5.44 RBS Spectra of Al-30at.%Cu alloy after (e) 300 s and (f) 600 s immersion in zirconium-based conversion coating bath. The bars indicate energies corresponding to Al, Cu, Zr, F and O at the surface.

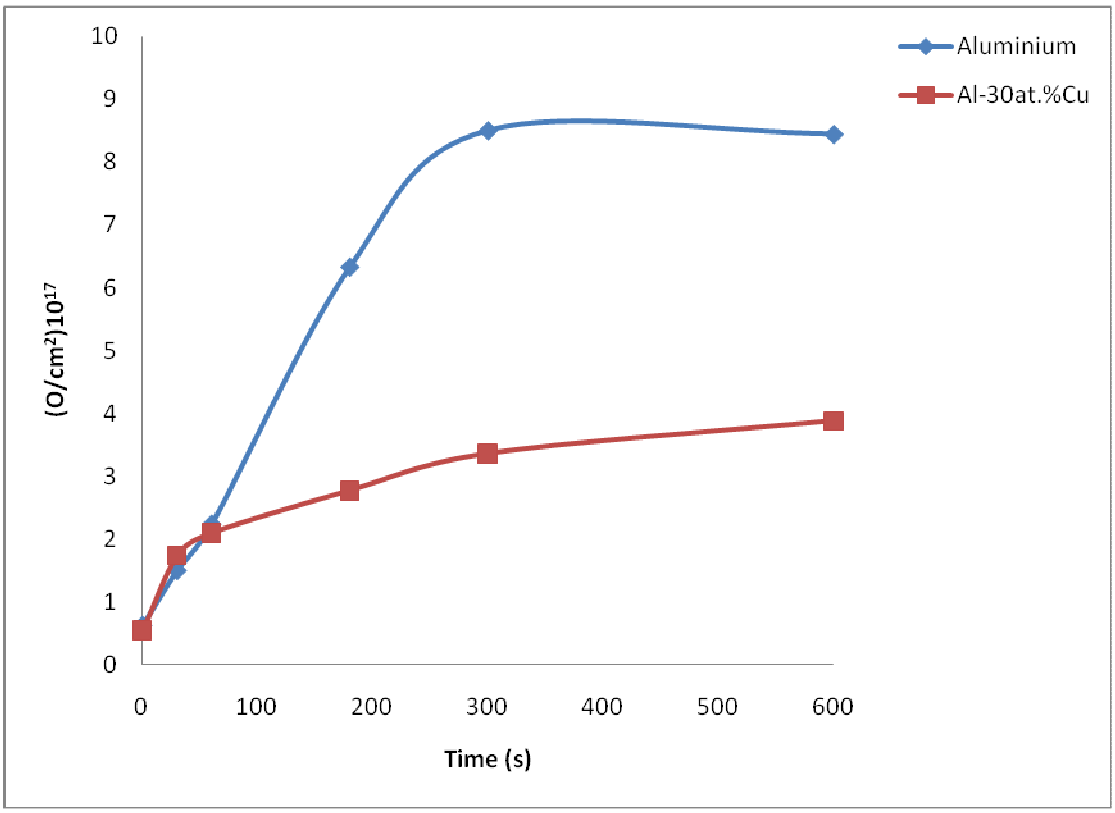

Figure 5.45 Oxygen quantities detected by nuclear reaction analyses of the conversion coatings developed on superpure aluminium and Al-30at.%Cu alloy.

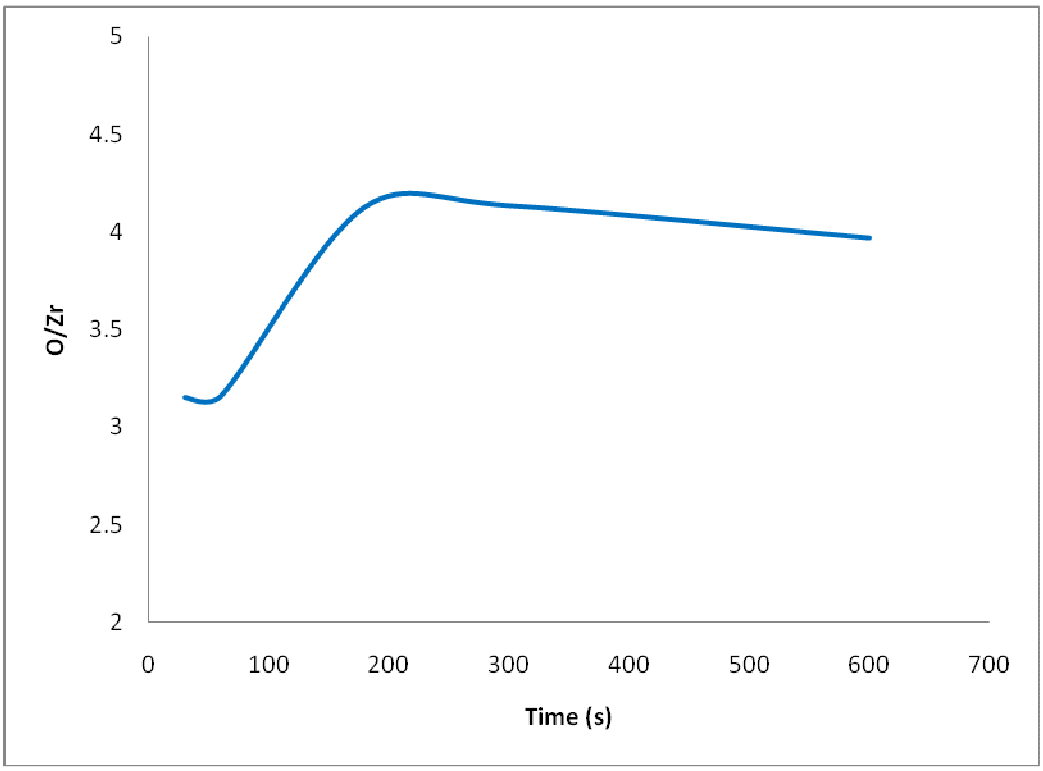

Figure 5.46 Variation of the ratio of oxygen to zirconium with immersion time in the conversion treatment bath.

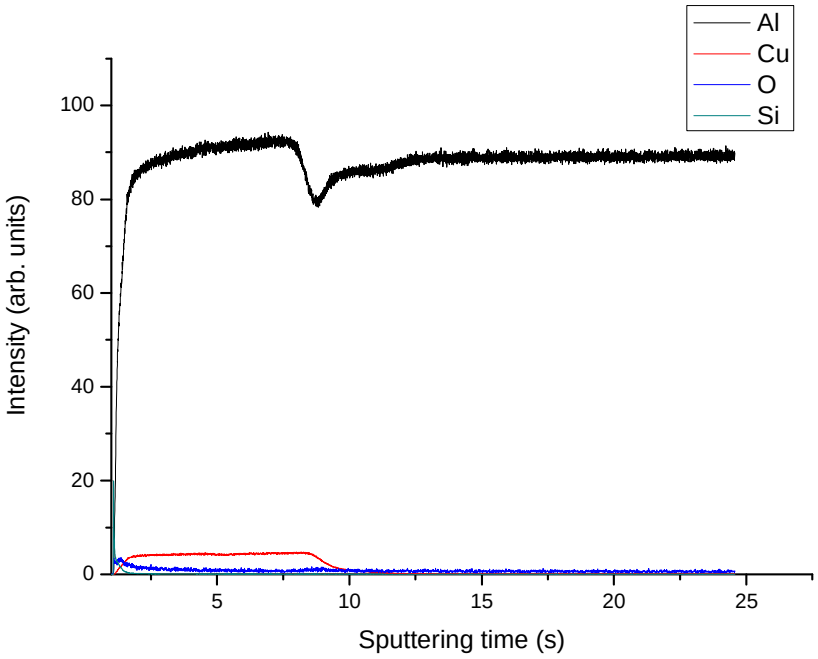

(a)

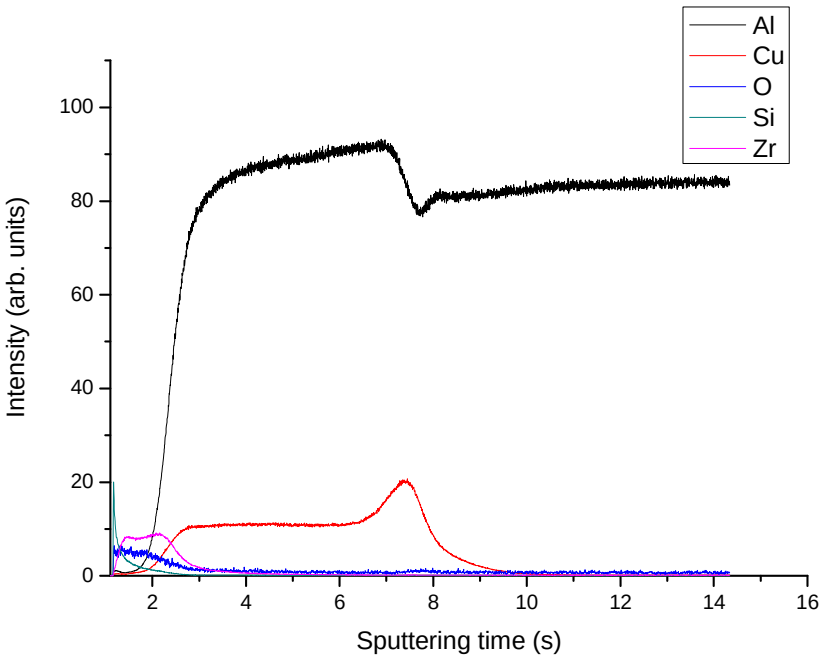

(b)

Figure 5.47 GDOES depth profile of the Al-1.0at.%Cu alloy after (a) 0 s and (b) 30 s of immersion in the zirconium-based conversion coating solution.

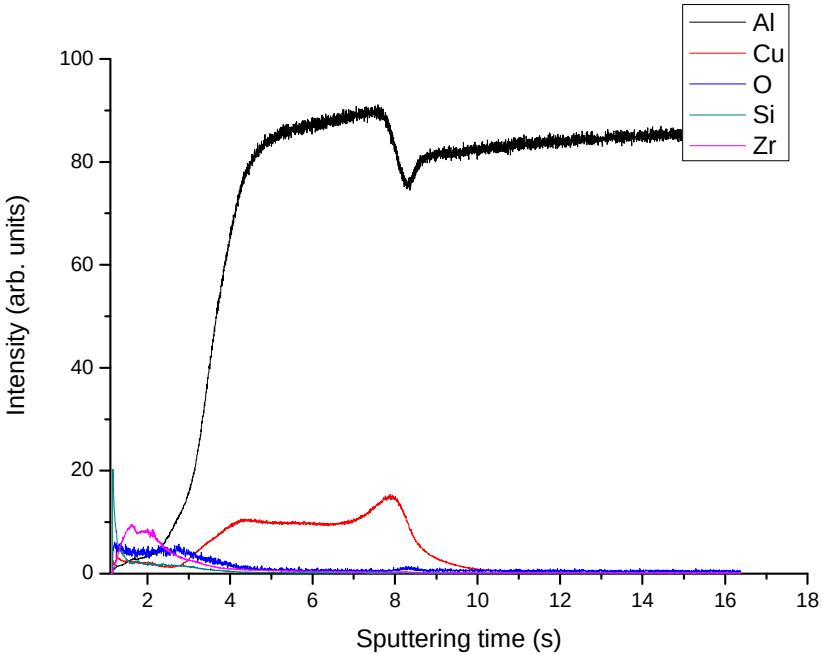

(c)

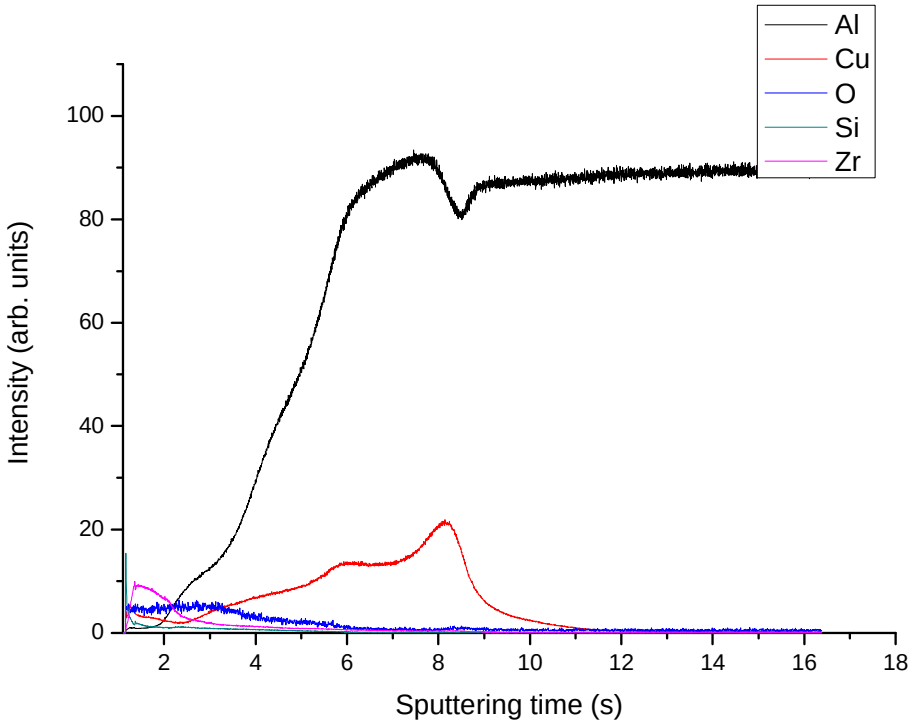

(d)

Figure 5.47 GDOES depth profile of the Al-1.0at.%Cu alloy after (c) 180 s and (d) 300 s of immersion in the zirconium-based conversion coating solution.

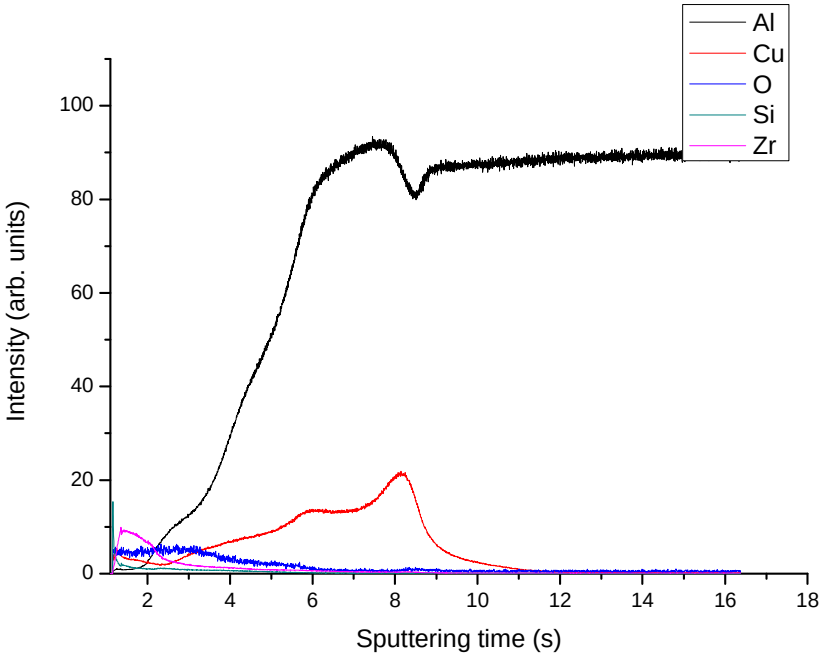

(e)

Figure 5.47 GDOES depth profile of the Al-1.0at.%Cu alloy after (e) 600 s of immersion in the zirconium-based conversion coating solution.

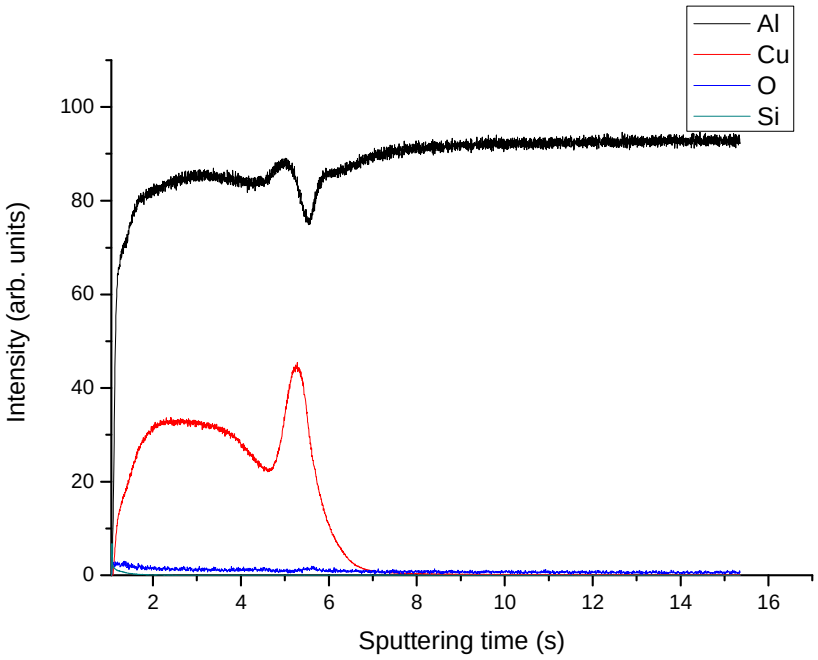

(a)

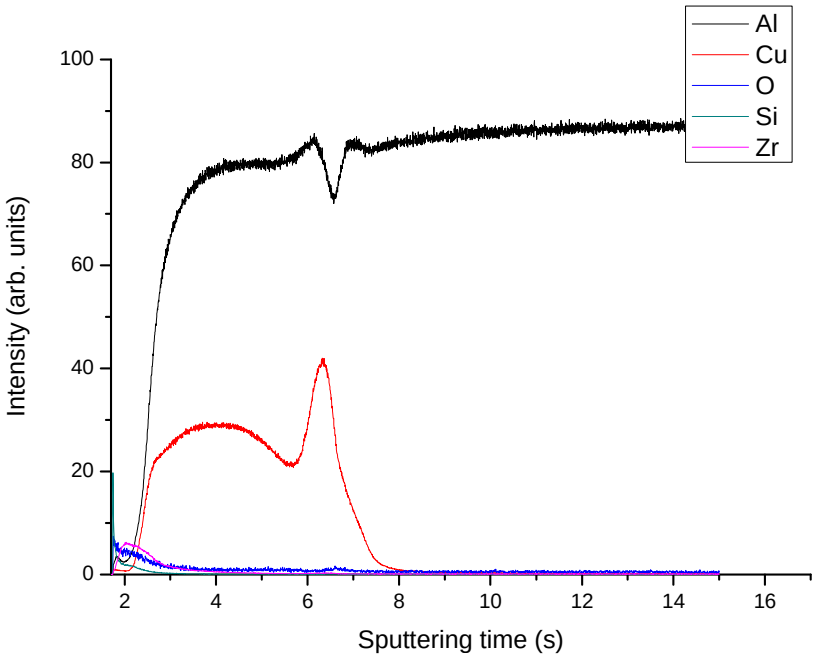

(b)

Figure 5.48 GDOES depth profile of the Al-10at.%Cu alloy after (a) 0 s and (b) 30 s of immersion in the zirconium-based conversion coating solution.

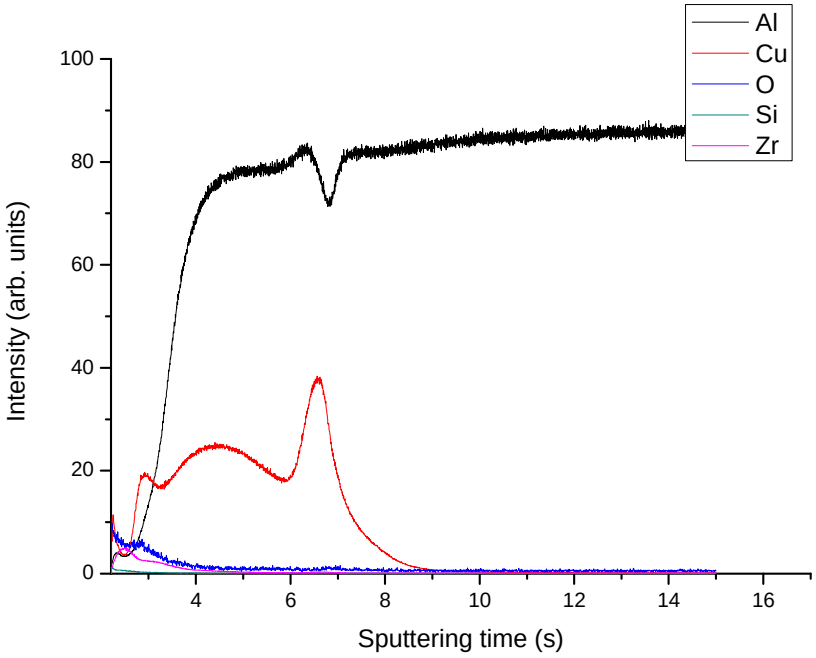

(c)

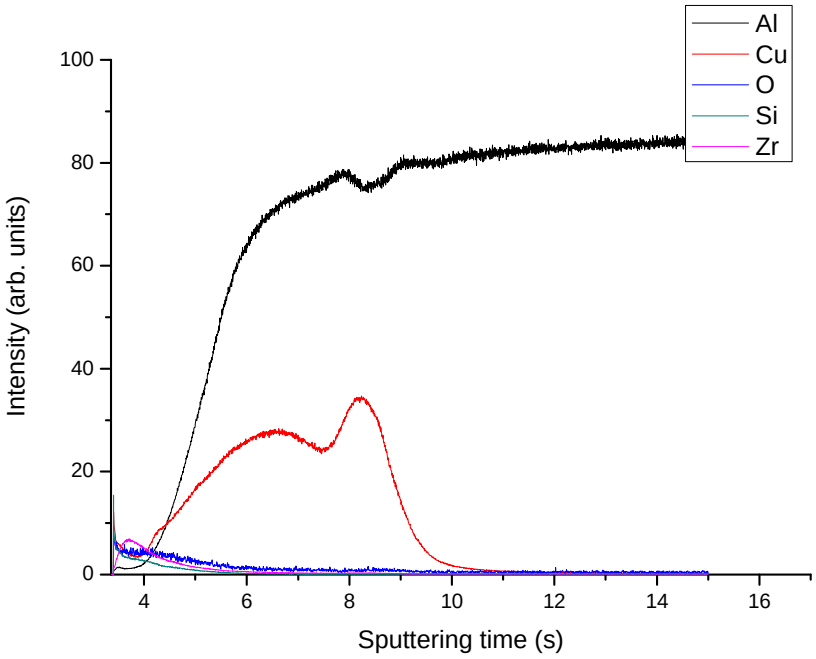

(d)

Figure 5.48 GDOES depth profile of the Al-10at.%Cu alloy after (c) 180 s and (d) 300 s of immersion in the zirconium-based conversion coating solution.

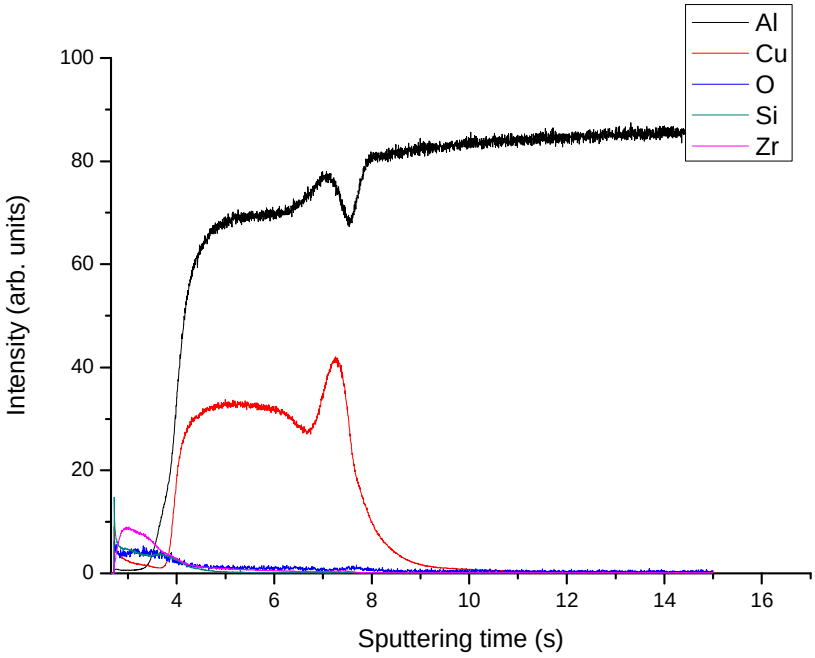

(e)

Figure 5.48 GDOES depth profile of the Al-10at.%Cu alloy after (e) 600 s of immersion in the zirconium-based conversion coating solution.

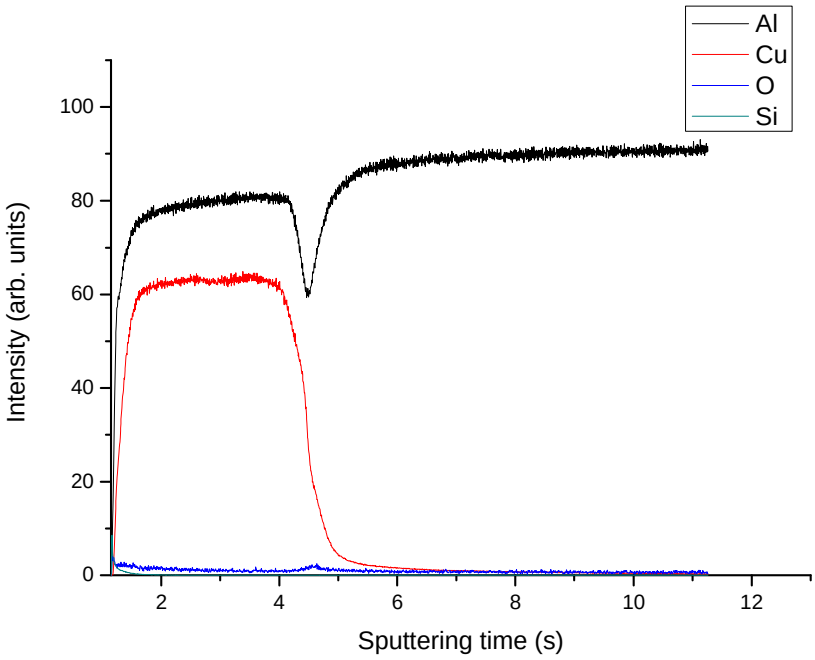

(a)

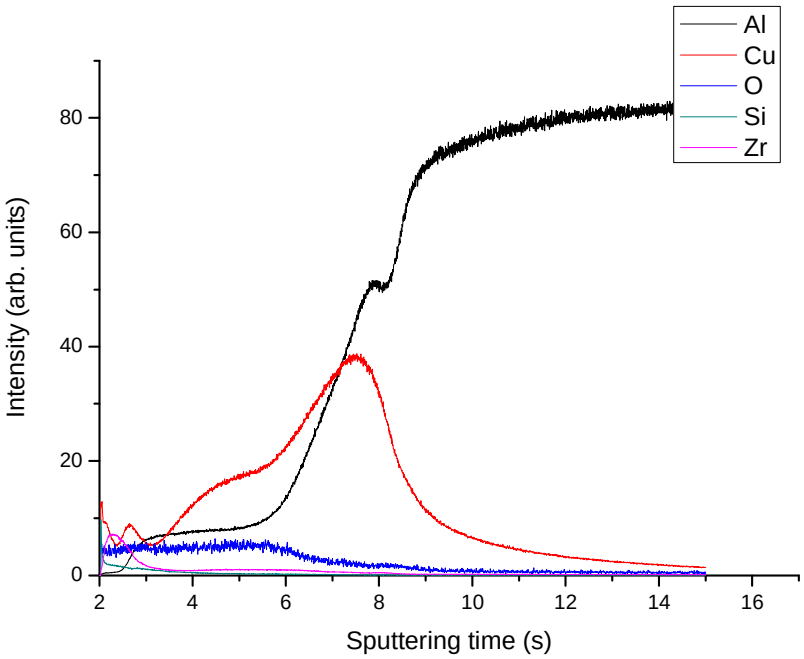

(b)

Figure 5.49 GDOES depth profile of the Al-30at.%Cu alloy after (a) 0 s and (b) 30 s of immersion in the zirconium-based conversion coating solution.

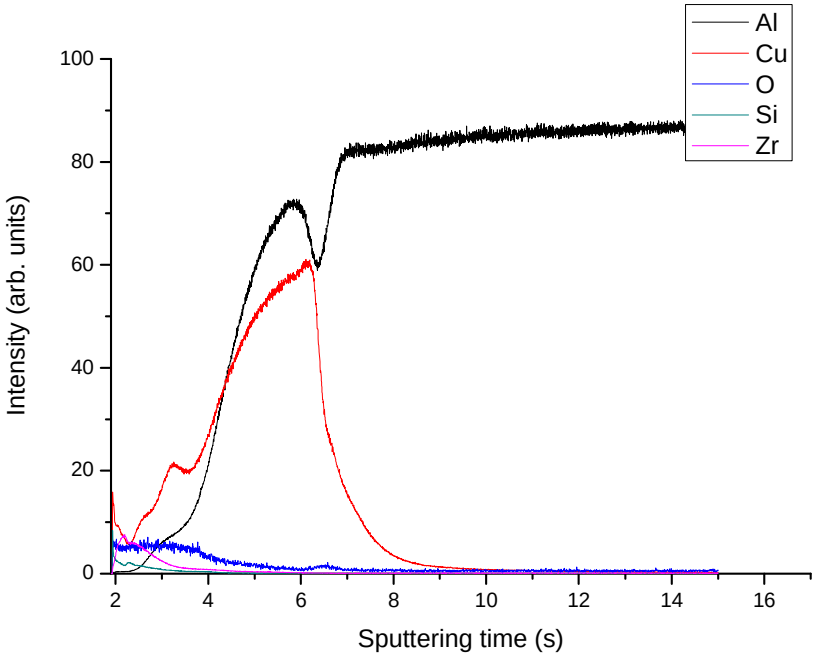

(c)

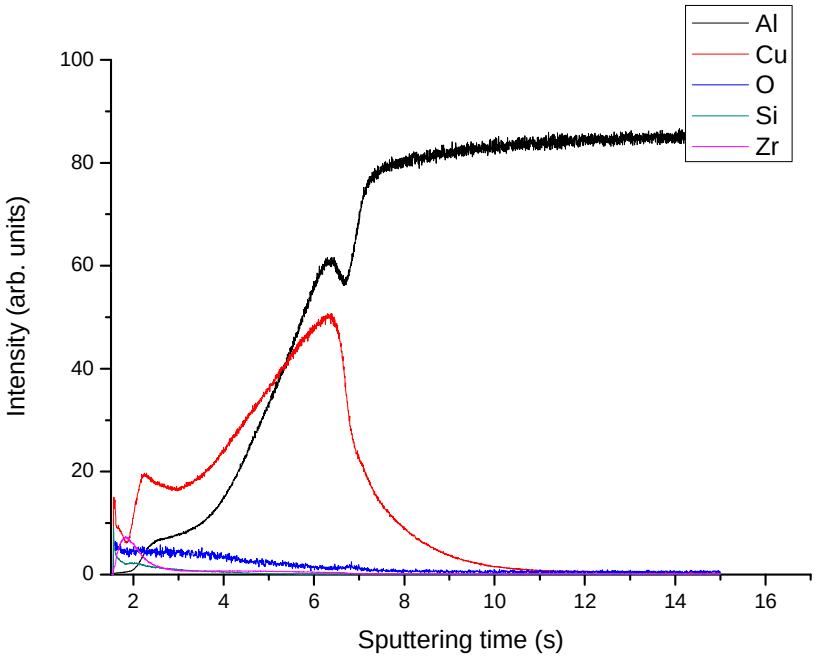

(d)

Figure 5.49 GDOES depth profile of the Al-30at.%Cu alloy after (c) 180 s and (d) of immersion in the zirconium-based conversion coating solution.

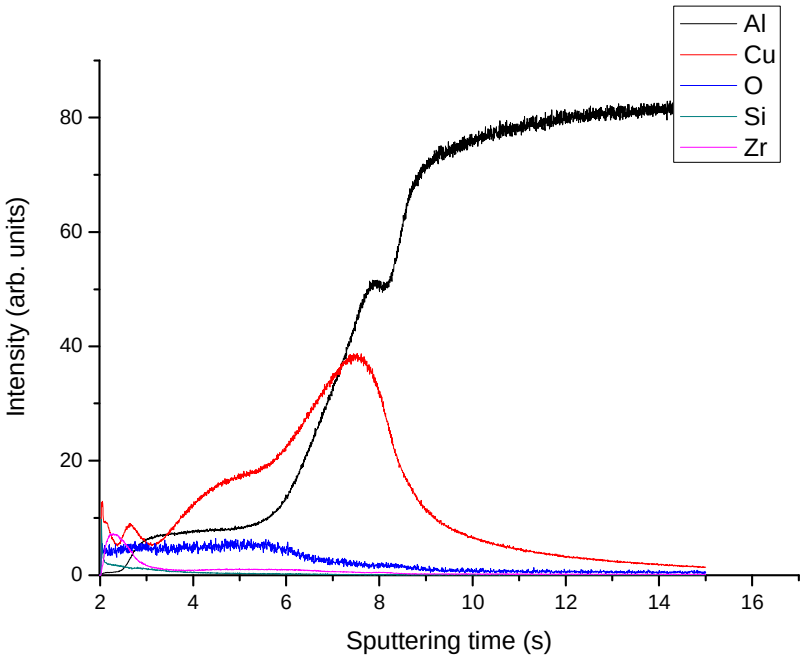

(e)

Figure 5.49 GDOES depth profile of Al-30at.%Cu after (e) 600 s of immersion in the zirconium-based conversion coating solution.

CHAPTER 6

6 ASSESSMENT OF THE EFFECTIVENESS OF THE ZIRCONIUM CONVERSION COATING PROTECTION

6.1 Introduction

The corrosion protection performance of zirconium-based conversion coatings can be influenced by many factors such as composition, microstructure and surface pre-treatment of the aluminium alloy substrate. As described in the previous chapter, the formation of zirconium conversion coating on aluminium alloys is highly heterogeneous. Corrosion of zirconium-based conversion coated substrates is likely to initiate at intermetallic compounds covered by thin coating layers, particularly after long-term exposure to the corrosive environments. Although the chemistry and structure of zirconium-based conversion coatings have been investigated, only a few studies have focused on the influence of alloying element such as copper on subsequent breakdown behaviour in chloride-containing solutions. In this section, the influence of the level of copper additions of the aluminium-copper alloys on zirconium-based conversion coating performance is studied.

Electrochemical measurements, including potential-time behaviour and polarisation behaviour of various surface treated alloys, were used to distinguish the influence of metal composition on the corrosion and protection behaviour of zirconium-based conversion coatings. All potentials quoted are referenced to the saturated calomel electrode (SCE) and the polarisation experiments on zirconium-based conversion coated specimens were carried out in 3.5 wt% NaCl solution. In order to characterise the inhibitive nature of the zirconium-based coatings formed, anodic and cathodic polarisation curves were collected for superpure aluminium and aluminium alloys coupons in aerated and deaerated 3.5 wt.% NaCl solution. Anodic and cathodic polarisation was carried out at a scan rate of 16.995 mV/min. Polarisation curves were replicated a minimum of 2 times in aerated and deaerated solutions. The exposed specimen area of each specimen coupons was nominally 1 cm^2.

6.2 Electrochemical Evaluation

All polarisation curve measurements were preceded by a 2 hours measurement of the open circuit potential (OCP). Anodic polarisation curves were initiated -5 mV below the OCP and finishing at +1000 mV above the OCP. A scan rate of 16.995 mV/min was used in all the experiments. Cathodic polarisation curves were initiated +5 mV from the OCP and terminated -1000 mV below the OCP.

6.2.1 Potential-time response

6.2.1.1 Superpure aluminium

The potential-time behaviour of the untreated and treated superpure aluminium and aluminium-copper model alloys prior to cathodic and anodic polarisation measurements is shown in Figures 6.1 (a) and 6.1 (b) respectively. Considering the potential-time behaviour of superpure aluminium before cathodic polarisation, the untreated aluminium specimen adopted an initial potential of -850 mV (SCE), after which the potential then decreased gradually to a value of -1280 mV after 6000 s. The potentials of the treated superpure aluminium specimens in 3.5 wt% NaCl solution showed a similar trend to that observed for the untreated specimen, with an increase of potential immediately on immersion which was followed by a relatively sharp decrease in potential. The initial immersion and steady state potential values were slightly different for all the treatment times. For the specimen given a 30 s treatment time, the potential of the specimen at the time of immersion was -966.33 mV (SCE). After 4000 s, the potential reached a steady state value of -1349.5 mV. For the specimen treated for 60 s in the conversion bath, the potential of the specimen at the time of immersion was -847.56 mV. After 4000 s, the potential reached a steady state value of -1365.7 mV. The specimen treated for 180 s adopted an initial potential of -1010.9 mV initially, after which the potential decreased sharply to -1345.1 mV after 5000 s in the chloride solution. For the superpure aluminium specimen treated for 300 s, the potential at the time of immersion was -1039.9 mV. After 4000 s, the potential reached a steady state value of -1349.2 mV. For the 600 s treated specimen, the potential showed a similar trend to the other treatment times but with a decrease in potential from the initial open circuit potential value of -1157 mV to -1274.7 mV after 2288 s. The potential then

further decreases slightly to a steady value -1289.2 mV after 6440 s over the period of immersion in the NaCl solution.

Figure 6.1 (b) reveals the potential-time behaviour of the untreated and treated superpure aluminium specimens recorded during immersion in deaerated 3.5 wt% NaCl solution. For the untreated superpure aluminium electrodes, it is evident that after the initial potential of -1473 mV (SCE), there was a steep rise in potential being followed by a decrease in potential from the maximum value -1390 mV (SCE) after 1000 s immersion in the chloride solution, to a relatively constant value of -1465 mV. The potential-time response of the superpure aluminium specimen treated for 30 s shows an initial potential of -1433.4 mV; this potential increased gradually to -1396.5 mV over 3000 s; thereafter, it increased slowly over 7000 s to -1383.2 mV. For the specimen treated for 60 s, the potential dropped from the initial value of -1415.1 mV to -1429.2 mV after 250 s, and recovered to -1418.6 mV (SCE) after 1000 s; after which the potential was maintained in the range of -1416.9 mV to -1415.0 mV after 3000 s. Thereafter, the potential increased slightly and, after 7000 s, it reached a value of -1399.9 mV. For the 180 s treated specimen, the potential showed a similar trend to the specimen treated in the zirconium-based bath for 60 s, with a relatively sharp decrease in potential from the initial value of -1375.3 mV to -1403.2 mV after 380 s. The potential then rose to -1389.2 mV (SCE) after 3066 s and maintained a value in the range of -1388.4 mV to -1387.5 mV over the period of immersion in the chloride solution. The specimen treated for 300 s also showed a similar trend to the ones treated for 60 s and 180 s, with a decrease in potential from the initial value of -1345.9 mV to -1418.2 mV after 867 s. Thereafter, the potential increased to -1404.4 mV (SCE) after 3000 s and maintained a value in the range of -1397.1 mV to -1395.8 mV over the whole period of immersion in the sodium chloride solution. For the superpure aluminium specimen treated in the zirconium bath for 600 s, an initial potential of -1233.7 mV was adopted at the time of immersion in the chloride solution. After the initial potential at the time of immersion, the potential of the specimen fell rapidly to -1333.5 mV (SCE) after 102 s; subsequently, the potential slowly decreased to -1402.4 mV after 2724 s. Thereafter, the potential remained approximately constant at a value in the range of -1403.7 mV to -1397.8 mV.

Compared with the potential value of the untreated superpure aluminium specimen in deaerated sodium chloride solution, the immersion of the specimens in the zirconium-based bath solution increased the open circuit potential of the treated specimens, suggesting an anodic inhibition role of the zirconium-based conversion coatings formed on the superpure aluminium substrates. It was also observed that the open circuit potential of the conversion coated specimens increased with the increase in treatment time. However, under the naturally aerated conditions, the conversion treatment of the superpure aluminium substrates resulted in a decrease in the open circuit potential values compared with the untreated specimen.

6.2.1.2 Aluminium-copper model alloys

Figure 6.2 is representative of the variation in open circuit potential (E_{corr}), with time for untreated and treated aluminium-copper model alloys containing 1, 5, 10 and 30 at.% Cu, recorded during immersion in naturally aerated sodium chloride solution. In contrast with the superpure aluminium specimens, the observed open circuit potential were not stable with fluctuations in potential being more pronounced, especially with high copper content alloys. The observed fluctuations in open circuit potential of the treated and untreated aluminium copper model alloys requires further consideration of the cathodic and anodic polarisation behaviour of the alloys which contributes to the monitored potential response with time.

The variation of open circuit potential with time for the Al-1.0at.%Cu alloy observed during immersion of the untreated and treated specimens in deaerated 3.5 wt% NaCl solution is shown in Figure 6.3. An initial open circuit potential of -900 mV (SCE) at the time of immersion, was evident for the as-sputtered alloy, after which it decreased at a steep rate to -1290 mV after 1000 s of immersion in the chloride solution followed by a period of rapid potential fluctuations between -1278.1 mV and -1246.8 mV. For the alloys treated for 30 s in the zirconium bath, the initial potential was -1383.3 mV (SCE). A small peak (1372.3 mV) was observed after 102 s which increased gradually to -1248.3 mV after 1795 s and, thereafter, remained in the range -1246.8 mV to -1220.8 mV for the duration of the run. For the specimen treated for 60 s, a similar trend to the 30 s treatment time was observed. The initial potential was -1015.5 mV after which the potential then increased to -678.2 mV after 4000 s and maintained a value in the range

of -672.8 mV to -666.2 mV over the period of immersion in the NaCl solution. After the initial open circuit potential of -643.9 mV (SCE), observed for the alloy treated for 180s, the potential fell to -855.58 mV after 3500 s and this potential was maintained for the next 500 s, after which the potential did not stabilise, but continued to drift in a noble direction. This trend was continued with the longer treatment times of 300 s and 600 s with the initial open circuit potential of -939.95 mV and -776.59 mV respectively.

Figure 6.4 shows the potential-time behaviour of the Al-5.0at.%Cu alloy in deaerated 3.5 wt% NaCl solution before and after conversion treatment. The initial open circuit potential of the as-sputtered alloy at the time of immersion was approximately -903 mV (SCE). The potential dropped rapidly to -1122 mV in the early stages of immersion in sodium chloride solution and recovered to -955 mV after 550 s with a subsequent fall to -1135 mV after 2267 s; this was followed by a slight increase of potential with time up to a maximum value of -975.6 mV. The specimens treated for 30 s initially adopted a potential of -875.09 mV (SCE) in the chloride solution. The potential then increased slightly to -843 mV after 410 s of immersion in the chloride solution and this potential was then maintained in the range -851 mV to -843 mV for the next 491 s; the potential increased to – 495.19 mV after 4323 s and, thereafter, the potential behaviour was characterised by frequent fluctuations for the rest of the duration of immersion in the chloride solution. The potential-time responses of the specimens treated for 60 s, 180 s, 300 s and 600 s were characterised by frequent fluctuations in potential of up 167 mV, 177 mV, 289 mV and 218 mV in magnitude respectively. These fluctuations in potential are usually attributed to the effects of localised corrosions such as pitting.

In contrast, when the alloy copper content was further increased to 10 at.% and 30 at.% (Figures 6.5 and 6.6), the open circuit potentials were generally characterised by pronounced fluctuations in potential for the untreated and treated alloys. This suggests that the conversion coated high copper-content aluminium alloys may be more susceptible to pitting attack than superpure aluminium and those alloys containing low levels of copper.

6.2.2 Cathodic polarisation

6.2.2.1 Superpure aluminium

The cathodic polarisation response of the treated and untreated superpure aluminium in aerated 3.5 wt.% NaCl solution is shown in Figure 6.7. The cathodic polarisation curves of the treated superpure aluminium specimens were shifted to lower potentials compared to the as-sputtered specimens. The corrosion current density was determined for each specimen by the ACM analysis software. The corrosion current density values obtained are plotted as a function of treatment times in the zirconium-based solution in Figure 6.8. The plot shows that the corrosion current densities of superpure aluminium specimens increases after shorter treatment times (30 s and 60 s), but decreases as the treatment time was increased (180 s, 300 s and 600 s) when compared with the corrosion current density of the untreated specimen. Due to the presence of thicker coating deposition, the longer treatment times resulted in significantly lower corrosion current density. Specimens after cathodic polarisation studies were observed by optical microscopy and the surface appearance for various treatment conditions are displayed in Figures 6.9 (a) – 6.9 (f). After the cathodic polarisation, few pits were found on the surface of the conversion treated superpure aluminium specimens. In contrast, some dark corroded areas, with obvious pits were found on the as-sputtered superpure aluminium specimen, suggesting that the conversion treated specimens possess better corrosion resistance compared with the untreated specimen. The results of the optical microscopy investigations of the as-sputtered and conversion treated superpure aluminium surfaces subjected to intensive cathodic polarisation supports the above electrochemical features.

6.2.2.2 Al-1.0at.%Cu alloy

The cathodic polarisation behaviour of the untreated and zirconium conversion coated Al-1.0at.%Cu alloys are shown in Figure 6.10. For the as-sputtered alloy, the initial open circuit potential shifted in the positive direction and the diffusion controlled cathodic current density was about 4.17×10^{-6} A/cm^2. After the relatively short treatment time of 30 s, a limiting current density was not clearly evident; a decrease of cathodic current density (2.52×10^{-6} A/cm^2 and 1.24×10^{-6} A/cm^2) was observed with further increase of treatment time to 60 s and 180 s respectively. Increased cathodic

current densities were recorded with further increase in treatment time (300 s and 600 s). The corrosion current density (I_{corr}) values obtained after polarisation is plotted as a function of treatment times in the zirconium-based solution in Figure 6.11. The plot shows that the corrosion current densities of the Al-1.0at.%Cu alloy decrease after shorter treatment times (30 to 180 s) in the zirconium bath compared with the as-sputtered specimen. However, the corrosion current density increases with increase in treatment time (300 s and 600 s) compared with the corrosion current density of the as-sputtered alloy. After cathodic polarisation studies, the polarised specimens were observed under an optical microscope and the corresponding surface appearance after for various treatment times is displayed in Figures 6.12 (a) – 6.12 (f). After cathodic polarisation, several small pits of a few microns in size were found on the as-sputtered and the alloy specimen conversion coated for 30 s. In contrast, the appearance of the alloy specimen coated for 60 s revealed that the corrosion attack is less severe in this alloy after this treatment time compared with all other treatment conditions. The corrosion attack appeared to be more severe on the surface of the alloy specimen conversion coated for 600 s.

6.2.2.3 Al-5.0at.%Cu alloy

Figure 6.13 shows the cathodic polarisation behaviour of the as-sputtered and conversion coated Al-5.0at.%Cu alloy. The limiting current density of the as-sputtered specimen is 3.33×10^{-6} A/cm^2. For the 180 s and 300 s treatment times, the diffusion controlled process was not apparent; however, a small increase of the cathodic current density was revealed compared with the as-sputtered alloy. Here, the effect of the zirconium conversion coating formed on the alloy surface is the reduction in the open circuit potential observed, as well as an increase in the cathodic current densities. In Figure 6.14, the corrosion current density (I_{corr}) values obtained after polarisation of the alloy is plotted as a function of immersion times in the zirconium-based solution. The plot shows that the corrosion current density of the Al-5.0at.%Cu alloy increases during the polarisation of the specimen treated for 30 s in the zirconium bath, after which the corrosion current density decreases with increase in treatment time in the coating bath. The surface of the zirconium conversion treated alloy specimens after polarisation tests were examined using optical microscopy and the corrosion morphologies revealed are displayed in Figures 6.15 (a) – 6.15 (f). After cathodic polarisation, several small pits of

a few microns in size were observed on the as-sputtered alloy and the alloy specimen conversion coated for 30 s. Some blisters were observed on the surface of the alloy after prolonged treatment time of 600 s. The dark colour observed on the surface of the alloy specimen after this conversion treatment time is likely due to corrosion product developed on the surface of the alloy.

6.2.2.4 Al-10at.%Cu alloy

A typical cathodic polarisation curve obtained for as-sputtered and treated specimens of Al-10at.%Cu alloy in contact with 3.5 wt.% NaCl solutions is shown in Figure 6.16. For the as-sputtered alloy (0 s), a limiting current density of 5.76×10^{-6} A/cm^2, was evident. The influence of treatment in the zirconium bath is to increase the cathodic current densities compared with the untreated specimen but not to marked extents since typical cathodic current densities were of the order of 10^{-6} A/cm^2; however, a decrease of cathodic current densities was revealed with increase in treatment time in the conversion bath solution. The corrosion current density (I_{corr}) values obtained after polarisation is plotted as a function of treatment times in the zirconium-based solution in Figure 6.17. The plot shows that the corrosion current density of the Al-10at.%Cu alloy increases after shorter treatment times (30 to 60 s) in the zirconium bath. However, the least corrosion current density was recorded for specimen treated for 600 s. After the polarisation tests, the alloys were observed by an optical microscope in order to study the morphology and evolution of corrosion products formed on the material surface. Figures 6.18 (a) – 6.18 (e) show the presence of pits with different sizes on the surfaces of the alloy specimens after cathodic polarisation. However, only a few discrete blisters and corrosion products were observed on the surface of alloy surface coated for 600 s (Figure 6.18 (f)), indicating good resistance to localised corrosion. This is likely due to the presence of thick oxide layer (confirmed by the NRA results) developed after prolonged conversion treatment time of 600 s.

6.2.2.5 Al-30at.%Cu alloy

The cathodic polarisation behaviour of the as-sputtered and treated alloy in chloride solution is shown in Figure 6.19. The cathodic behaviour of the untreated (0 s) specimen revealed a limiting current density of 2.15×10^{-5} A/cm^2. A significant

reduction in the cathodic current density is revealed for the conversion coated alloy specimens. However, the least cathodic current density was recorded for specimens conversion coated for 60 s. Typical current densities of the conversion coated specimens were of the order 10^{-5} A/cm^2. Figure 6.20 shows the influence of the treatment time on the corrosion current density of the conversion coated alloy. The plot shows that the corrosion current densities of the Al-30at.%Cu alloy increases initially after shorter treatment times (30 to 60 s) in the zirconium bath, but it reduces after longer treatment times. The specimens were observed after the polarisation tests by optical microscopy in order to study the corrosion morphology on the surface of the alloys. Figures 6.21 (a) – 6.21 (f) show the presence of blisters on the surface of the alloy specimens after polarisation. Significant level of blistering is observed on the surface of the alloy specimens treated in the zirconium conversion coating bath for relatively short conversion treatment times.

6.2.3 Anodic polarisation

6.2.3.1 Superpure aluminium

Figure 6.22 shows typical anodic polarisation curves obtained with as-sputtered and conversion treated superpure aluminium exposed to deaerated 3.5 wt.% NaCl solutions. All the specimens showed classical passive regions with the current density practically independent of applied potential up to the pitting potentials of the specimens. Upon polarisation, a passive current density of 2.30×10^{-7} A/cm^2 was observed for the untreated (as-sputtered) alloy. An increase in open circuit and pitting potentials is revealed for conversion coated specimen compared with the as-sputtered superpure aluminium specimen. The specimen treated for 60 s has the higher pitting potential of 668.66 mV. The anodic current densities decreased with increasing treatment time except for the specimens treated for longer immersion time of 600 s, where a current density of 1.53×10^{-7} A/cm^2 was observed. Figure 6.23 shows the influence of the treatment time on the corrosion current density of the conversion coated superpure aluminium specimens during anodic polarisation measurements. The plot shows that the corrosion current densities of the superpure aluminium specimen treated for 30 s in the conversion bath increases initially, but the corrosion current density value reduces significantly for specimen treated for 60 s in the conversion bath. However, after longer

treatment times the plot shows that the corrosion current densities of the superpure aluminium specimens increases during anodic polarisation measurement.

6.2.3.2 Al-1.0at.%Cu alloy

Figure 6.24 displays the anodic polarisation curves recorded in 3.5 wt.% NaCl solution for Al-1.0at.%Cu alloy treated for 0 s, 60 s, 180 s, 300 s and 600 s in the zirconium-based conversion baths. The polarisation curves show that the increase in treatment time give rise to changes in both the anodic current density and the pitting potential of the specimens of the Al-1.0at.%Cu alloy. When the alloy specimens were conversion treated in the conversion baths, an increase is produced in the corrosion potential for various treatment conditions. For the specimens treated in the zirconium conversion bath for 60 s, pitting commenced almost from the commencement of polarisation. Pitting of the alloy specimens occurred at potential of about 714, 484, 299 and 354 mV above E_{corr} for specimens treated for 0, 30, 180 and 300 s respectively in the conversion bath solution. The anodic reaction on the as-sputtered and conversion treated Al-1.0at.%Cu alloy appears to be controlled by the pitting of the alloy in chloride solution. Thus, the alloy specimens immersed for 30 s in the conversion treatment bath provides significant barrier protection for the Al-1.0at.%Cu alloy. The corrosion current density (I_{corr}) values obtained (using the ACM analysis software) after polarisation is plotted as a function of treatment times in the zirconium-based conversion bath solution is shown in Figure 6.25. The plot shows that the corrosion current densities of the Al-1.0at.%Cu alloy decreased significantly for specimens treated for the shorter treatment time of 30 s in the zirconium bath. However, the highest corrosion current density was recorded for specimen treated for 180 s.

6.2.3.3 Al-5.0at.%Cu alloy

Anodic polarisation curves in deaerated 3.5 wt.% NaCl solution for the Al-5.0at.%Cu alloy in the as-sputtered and conversion treated conditions are shown in Figure 6.26. No passive region is evident for the treated alloy specimens after the various treatment times but the open circuit potential shifted to more positive values for the conversion treated specimens. Figure 6.27 shows that the corrosion current density (obtained using the ACM analysis software) of the alloy increases sharply for specimens treated for 30 s

but subsequently the corrosion current density of the specimen decreased as treatment times increases; however, the corrosion current density values of the alloy after prolonged treatment times (above 30 s) were found to be higher compared with that for the as-sputtered alloy specimen.

6.2.3.4 Al-10at.%Cu alloy

The anodic polarisation behaviour of the Al-10at.%Cu alloy in 3.5 wt.% NaCl solution before and after treatment in the zirconium-based conversion bath is shown in Figure 6.28. With the exception of the alloy specimen conversion coated for 180 s, the influence of treatment in the zirconium bath is to increase the open circuit potential and the anodic current densities compared with the as-sputtered alloy specimen. The corrosion current density (I_{corr}) values determined by ACM analysis software after polarisation are plotted as a function of treatment times in the zirconium-based solution as shown in Figure 6.29. The plot shows that the corrosion current densities of the Al-10at.%Cu alloy increased as treatment times increased except for specimens treated for 180 s in the zirconium bath. Thus, the treatment time of 180 s appears to provide some optimised protection for the Al-10at.%Cu alloy.

6.2.3.5 Al-30at.%Cu alloy

Figure 6.30 shows the anodic polarisation behaviour of the Al-30at.%Cu alloy specimens in the as-sputtered and treated condition, in deaerated chloride solution. A comparison of Figure 6.30 indicates that the specimen treated for 180 s in the conversion coating bath has an extensive passive region extending from -834.12 mV to the pitting potential of -521.95 mV. The open circuit potential was at a lower value and was significantly distanced from the pitting potential. No passive region is observed for the other treatment times except for the alloy specimen immersed in the conversion bath for 300 s with a passive region extending from -814.61 mV to the pitting potential of -758.52 mV. With the exception of the alloy specimen treated for 600 s in the conversion bath solution, the passive current densities recorded for the treated alloy specimens decreased compared to that of the as-sputtered (0 s) specimen. Figure 6.31 shows the plot of the corrosion current density as a function of treatment time. It is clear from the plot that the corrosion current densities of the Al-30at.%Cu alloy decreases initially for

specimens treated for 30 s, but increased slightly for shorter treatment time of 60 s. However, the lowest corrosion current density for the Al-30at.%Cu alloy was recorded for specimens treated for 180 s in the conversion bath solution. Thus, the treatment time of 180 s appears to provide significant barrier protection for the Al-30at.%Cu alloy.

6.3 Filiform Corrosion Testing

As the use of aluminium alloys is continuously increasing in the automotive and aerospace industries, filiform corrosion of these alloys in a range of service conditions and applications has become a growing concern. Improving the anti-corrosion and adhesion properties of conversion coating layer/aluminium alloy interface is significant to the quality of films and applied coatings formed on aluminium alloys. Filiform corrosion, which is characterised by a lateral propagation of filaments, usually occurs at defects in the coating and, this results in poor coating integrity such as delamination and blistering. The purpose of this section is to examine the effect of zirconium-based conversion treatment on filiform corrosion on aluminium and binary aluminium-copper alloys. Scribed specimens in both as-sputtered and conversion treated conditions were tested in anticipation that the filiform corrosion test results will provide information regarding the protective effects of the conversion layers formed on the conversion treated specimens. Corrosion was initiated by introducing droplets of 16 wt.% HCl solution into the scribe for 2-3 minutes. At the end of the filiform corrosion test, which consisted of 3000 h exposure in the humidity chamber, the extent of filiform corrosion on the various specimens were compared qualitatively by analysing the images from the digital scanner and quantitatively by measuring and reporting the average maximum filament length using the Digimizer image analyser software. The information obtained in the preceding chapters should also be useful in explaining the differences in filiform corrosion kinetics.

6.3.1 Filiform corrosion morphology and kinetics

The filiform corrosion susceptibility of the specimens was assessed by the average of the three longest corrosion filaments measured perpendicular to the scribe. The corrosion test results obtained in this study are summarised in Figures 6.32 - 6.36 and the digital images showing the filiform corrosion morphology of the superpure

aluminium and the model aluminium-copper alloys following 3000 h of exposure in the humidity chamber are displayed in Figures 6.37 - 6.41.

A comparison of Figure 6.32 for the superpure aluminium specimens indicates that the as-sputtered (0 s) aluminium substrate was highly susceptible to filiform corrosion. It can be seen that the zirconium-based conversion treatments significantly reduce the length of the longest filaments formed on the conversion treated superpure aluminium substrates. At the end of 3000 h exposure in the humidity chamber, specimens treated for 30 s showed significant resistance to filiform corrosion while those treated for 300 s in the zirconium-based conversion bath showed significantly more corrosion attack when compared with the other treatment times.

For the Al-1.0at.%Cu alloy specimens (Figure 6.33), the zirconium-based conversion treatment gave a significant improvement in corrosion resistance relative to the as-sputtered (0 s) specimens. The specimens treated for 180 s in the zirconium conversion bath were most severely affected by filiform corrosion than the other treatment times. An immersion time of 300 s gave a significant improvement to the filiform corrosion resistance of the Al-1.0at.Cu alloy compared with the other conversion treatment times. The filiform growth rate on the as-sputtered specimen was approximately more than twice that on specimen treated for 300 s in the conversion bath solution.

The filament growth on the alloy specimen treated for 600 s almost stopped after 840 h of exposure while on the as-sputtered alloy specimens, the filament growth continued in a linear relationship with exposure time in the humidity chamber (Figure 6.34). Again, the Al-5.0at.%Cu alloy in the as-sputtered condition exhibited a high susceptibility to filiform corrosion attack compared to the conversion treated alloy specimens. No significant decrease in filament length was revealed for the specimen of Al-5.0at.%Cu alloy after conversion treatment for 180 s compared with the as-sputtered specimen. After 3000 h of exposure to the humid environment, a considerable decrease in average filament length was obtained by conversion treatment of the Al-5.0at.%Cu alloy, as observed in Figures 6.34 and 6.39.

The influence of conversion treatment times on the susceptibility of the Al-10at.%Cu alloy is summarised in Figure 6.35. The highest corrosion susceptibility was still observed on the as-sputtered alloy while the conversion treated alloy exhibited less

corrosion susceptibility throughout the exposure time. The treatment times of 30 and 60 s have a strong inhibiting effect on the filiform corrosion properties of the Al-10at.%Cu alloy, while the longer conversion treatment time (180 s – 600 s) resulted in less significant corrosion resistance.

The as-sputtered Al-30at.%Cu alloy specimens exhibited severe attack in the early stage of exposure (Figures 6.36 and 6.41(a)). Unlike the Al-10at.%Cu alloy, where shorter treatment times in the conversion bath, gives rise to a superior resistance to filiform corrosion, the Al-30at.%Cu alloy specimens treated for longer immersion times of 180 s and above, in the zirconium bath, significantly improved the corrosion resistance of the alloy. The lowest corrosion susceptibility was observed on specimens conversion treated for 600 s.

6.4 Salt Spray Testing

Salt spray testing was carried out on acrylic-coated as-sputtered and selected conversion coated specimens in order to assess the effect of conversion coating time and copper content of aluminium-copper alloys on coating resistance. As described in section 3.15.2, the salt spray testing was performed in a 5 wt% NaCl salt fog. The acrylic-coated coupons for selected conversion coating conditions were scribed and exposed to 1000 h of salt fog under conditions identical to those of the uncoated (as-sputtered) specimens. The specimens were inspected regularly and photographs were recorded before, during and at the termination of the test (1000 h of exposure in the salt spray cabinet) to assess the level of corrosion damage that occurred during the 1000 h of ASTM B117 salt spray testing.

Figures 6.42 – 6.46 shows photographs of scribed acrylic coated specimens (in the as-sputtered and conversion treated conditions) illustrating the type of corrosion damage observed after exposure to the salt fog for 1000 h. The specimens were ranked from “0” to “5” according to the number of pits and the corrosion product accumulated. A ranking of “0” indicates the best performance while ranking of “5” indicate severe corrosion. A complete listing of the degree of corrosion damage observed after 168, 336, 504 and 1000 h exposure in the salt spray chamber is found in Table 6.1.

Table 6.1 Rankings of the degree of corrosion of specimens after salt spray testing for 168 h, 504 h and 1000 h.

Specimen	Conversion treatment time	Visual inspection			
		168 h	336 h	504 h	1000 h
Superpure aluminium	0 s	2	2	2	4
	30 s	1	1	1	3
	180 s	0	1	2	2
	300 s	2	2	2	2
	600 s	2	2	2	3
Al-1.0at.%Cu	0 s	2	2	3	4
	30 s	2	2	2	2
	180 s	1	1	3	4
	300 s	2	3	3	3
	600 s	2	2	2	3

Table 6.1: (continued)

Specimen	Conversion treatment time	Visual inspection			
		168 h	336 h	504 h	1000 h
Al-5.0at.%Cu	0 s	3	4	4	5
	30 s	3	3	3	4
	180 s	2	2	2	4
	300 s	2	2	2	4
	600 s	2	2	2	3
Al-10at.%Cu	0 s	3	4	4	5
	30 s	2	2	3	4
	180 s	2	3	3	4
	300 s	3	3	3	4
	600 s	2	3	3	5
Al-30at.%Cu	0 s	4	5	5	5
	30 s	3	5	5	5
	180 s	2	4	5	5
	300 s	3	4	5	5
	600 s	4	5	5	5

Figures 6.47 – 6.50 show the effect of copper content in the aluminium-copper alloys and the zirconium-based conversion treatment time on corrosion damage. After 168 h of exposure (Figure 6.47), the superpure aluminium specimen treated in the zirconium-based conversion treatment bath for 180 s displayed the best overall performance with no observed pitting, blistering and complete protection of the scribe. All other treated specimens exposed to the salt fog displayed some pitting, blistering, attack in the scribe, or some combination of two or three forms of corrosion attack. A significant effect of the conversion treatment time on the performance of the conversion coating was also noted. The specimens (superpure aluminium and Al-Cu alloys) treated for 180 s appears to exhibit strong to moderate corrosion protection as shown in Figure 6.47. For the Al-5.0at.%Cu alloy, the specimens treated for 180, 300 and 600 s in the conversion bath all have the same performance, much better compared to the as-sputtered and 30 s treated specimens. The aluminium-copper alloys treated in the zirconium conversion bath for 180 s showed little dependence on the percentage copper concentration for the Al-1.0at.%Cu alloys (strong performance). However, the 180 s conversion coated Al-5.0at.%Cu, Al-10at.%Cu and Al-30at.%Cu alloys all exhibited similar performances (moderate).

After 336 and 504 h of exposure (Figures 6.48 – 6.49), the superpure aluminium specimens treated for 180 s performed better than the copper-containing aluminium alloys. A significant effect of percentage copper composition of the alloys on the corrosion performance of the conversion treated alloys was observed. At the end of the 504 h of exposure, the aluminium-copper alloys containing moderate levels of copper (Al-1.0at.%Cu and Al-5.0at.%Cu alloys) performed better than those with higher percentages of copper in their composition. Moderate coating performance was observed on all the conversion treated Al-30at.%Cu alloy specimens after 336 h of exposure. Heavy corrosion product, severe pitting and blistering were observed on the as-sputtered and conversion coated Al-30at.%Cu alloy specimens exposed for 504 h. This clearly showed that the zirconium-based conversion treatment failed on this copper-rich aluminium alloy within 504 h of exposure to the salt spray chamber.

At the end of 1000 h exposure to the salt spray, the conversion coated superpure aluminium specimens exhibited moderate to high coating performances. The specimens conversion treated for 180 s exhibited good corrosion performance compared with all

other treatment times. For the aluminium-copper alloys containing moderate levels of copper (Al-1.0at.%Cu and Al-5.0at.%Cu alloys), the 180 s conversion treatment time offers improved performance than all other conversion treatment times (Figure 6.50). Specifically, all the A-30at.%Cu alloy specimens were severely corroded. It is noted that the salt spray testing did change the appearance of the tested specimens. The surfaces of the specimens treated for 60 and 180 s were not as dark as all other A-30at.%Cu alloy specimens exposed to the salt fog for 1000 h (see Figure 6.46). From the results above, it can be concluded that both the conversion treatment time and the percentage copper composition of the copper-containing aluminium alloys have significant effect on the coating performance of zirconium-based conversion treated superpure aluminium and aluminium-copper alloys.

6.5 Discussion

The potential-time and polarisation records of the specimens reveal that the conversion treatment time influences the behaviour of the zirconium-based conversion coatings formed on the alloy surfaces in the presence of chloride species. In order to compare the influence of the zirconium conversion coating on aluminium-copper alloys, their behaviour on superpure aluminium (with no deliberate alloying addition) is considered initially, thus providing a basis for comparing the alloy behaviour.

6.5.1 Electrochemical corrosion behaviour of the coatings

6.5.1.1 Polarisation studies of superpure Aluminium

The open circuit potential and polarisation behaviour reveal that as-sputtered superpure aluminium specimen in 3.5 wt.% NaCl solution is in the passive region under natural immersion conditions, with a potential of approximately -1255 mV, which is well below the pitting potential of –745 mV. Under this condition, the superpure aluminium specimen is in the passive state with the initial air-formed alumina film presenting a passive surface in the aqueous solution [63-65]. In chloride-containing environment however, localised breakdown of the protective aluminium oxide film, proceeding at sites of mechanical flaws is repaired. Hence, repassivation proceeds spontaneously at the potential of natural immersion [169].

After shorter immersion times of 60 s in the conversion bath solution, the cathodic current density was reduced. Such behaviour indicates that after this treatment time, the zirconium conversion coating significantly blocks the path of the oxygen reduction reaction. Hence, the corrosion current density of the shorter immersion time of 60 s in the zirconium bath indicates the best inhibition performance compared to other treatment times.

The anodic polarisation curve of the as-sputtered superpure aluminium specimen in deaerated sodium chloride solution reveals a passive region below the pitting potential. The passive current density was of the order of 10^{-7} A/cm^2 and the pitting potential was -750 mV. For the conversion coated specimens treated for relatively short periods (30, 60, 180 s), the passive current densities were approximately the same as that obtained for the as-sputtered specimen. However, for specimens immersed for 300 s, the passive current density was reduced, but remained in the order of 10^{-7} A/cm^2 while a slight (in the order of 10^{-7} A/cm^2) increase in current density was observed for the specimen treated for 600 s in the zirconium bath. This is likely due to the presence of some defects in the coatings developed on the superpure aluminium specimen after the prolonged treatment time of 600 s. With the exception of the specimens conversion treated for the 60 s, which shows a large increase in pitting potential, the increases in the pitting potential of all the other treatment times were low. The behaviour of the aluminium specimens treated for 60 s in the zirconium bath i.e. reduction of the passive current density and increase in pitting potential suggest that the zirconium-based conversion coatings formed on the aluminium substrate modifies the behaviour of the superpure aluminium substrate at flaw sites thus limiting the dissolution of Al^{3+} ions. The ZrO_2 layer strongly reduces the area available for cathodic reactions, which is expected to take place only in the areas of film containing defects and thus, it blocks the path for oxygen reduction reaction.

By comparing the cathodic and anodic polarisation curves (Figures 6.7 and 6.22) for superpure aluminium, it is evident that in deaerated solutions the corrosion potential of aluminium was significantly shifted to more negative potential values compared to the corrosion potential exhibited by superpure aluminium in aerated solution. This phenomenon indicates that, in aerated solution, oxygen reduction reaction taking place

on the aluminium surface is a decisive cathodic process determining the open circuit potential of aluminium [13].

6.5.1.2 Polarisation studies of the binary model Al-Cu alloys

The behaviour of the as-sputtered aluminium-copper (1.0, 5.0, 10 and 30 at.% Cu) alloy in 3.5 wt.% NaCl solution differs from that of the superpure aluminium. The deliberate addition of the copper alloying element contributes to the change in the measured open circuit potential. Additionally, second phase particles such as Al_2Cu (identified by XRD study) is present in these alloys, with potential differences from the adjacent matrix, creating additional cathodic and anodic sites on the alloy substrate.

The open circuit potential of the as-sputtered Al-1.0at.%Cu, Al-5.0at.%Cu, Al-10at.%Cu and Al-30at.%Cu alloy in aerated sodium chloride solution are -725.91, 718.69, 762.58 and 710.08 mV respectively. These values are very close to the pitting potential of superpure aluminium. Thus, thermodynamically, the addition of copper alloying element shifts the open circuit potential in the positive direction which is in good agreement with the results obtained by Galvele et al [31].

The cathodic polarisation curves of the various alloys reveal that the cathodic reaction of the as-sputtered alloys is mainly that of oxygen reduction, with a limiting current density in the range of 10^{-6} A/cm^{-2} for the Al-1.0at.%Cu, Al-5.0at.%Cu, and Al-10at.%Cu alloys which is 10 times greater than that for superpure aluminium. However, for the Al-30at.%Cu alloy, a limiting current density in the range of 10^{-5} A/cm^{-2}, which is 100 times greater than that for superpure aluminium, was obtained. Hence, it is evident that for aluminium alloys with deliberate copper alloying element, the relatively noble Al_2Cu intermetallic particles create increased population densities of the effective cathodic sites to support the oxygen reduction reaction. Furthermore, in terms of kinetics, the exchange current density for oxygen reduction reaction at such sites is greater than the active flaw sites on superpure aluminium substrates.

The Al-1.0at.%Cu alloy specimens conversion coated for 60 s and 180 s exhibit a strong and moderate increase in open circuit potential respectively and a strong reduction (for specimens coated for 60 s) of the cathodic current density compared to the as-sputtered alloy, thus indicating that zirconium conversion coating layer formed

after this treatment times inhibit cathodic reactions. Furthermore, the corrosion potentials of the conversion treated alloy specimens were displaced in the negative direction. This suggests the tendency of the zirconium conversion coatings to inhibit the cathodic reactions. The cathodic reaction taking place on both the surface of the as-sputtered and conversion coated alloy is that of oxygen reduction and water reduction. The first reaction is the most likely to occur during polarisation while the second reaction takes place only at relatively negative potentials [301]. Therefore, the increase of current density visible for all polarisation curves in Figure 6.10 at potentials more negative than -1125 mV (SCE) is probably due to water reduction.

With the exception of the Al-5.0at.%Cu alloy conversion coated for 600 s which exhibited a moderate increase in the open circuit potential, all the other conversion coated specimens exhibit moderately low decrease in open circuit potential compared with the as-sputtered alloy, and, after this conversion treatment time, the lowest corrosion current density was exhibited. This indicates that the conversion coatings formed on the alloy surface after 600 s conversion treatment time, inhibit the cathodic reaction. The cathodic reaction taking place in this alloy is similar to that observed on the Al-1.0at.Cu alloy but with water reduction reaction taking place at potentials more negative than approximately -1000 mV (SCE).

For the conversion coated Al-10at.%Cu alloy, a slight increase in open circuit potential is evident compared with the as-sputtered alloy in aerated chloride solution. However, the corrosion potential of the sputtered alloy was shifted to more positive values as a result of the conversion treatment process. This positive shift in the corrosion potentials of the conversion treated alloy suggests that conversion coating formed on this alloy exhibit little or no efficient barrier protection. With the exception of the alloy specimen conversion coated for 600 s, which exhibited a slightly reduced corrosion current density, the 30, 60, 180 and 300 s conversion treatment times are associated with relatively high corrosion current densities. This also suggests that the conversion coatings formed on the alloy after these treatment times will provide less efficient barrier protection against the anodic dissolution of the alloy under the aggressive conditions investigated.

Compared with the as-sputtered Al-30at.%Cu alloy, a slight decrease in open circuit potential was observed for the conversion treated alloy. However, the conversion coated

Al-30at.%Cu alloy also exhibited a slight positive shift in the corrosion potential compared with the as-sputtered alloy. This positive shift in corrosion potential is similar to that observed for the conversion treated Al-10at.%Cu alloy. The rather slight increase in corrosion potential observed for this alloy indicates that the conversion treatment gives little or no barrier protection against the cathodic reaction taking place.

The difference between the corrosion potential (E_{corr}) and the pitting potential (E_{pit}) can be used to evaluate pitting corrosion resistance of the conversion treated specimens. For the conversion treated Al-1.0at.%Cu alloy specimens, an increase in open circuit potential and pitting potential is observed. Anodic polarisation curves for the conversion treated alloy specimens in deaerated sodium chloride solution were characterised by a positive shift in the corrosion potential and a high open circuit potential relative to the as-sputtered alloy. The anodic polarisation curves are strongly influenced by the existence of defects in the conversion coatings formed on the alloy. However, the shorter conversion treatment time of 30 s displayed a significant effect (E_{corr} was shifted to more negative value) although the open circuit potential was similar and the pitting potential remained almost the same for the as-sputtered alloy. This indicates that the conversion coatings formed on the alloy specimen after the shorter treatment time of 30 s acts to reduce the anodic reaction on the alloy.

Anodic polarisation curves for the conversion treated Al-5.0at.%Cu alloy specimens were characterised by a strong positive shift in the corrosion potential and a high open circuit potential and anodic current densities relative to the as-sputtered alloy. However, the conversion treated Al-5.0at.%Cu alloy specimens did not show an extended passive region compared with that exhibited by the as-sputtered alloy specimen. This indicates that the conversion coating formed on the alloy, most likely exhibits several defects in the conversion layer mainly in the form of cracks or small coating portions detached from the alloy substrate. Hence, the zirconium conversion coating does not modify the behaviour at flaw sites.

For the Al-10at.%Cu alloy, a similar behaviour to that exhibited by the conversion treated Al-5.0at.%Cu alloy is observed. Although positive shifts in corrosion potentials were observed for the conversion treated alloy, the anodic current densities were also shifted towards more positive values. Hence, for this alloy, the zirconium conversion

treatment does not provide significant anodic barrier properties. This is likely due to cracks or flaws in the coatings formed on the alloy.

An evaluation of zirconium conversion treatment for the corrosion protection of the Al-30at.%Cu alloy shows that the zirconium-based conversion coating protects the alloy surface from pitting by suppressing the corrosion potential while transporting the pitting potential to more positive values. The anodic polarisation curve for the alloy conversion treated for 180 s exhibit an extended passive range characterised by a very low anodic current density. The corrosion current density for the 180 s conversion treatment time is much lower than that for the as-sputtered alloy including all other treatment times. This indicates that the conversion coatings formed on the alloy after 180 s immersion in the zirconium-based conversion solution are able to protect the substrate by providing a good barrier against localised corrosion attack.

By comparing the cathodic and anodic polarisation curves for each of the as-sputtered superpure aluminium and Al-Cu model alloys, it is evident that in deaerated solutions the corrosion potentials of the superpure aluminium, Al-1.0at.%Cu and Al-5.0at.%Cu alloys were significantly shifted to more negative potential values compared with their corrosion potential in aerated solution. This phenomenon indicates that in aerated solution oxygen reduction taking place on the aluminium surface is a decisive cathodic process determining the open circuit potential of aluminium. On the other hand, the corrosion potentials of the Al-10at.%Cu and Al-30at.%Cu alloys changed far less as a result of the deaerated condition, revealing that reduction of dissolved oxygen is a slow process on the surface of these alloys.

6.5.2 Filiform corrosion

Several studies on filiform corrosion of painted aluminium [136, 141, 301] have emphasised the significance of the near-surface substrate microstructure. Highly deformed surface layers (of the order 1 μm in thickness) on rolled aluminium sheet may become electrochemically active as a result of subsequent heat treatment. The high susceptibility of aluminium alloys to filiform corrosion was primarily attributed to a fine distribution of cathodic intermetallic particles in the surface layer [141, 301]. Filiform corrosion is usually initiated at areas of defects in the oxide layer. The filiform corrosion filaments consists of two parts namely, an active head and a trailing tail.

Filament propagation is driven by oxygen which diffuses through the filament tail and leads to the separation of anodic and cathodic regions. This implies that the principal site of cathodic oxygen reduction lies towards the trailing edge while that of the anodic metal dissolution lies towards the leading edge of the filament head. The aluminium chloride and other hydrolysis products of aluminium salt solution that are formed maintained a low pH [128]. When this condition is sufficiently aggressive, it weakens the adhesion of the coating and thus initiates filiform corrosion. Therefore, efficient inhibition of the reduction reactions occurring at the cathodic particles should be an important characteristic of conversion coatings to prevent filiform corrosion.

In this study, the results obtained for the zirconium-based conversion treated specimens indicate that the formation of the conversion coating significantly reduced the extent of continuous disbonding along the scribe. Since filiform corrosion attacks shorter than 2 mm are normally considered to be an acceptable result in this test, evidently, good filiform corrosion resistance can be obtained by the zirconium-based conversion treatment. Although acceptable results were obtained for the as-sputtered specimens, the zirconium-based conversion coating possesses the ability to inhibit the corrosion process and to provide better coating adhesion. The results obtained for all the conversion treatment time indicate that poor zirconium conversion coating coverage (obtained after shorter immersion times) of the aluminium and alloy matrixes does not necessarily imply a poor filiform corrosion resistance conversion coated specimens. Filiform corrosion studies conducted by Afseth et al [141], provided strong evidence that filiform corrosion is largely controlled by microgalvanic coupling between the aluminium matrix and noble second phase particles. Thus, the efficient inhibition of the cathodic activity on intermetallic particles is likely more important than complete coverage of the aluminium matrix as far as filiform corrosion resistance is concerned. Poor zirconium conversion coating (ZrCC) coverage may, however, cause reduced adhesion to paints and adhesives since the aluminium oxide/polymer interface area would exhibit a lower hydrolytic stability than the ZrCC/polymer interface.

6.5.3 Salt spray

Salt spray testing provides information about the combined impact of corrosion attack and adhesion. ASTM B117 salt spray testing examined the degree of uniformity and

porosity of the coating layer and also revealed general information about the barrier properties of the zirconium-based conversion coating. The results in Figures 6.47 – 6.50 indicated that the superpure aluminium specimen coated for 180 s in the zirconium conversion bath solution, performed successfully and protected the sputtered-deposited superpure aluminium specimens from corrosion attack by pitting throughout the entire salt spray exposure time of 1000 h. It appears that the conversion coating formed on Al-1.0at.%Cu, Al-5.0at.%Cu and Al-10at.%Cu alloys after 180 s immersion conversion bath exhibit some barrier properties against corrosion attack in the salt fog. However, for the Al-30at.%Cu alloy, the results in Figures 6.49 – 6.50 indicated the alloy specimens conversion coated for 180 s exhibited a moderate level of protection. However, at the end of the 504 h exposure to the salt fog, no single conversion treatment time is successful on the Al-30at.%Cu alloy. It appears that the scribe on the alloy allowed the penetration of NaCl solution into the alloy substrates. The porosity of the conversion coating act as a transport conduit for the aggressive chloride solution and delamination and blistering of the coating were evident at the end of 168 h of salt spray exposure. Thus, it can be concluded that the bad corrosion protection of the Al-30at.%Cu alloy is due to the porosity and poor adhesion properties of the conversion coating.

6.6 Summary

A simple and environmentally friendly zirconium-based conversion coating treatment has been examined and tested for the corrosion protection of aluminium alloys. The following is a summary of key findings.

1. An increase of the copper concentration in the nominal composition of the binary Al-Cu alloys increased the activity of the conversion treated alloys compared with the conversion treated superpure aluminium specimens. Thus, aluminium-copper alloys are more difficult to protect due to copper enrichment which hinders passivation reaction when the alloy are conversion treated.

2. The zirconium-based conversion layer formed on the superpure aluminium specimens strongly reduces the area available for cathodic reaction

3. The zirconium-based conversion coating formed after 60 s and 180 s of treatment provides good corrosion resistance which can be attributed to the high stability of the compounds that constitute the surface oxide layer, and good adhesion properties.

4. The application of a zirconium-based conversion coating to the Al-30at.%Cu alloy improves the anodic inhibition of the alloy and reduces the corrosion current density.

5. The results of the filiform corrosion test obtained for all the conversion treatment time indicate that poor zirconium conversion coating coverage of the aluminium and alloy matrixes does not necessarily imply a poor filiform corrosion resistance conversion coated specimens.

6. The results obtained after exposure of superpure aluminium, Al-1.0at.%Cu, Al-5.0at.%Cu and Al-10at.%Cu alloys reveal that the zirconium-based conversion coatings provided good coating adhesion and barrier properties against corrosion attack in the salt fog

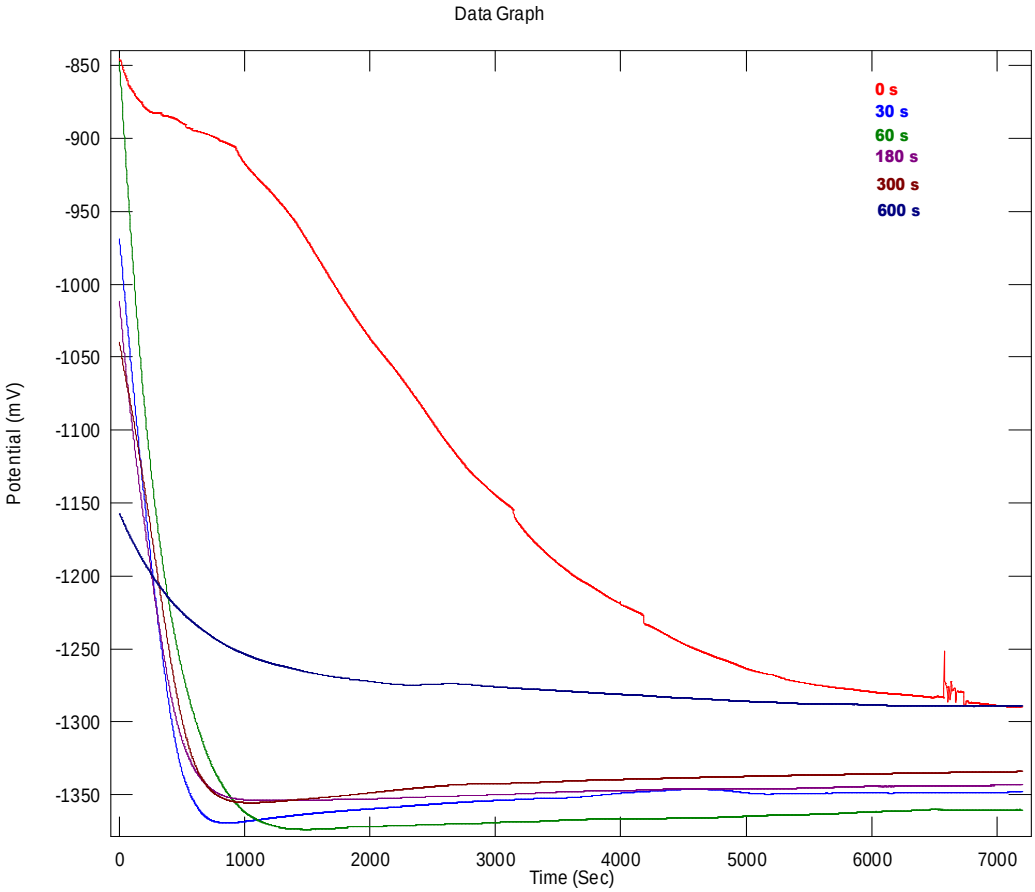

Figure 6.1 (a) A comparison of potential-time response of untreated and treated superpure aluminium specimens in aerated 3.5 wt.% NaCl solution.

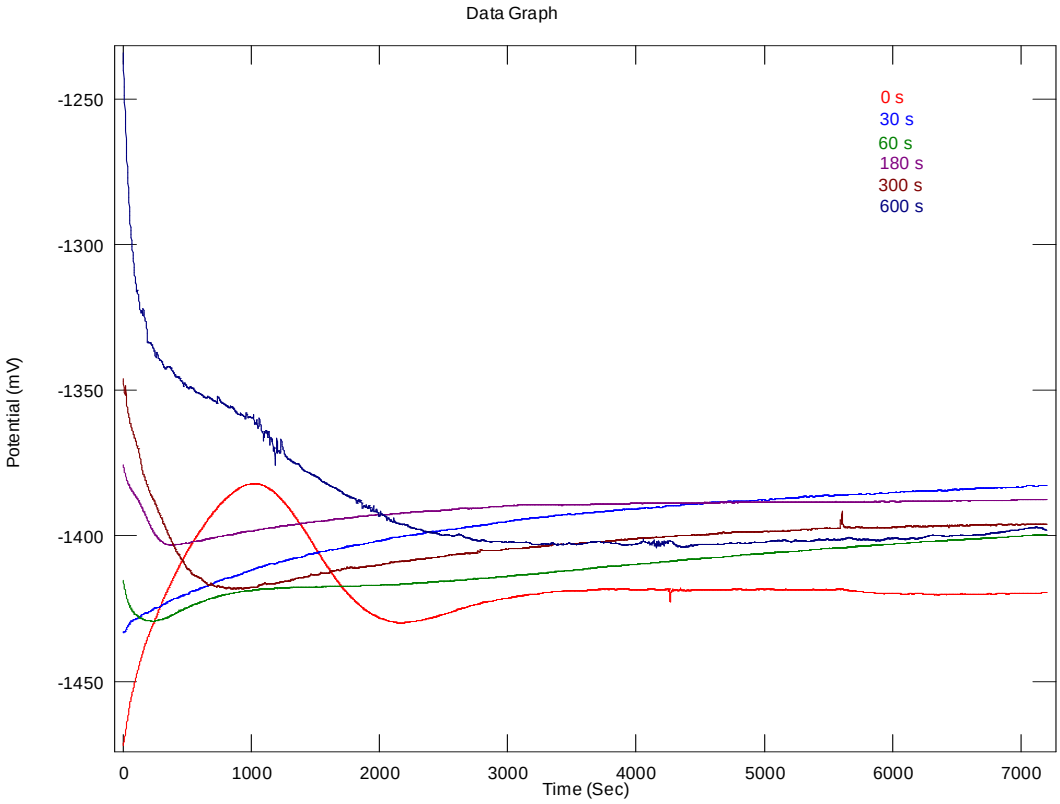

Figure 6.1 (b) A comparison of potential-time response of untreated and treated superpure aluminium specimens in deaerated 3.5 wt.% NaCl solution.

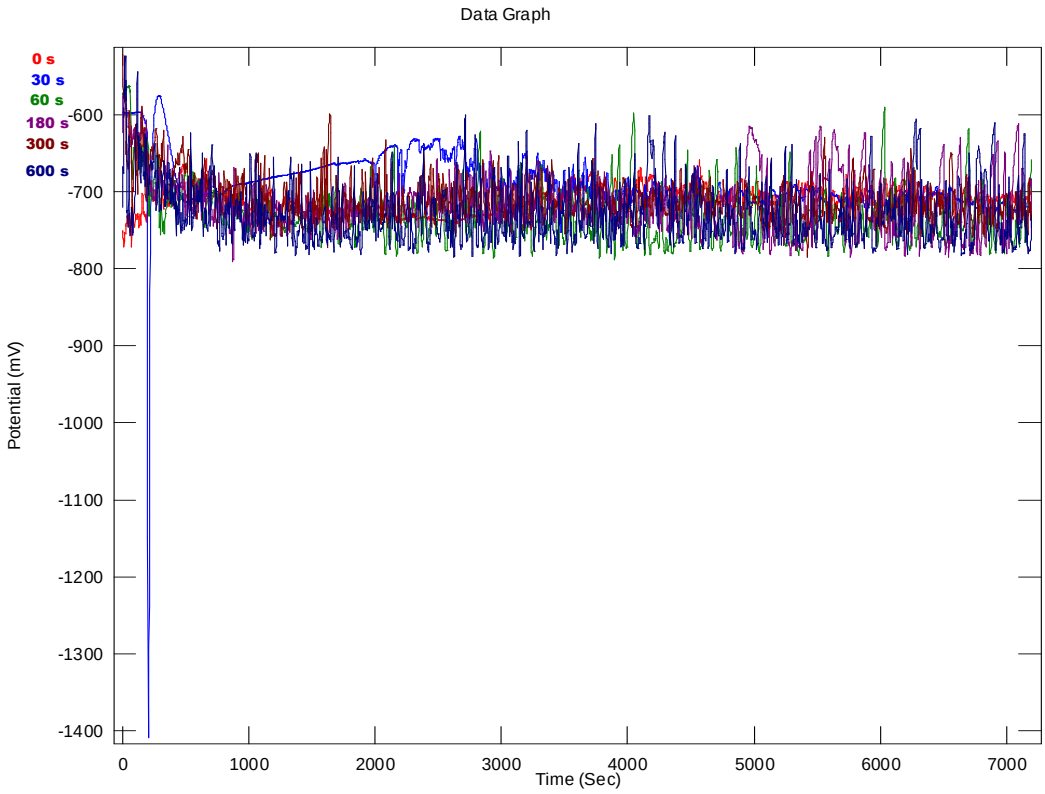

Figure 6.2 A comparison of potential-time response of untreated and treated the Al-1.0at.%Cu model alloys in naturally aerated 3.5 wt.% NaCl solution.

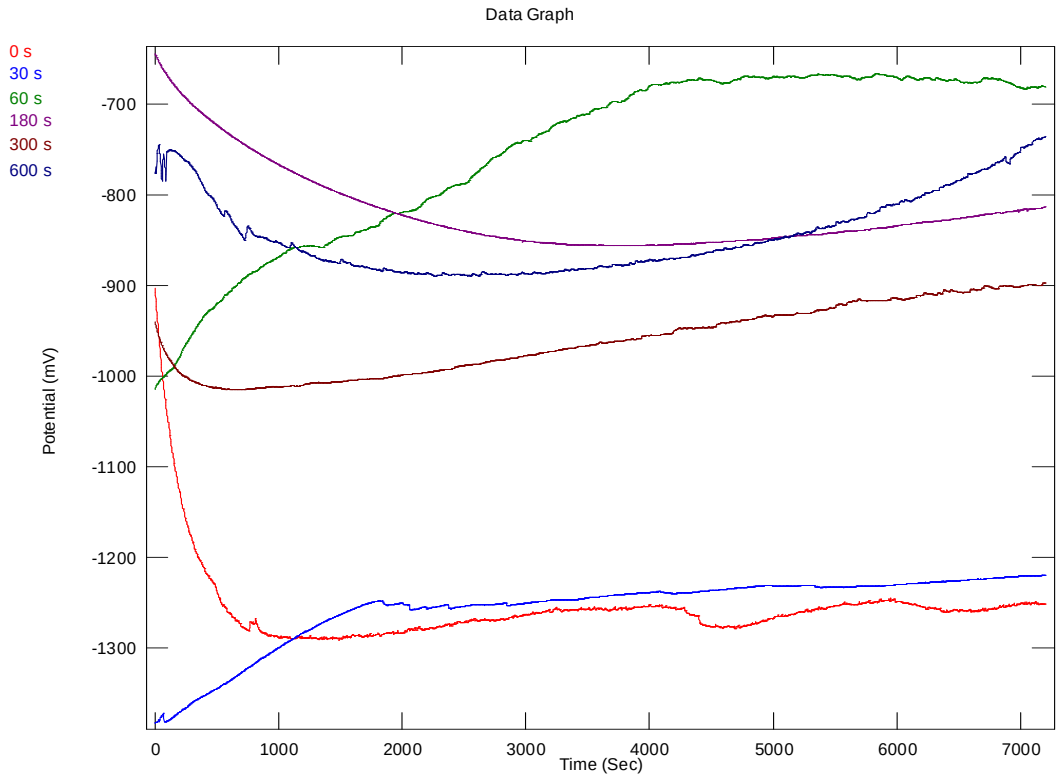

Figure 6.3 A comparison of potential-time response of untreated and treated the Al-1.0at.%Cu alloy in deaerated 3.5 wt.% NaCl solution.

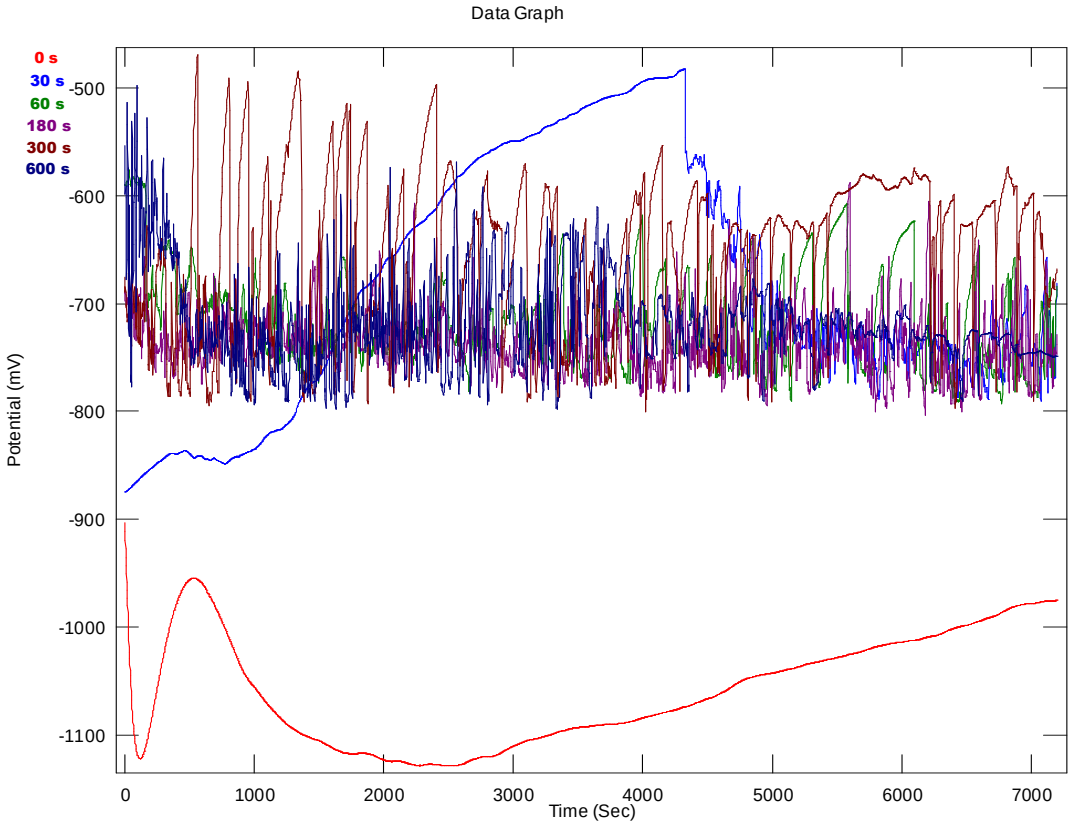

Figure 6.4 A comparison of potential-time response of untreated and treated the Al-5.0at.%Cu alloy in deaerated 3.5 wt.% NaCl solution.

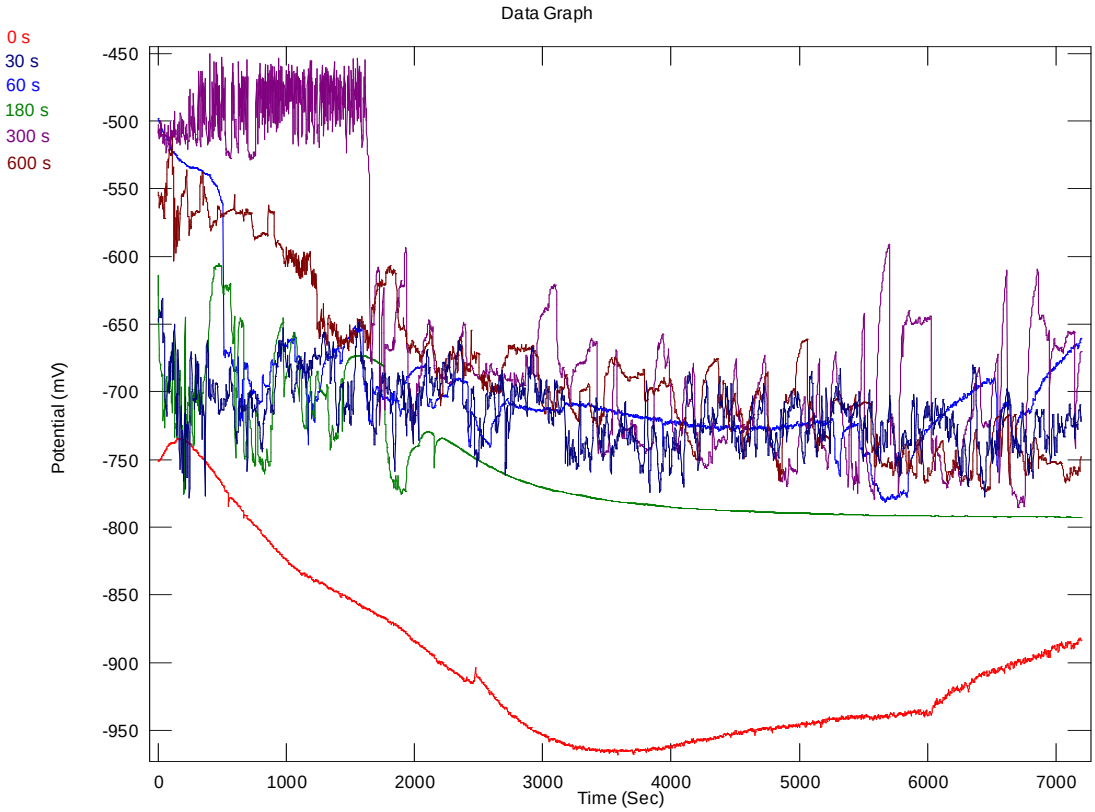

Figure 6.5 A comparison of potential-time response of untreated and treated the Al-10at.%Cu alloy in deaerated 3.5 wt.% NaCl solution.

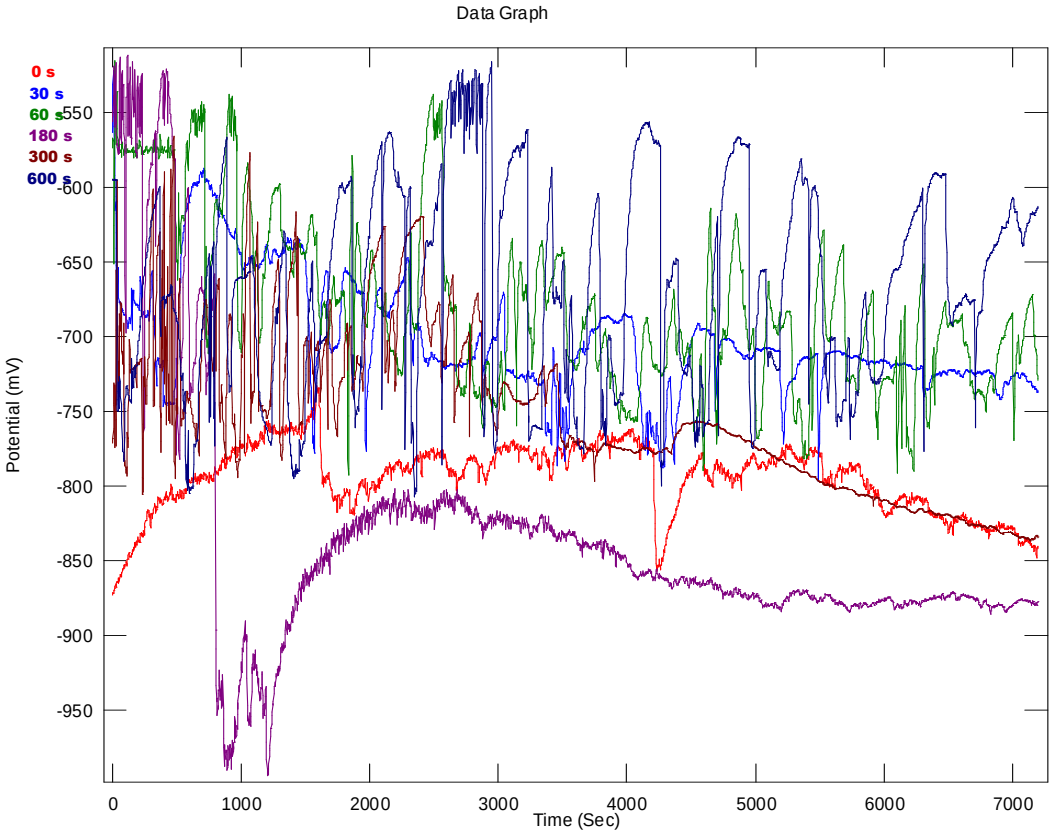

Figure 6.6 A comparison of potential-time response of untreated and treated the Al-30at.%Cu alloy in deaerated 3.5 wt.% NaCl solution.

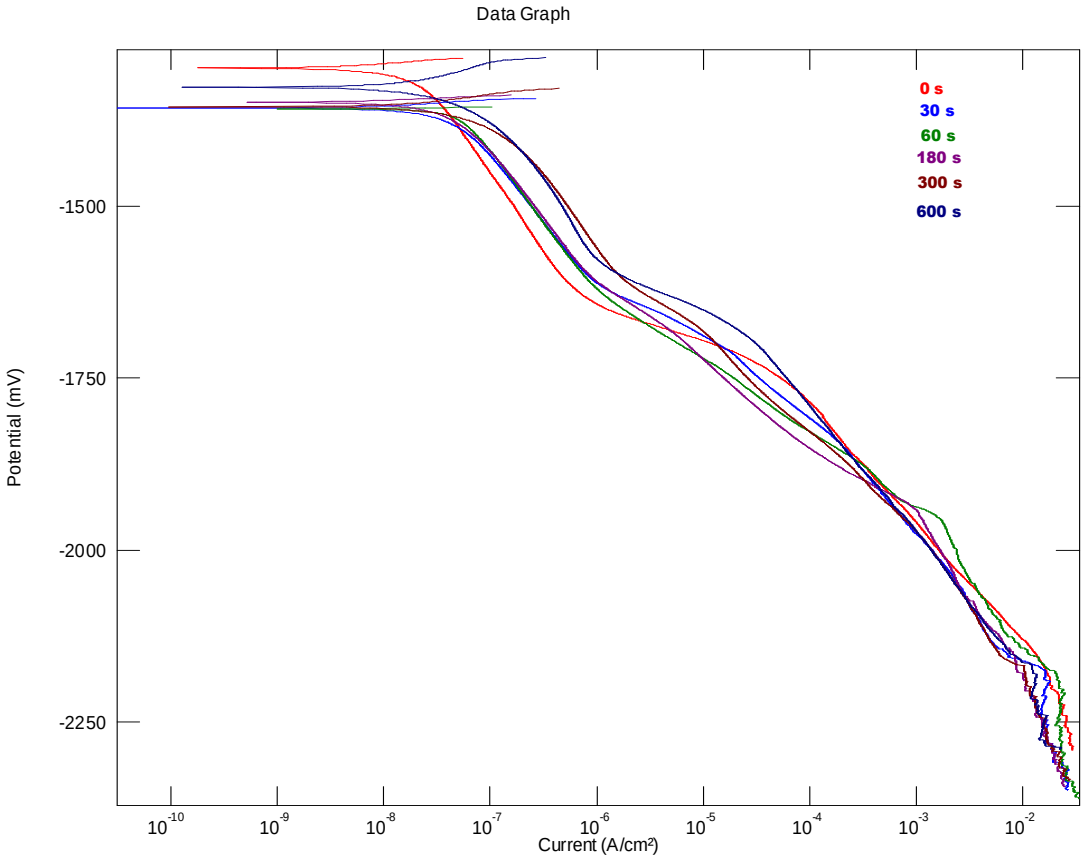

Figure 6.7 Cathodic polarisation response of untreated and treated superpure aluminium specimens in aerated 3.5 wt.% NaCl solution.

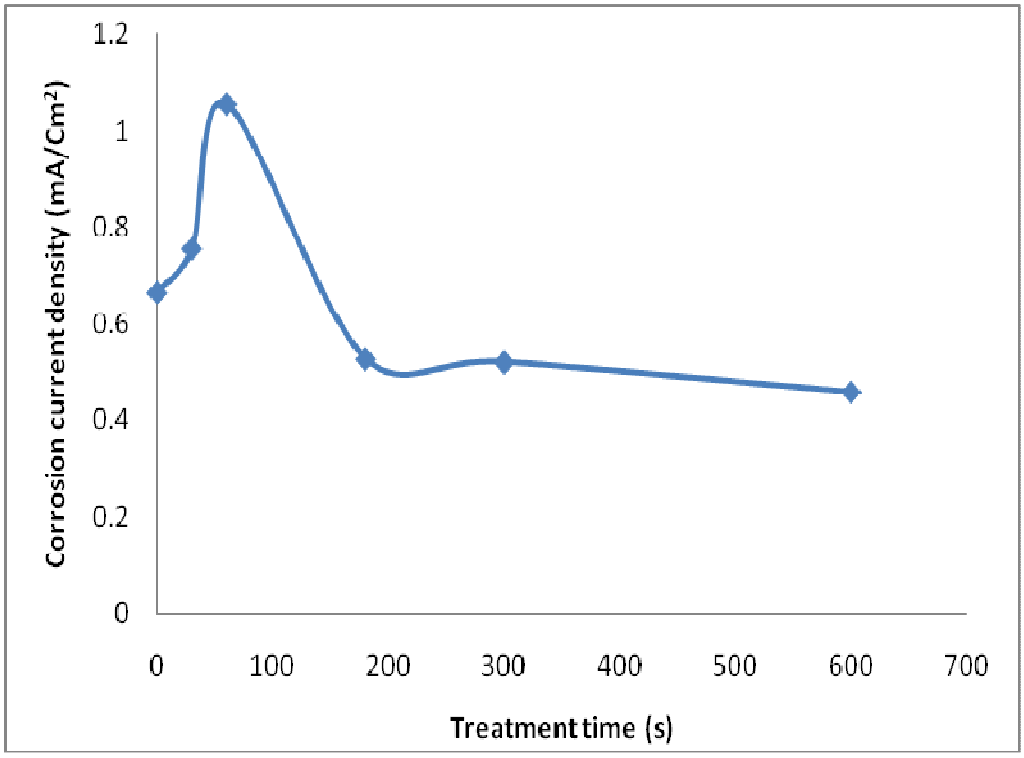

Figure 6.8 The relationship between corrosion current density and treatment times for superpure aluminium specimens in aerated 3.5 wt.% NaCl solution.

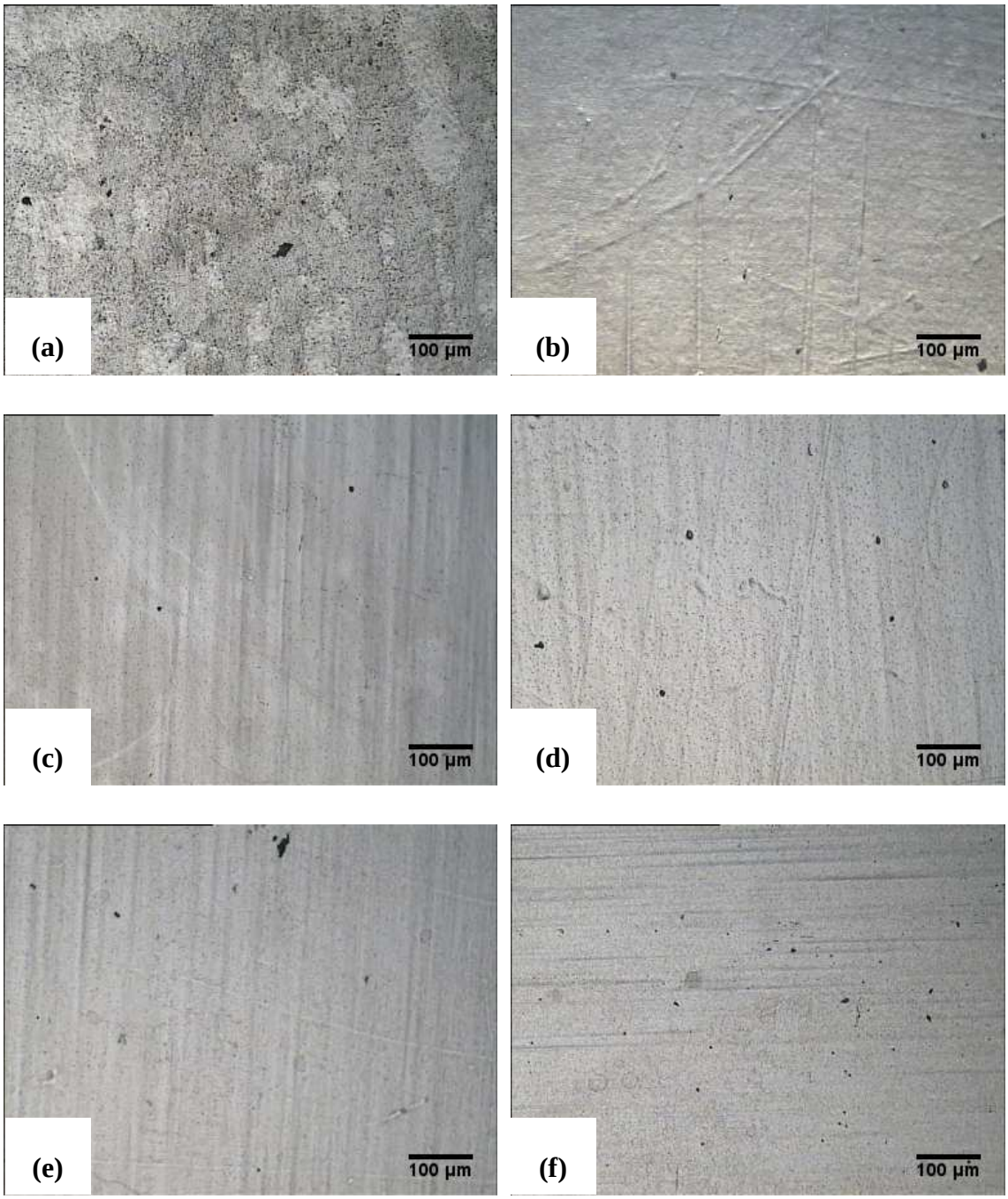

Figure 6.9 Optical micrographs of the treated and untreated superpure aluminium specimens after cathodic polarisation in aerated 3.5 wt.% NaCl solution. (a) 0 s (b) 30 s (c) 60 s (d) 180 s (e) 300 s and (f) 600 s treatment times in zirconium-based conversion treatment solution.

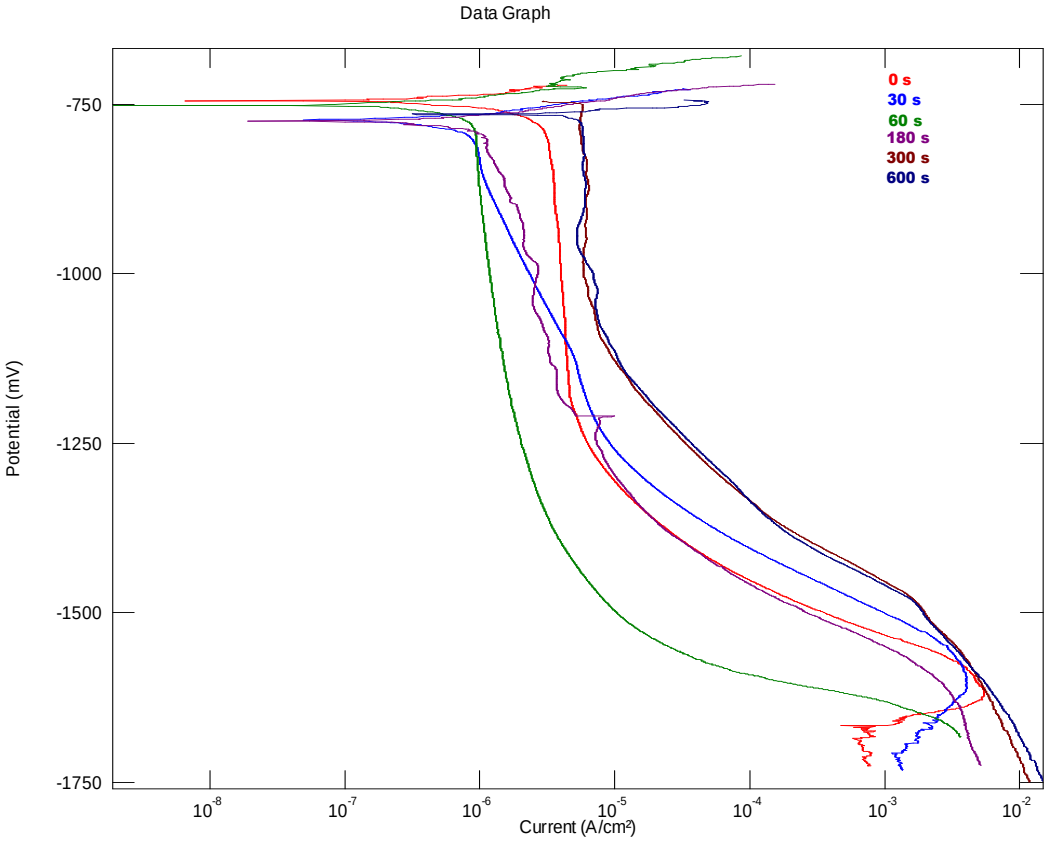

Figure 6.10 Cathodic polarisation response of untreated and treated Al-1.0at.%Cu alloys in aerated 3.5 wt.% NaCl solution.

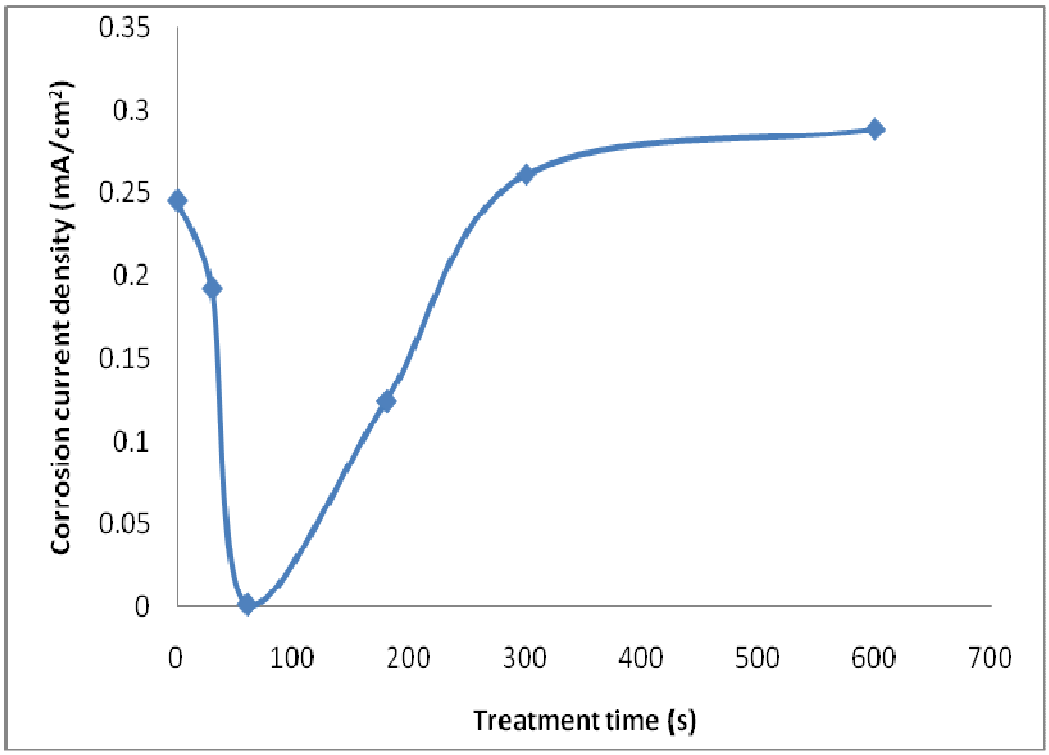

Figure 6.11 The relationship between corrosion current density and treatment times for Al-1.0at.%Cu alloys in aerated 3.5 wt.% NaCl solution.

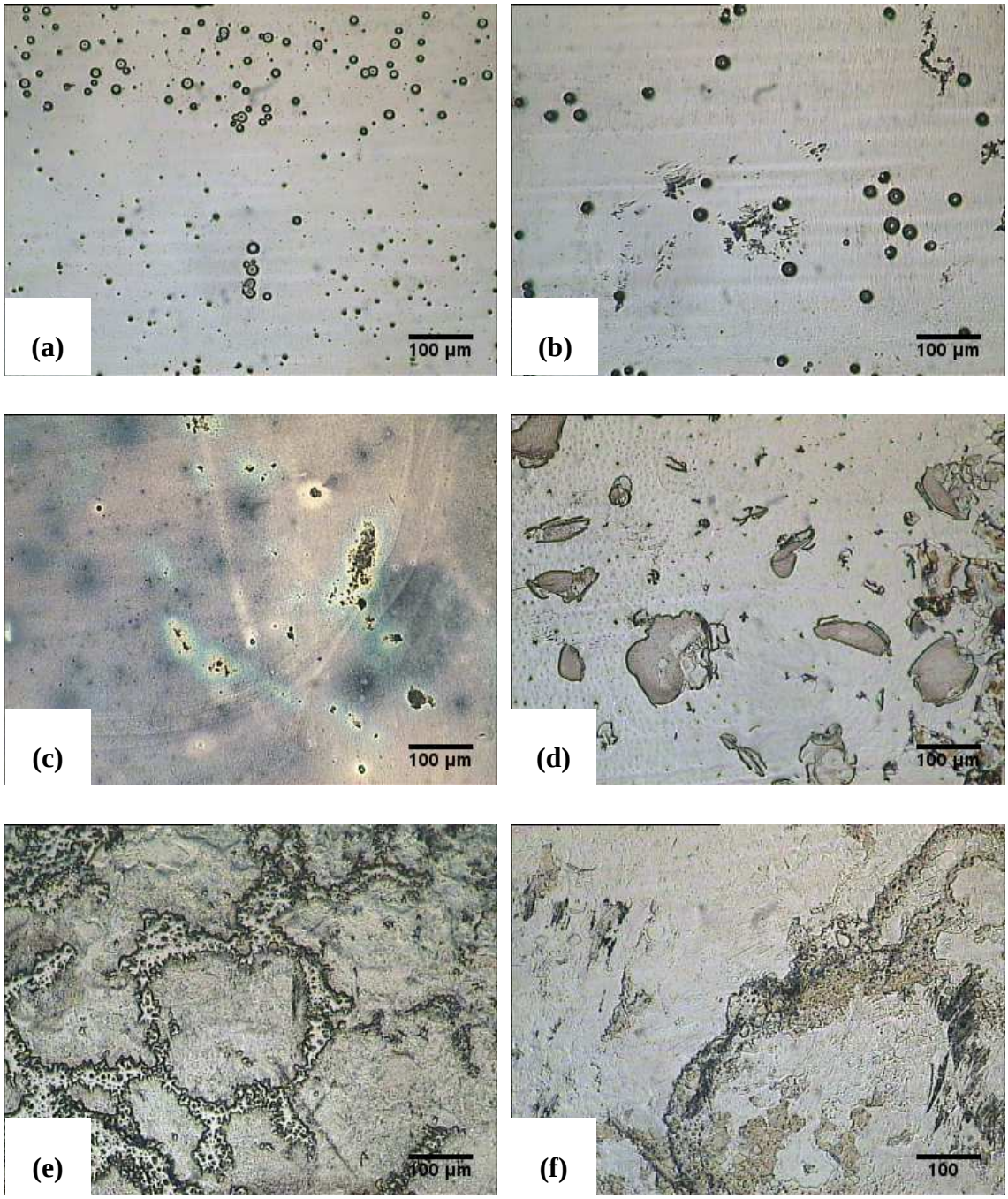

Figure 6.12 Optical micrographs of the treated and untreated Al-1.0at.%Cu alloy after cathodic polarisation in aerated 3.5 wt.% NaCl solution. (a) 0 s (b) 30 s (c) 60 s (d) 180 s (e) 300 s and (f) 600 s treatment times in zirconium-based conversion treatment solution.

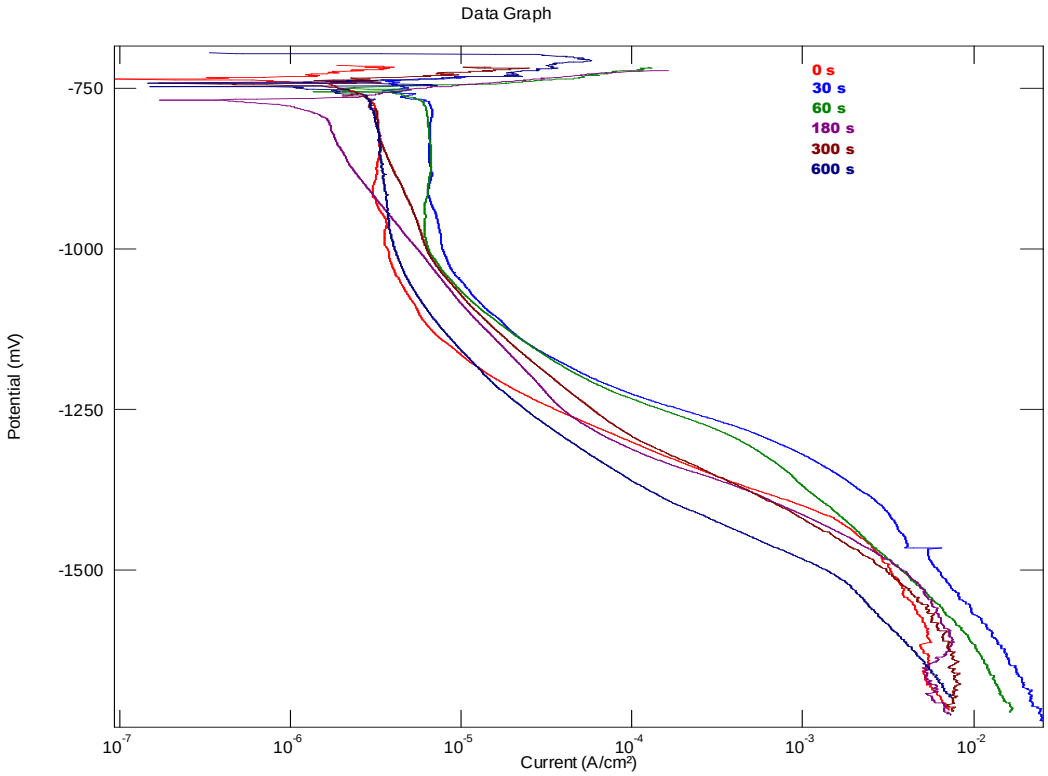

Figure 6.13 Cathodic polarisation response of untreated and treated Al-5.0at.%Cu alloys in aerated 3.5 wt.% NaCl solution.

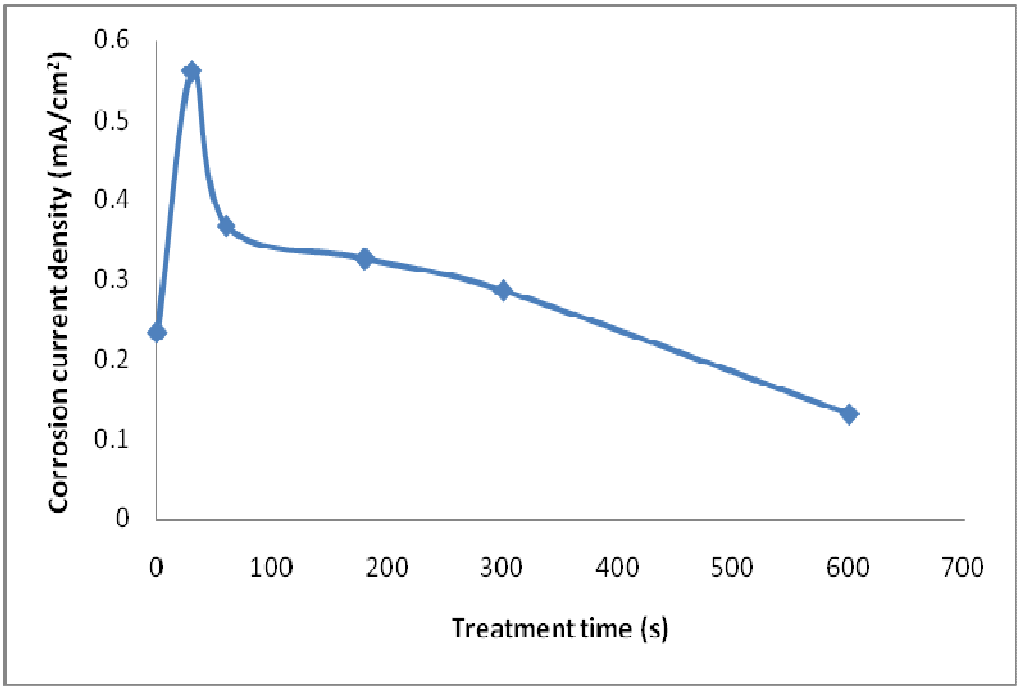

Figure 6.14 The relationship between corrosion current density and treatment times for Al-5.0at.%Cu alloys in aerated 3.5 wt.% NaCl solution.

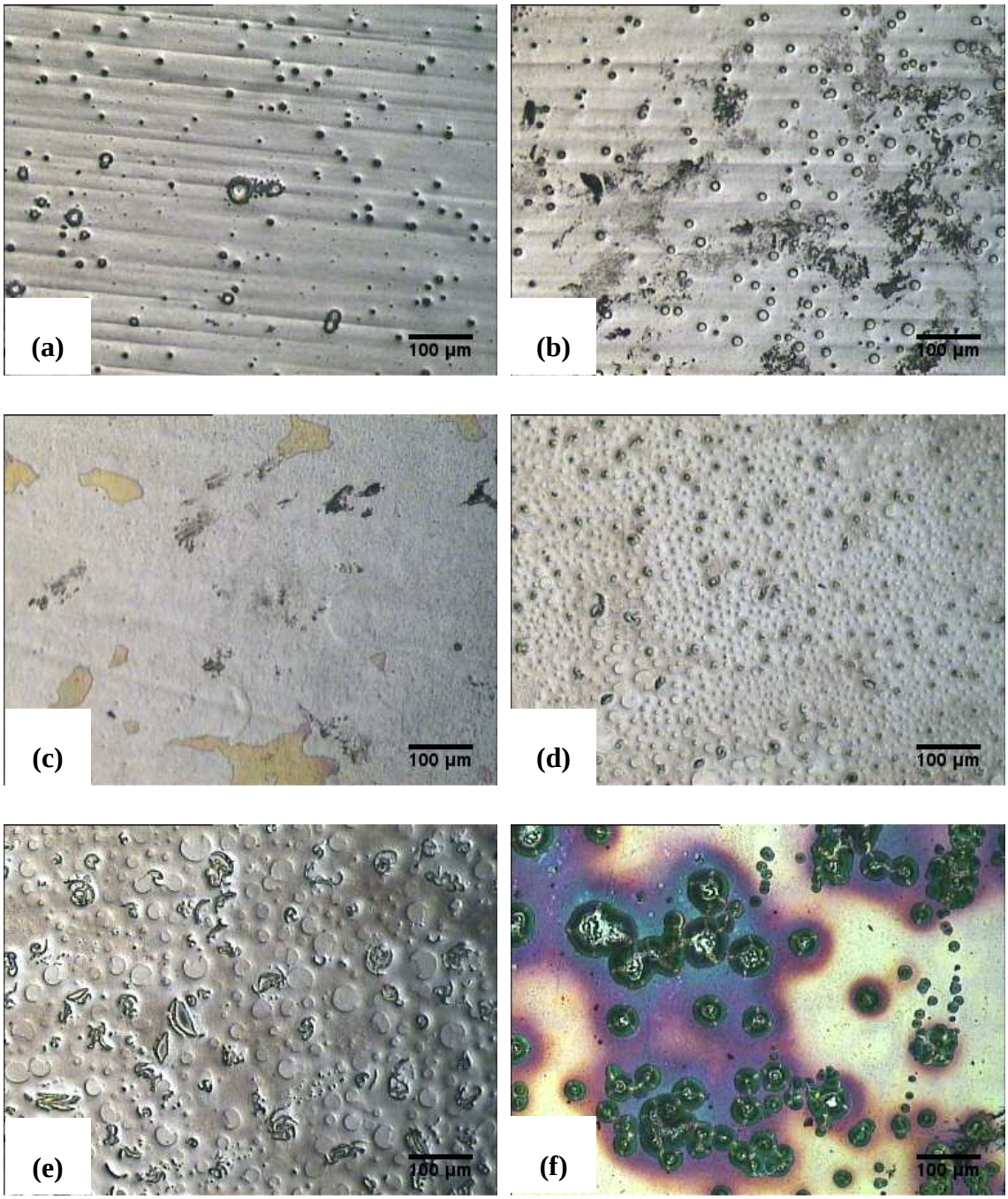

Figure 6.15 Optical micrographs of the treated and untreated Al-5.0at.%Cu alloy after cathodic polarisation in aerated 3.5 wt.% NaCl solution. (a) 0 s (b) 30 s (c) 60 s (d) 180 s (e) 300 s and (f) 600 s treatment times in zirconium-based conversion treatment solution.

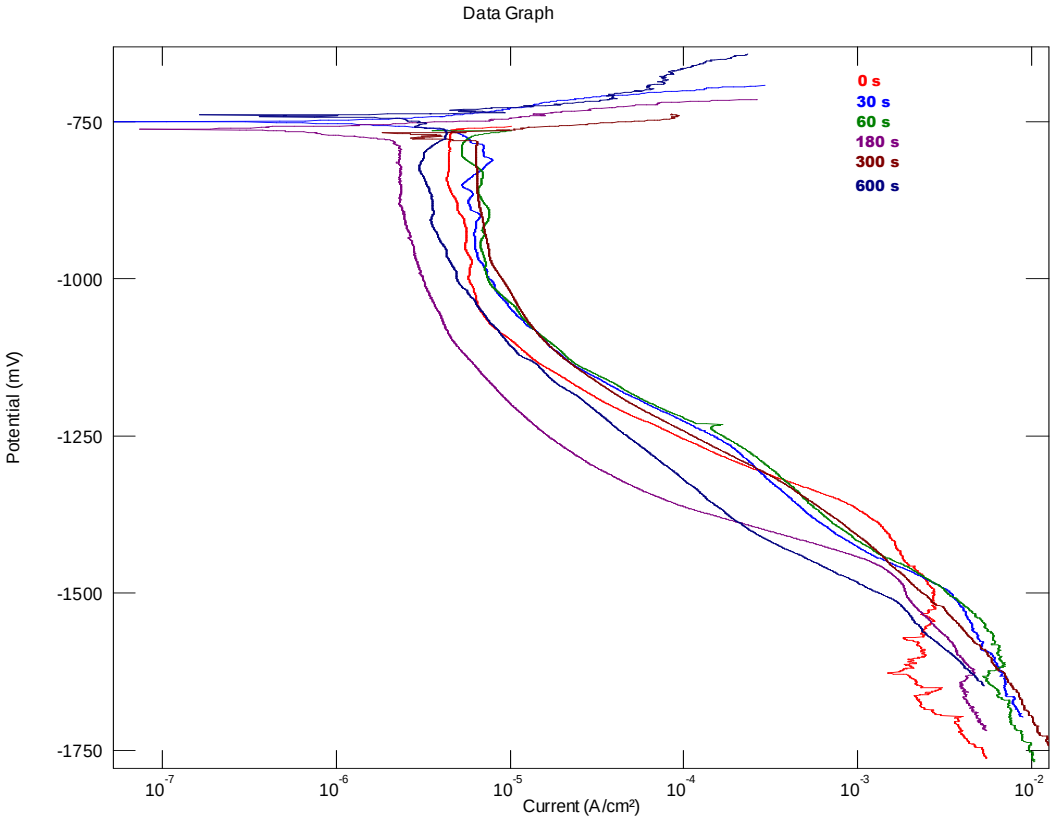

Figure 6.16 Cathodic polarisation response of untreated and treated Al-10at.%Cu alloys in aerated 3.5 wt.% NaCl solution.

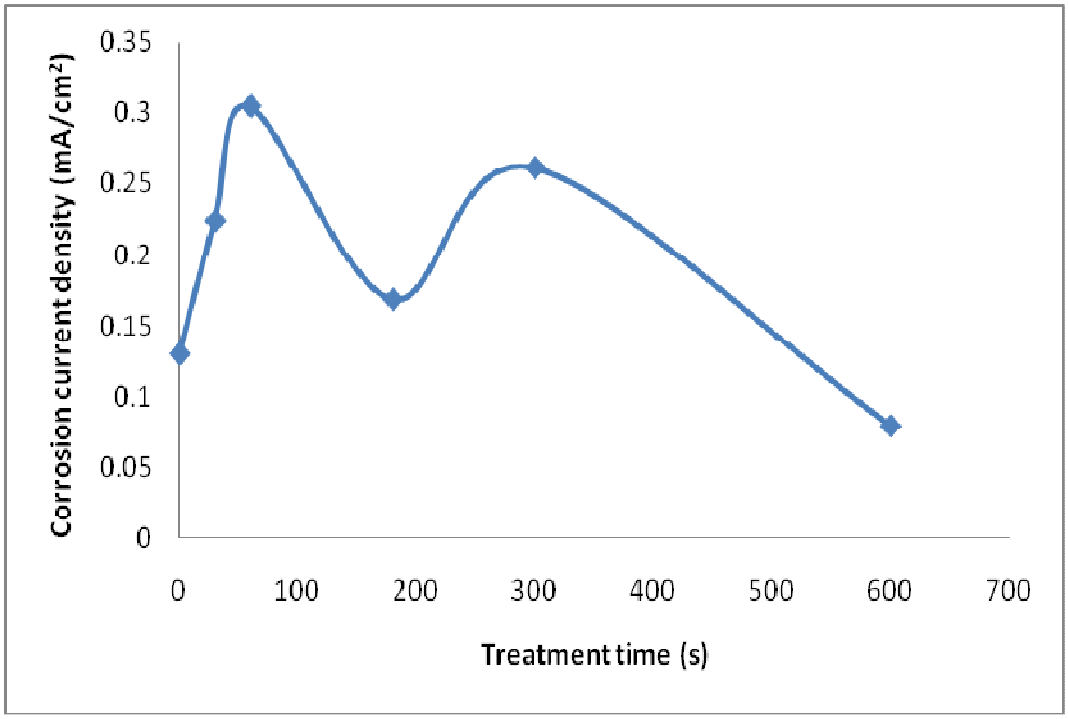

Figure 6.17 The relationship between corrosion current density and treatment times for Al-10at.%Cu alloys in aerated 3.5 wt.% NaCl solution.

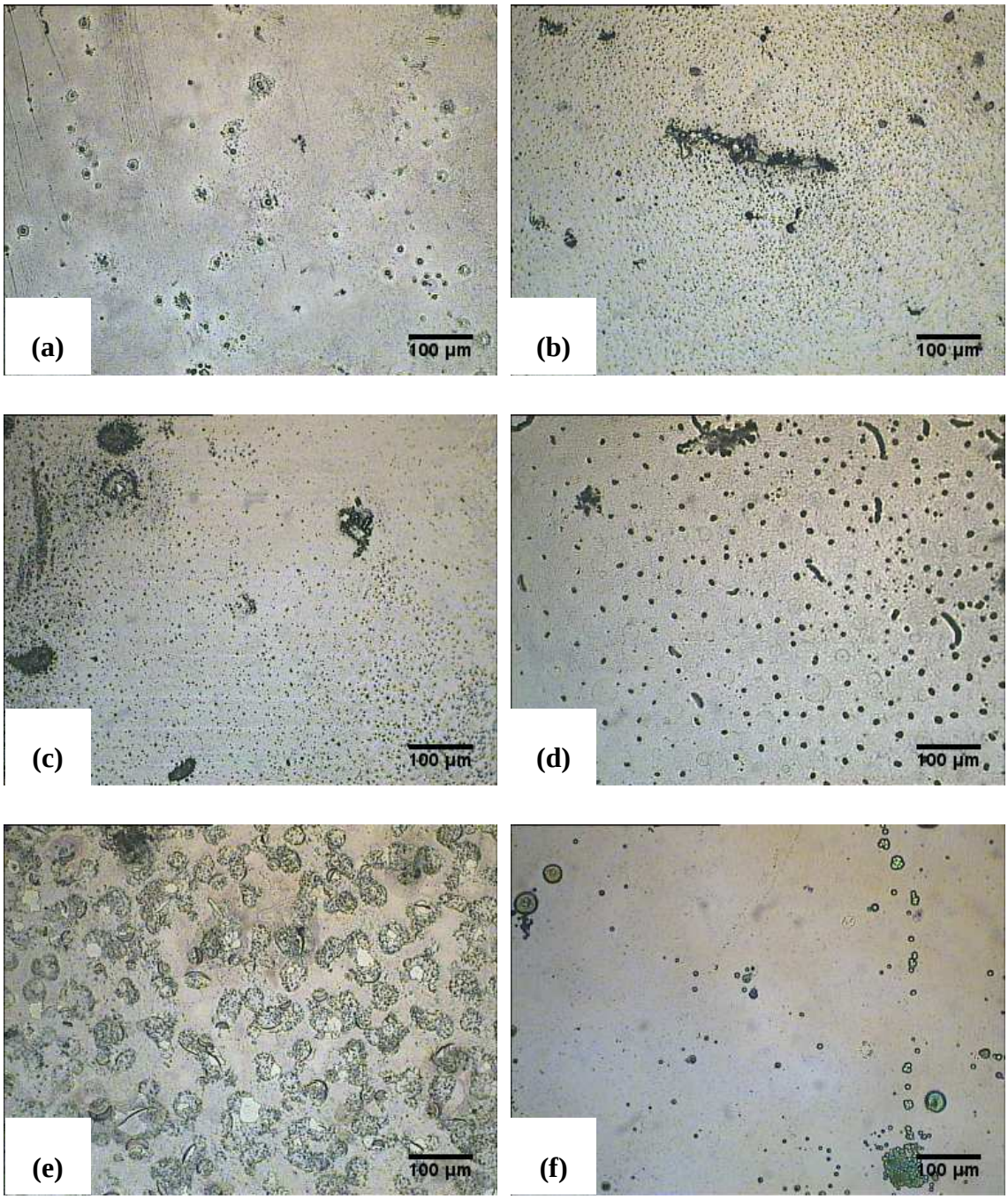

Figure 6.18 Optical micrographs of the treated and untreated Al-10at.%Cu alloy after cathodic polarisation in aerated 3.5 wt.% NaCl solution. (a) 0 s (b) 30 s (c) 60 s (d) 180 s (e) 300 s and (f) 600 s treatment times in zirconium-based conversion treatment solution.

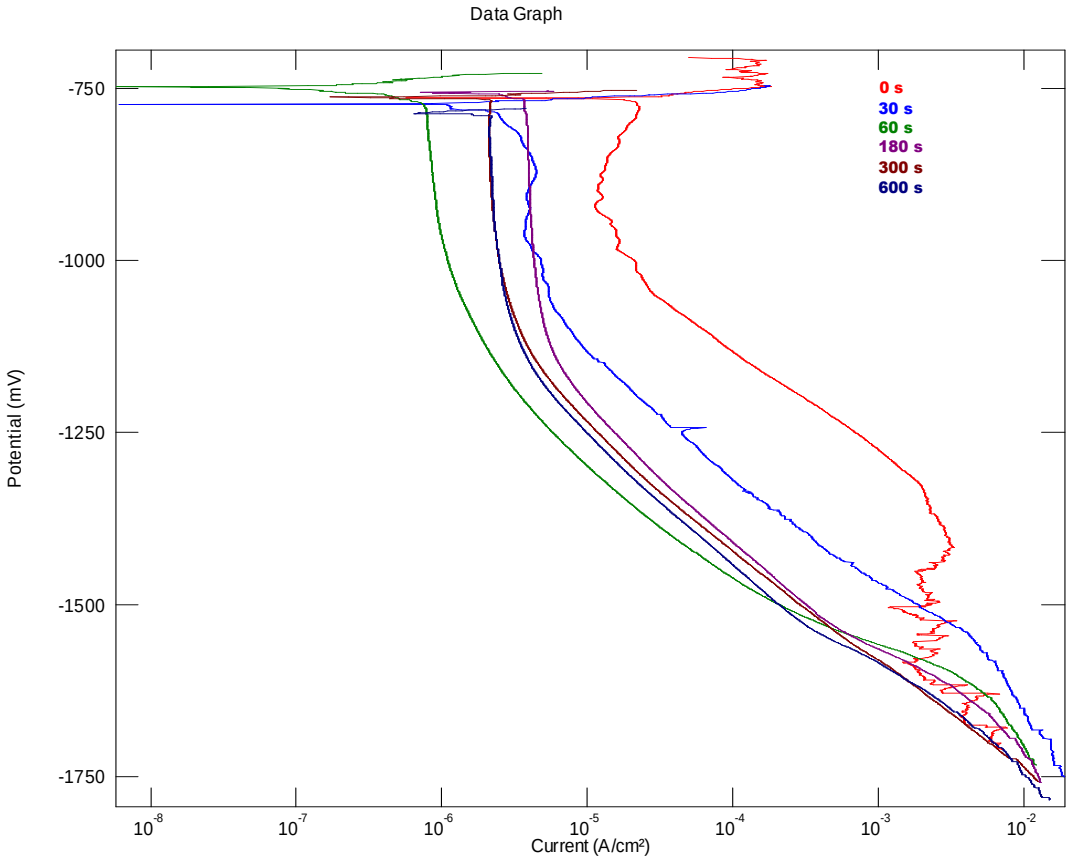

Figure 6.19 Cathodic polarisation response of untreated and treated Al-30at.%Cu alloys in aerated 3.5 wt.% NaCl solution.

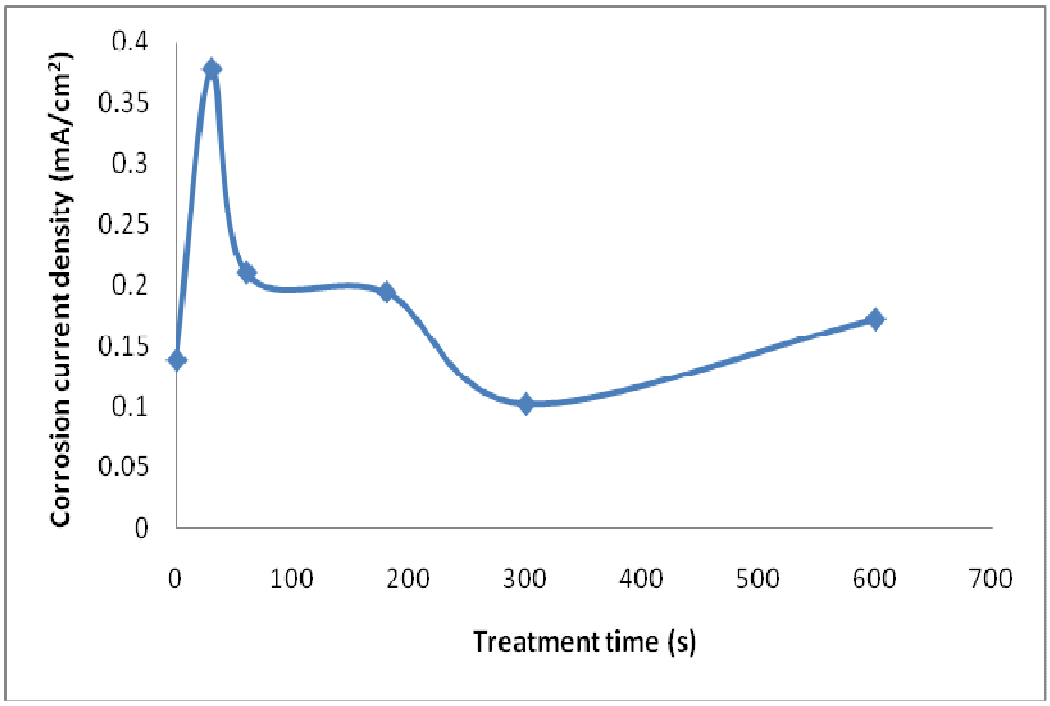

Figure 6.20 The relationship between corrosion current density and treatment times for Al-30at.%Cu alloys in aerated 3.5 wt.% NaCl solution.

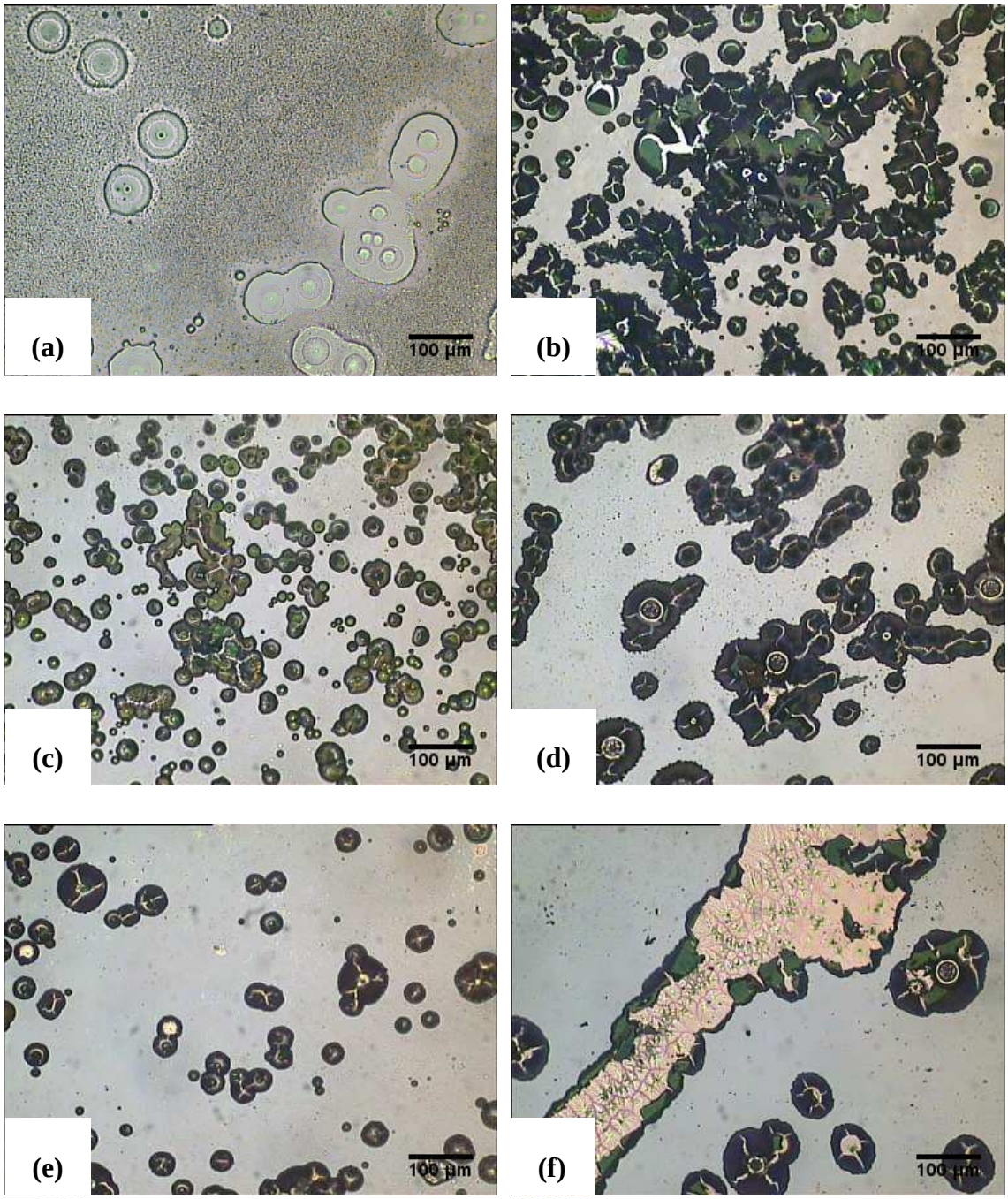

Figure 6.21 Optical micrographs of the treated and untreated Al-30at.%Cu alloy after cathodic polarisation in aerated 3.5 wt.% NaCl solution. (a) 0 s (b) 30 s (c) 60 s (d) 180 s (e) 300 s and (f) 600 s treatment times in zirconium-based conversion treatment solution.

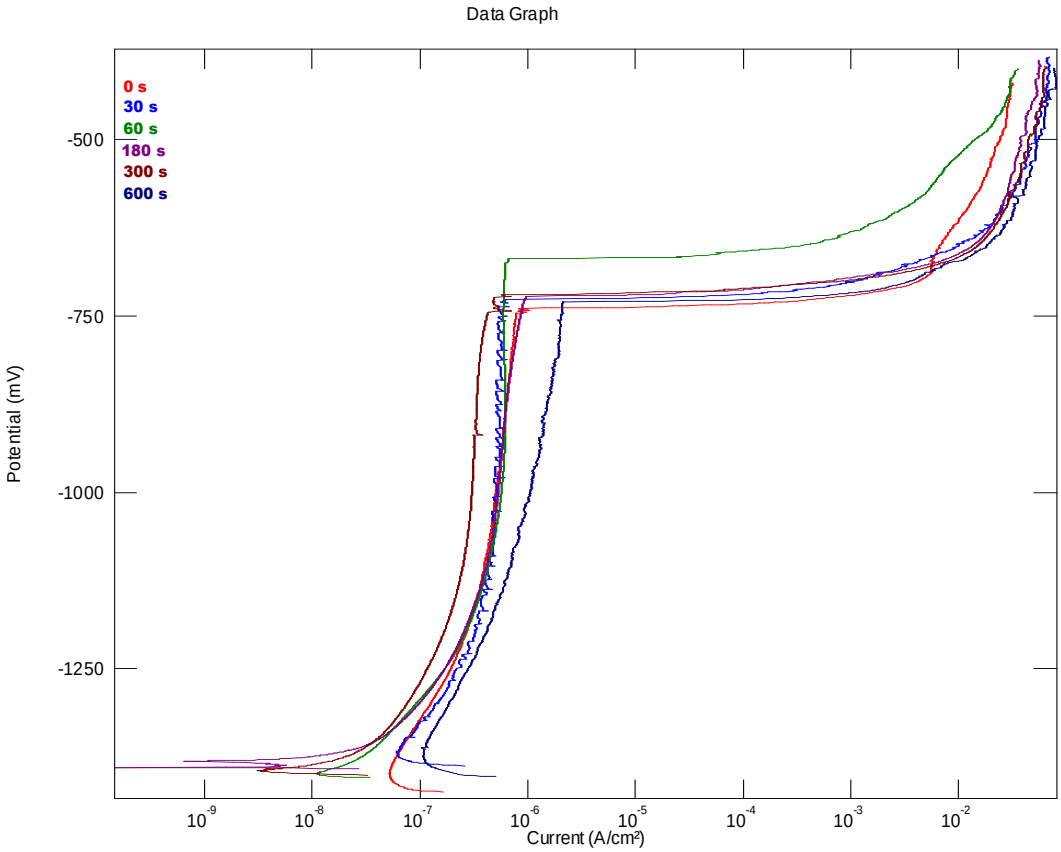

Figure 6.22 Anodic polarisation response of untreated and treated superpure aluminium in deaerated 3.5 wt.% NaCl solution.

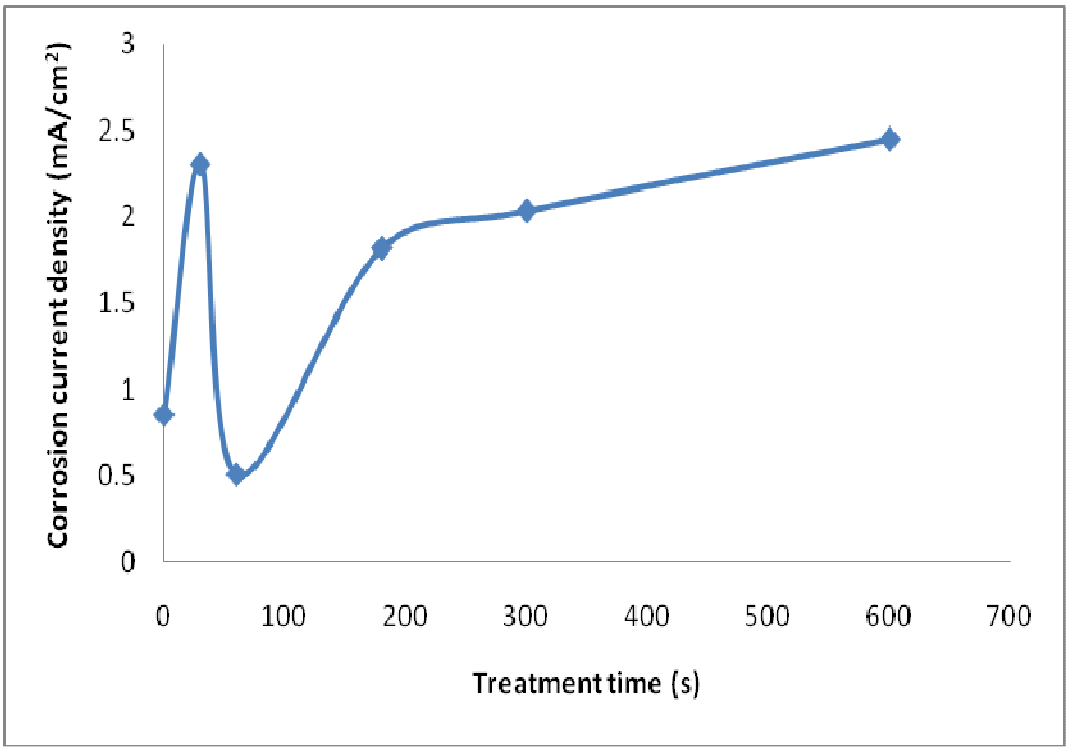

Figure 6.23 The relationship between corrosion current density and treatment times for superpure aluminium specimen in deaerated 3.5 wt.% NaCl solution.

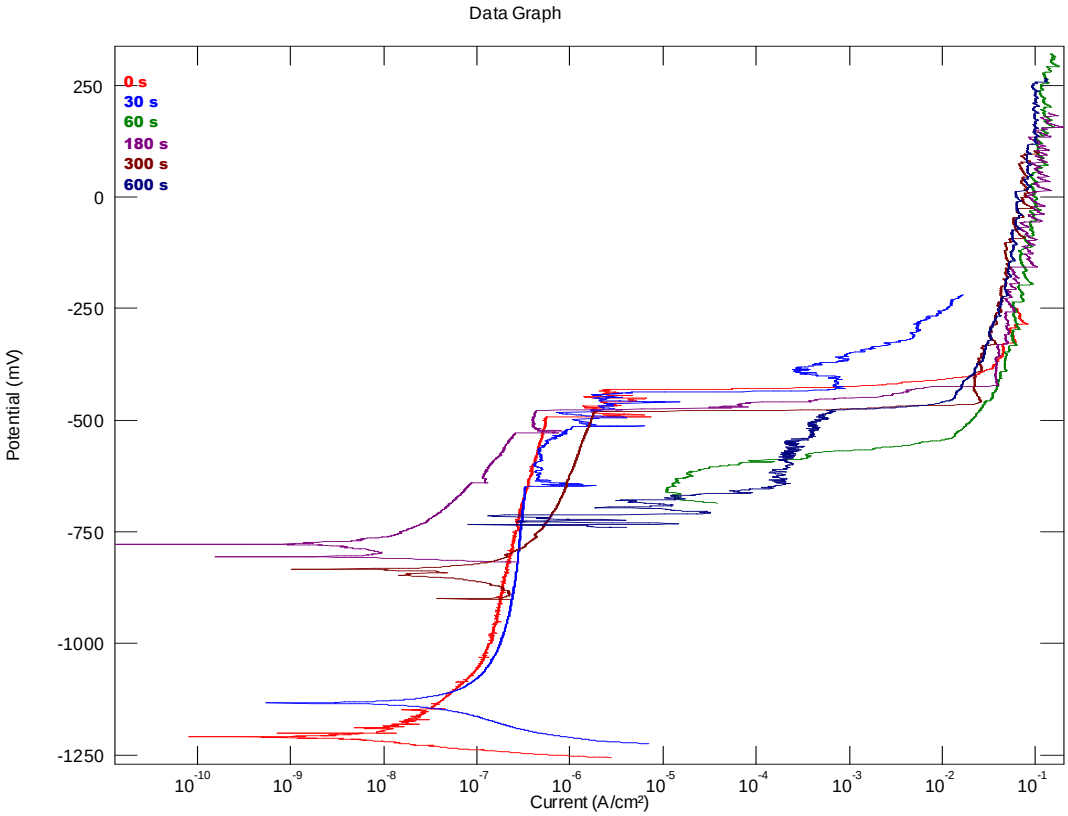

Figure 6.24 Anodic polarisation response of untreated and treated Al-1.0at.%Cu alloy in deaerated 3.5 wt.% NaCl solution.

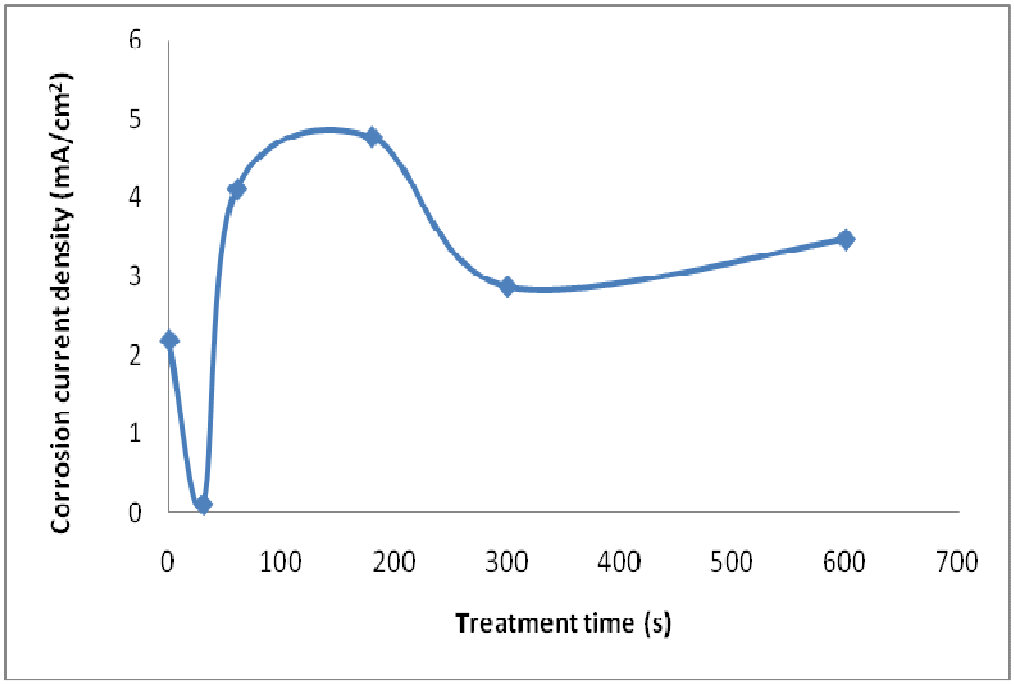

Figure 6.25 The relationship between corrosion current density and treatment times for Al-1.0at.%Cu alloys in deaerated 3.5 wt.% NaCl solution.

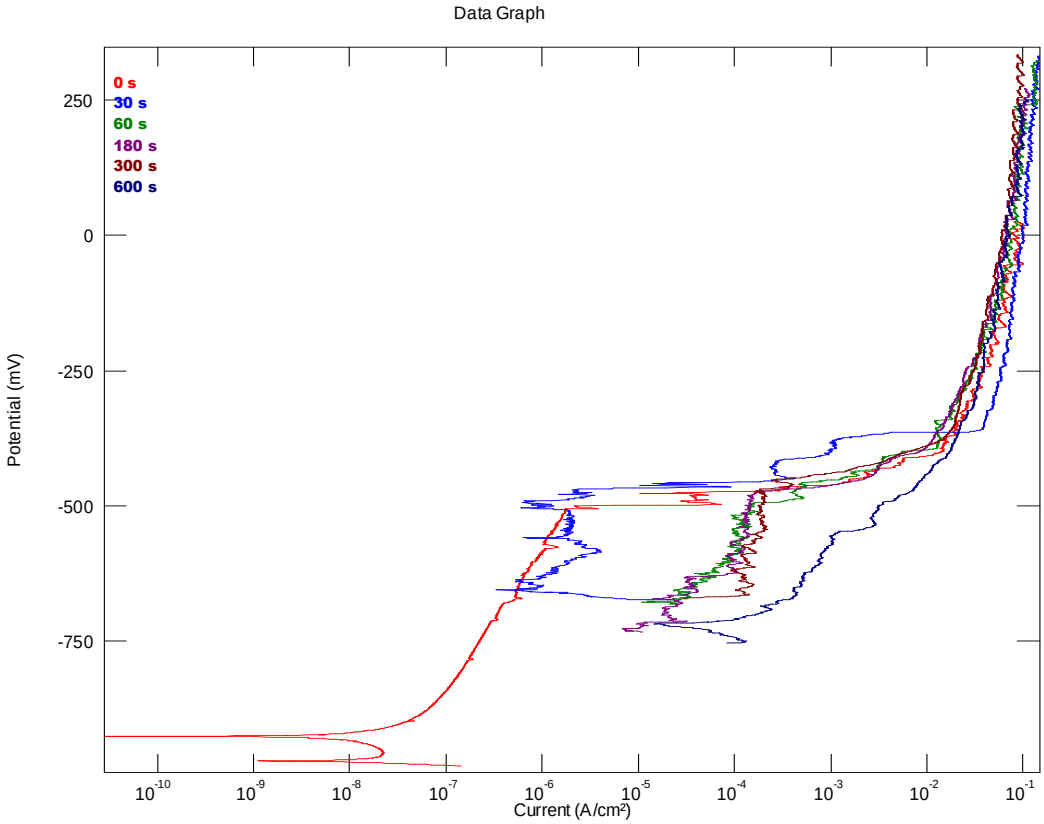

Figure 6.26 Anodic polarisation response of untreated and treated Al-5.0at.%Cu alloy in deaerated 3.5 wt.% NaCl solution.

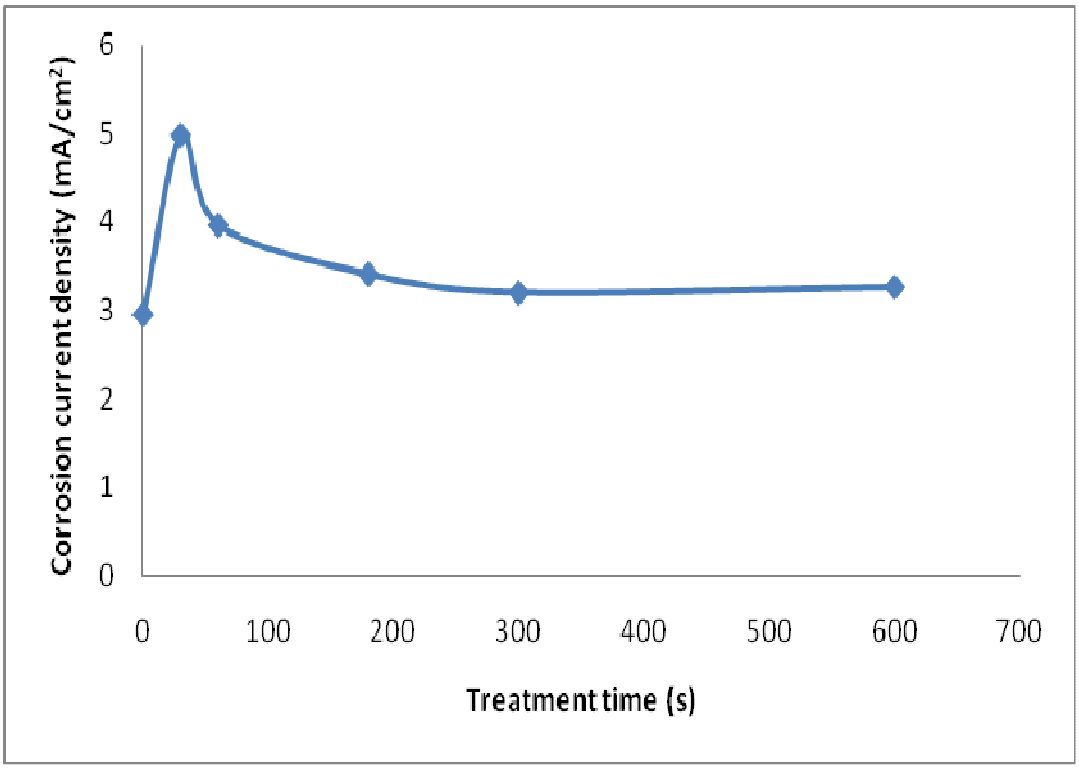

Figure 6.27 The relationship between corrosion current density and treatment times for Al-5.0at.%Cu alloys in deaerated 3.5 wt.% NaCl solution.

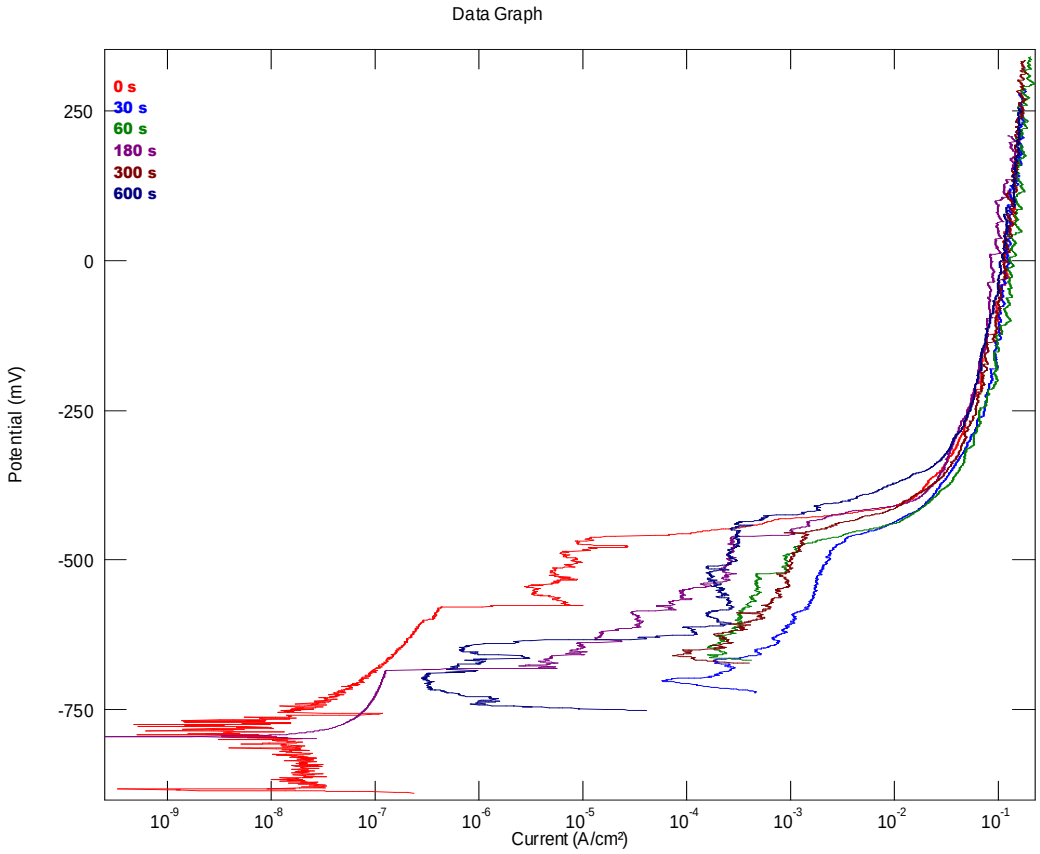

Figure 6.28 Anodic polarisation response of untreated and treated Al-10at.%Cu alloy in deaerated 3.5 wt.% NaCl solution.

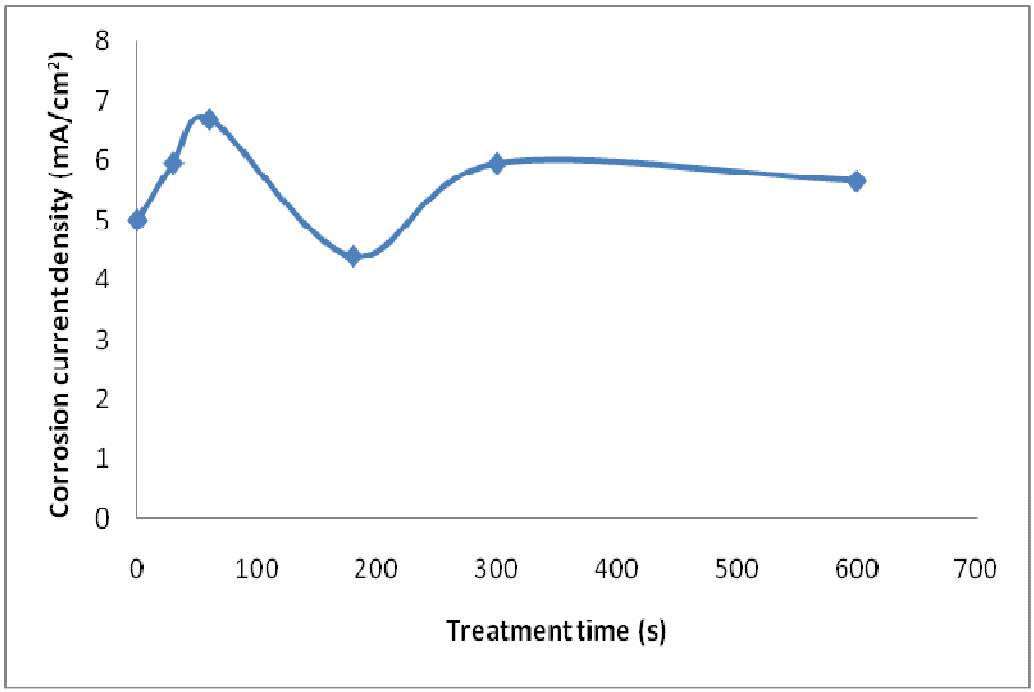

Figure 6.29 The relationship between corrosion current density and treatment times for Al-10at.%Cu alloys in deaerated 3.5 wt.% NaCl solution.

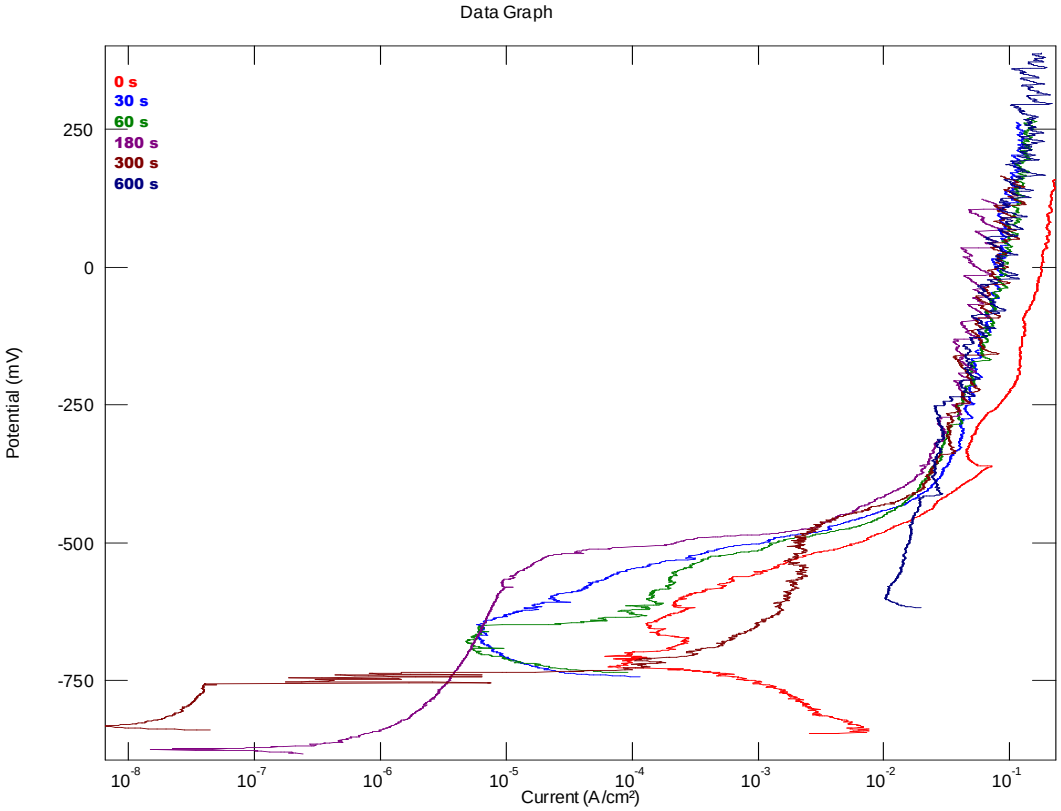

Figure 6.30 Anodic polarisation response of untreated and treated Al-30at.%Cu alloy in deaerated 3.5 wt.% NaCl solution.

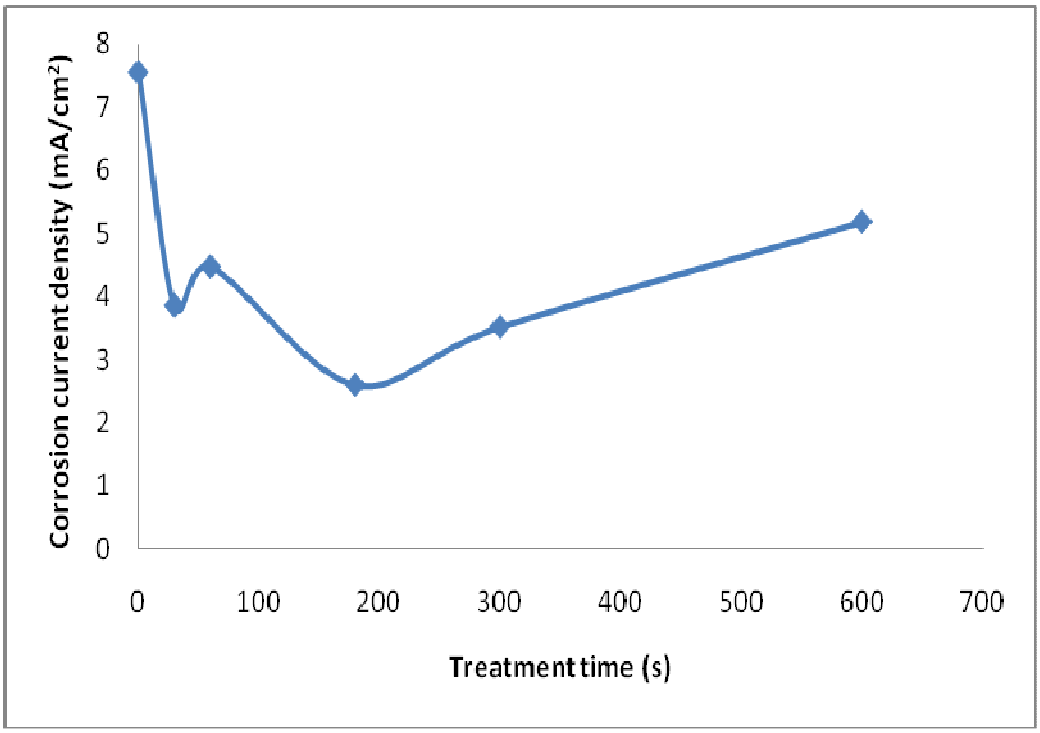

Figure 6.31 The relationship between corrosion current density and treatment times for Al-30at.%Cu alloys in deaerated 3.5 wt.% NaCl solution.

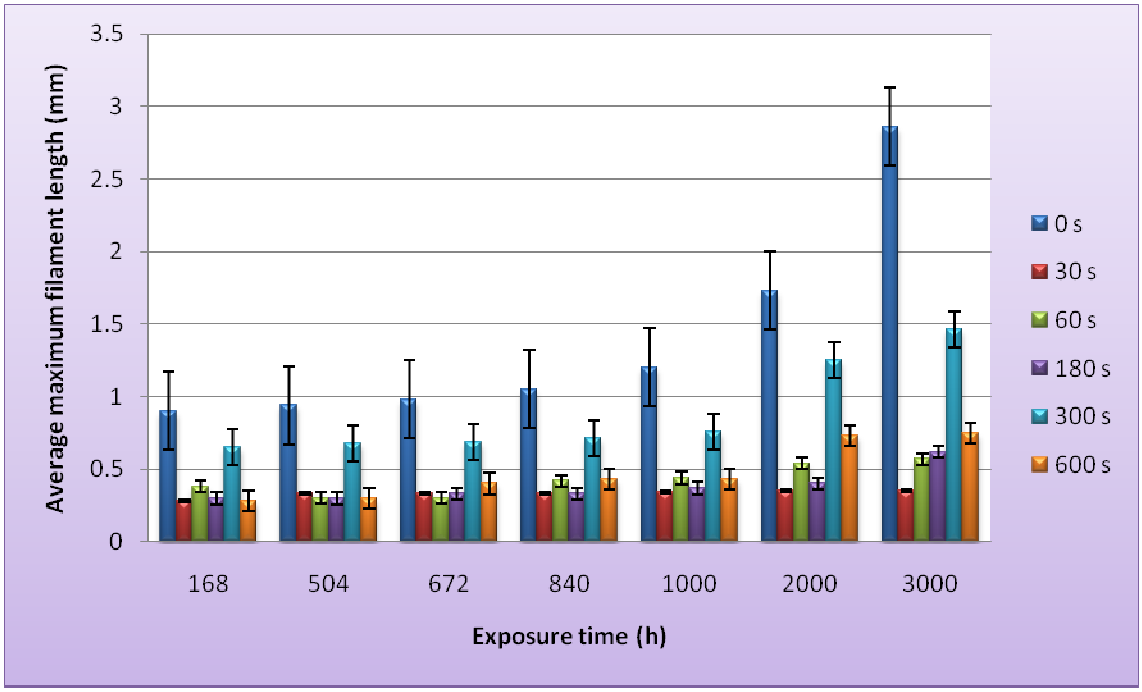

Figure 6.32 Average maximum filament lengths as a function of exposure time developed on as-sputtered (0 s) and conversion treated superpure aluminium specimens.

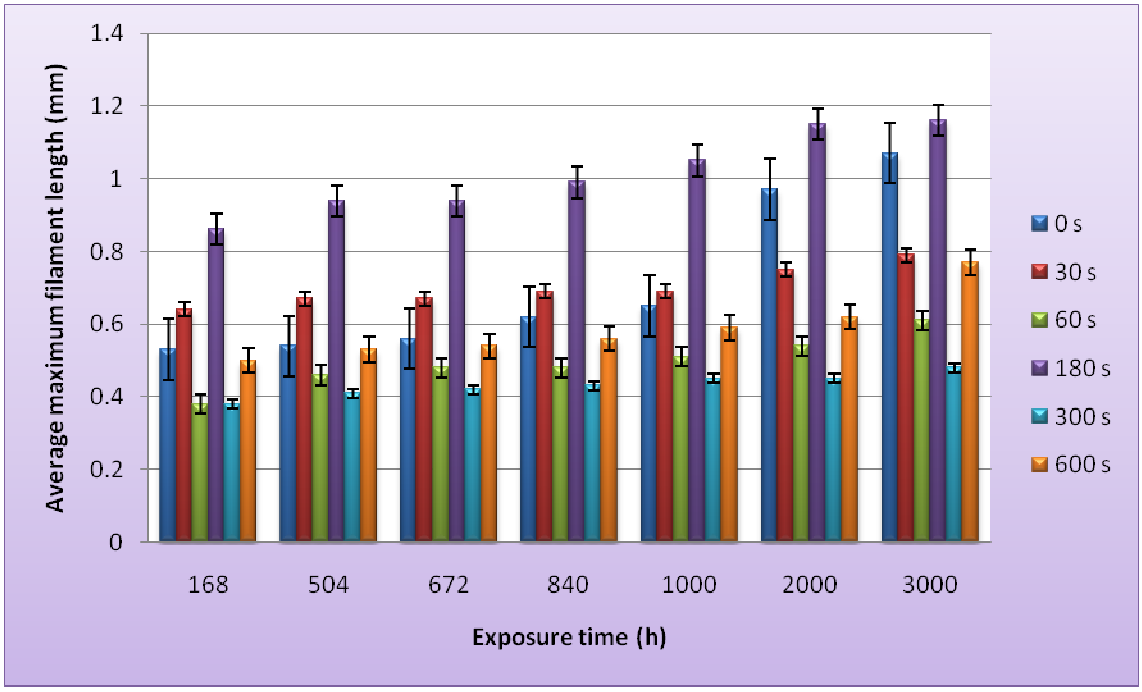

Figure 6.33 Average maximum filament lengths as a function of exposure time developed on as-sputtered (0 s) and conversion treated Al-1.0at.%Cu alloy specimens.

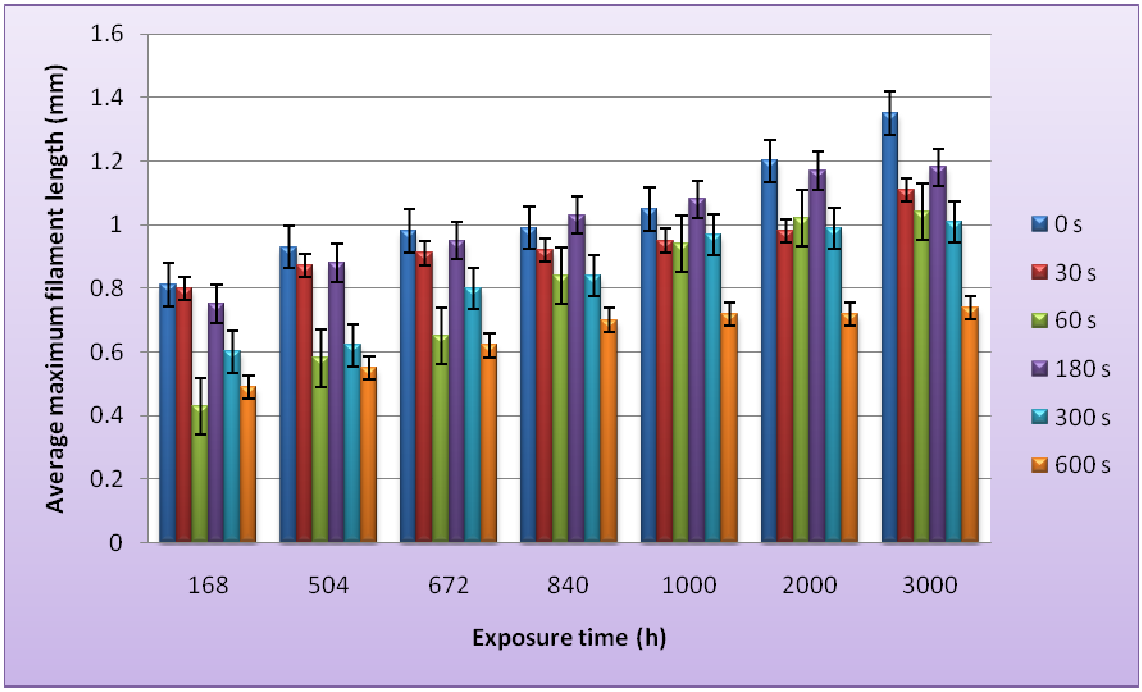

Figure 6.34 Average maximum filament lengths as a function of exposure time developed on as-sputtered (0 s) and conversion treated Al-5.0at.%Cu alloy specimens.

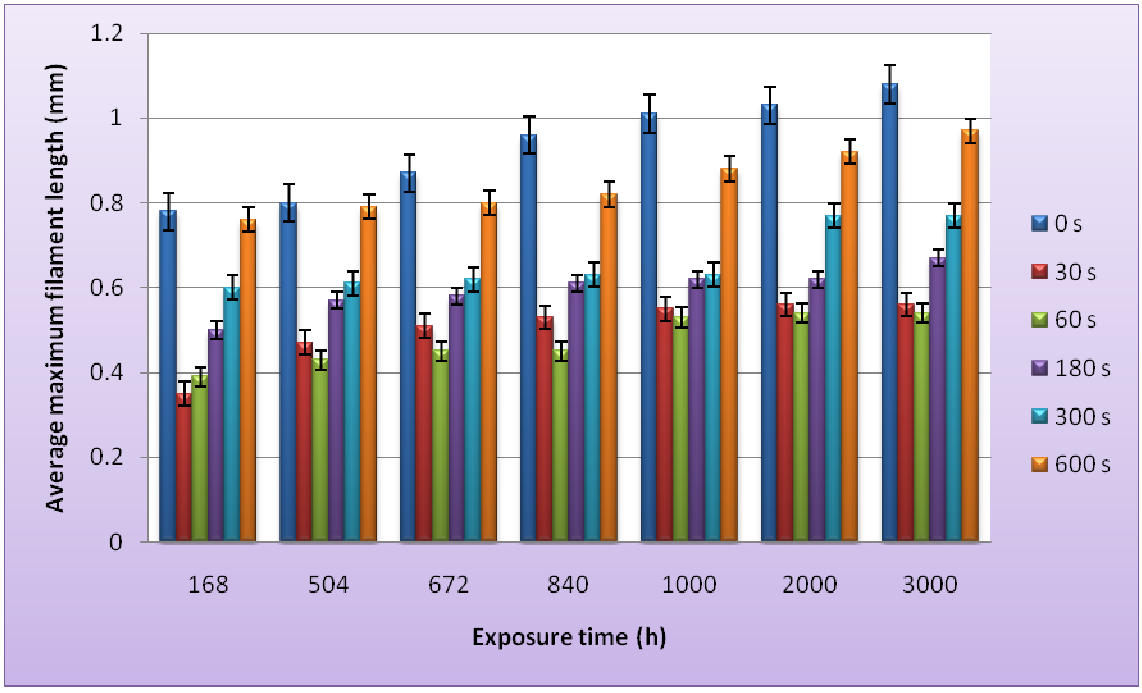

Figure 6.35 Average maximum filament lengths as a function of exposure time developed on as-sputtered (0 s) and conversion treated Al-10at.%Cu alloy specimens.

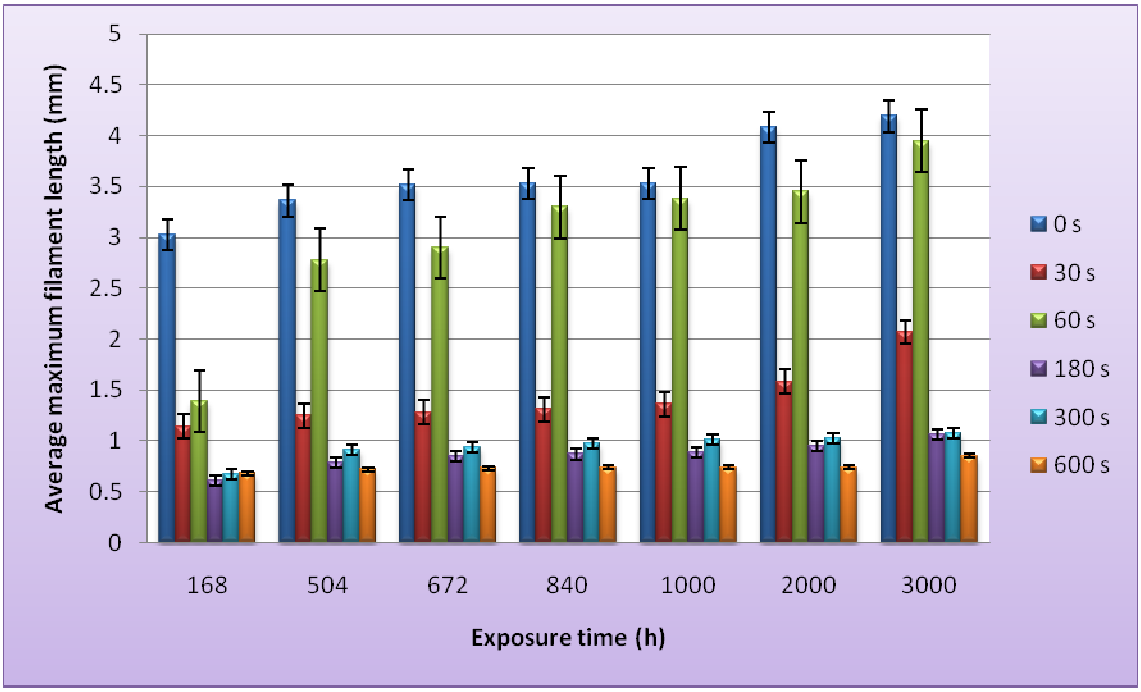

Figure 6.36 Average maximum filament lengths as a function of exposure time developed on as-sputtered (0 s) and conversion treated Al-30at.%Cu alloy specimens.

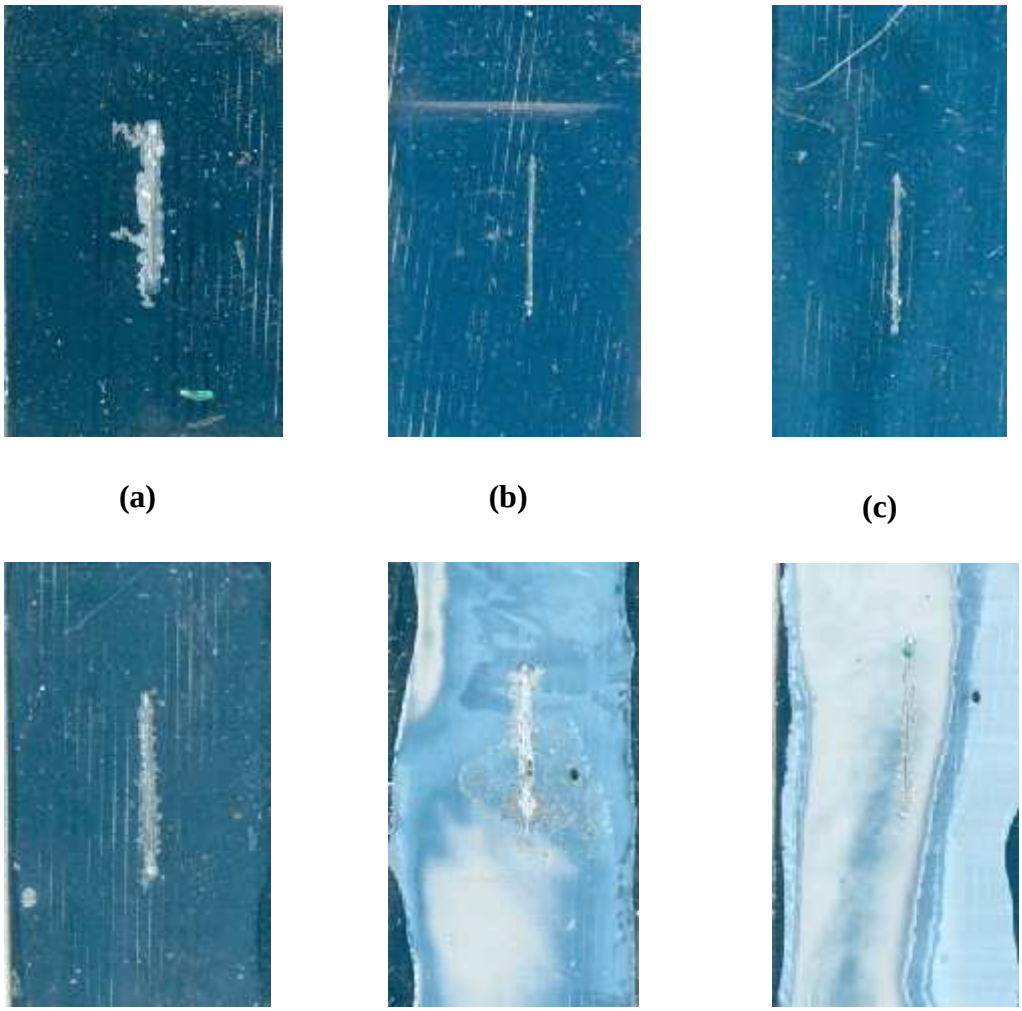

Figure 6.37 Digital images of filiform corrosion morphology of superpure aluminium after 3000 h exposure (a) as-sputtered (0 s), (b) 30 s, (c) 60 s, (d) 180 s, (e) 300 s and (f) 600 s conversion treated specimens.

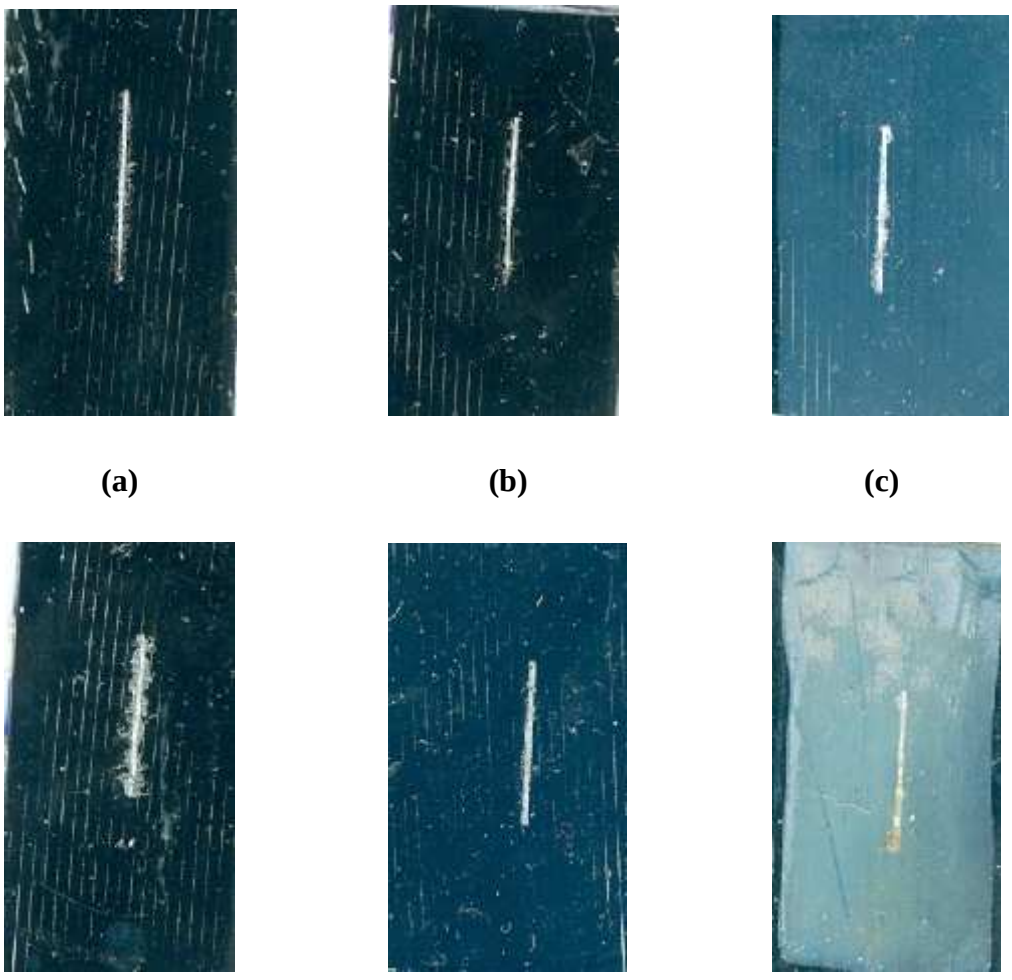

Figure 6.38 Digital images of filiform corrosion morphology of the Al-1.0at.%Cu alloy after 3000 h exposure (a) as-sputtered (0 s), (b) 30 s, (c) 60 s, (d) 180 s, (e) 300 s and (f) 600 s conversion treated specimens.

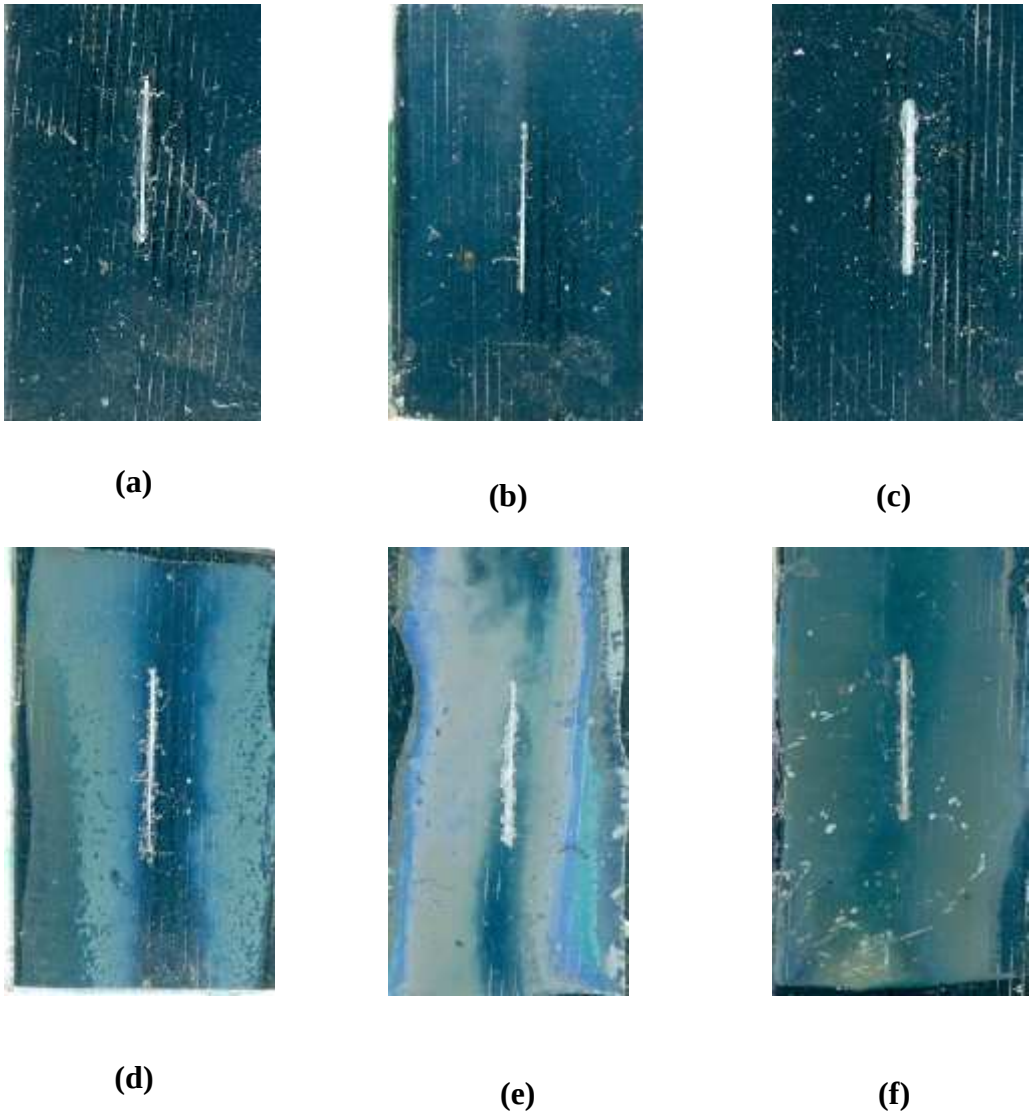

Figure 6.39 Digital images of filiform corrosion morphology of the Al-5.0at.%Cu alloy after 3000 h exposure (a) as-sputtered (0 s), (b) 30 s, (c) 60 s, (d) 180 s, (e) 300 s and (f) 600 s conversion treated specimens.

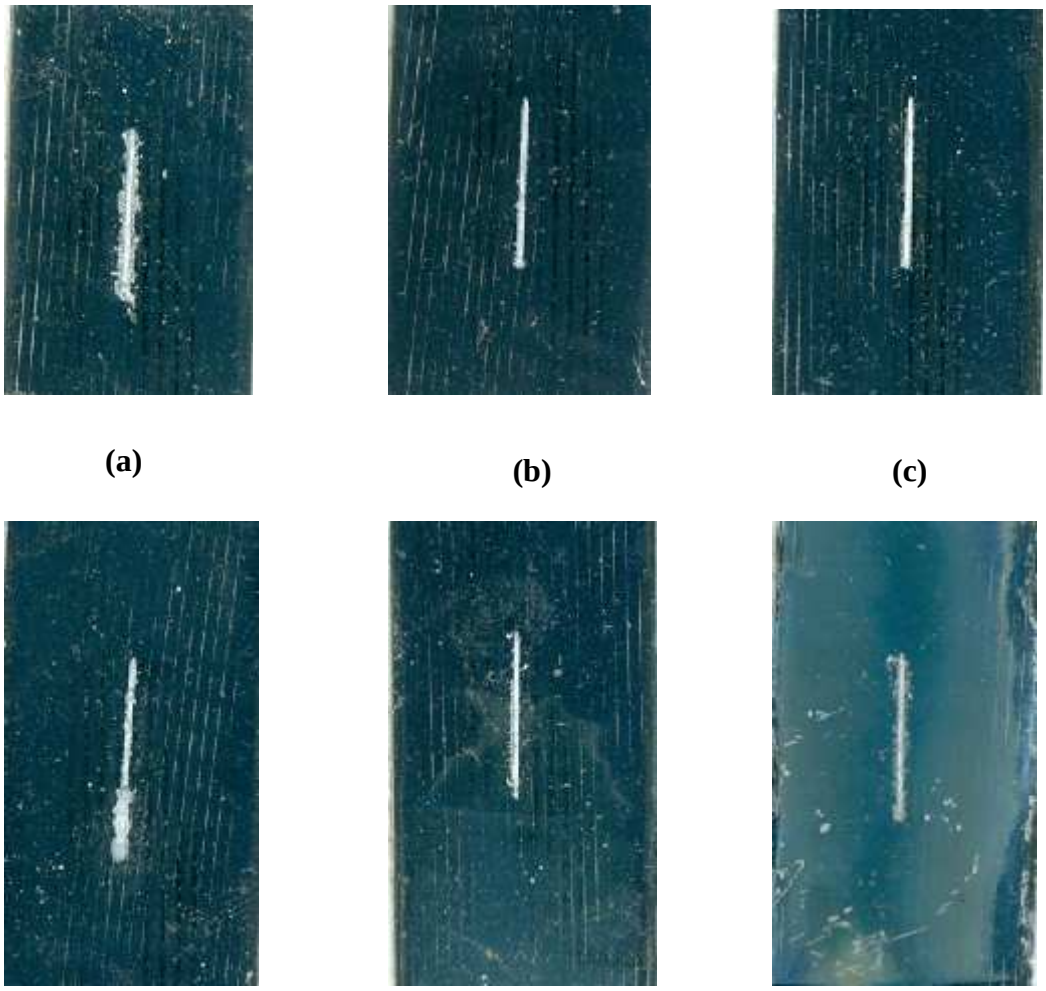

Figure 6.40 Digital images of filiform corrosion morphology of the Al-10at.%Cu alloy after 3000 h exposure (a) as-sputtered (0 s), (b) 30 s, (c) 60 s, (d) 180 s, (e) 300 s and (f) 600 s conversion treated specimens.

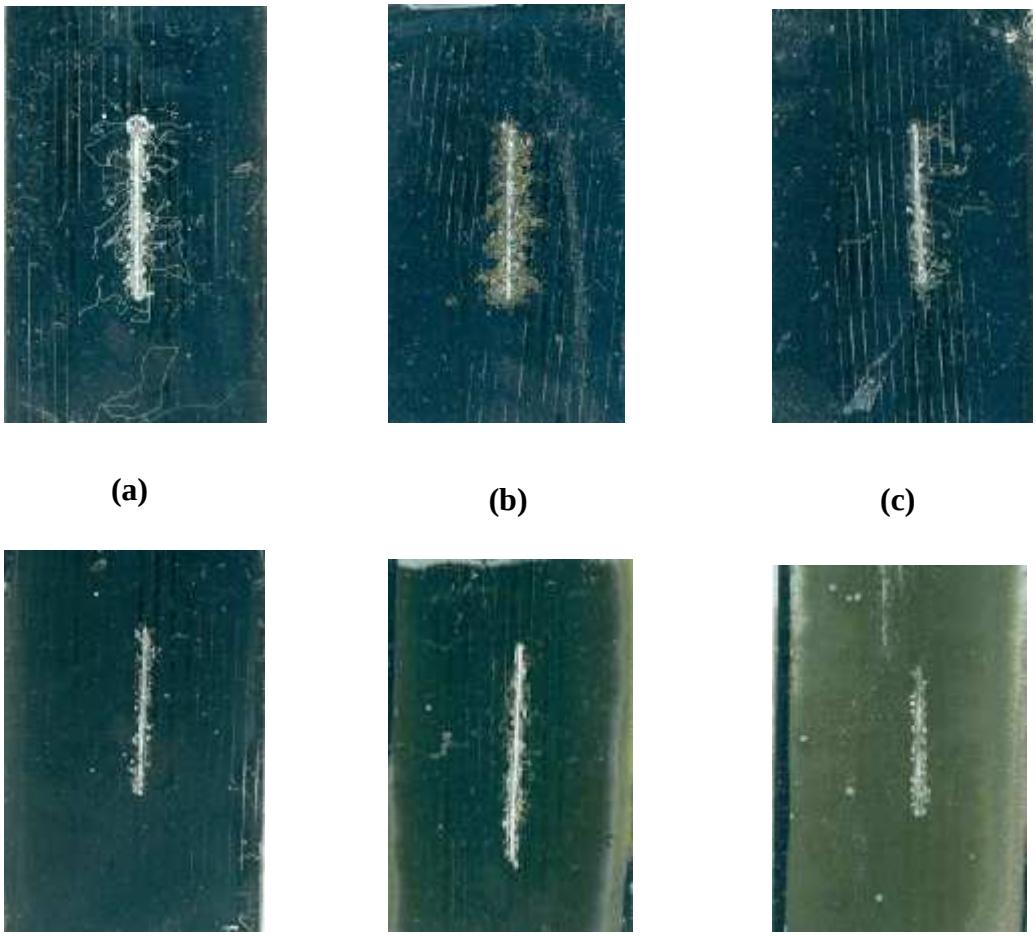

Figure 6.41 Digital images of filiform corrosion morphology of the Al-30at.%Cu alloy after 3000 h exposure (a) as-sputtered (0 s), (b) 30 s, (c) 60 s, (d) 180 s, (e) 300 s and (f) 600 s conversion treated specimens.

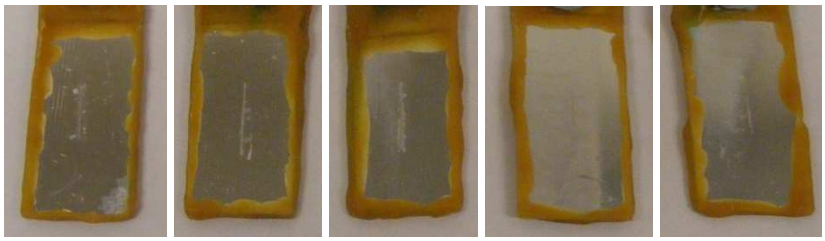

(a) **(b)** **(c)** **(d)** **(e)**

Figure 6.42 Photographs of superpure aluminium specimens after 1000 h exposure in the salt spray chamber. (a) as-sputtered (0 s), (b) 30 s, (c) 180 s, (d) 300 s and (e) 600 s of conversion treatment.

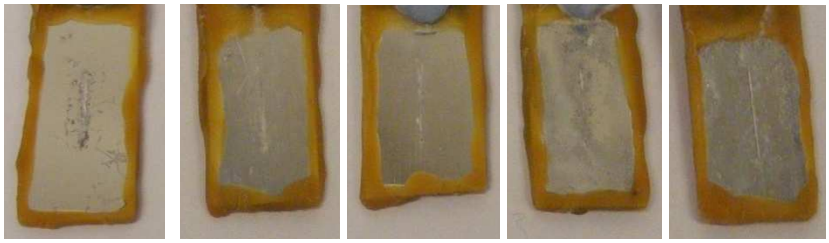

(a) **(b)** **(c)** **(d)** **(e)**

Figure 6.43 Photographs of the Al-1.0at.%Cu alloy specimens after 1000 h exposure in the salt spray chamber. (a) as-sputtered (0 s), (b) 30 s, (c) 180 s, (d) 300 s and (e) 600 s of conversion treatment.

(a) **(b)** **(c)** **(d)** **(e)**

Figure 6.44 Photographs of the Al-5.0at.%Cu alloy specimens after 1000 h exposure in the salt spray chamber. (a) as-sputtered (0 s), (b) 30 s, (c) 180 s, (d) 300 s and (e) 600 s of conversion treatment.

(a) **(b)** **(c)** **(d)** **(e)**

Figure 6.45 Photographs of the Al-10at.%Cu alloy specimens after 1000 h exposure in the salt spray chamber. (a) as-sputtered (0 s), (b) 30 s, (c) 180 s, (d) 300 s and (e) 600 s of conversion treatment.

(a) **(b)** **(c)** **(d)** **(e)**

Figure 6.46 Photographs of the Al-30at.%Cu alloy specimens after 1000 h exposure in the salt spray chamber. (a) as-sputtered (0 s), (b) 30 s, (c) 180 s, (d) 300 s and (e) 600 s of conversion treatment.

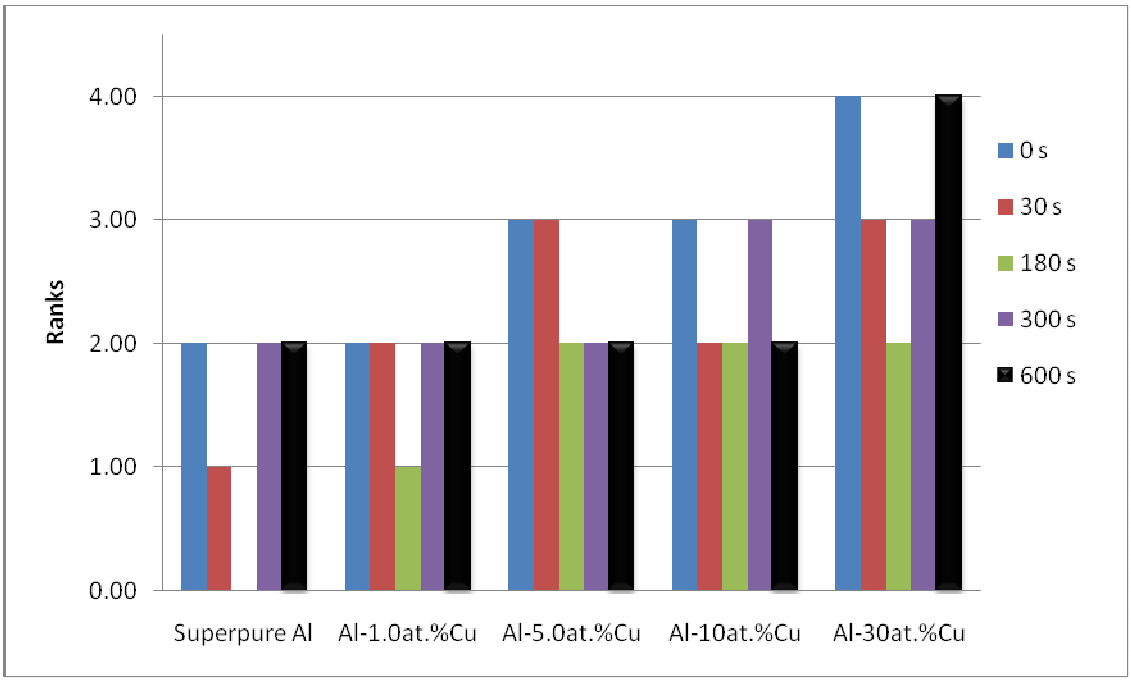

Figure 6.47 Rankings of the degree of corrosion at 168 h visual inspection for as-sputtered and conversion treated specimens.

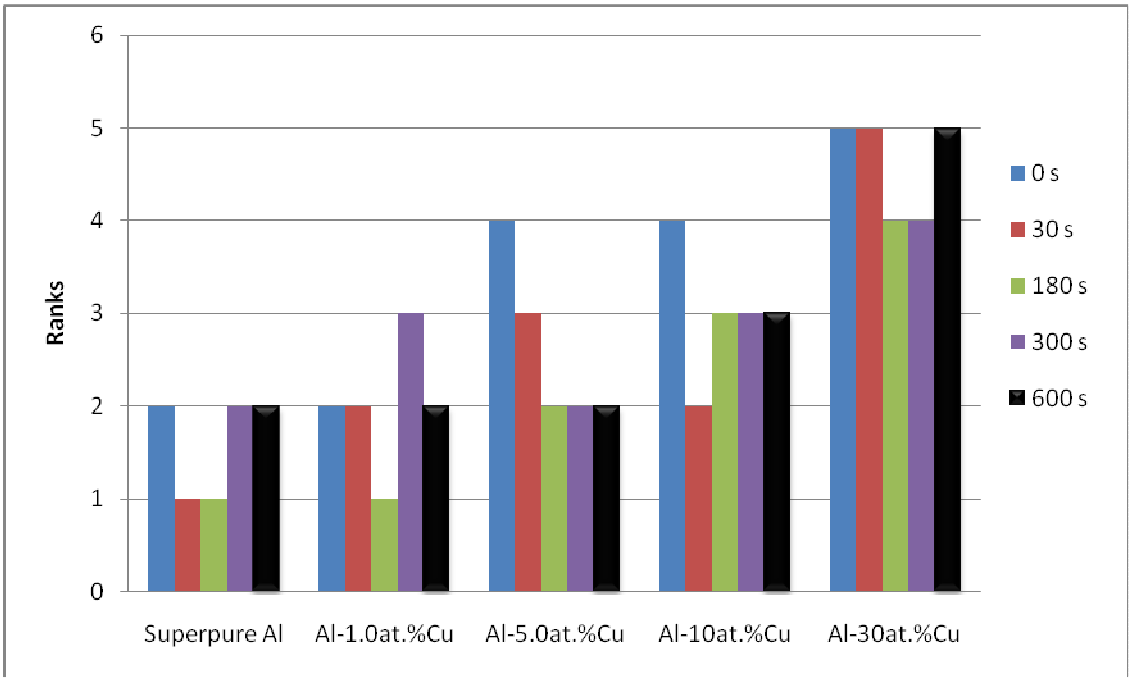

Figure 6.48 Rankings of the degree of corrosion at 336 h visual inspection for as-sputtered and conversion treated specimens.

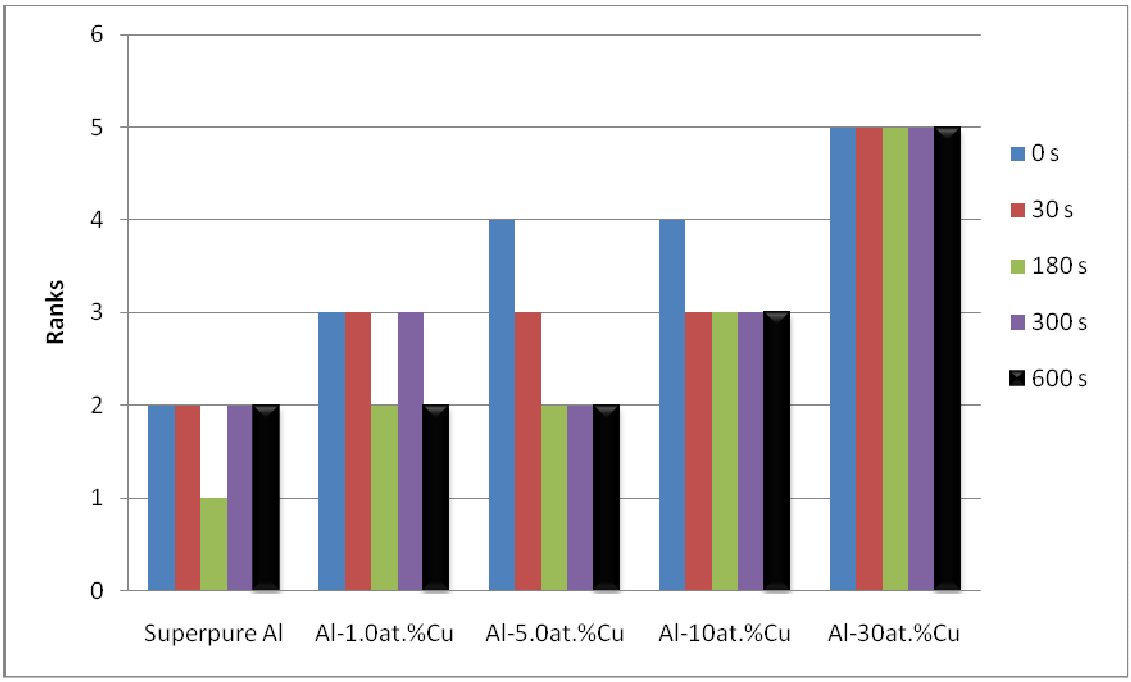

Figure 6.49 Rankings of the degree of corrosion at 504 h visual inspection for as-sputtered and conversion treated specimens.

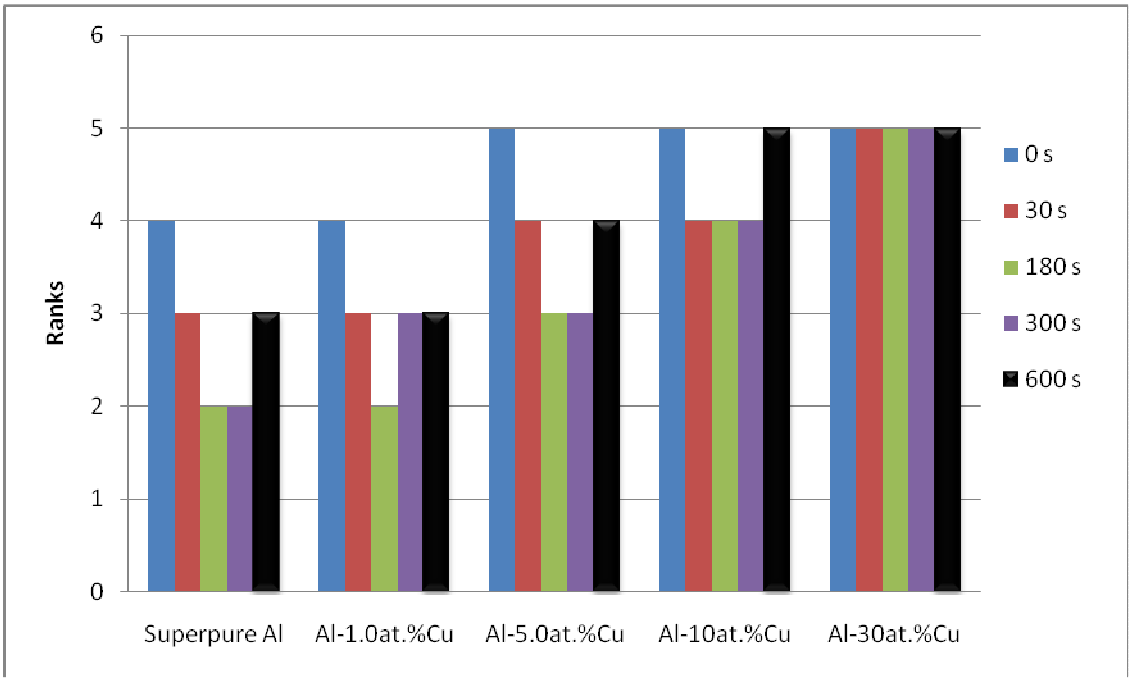

Figure 6.50 Rankings of the degree of corrosion at 1000 h visual inspection for as-sputtered and conversion treated specimens.

CHAPTER 7

7 CONCLUSIONS AND FUTURE WORK

7.1 Conclusions

The objectives of this study have been to develop a better understanding of the zirconium conversion coating formation process and its corrosion inhibition mechanisms. Research in three areas has been carried out to achieve those objectives: coating formation process on aluminium and effects of conversion treatment time (immersion time) and copper content of the aluminium-copper binary alloys on coating formation and corrosion inhibition mechanisms of zirconium-based conversion coatings. Electrochemical approaches in combination with material characterisation techniques were employed to correlate the compositions and microstructures of copper-containing aluminium alloys to localised corrosion and protection by zirconium conversion coating. The following is a list of the main findings:

1. Aluminium-copper binary alloys are less susceptible to pit initiation compared with aluminium in its pure state provided that the alloyed copper is retained in solid solution. This effect is evident in the present work with pitting potential increasing with copper content in aluminium-copper solid solution alloys. However, the corrosion rates of aluminium-copper alloys containing up to 30at.% copper were found to increase with increasing copper content, indicating that the barrier corrosion resistance of aluminium alloys will decrease with increasing copper content. This effect was attributed to galvanic cells created by formation of minute copper particles or films deposited onto the alloy surface as a result of corrosion.

2. The zirconium conversion coating formation on superpure aluminium and aluminium-copper alloys is influenced by microstructural heterogeneity. The conversion coatings formed on the surface of aluminium are relatively homogenous while on aluminium-copper alloys, it is in most cases heterogeneous. The coating development on the superpure aluminium is suggested to proceed by the anodic dissolution of aluminium at anodic sites and

cathodic deposition of zirconium oxide species at cathodic sites. The cathodic sites are derived from flaws generated by impurity segregates in the superpure aluminium substrate. The conversion coating developed on model aluminium-copper binary alloys is suggested to proceed in the following manner; at immersion of alloy specimens in the conversion coating bath, the alumina oxide film is thinned in the acidic fluoride solution. Cathodic and anodic activities proceed on the alloy surface, but depend on the heterogeneous nature of the alloy material.

3. The zirconium-based conversion coating developed on superpure aluminium is not uniform in the initial stages of coating development. Such non-uniformity is generated from the presence of residual flaws, which arise from impurity segregates. Increasing the treatment time resulted in an increase in coating thickness, but little change in coating composition occurred as determined by RBS.

4. In high copper-content aluminium alloys, the initial coating growth developed with oxidation of aluminium only, while copper enriches in the alloy. However, copper is eventually incorporated into the coating when copper is sufficiently enriched in the alloy and thus, the thickness of the conversion coating formed then reduces over the general surface of the alloy specimen, with the coating subsequently formed on the alloys being relatively thin compared to that formed on the superpure aluminium substrates. Thus, the addition of alloying elements, with the formation of Al-1.0at.%Cu, Al-5.0at.%Cu, Al-10at.%Cu and Al-30at.%Cu alloys, reduces the growth rate of the conversion coating as well as the consumption of the alloy substrates. Therefore, increasing the conversion treatment time results in an increase in coating thickness for the superpure aluminium substrates, but little or no change in coating thickness occurred for aluminium-copper model alloys after prolonged immersion in the conversion bath solution.

5. The presence of the conversion coating on the aluminium matrix and model aluminium-copper binary alloys was indicated by the detection of the elements oxygen, zirconium, and aluminium which were labelled in the various RBS spectra for different treatment times. The zirconium-based conversion coating

developed on the specimens is composed of an outer layer of $ZrO_2.nH_2O$ with hydrated aluminium oxide adjacent to the metal /coating interface.

6. The corrosion protection provided by the conversion coating was studied by electrochemical measurements and accelerated corrosion tests. Comparing the corrosion behaviour of superpure aluminium with that of the alloy in chloride solution and the inhibition of corrosion offered by zirconium species, it is suggested that the mechanism of corrosion inhibition by zirconium is influenced by the amount of non-aluminium elements present in the superpure aluminium as impurities and alloying elements in the alloy, and treatment time in the zirconium bath.

7. The copper content in the alloy has two different effects on zirconium conversion coating protection. Copper is beneficial to zirconium conversion coating protection for the conversion treatments applied to aluminium-copper alloys. However, copper is detrimental if enriched on alloy surfaces with more copper content. Under free corrosion conditions in aerated chloride solutions, the corrosion potential increases as a result of copper enrichment on the surface; this facilitates the oxygen reduction reaction. As a result of this, the overall influence of copper on corrosion behaviour is detrimental, despite the increase in pitting potentials observed with copper-containing aluminium alloys.

8. The conversion coating formed after 60 s and 180 s of immersion in the zirconium-based conversion coating bath provide good corrosion resistance which can be attributed to the high stability of the compounds that constitute the surface oxide layer, and good adhesion properties.

7.2 Suggestions for Future Work

This work has opened up some issues that are of interest for future study of zirconium conversion coatings and other chrome-free conversion coatings. However, there are a number of issues that remain unresolved and new questions that have arisen over the course of this work. Therefore, the following is a list of suggestions for future research work.

1. Study of the relationship between surface roughness and pit initiation rate for superpure aluminium and aluminium-copper solid solution alloys will elucidate the mechanism of pit initiation further.

2. This study revealed the effects of ageing in dry air on the morphology of the coating. However, the structural and compositional changes of zirconium-based conversion coating during ageing need to be characterised in order to understand the effect of ageing on coating properties.

3. In this study, as-sputtered aluminium-copper alloys were not pre-treated prior to conversion coating treatment; however, in industrial contexts, aluminium surfaces are generally pre-treated with an acidic solution prior to immersion in a coating bath. Hence, the effect of a standard pre-treatment on corrosion protection performance of zirconium conversion coating should be studied.

4. In this study, coating formation and inhibition mechanism on superpure aluminium and model Al-Cu alloys were examined by complementary surface analytical techniques. It will be of interest however, to know how AA2xxx, AA6xxx and AA7xxx commercial alloys will behave in similar experiments. The roles of intermetallic particles on coating formation and protection mechanisms may also be examined. Careful characterisation is necessary to understand the corrosion behaviour and performance of the commercial aluminium alloys. The chemical composition of precipitates on grain boundaries and in the matrix, solute deplete zones, precipitate free zones, and coarse intermetallic compounds need to be examined using TEM and Auger electron spectroscopy (AES) in order to understand the effect of alloy temper on the corrosion performance of commercial aluminium alloys.

5. The results from this study showed the critical roles played by the zirconium-based conversion treatment bath composition on the coating formation and the inhibitive effect of zirconium-based conversion coating. These results may be applied to guide the development of and other chromate-free coating systems such as cerium, vanadate, molybdate and titanium based bath formulations. These coating bath chemistries may produce corrosion resistant coatings comparative with chromate conversion coatings on aluminium alloys. Further

investigation needs to be carried out on hybrid systems of zirconium (such as Zr-Ti) and the possibilities of conversion treatments systems containing a larger number of components. It will be constructive to extend the analyses to compare the observations with the performance of the surfaces for corrosion resistance, bonding and other applications.

6. It would also be desirable to extend the analysis to techniques such as X-ray photoelectron spectroscopy (XPS) and secondary ion mass spectroscopy (SIMS). These would allow the chemical state of elements in the conversion layer, the presence of hydrogen and the nature of the conversion layer to be analysed. In addition, focused ion beam (FIB) and scanning transmission electron microscopy (STEM) analytical techniques should be used to investigate the copper enrichment at the interface between zirconium conversion coating and aluminium alloys.

7. Polarisation studies, filiform corrosion and salt spray testing were employed in this work to evaluate the protection by zirconium conversion coatings. Electrochemical impedance spectroscopy (EIS) should be used to compare the results obtained in this work. Surface analyses using AES, XPS and X-ray absorption near edge structure (XANES) should be used to characterise specimens after long-term salt spray exposure since this will help in understanding the mechanism of zirconium conversion coating breakdown.

REFERENCES

1. Chen, L., Myung, N., Sumodjo, P.T.A., Nobe, K., *A comparative electrodissolution and localized corrosion study of 2024 Al in halide media.* Electrochimica Acta, 1999. **44**: p. 2751-2764.

2. Dymek, S., and Dollar, M., *TEM investigation of age-hardenable Al2519 alloy subjected to stress corrosion cracking tests.* Materials Chemistry and Physics, 2003. **81**: p. 286-288.

3. Fuente, D.d.l., Otero-Huerta, E. and Morcillo, M., *Studies of long-term weathering of aluminium in the atmosphere.* Corrosion Science, 2007. **49**: p. 3134-3148.

4. Guillaumin, V., and Mankowski, G., *Localized corrosion of 2024 T351 aluminium alloy in chloride media.* Corrosion Science, 1999. **41**: p. 421-438.

5. Komisarov, V., Talianker, M., and Cina, B., *The effect of retrogression and reaging on resistance to stress corrosion of an 8090 type aluminium alloy.* Materials Science and Engineering, 1996. **A 221**: p. 113-121.

6. Liu, X.F., *Filiform corrosion attack on pretreated aluminium alloy with tailored surface of epoxy coating.* Corrosion Science, 2007. **49**: p. 3494-3513.

7. Mishra, A.K., and Balasubramaniam, R., *Corrosion inhibition of aluminium alloy AA2014 by rare earth chlorides.* Corrosion Science, 2007. **49**: p. 1027-1044.

8. Moon, S.-M., Sakairi, M., and Takahashi, H., *Behavior of second-phase particles in Al5052 alloy during anodizing in a sulfuric acid solution.* Journal of Electrochemical Society, 2004. **151**(7): p. B399-B405.

9. Páez, M.A., Foong, T.M., Ni, C.T., Thompson, G.E., Shimizu, K., Habazaki, H., Skeldon, P. and Wood, G.C., *Barrier-type anodic film formation on an Al-3.5 wt% Cu alloy* Corrosion Science, 1996. **38**(1): p. 59-72.

10. Schafer, H., and Stock, H.R. and *Improving the corrosion protection of aluminium alloys using reactive magnetron sputtering.* Corrosion Science 2005. **49**(4): p. 953-964.

11. Solomon, J.S., and Hanlin, D.E., *AES and SEM characterization of anodised aluminium alloy adherends for adhesive bonding application.* Applications Of Surface Science, 1980. **4**: p. 307-323.

12. Zhou, W., Aung, N.N., Choudhary, A. and Kanouni, M. , *Heat-transfer corrosion behaviour of cast Al alloy.* Corrosion Science, 2008. **50**: p. 3308-3313.

13. Bakos, I., Szabó, S., *Corrosion behaviour of aluminium in copper containing environment.* Corrosion Science, 2008. **50**: p. 200-205.

14. Wernick, S., Pinner, R., and Sheasby, P.G., *The surface treatment and finishing of aluminium alloys*. Vol. 1. 1989, Teddington: Finishing Publication Ltd.

15. Bridenbaugh, P.R. *Aluminium - 2000 and beyond*. in *Aluminium Technology '86*. 1986: Institute of metals.

16. Pakes, A., Thompson, G.E., Skeldon, P., Morgan, P.C., and Shimizu, K., *Anodising of aluminium alloys in borax electrolyte*, in *Aluminium Surface Science and Technology (ASST 2000)*. 2000: UMIST Manchester. p. 404-409.

17. *Aerospace*. 2009 [cited 2009 12/11/2009]; Available from: http://www.world-aluminium.org/About+Aluminium/Applications+and+Products/Transportation/Aerospace.

18. Miller, W.S., Zhuang, L., Bottema, J., Wittebrood, A.J., Smet, P.De., Haszler A., and Vieregge, A., *Recent development in aluminium alloys for the automotive industry* Materials Science and Engineering A, 2000. **280**(1): p. 37-49.

19. Mizun, K., and Takagi, Y., *Surface analysis of aluminium alloys for automotive body panels*, in *Nippon steel technical report*. 1996. p. 13-21.

20. *History Of Aluminum: facts and information on aluminum*. 2006 [cited 2009 11/11/2009]; Available from: http://www.historyofaluminum.com/usage.php.

21. *Handbook of corrosion data*, ed. B. Craig. 1989: ASM International.

22. Bethencourt, M., Botana, F.J., Cano, M.J., Marcos, M., Sánchez-Amaya, J.M., and González-Rovira, L., *Behaviour of the alloy AA2017 in aqueous solutions of NaCl. Part 1: corrosion mechanisms.* Corrosion Science, 2009. **51**: p. 518-524.

23. Liu, Y., Arenas, M.A., Garcia-Vergara, S.J., Hashimoto, T., Skeldon, P., Thompson, G.E., Habazaki, H., Bailey, P., and Noakes,T.C.Q., *Behaviour of copper during alkaline corrosion of Al-Cu alloys.* Corrosion Science, 2008. **50**: p. 1475-1480.

24. Cohen, S.M., *Review: Replacement for chromium pretreatments on aluminium.* Corrosion Engineering, 1995. **51**(1): p. 71-78.

25. Buchheit, R.G., Grant, R.P., Hlava, P.F., Mckenzie, B., and Zender, G.L., *Local Dissolution Phenomena Associated with S Phase (Al2CuMg) Particles in Aluminum Alloy 2024-T3.* Journal of Electrochemical Society, 1997. **144**(8): p. 2621-2628.

26. Corson, M.G., *Aluminium the metal and its alloys*. 1926, London: Chapman & Hall Ltd.

27. Hamdy, A.S., Beccaria, A.M. and Temtchenko, T., *Corrosion protection of AA6061 T6 by fluoropolymer coatings in NaCl solution.* Surface and Coating Technology, 2002. **155**: p. 176-183.

28. Ahmad, Z., Ul-Hamid, A., and Abdul-Aleem, B.J., *The corrosion behavior of scandium alloyed Al 5052 in neutral sodium chloride solution* Corrosion Science, 2001. **43**: p. 1227-1243.

29. Muller, I.L., and Galvele, J.R., *Pitting potential of high purity binary aluminium alloys—I. Al-Cu alloys. Pitting and intergranular corrosion* Corrosion Science, 1977. **17**(3): p. 179-193.

30. Urushino, K., and Sugimoto, K., *Stress-corrosion cracking of aged Al-Cu-Mg alloys in NaCl solution* Corrosion Science, 1979. **19**(4): p. 225-236.

31. Galvele, J.R., and De Micheli, S.M.De, *Mechanism of intergranular corrosion of Al-Cu alloys.* Corrosion Science, 1970. **10**: p. 795-807.

32. Bohni, H., and Uhlig, H.H., *Environmental factors affecting the critical pitting potential of aluminium.* Journal of Electrochemical Society, 1969. **116**(7): p. 906-914.

33. Liu, Y., Thompson, G.E., Skeldon, P., Smith, C.J.E., and Shimizu, K., in *Aluminium Surface Science and Technology (ASST 2000)*. 2000: UMIST Manchester. p. 479.

34. Hagans, P.L., and Haas, C.M. , *Influence of metallurgy on the protective mechanism of chromium-based conversion coatings on aluminum-copper alloys.* Surface and Interface Analysis, 1994. **21**: p. 65-78.

35. Juffs, L., Hughes, A.E., Furman, S., and Paterson, P.J.K., *The use of macroscopic modelling of intermetallic phases in aluminium alloys in the study of ferricyanide accelerated chromate conversion coatings.* . Corrosion Science, 2002. **44**(8): p. 1755-1781.

36. McGovern, W.R., Schmutz, P., Buchheit, R.G., McCreery, R.L., *Formation of chromate conversion coatings on Al-Cu-Mg intermetallic compounds and alloys.* Journal of the Electrochemical Society, 2000. **147**(12): p. 4494-4501.

37. Vasquez, M.J., Halada, G.P., and Clayton, C. R., *The application of synchrotron-based spectroscopic techniques to the study of chromate conversion coatings* Electrochimica Acta, 2002. **47**(19): p. 3105-3115

38. Reboul, M.C., Warner, T.J., Mayet, H., and Baroux, B., *A ten-step mechanism for the pitting corrosion of aluminium*. Aluminium alloys their physical and mechanical properties 1996: Transtec publications. 1553-1558.

39. Elboujdaini, M., Ghali, E., Barradas, R.G., and Girgi, M., *An electrochemical investigation of the behaviour of aluminum alloys in different electrolytes* Corrosion Science, 1990. **30**(8-9): p. 855-867.

40. Pyun, S.-I., and Lee, E.-J., *Effect of Halide ion and applied potential on repassivation behaviour of Al-1wt.%Si-0.5wt.%Cu alloy.* Electrochimica Acta, 1995. **40**(12): p. 1963-1970.

41. Cabot, P.L., Garrido, J.A., Perez, E., Moreira, A.H., Sumodjo P.T.A., and Proud, W.G, *EIS study of heat-treated Al-Zn-Mg alloys in the passive and transpassive potential regions.* Electrochimica Acta, 1995. **40**(4): p. 447-454.

42. Kim, J.-D., and Pyun, S.-I, *Effects of electrolyte composition and applied potential on the repassivation kinetics of pure aluminium.* Electrochimica Acta, 1995. **40**(12): p. 1863-1869.

43. Nguyen, T.H., and Foley, R.T., *On the mechanism of pitting of aluminium.* Journal of Electrochemical Society, 1979. **126**(11): p. 1855-1860.

44. Moshier, W.C., Davis, G.D., Ahearn, J.S., and Hough, H.F., *Corrosion Behavior of Aluminum-Molybdenum Alloys in Chloride Solutions.* Journal of Electrochemical Society, 1987. **134**(11): p. 2677-2684

45. Blackwood, D.J., and Chong, A.S.L., *Pitting corrosion on aluminium in absence of chloride.* British Corrosion Journal, 1998. **33**(3): p. 219-224.

46. Arvin, C.L., Jiang, J., and Miller, A.E., *Corrosion inhibition of Al and Al alloys with permanganate solutions*, in *Corrosion 2001*. 2001, NACE International.

47. Brown, G.M., Shimizu, K., Kobayashi, K., Thompson, G.E., and Wood, G.C., *The development of chemical conversion coatings on aluminium* Corrosion Science, 1993. **35**(1-4): p. 253-256.

48. Thompson, G.E., *Corrosion and filming behaviour of aluminium and its alloys.* Material Science Forum 1996. **217-222**: p. 95-106.

49. Richards, J.W., *Aluminium: its history, occurence, properties, metallurgy and applications, including its alloys*. 1887, Philadelphia: Henry Carey Baird & CO.

50. Habashi, F., *Handbook of aluminium: alloy production and minerals* Alloy production and materials manufacturing ed. G.E. Totten, and Mackenzie, D.S. Vol. 2. 2003: Marcel Dekker, Inc. 1-45.

51. Sheasby, P.G., and Pinner, R., *The surface treatment of aluminium and its alloys*. 6th ed. Vol. 1. 2001: Finishing Publications Ltd.

52. Davis, J.R., ed. *Corrosion of aluminium and aluminium alloys*. 1999, ASM International. 1-43.

53. Hind, A.R., Bhargava, S.K., and Grocott, S.C., *The surface chemistry of Bayer process solids: a review* Colloids and Surfaces A: Physicochem. Eng, 1999. **146**: p. 359-374.

54. Sverdlin, A., *Handbook of aluminium: physical metallurgy and processes* Alloy production and materials manufacturing ed. G.E. Totten, and Mackenzie, D.S. Vol. 1. 2003: Marcel Dekker, Inc. p. 33-79.

55. Embury, J.D., *Strengthening mechanisms in Al alloys - an overview of natural limits and engineering possibilities.* Material Science Forum, 1996. **217-222**: p. 57-70.

56. Woodward, R. *Aluminium and Aluminium Alloys - Designations*. Materials Information Service 2001 [cited; Available from: http://www.azom.com/Details.asp?ArticleID=310.

57. Moshier, W.C., Davis, G.D., and Ahearn, J.S., *The corrosion and passitivity of aluminium exposed to dilute sodium sulfate solutions.* Corrosion Science, 1987. **27**(8): p. 785-801.

58. Saiz, E., Tomsia, A.P., and Suganuma, K., *Wetting and strength issues at Al/α-alumina interfaces.* Journal of European Ceramic Society, 2003. **23**: p. 2787-2796.

59. Sathiyakumar, M., and Gnanam, F.D., *Influence of additives on density, microstructure and mechanical properties of alumina.* Journal of Materials Processing Technology, 2003. **133**: p. 282-286.

60. Čička, R., Trnovcová, V., Yu, M., Starostin, and Bošák, O., *Microstructure and electrical properties of near-eutectic alumina-zirconia composites.* Journal of Optoelectronics and Advanced Materials, 2006. **8**(4): p. 1460-1465.

61. Nguyen, T.H., and Foley, R.T., *The chemical nature of aluminium corrosion III. The dissolution mechanism of aluminium and aluminium powder in various electrolytes.* Journal of Electrochemical Society, 1980. **127**: p. 2563-2566.

62. Feret, F.R., Roy, D., and Boulanger, C., *Determination of alpha and beta alumina in ceramic alumina by X-ray diffraction.* Spectrochimica Acta Part B: Atomic Spectroscopy, 2000. **55**(7): p. 1051-1061.

63. Alwitt, R.S., *Some physical and dielectric properties of hydrous alumina films.* Journal of Electrochemical Society, 1971. **118**(11): p. 1730-1733.

64. Hart, R.K., *The formation of films on aluminium immersed in water.* Transactions of the Faraday Society, 1957. **53**: p. 1020-1027.

65. Vedder, W., and Vermilyea, *Aluminium + water reaction.* Transactions of the Faraday Society, 1969. **65**: p. 561-584.

66. Alwitt, R.S., *The growth of hydrous oxide films on aluminium* Journal of Electrochemical Society, 1974. **121**(10): p. 1322-1328.

67. MacDonald, D.D., and Butler, P., *The thermodynamics of the aluminium-water system at elevated temperatures.* Corrosion Science, 1973. **13**: p. 259-274.

68. Mesmer, R.E., and Baes Jr., C.F., *Acidity measurements at elevated temperatures. V. Aluminium ion hydrolysis.* Inorganic Chemistry, 1971. **10**(10): p. 2290-2296.

69. MacDonald, D.D., Butler, P., and Owen, D., *Hydrothermal hydrolysis of Al^{3+} and the precipitation of boehmite from aqueous solution* Journal of Physical Chemistry, 1973. **77**(20): p. 2474-2479.

70. alumatter. *AluMatter. Materials Science and Engineering 2* 2006 [cited 21/09/2006]; Available from: http://aluminium.matter.org.uk/content/html/eng/default.asp?catid=4&pageid=-15045.

71. Osorio, W.R., Freire, C.M., and Gacia, A., *The role of macrostructural morphology and grain size on the corrosion resistance of Zn and Al castings.* Materials Science and Engineering 2005. **A 402**: p. 22-32.

72. Donelan, P., *Modelling microstructural and mechanical properties of ferritic ductile cast iron.* Materials Science and Technology, 2000. **16**: p. 261-269.

73. Santos, C.A., Quaresma, J.M.V. and Garcia A., *Determination of transient interfacial heat transfer coefficients in chill mold castings.* Journal of Alloys and Compounds 2001. **319**(1-2): p. 174-186.

74. Osorio, W.R., Santos, C.A., Quaresma, J.M.V., and Gacia, A., *Mechanical properties as a function of thermal parameters and microstructure of Zn-Al castings.* Journal of Material Processing Technology, 2003. **143**: p. 703-709.

75. Siqueira, C.A., Cheung, N., and Garcia, A., *Solidification thermal parameters affecting the columnar-to-equiaxed transistion.* Metallurgical and materials Transactions A, 2002. **33A**: p. 2107-2118.

76. Kurzydłowski, K.J., Ralph, B., Bucki, J.J., and Garbacz, A., *The grain boundary character distribution effect on the flow stress of polycrystals: the influence of crystal lattice texture.* Materials Science and Engineering, 1996. **A205**: p. 127-132.

77. Quaresma, J.M.V., Santos, C.A., and Garcia, A., *Correlation between unsteady-state solidification conditions, dendrite spacings, and mechanical properties of Al-Cu alloys.* Metallurgical and materials Transactions A, 2000. **31A**: p. 3167-3178.

78. Hall, E.O., *Yield point phenomena in metals and alloys*. 1970: Macmillian, London.

79. Hall, E.O., *The deformation and ageing of mild steel: III discussion of results.* Proceedings of the Physical Society. Section B, 1951. **64**(9): p. 747-752.

80. Henry, S., Minghetti,T., and Rappaz, M., *Dendrite growth morphologies in aluminium alloys.* Acta Materialia, 1998. **46**(18): p. 6431-6443.

81. Sieniawski, R., Filip, R., and Ziaja, W., *The effect of microstucture on the mechanical properties of two-phase titanium alloys.* Materials & Design, 1997. **18**(4/6): p. 361-363.

82. Mazzolani, F.M., *Aluminium alloy structures*. 2nd ed. 1995: E & FN Spon, London. p. 1-26.

83. Mathers, G., *The welding of aluminium and its alloys*. 2002: Woodhead Publishing Limited, Abington. p. 35-45.

84. Roberge, P.R. and *Handbook of corrosion engineering*. 2000, New York. : McGraw-Hill, Inc.

85. Nathan, C.C., *Corrosion inhibitors*. 1981, Philadelphia: Bertz Laboratories Inc. p. 240-242.

86. Vander Voort, G.F., *Analytical characterization of aluminium, steel, and superalloys*, ed. D.S. MacKenzie, and Totten, G.E. 2006: CRC Press, Taylor & Francis Group. p. 55-58.

87. De Graeve, I., and Hirsch, J. *AluMatter: Materials Science and Engineering - alloying*. [cited 21/09/2006]; Available from: http://aluminium.matter.org.uk/content/html/eng/default.asp?catid=214&pageid=2144417087.

88. Kaufman, J.G., *Introduction to aluminium alloys and tempers*. 2000: ASM International. p. 1-48.

89. DeJong, H.F., and Martens, J.H.M., *Investigation of the pitting potential of rapidly solidified aluminium-lithium alloys.* Aluminium, 1985. **61**(6): p. 416.

90. Niskanen, P., Sanders, T.H., Rinker Jr., J.G., and Marek, M., *Corrosion of aluminium alloys containing lithium.* Corrosion Science, 1982. **22**(4): p. 283-304.

91. Lifka, B.W., *Corrosion of aluminium and aluminium alloys*. Corrosion Engineering Handbook, ed. P.A. Schweitzer. 1996: Marcel Dekker, Inc. p. 99-155.

92. Zahavi, J., and Yahalom, J., *Exfoliation corrosion of AlMgSi alloys in water.* Journal of Electrochemical Society, 1982. **129**(6): p. 1181-1185.

93. Meng, Q., and Frankel, G.S. , *Effect of copper content on chromate conversion coating protection of 7xxx-T6 aluminium alloys.* Corrosion Science, 2004. **60**(10): p. 897-905.

94. Thompson, G.E., *Conversion coatings. 5202*, in *TALAT Lecture*. 1994, European Aluminium Association. p. 1-9.

95. Wloka, J., and Virtanen, S., *Microstructural effects on the corrosion behavior of high-Strength Al–Zn–Mg–Cu alloys in an overaged condition.* Journal of Electrochemical Society, 2007. **154**(8): p. C411-C423.

96. Burleigh, T.D., *Handbook of aluminium*. Alloy production and materials manufacturing ed. G.E. Totten, and Mackenzie, D.S. Vol. 2. 2003: Marcel Dekker, Inc. p. 421-463.

97. Lucas, K.A., and Clarke, H., *Corrosion of aluminium-based metal matrix composites*. 1993: Research Studies Ltd., Somerset England. p. 25-48.

98. Twite, R.L., and Bierwagen, G.P., *Review of alternatives to chromate for corrosion protection of aluminium aerospace alloys.* Progress in Organic Coatings, 1998. **33**: p. 91-100.

99. Moore, K.L., Sykes, J.M., and Grant, P.S., *An electrochemical study of repassivation of aluminium alloys with SEM examination of the pit interiors using resin replicas.* Corrosion Science, 2008. **50**: p. 3233-3240.

100. Szklarska-Smialowska, Z., *Pitting corrosion of aluminium.* Corrosion Science, 1999. **41**(9): p. 1743-1767.

101. Bocher, F., Flower, -H.M., and Ryan, M.P., *The effect of microstructure on localized corrosion in creep age-formable aluminium alloys: identification of intermetallic particles and pit initiation sites.* Journal of Electrochemical Society, 2006. **153**(12): p. B551-B554.

102. Mondolfo, L.F., *Aluminium alloys: structure and properties*. 1976: Butterworths. p. 120-150.

103. Dallek, S., and Foley, R.T., *Mechanism of pit initiation on aluminum alloy type 7075.* Journal of Electrochemical Society, 1976. **123**(12): p. 1775-1782.

104. Nguyen, T.H., and Foley, R.T., *Aluminium powder in various electrolytes.* Journal of Electrochemical Society, 1980. **127**(12): p. 2563-2566.

105. Wexler, S.B.d., and Galvele, J.R., *Anodic behavior of aluminium straining and a mechanism for pitting.* Journal of Electrochemical Society, 1974. **121**(10): p. 1271-1276.

106. Hœrlé, S., Malki, B., Baroux, B., *Corrosion current fluctuations at metastable to stable pitting transition of aluminium.* Journal of Electrochemical Society, 2006. **153**(12): p. B527-B532.

107. Barbucci, A., Bruzzone, G., Delucchi, M., Panizza, M., and Cerisola, G., *Breakdown of passivity of aluminium alloys by intermetallic phases in neutral chloride solution.* Intermetallics, 2000. **8**: p. 305-312.

108. Tomcsanyi, L., Varga, K., Bartik, I., Horanyi, G., and Maleczki, E., *Electrochemical study of the pitting corrosion of aluminium and its alloys - II. Study of the interaction of chloride ions with a passive film on aluminium and initiation of pitting corrosion.* Electrochimica Acta, 1989. **34**(6): p. 855-859.

109. Okada, T., *Pit nucleation originated by coupling of perturbations with local anodic sites on passive metals.* Electrochimica Acta, 1988. **33**(3): p. 389-395.

110. Bellinger, N.C., Komorowski, J.P., Liao, M., Carmody, D., Foland, T. and Peeler, D. . *Preliminary study into the effect of exfoliation corrosion on aircraft structural integrity*. in *6th Joint FAA/DoD/NASA Aging Aircraft Conference.* 2002.

111. Serna, L.M., Johnson, C.M., Wall, F.D., and Barbour, J.C., *Effect of implanted Cl and deposited oxides on the pitting behavior of aluminium.* Journal of Electrochemical Society, 2005. **152**(7): p. B244-B249.

112. Atanasoska, L.D., Drazic, D.M., Despic, A.R., Zalar, A., *Chlorine ion penetration into oxide films on aluminium Auger and XPS studies.* Journal of Electroanal. Chem., 1985. **182**: p. 179-186.

113. Sinyavskii, V.S., Ulanova, V.V. and Kalinin, V.D., *On the mechanism of intergranular corrosion of aluminium alloys.* Protection of Metals, 2004. **40**(5): p. 481-490.

114. Streicher, M.A., *Pitting corrosion of 18Cr-8Ni stainless steel.* Journal of Electrochemical Society, 1956. **103**(7): p. 375-390.

115. Monticelli, C., Brunoro, G., Frignani, A., and Trabanelli, G., *Evaluation of corrosion inhibitors by electrochemical noise analysis.* Journal of Electrochemical Society, 1992. **139**(3): p. 706-711.

116. Adams, A.A., Eagle, K. E., and Foley, R. T., *Synergistic effects of anions in the corrosion of aluminum alloys.* Journal of Electrochemical Society, 1972. **119**(12): p. 1692-1694

117. McKissick, A.M., Adams, Jr., A.A., and Foley, R.T., *Synergistic effects of anions in the corrosion of aluminum alloys.* Journal of Electrochemical Society, 1970. **117**(11): p. 1459-1460.

118. Fontana, M.G., *Corrosion Engineering*. 1986, New York: Mcgraw-Hill, Inc. 51-152, 236-238.

119. Gordard, H.P., Jepson, W.B., Bothwell, M.R., Kane, R.L., *The corrosion of light metals*. 1967: J. Wiley and Sons Inc., New York. p. 70-73.

120. Scully, J.C., *The fundamentals of corrosion* 3rd ed. 1990: Pergamon Press. p. 165-204.

121. Keddam, M., and Kuntz, C., Takenouti, H., Schuster, D., and Zuili, D., *Exfoliation corrosion of aluminium alloys examined by electrode impedance.* Electrochimica Acta, 1997. **42**(1): p. 87-97.

122. Liu, T.Y., Robinson, J. S., and McCarthy, M. A., *The influence of hot deformation on the exfoliation corrosion behaviour of aluminium alloy 2025.* Journal of Materials Processing Technology, 2004. **153-154**: p. 185-192.

123. Damborenea, J.D., Martín, I., *Electrochemical behaviour of aluminium alloys in exfoliation solution*. Progress in the understanding and prevention of corrosion, ed. J.M. Costa, and Mercer, A.D. Vol. 2. 1993, London: The Institute of Materials. 961-967.

124. Rudolph, E.F., *Corrosion on aircraft.* 1961.

125. Marsh, Z., Marsch, J. and Scantlebury, J.D., *Filiform corrosion of aluminium alloy 3003 H14 under humid and immersed conditions.* Journal of Corrosion Science and Engineering, 1999. **2**(36): p. 1-8.

126. Mol, J.M.C., Hinton, B.R.W., Van Der Weijde, D.H., De Wit, J.H.W., and Van Der Zwaag, S., *A filiform corrosion and potentiodynamic polarisation study of some aluminium alloys.* Journal of Materials Science, 2000. **35**: p. 1629-1639.

127. Leblanc, P.P., and Frankel, G.S., *Investigation of filiform corrosion of epoxy-coated 1045 carbon steel by scanning Kelvin probe force microscopy.* Journal of Electrochemical Society 2004. **151**(3): p. B105-B113.

128. LeBozec, N., Persson, D., Thierry, D. and Axelsen, S.B., *Effect of climatic parameters on filiform corrosion of coated aluminium alloys.* NACE, 2004. **60**(6): p. 584- 592.

129. Bautista, A., *Filiform corrosion in polymer-coated metals* Progress in Organic Coatings, 1996. **28**(1): p. 49-58.

130. Ruggeri, R.T., and Beck, T.R., *An analysis of mass transfer in filiform corrosion.* Corrosion, 1983. **39**(11): p. 452-465.

131. McMurray, H.N., Williams, G., O'Driscoll, S., *Chromate inhibition of filiform corrosion on organic coated AA2024-T3 studied using the Scanning Kelvin Probe.* Journal of Electrochemical Society, 2004. **151**(7): p. B406-B414.

132. de Wit, J.H.W., *New knowledge on localized corrosion obtained from local measuring techniques* Electrochimica Acta, 2001. **46**(24-25): p. 3641-3650.

133. Grundmeier, G., Schmidt, W., and Stratmann, M., *Corrosion protection by organic coatings: electrochemical mechanism and novel methods of investigation* Electrochimica Acta, 2000. **45**(15-16): p. 2515-2533.

134. Schmidt, W., and Stratmann, M., *Scanning kelvinprobe investigations of filiform corrosion on aluminum alloy 2024-t3* Corrosion Science, 1998. **40**(8): p. 1441-1443.

135. Kayes, A.J., Robinson, M.J. and Impey, S., *The influence of cleaning and surface treatment on filiform corrosion of aluminium alloys.* Journal of Corrosion Science Engineering 2: Extended abstract 1, 1999.

136. Leth-Olsen, H., and Nisancioglu, K., *Filiform corrosion of aluminium sheet. I. corrosion behaviour of painted material.* Corrosion Science, 1998. **40**(7): p. 1179-1194.

137. Afseth, A.N., J.H., Scamans, G.M, Nisancioglu, K., *Effect of heat treatment on filiform corrosion of aluminium alloy AA3005.* Corrosion Science, 2001. **43**(11): p. 2093-2109.

138. Afseth, A.N., J.H., Scamans, G.M, Nisancioglu, K., *Influence of heat treatment and surface conditioning on filiform corrosion of aluminium alloy AA3005 and AA5754.* Corrosion Science, 2001. **43**(12): p. 2359-2377.

139. Afseth, A.N., J.H., Scamans, G.M, Nisancioglu, K., *Effect of heat treatment on electrochemical behaviour of aluminium alloy AA3005.* Corrosion Science, 2002. **44**(1): p. 145-162.

140. Afseth, A.N., J.H., Scamans, G.M, Nisancioglu, K., *Filliform corrosion of AA3005 aluminium analogue model alloys.* Corrosion Science, 2002. **44**(11): p. 2543-2559.

141. Afseth, A.N., J.H., Scamans, G.M, Nisancioglu, K., *Effect of thermo-mechanical processingon filiform corrosion of aluminium alloy AA3005.* Corrosion Science, 2002. **44**(11): p. 2491-2506.

142. Ambat, R., Davenport, A.J., Afseth, A., and Scamans, G., *Electrochemical behaviour of active surface layer on rolled aluminium alloy sheet.* Journal of Electrochemical Society, 2004. **151**(2): p. B53-B58.

143. Nisancioglu, *Electrochemical Behavior of Aluminum-Base Intermetallics Containing Iron.* Journal of Electrochemical Society, 1990. **137**(1): p. 69-77.

144. Oldham, K.B., *Galvanic corrosion resulting from rupture of a protective metallic coating.* Journal of Applied electrochemistry, 1972. **2**: p. 183-191.

145. Craig, B.D., *Fundamental aspects of corrosion films in corrosion science*. 1991: Plenum Press, New York.

146. Oñoro, J., *Electrochemical behaviour of aluminium alloys in exfoliation solution*. Progress in the understanding and prevention of corrosion, ed. J.M. Costa, and Mercer, A.D. Vol. 2. 1993, London: The Institute of Materials. 1447-1452.

147. Davo, B., Conde, A., and Damborenea, J.de., *Stress corrosion cracking of B13, a new high strength aluminium lithium alloy.* Journal of Corrosion Science 2006.

148. Popović, M., and Romhanji, E. , *Stress corrosion cracking susceptibility of Al-Mg alloy sheet with high Mg Content.* Journal of Materials Processing Technology 2002. **125-126**: p. 275-280.

149. Xiaodong, L., and Frankel, G.S., *Effect of comprehensive stress on localised corrosion in AA 2024-T3.* Journal of Corrosion Science, 2006. **48**: p. 3309-3329.

150. Qiao, L., and Mao, X., *Thermodynamic analysis on the role of hydrogen in anodic stress corrosion cracking.* Acta Metallurgica et Materialia, 1995. **43**(11): p. 4001-4006.

151. Song, R.G., Dietzel, W., Zhang, B.J., Liu, W.J., Tseng, M.K. and Atrens, A., *Stress corrosion cracking snd hydrogen embrittlement of an Al-Zn-Mg-Cu alloy.* Acta Materialia 2004. **52**: p. 4727-4743.

152. Garcia-Vergara, S., Colin, F., Skeldon, P., Thompson, G.E., Bailey, P., Noakes, T.C.Q., Habazaki, H., and Shimizu, K., *Effect of copper enrichment on the electrochemical potential of binary Al-Cu alloys.* Journal of Electrochemical Society, 2004. **151**(1): p. B16-B21.

153. Buchheit, R.G., *A compilation of corrosion potentials reported for intermetallic phases in aluminium alloys.* Journal of Electrochemical Society, 1995. **142**(11): p. 3994-3996.

154. Dimogerontakis, T., Kompotiatis, L., and Kaplanoglou, I., *Oxygen evolution during the formation of barrier type anodic film on 2024-T3 aluminium alloy.* Corrosion Science, 1998. **40**(11): p. 1939-1951.

155. Campestrini, P., van Westing, E.P.M., van Rooijen, H.W., and de Wit, J.H.W., *Relation between microstructural aspects of AA2024 and its corrosion behaviour investigated using AFM scanning potential technique.* Corrosion Science, 2000. **42**(11): p. 1853-1861.

156. Idrac, J., Mankowski, G., Thompson, G., Skeldon, P., Kihn, Y., and Blanc, C., *Galvanic corrosion of aluminium-copper model alloys.* Electrochimica Acta, 2007. **52**: p. 7626-7633.

157. Duthil, J.-P., Mankowski, G., and Giusti, A., *The synergetic effect of chloride and sulphate on pitting corrosion of copper.* Corrosion Science, 1996. **38**(10): p. 1839-1849.

158. Mankowski, G., Duthil, J. P., and Giusti, A., *The pit morphology on copper in chloride- and sulphate-containing solutions.* Corrosion Science, 1997. **39**(1): p. 27-42.

159. Liu, Y., *Protection of aluminium 2014-T6 alloy by chromate species*, in *Corrosion and Protection Centre*. 2001, Ph.D Thesis, University of Manchester. p. 27-30.

160. Blanc, C., Lavelle, B., Mankowski, G., *The role of precipitates enriched with copper on the susceptibility to pitting corrosion of the 2024 aluminium alloy.* Corrosion Science, 1997. **39**(3): p. 495-510.

161. Kim, Y., and Buchheit, R.G., *A characterization of the inhibiting effect of Cu on metastable pitting in dilute Al-Cu solid solution alloys.* Electrochimica Acta, 2007. **52**: p. 2437-2446.

162. Böhni, H., Suter, T., and Schreyer, A., *Micro- and nanotechniques to study localized corrosion.* Electrochimica Acta, 1995. **40**(10): p. 1361-1368.

163. Dimitrov, N., Mann, J.A., Vukmirovic, M., and Sieradzki, K., *Dealloying of Al2CuMg in Alkaline Media.* Journal of Electrochemical Society, 2000. **147**(9): p. 3283-3285.

164. Hardwick, D.A., Thompson, A.W., and Bernstein, I.M., *The effect of copper content and microstructure on the hydrogen embrittlement of AI-6Zn-2Mg alloys.* Metallurgical and materials Transactions A, 1983. **14**(12): p. 2517-2526.

165. Meng, Q., and Frankel, G.S., *Effect of Cu content on corrosion behavior of 7xxx series aluminum alloys.* Journal of Electrochemical Society, 2004. **151**(5): p. B271-B283.

166. Sarkar, B., Marek, M., and Starke, E,A., *The effect of copper content and heat treatment on the stress corrosion characteristics of Ai-6Zn-2Mg-X Cu alloys.* Metallurgical and materials Transactions A, 1981. **12**(11): p. 1939-1943.

167. Scully, J.R., Peebles, D. E., Romig, A. D., Frear, D. R., and Hills, C. R., *Metallurgical factors influencing the corrosion of aluminum, Al-Cu, and Al-Si alloy thin films in dilute hydrofluoric solution.* Metallurgical and materials Transactions A, 1992. **23**(9): p. 2641-2655.

168. Suter, T., and Alkire, R.C., *Microelectrochemical studies of pit Initiation at single inclusions in Al 2024-T3.* Journal of Electrochemical Society, 2001. **148**(1): p. B36-B42.

169. Galvele, J.R., *Transport processes and the mechanism of pitting of metals.* Journal of Electrochemical Society, 1976. **123**(4): p. 464-474.

170. Muller, I.L., and Galvele, J.R., *Pitting potential of high purity binary aluminium alloys—II. Al-Mg and Al-Zn alloys.* Corrosion Science, 1977. **17**(12): p. 995-1007.

171. Ramgopal, T., and Frankel, G.S., *Role of alloying additions on the dissolution kinetics of aluminium binary alloys using artificial crevice electrodes.* Corrosion, 2001. **57**(8): p. 702-711.

172. Gorman, J.D., Johnson, S.T., Johnston, P.N., Paterson, P.J.K. and Hughes, A.E., *The characterisation of Ce-Mo-based conversion coatings on Al-alloys: part II.* Corrosion Science, 1996. **38**(11): p. 1977-1990.

173. Schmutz, P., and Frankel, G.S., *Corrosion study of AA2024-T3 by scanning kelving probe force microscopy and in situ atomic microscopy scratching.* Journal of Electrochemical Society, 1998. **145**(7): p. 2295-2306.

174. Leard, R.R., and Buchheit, R.G., *Electrochemical characterization of copper-bearing intermetallic compounds and localized corrosion of Al-Cu-Mg-Mn alloy 2024.* Material Science Forum, 2002. **396-402**: p. 1491-1496.

175. Zhang, W., Hurley, B. and Buchheit, R.G., *Characterization of chromate conversion coating formation and breakdown using electrode arrays.* Journal of The Electrochemical Society 2002. **149** (8): p. B357-B365.

176. Mazurkiewicz, B., and Piotrowski, A., *The electrochemical behaviour of the Al2Cu intermetallic compound.* Corrosion Science, 1983. **23**(7): p. 697-707.

177. Buchheit, R.G., Boger, R.K., Caroll, M.C., Leard, R.M., Paglia, C., and Searles, J.L., *The electrochemistry of Intermetallic particles and localised corrosion in Al alloys.* Journal of Metals, 2001. **53**(7): p. 29-33.

178. Kowal, K., Deluccia, J., Josefowicz, J.Y., Laird, C., and Farrington, G.C., *In situ atomic force microscopy observations of the corrosion behavior of aluminium-copper alloys.* Journal of Electrochemical Society, 1996. **143**(8): p. 2471-2481.

179. Osorio, W.R., Spinelli, J.E., Freire, C.M.A, Cardona, M.B., and Gacia, A. , *The role of Al_2Cu and of dendritic refinement on surface corrosion resistance of hypoeutectic Al-Cu alloys immersed in H_2SO_4.* Journal of Alloys and Compounds, 2007. **443**: p. 87-93.

180. Scully, J.R., Knight, T. O., Buchheit, R. G., Peebles, D. E., *Electrochemical characteristics of the Al_2Cu, Al_3Ta and Al_3Zr intermetallic phases and their relevancy to the localized corrosion of Al alloys.* Corrosion Science, 1993. **35**(1-4): p. 185-195.

181. Buchheit, R.G., *The electrochemistry of θ (Al_2Cu), S (Al_2CuMg) and T_1 (Al_2CuLi) and localised corrosion and environment assisted cracking in high strength Al alloys.* Material Science Forum, 2000 **331-337**: p. 1641-1646.

182. Buchheit, R.G., Martinez, M.A., and Montes, L.P., *Evidence for Cu ion formation by dissolution and dealloying the Al_2CuMg intermetallic compound in rotating ring-disk collection experiments.* Journal of Electrochemical Society, 2000. **147**(1): p. 119-124.

183. Obispo, H.M., Murr, L.E., Arrowood, R.M., and Trillo, E.A., *Copper deposition during the corrosion of aluminium alloy 2024 in sodium chloride solutions.* Journal of Materials Science, 2000. **35**: p. 3479-3495.

184. Annamalai, V., Hiskey, J. B., and Murr, L. E., *The effects of kinetic variables on the structure of copper deposits cemented on pure aluminum discs: A scanning electron microscopic study.* Hydrometallurgy, 1978. **3**(2): p. 163-180.

185. Annamalai, V., and Murr, L. E., *Effects of the source of chloride ion and surface corrosion patterns on the kinetics of the copper-aluminum cementation system.* Hydrometallurgy, 1978. **3**(3): p. 249-263.

186. Gao, M., Feng, C.R., and Wei, R.P., *An analytical electron microscopy study of constituent particles in commercial 7075-T6 and 2024-T3 alloys.* Metallurgical and Materials Transactions A, 1998. **29A**(4): p. 1145-1151.

187. Zhu, D., and van Ooij, W.J., *Corrosion protection of AA 2024-T3 by bis-[3-(triethoxysilyl)propyl]tetrasulfide in neutral sodium chloride solution. Part 1: corrosion of AA 2024-T3.* Corrosion Science, 2003. **45**(10): p. 2163-2175.

188. Blanc, C., Gastaud, S., and Mankowski, G., *Mechanistic studies of the corrosion of 2024 aluminium alloy in nitrate solutions.* Journal of Electrochemical Society, 2003. **150**(8): p. B396-B404.

189. Wei, R.P., Liao, C.-H., and Gao, M., *A transmission electron microscopy study of constituent-particle-induced corrosion in 7075-T6 and 2024-T3 aluminium alloys.* Metallurgical and Materials Transactions A, 1998. **29A**(4): p. 1153-1160.

190. Blanc, C., Freulon, A., Lafont, M.-C.,Kihn, Y., Mankowski, G., *Modelling the corrosion behaviour of Al2CuMg coarse particles in copper-rich aluminium alloys.* Corrosion Science, 2006. **48**(11): p. 3838-3851.

191. Schmutz, P., and Frankel, G.S., *Characterisation of AA2024-T3 by scanning kelving probe force microscopy.* Journal of Electrochemical Society, 1998. **145**(7): p. 2285-2295.

192. Seri, O., *The effect of NaCl concentration on the corrosion behavior of aluminum containing iron.* Corrosion Science, 1994. **36**(10): p. 1789-1803.

193. Zoeller, T.L., and Sanders Jr., T.H., *The rate of solidification and the effects of local composition on the subsequent nucleation of $Al_{20}Cu_2Mn_3$ phase in Al-4Cu-0.3Fe-0.4Mn-0.2Si alloys.* Journal of Physics IV, 2004. **120**: p. 61-68.

194. Guillaumin, V., and Mankowski, G., *Localized corrosion of 2024 T351 aluminium alloy in chloride media.* Corrosion Science, 1998. **41**(3): p. 421-438.

195. Chen, G.S., Gao, M., and Wei, R.P., *Microconstituent-induced pitting corrosion in aluminium alloy 2024-T3.* Corrosion, 1996. **52**(1): p. 8-15.

196. Goeminne, G., Terryn, H., and Vereecken, J., *Characterisation of conversion layers on aluminium by means of electrochemical impedance spectroscopy.* Electrochimica Acta 1995. **40**(4): p. 479-486.

197. Digby, R.P., and Packan, D.E. , *Pretreatment of aluminium: topography, surface chemistry and adhesive bond durability.* Int. Journal of Adhesion and Adhesives 1995. **15**: p. 61-71.

198. Bibber, J.W., *A chrome-free conversion coating and sealant for aluminium and its alloys.* Journal of Corrosion 1999(paper no 491).

199. Nordlien, J.H., Walmsley, J.C., Østerberg, H. and Nisancioglu, K., *Formation of a zirconium-titanium based conversion layer on AA 6060 aluminium.* Surface and Coatings Technology, 2002. **153**: p. 72-78.

200. Katzman, H.A., and Malouf, G.M., *Corrosion-protective chromate coatings on aluminium.* Applications of Surface Science, 1979. **2**: p. 416-432.

201. Textor, M., and Amstutz, M., *Surface analysis of thin films and interfaces in commercial aluminium products.* Analytica Chimica Acta, 1994. **297**: p. 15-26.

202. Leggat, R.B., Taylor, S.A. and Taylor, S.R., *Adhesion of epoxy to hydrotalcite conversion coatings: 1. Correlation with wettability and electrokinetic measurements.* Colloids and Surfaces A: Physicochem. Eng, 2002. **Aspect 210**: p. 69-81.

203. Hyland, M.M., *Surface chemistry of adhesion to aluminium*. Handbook of Aluminium: Alloy production and materials manufacturing, ed. G.E.a.M. Totten, D.S. Vol. 2. 2003: Marcel Dekker Inc., New York. p. 465-482.

204. De Wit, J.H.W., and Lenderink, H.J.W., *Electrochemical impedance spectroscopy as a tool to obtain mechanistic information on the passive behaviour of aluminium.* Electrochimica Acta, 1996. **41**(7/8): p. 1111-1119.

205. Clarke, W.J., and McCreery, R.L., *Inhibition of corrosion-related reduction processes via chromium monolayer formation.* Journal of Electrochemical Society, 2002. **149**(9): p. B379-B386.

206. Uhlig, H.H., *Adsorbed and reaction-product films on metals.* Journal of Electrochemical Society, 1950. **97**(11): p. 215C-220C.

207. Hamdy, A.S., Beccaria, A.M. and Traverso, P., *Corrosion protection of aluminium metal-matrix composites by cerium conversion coatings.* Surface and Interface Analysis 2002. **34**: p. 171-175.

208. Lunder, O., Walmsley, J.C., Mack, P. and Nisancioglu, K., *Formation and characterisation of a chromate conversion coating on AA6060 aluminium.* Corrosion Science 2005. **47**(7): p. 1604-1624.

209. Dabalà, M., Armelao, L., Buchberger, A. and Calliari, I., *Cerium-based conversion layers on layers on aluminium alloys.* Applied Surface Science, 2001. **172**(3-4): p. 312-322.

210. Leggat, R.B., Taylor, S.R. and Buchheit, R.G., *Corrosion performance of field-applied chromate conversion coatings.* NACE: Corrosion Engineering Section, 2002. **58**(3): p. 283-291.

211. Zhao, J., Xia, L., Sehgal, A., Lu, D., Mccreery, R.L. and Frankel, G.S., *Effects of chromate and chromate conversion coatings on corrosion of aluminium alloy 2024-T3.* Surface and Coatings Technology 2001. **140**: p. 51-57.

212. Kendig, M., Jeanjaquet, S., Addison, R. and Waldrop, J., *Role of hexavalent chromium in the inhibition of corrosion of aluminum alloys.* Surface and Coating Technology 2001. **140**(1): p. 58-66.

213. Campestrini, P., van Westing, E.P.M., and de Wit, J.H.W., *Influence of surface preparation on performance of chromate conversion coatings on Alcad 2024 aluminium alloy. Part I: Nucleation and growth.* Electrochimica Acta 2001. **46**: p. 2553-2571.

214. Bibber, J.W., *An overview of nonhexavalent chromium conversion coatings-Part 1: aluminium and its alloys.* Metal Finishing, 2001. **99**(12): p. 15-22.

215. Abd Rabbo, M.F., Richardson, J.A. and Wood, G.C., *A study of conversion coating development on aluminium in chromate/fluoride solutions using secondary ion mass spectrometry.* Corrosion Science, 1978. **18**: p. 117-123.

216. Asami, K., Oki, M., Thompson, G.E., Wood, G.C. and Ashworth, V., *Composition of the near surface regions of conversion coated aluminium.* Electrochimica Acta 1987. **32**(2): p. 337-343.

217. Lytle, F.W., Greegor, R.B., Bibbins, G.L., Blohowiak, K.Y., Smith, R.E. and Tuss, G.D., *An investigation of the structure and chemistry of a chromium-conversion surface layer on aluminium.* Corrosion Science 1995. **37**(3): p. 349-369.

218. Xia, L., and McCreery, R.L., *Chemistry of a chromate conversion coating on aluminium alloy AA2024-T3 probed by vibrational spectroscopy.* Journal of Electrochemical Society, 1998. **145**(9): p. 3083-3089.

219. Yu, Z., Ni, H., Zhang, G., and Wang, Y., *A study of the composition and structure of chromate conversion coating on aluminium.* Applied Surface Science 1992. **62**(217-221).

220. Xia, L., and McCreery, R.L., *Structure and function of ferricyanide in the formation of chromate conversion coatings on aluminium aircraft alloy.* Journal of Electrochemical Society 1999. **146**(10): p. 3696-3701.

221. Treverton, J.A., and Davies, N.C., *XPS studies of a ferricyanide accelerated chromate paint pretreatment film on an aluminium surface.* . Surface and Interface Analysis, 1981. **3**(2): p. 194-200.

222. Meng, Q., and Frankel, G.S., *Characterisation of chromate conversion coating on AA7075-T6 aluminium alloy.* Surface and Interface Analysis, 2004. **36**: p. 30-42.

223. Waldrop, J.R., and Kendig, M.W., *Nucleation of chromate conversion coating on aluminium 2024-T3 investigated by atomic force microscopy.* Journal of the Electrochemical Society, 1998. **145**(1): p. L11-L13.

224. Brown, G.M., and Kobayashi, K., *Nucleation and growth of a chromate conversion coating on aluminium alloy AA 2024-T3.* Journal of the Electrochemical Society, 2001. **148**(11): p. B457-B466.

225. Vasquez, M.J., Halada, G.P., and Clayton, C. R., and Longtin, J.P., *On the nature of the chromate conversion coating formed on intermetallic constituents of AA2024-T3.* Surface and Interface Analysis, 2002. **33**: p. 607-616.

226. Vasquez, M.J., Kearns, J.R., Halada, G.P., and Clayton, C. R., *Spatially resolved microchemical analysis of chromate-conversion-coated aluminium alloy AA2024-T3.* Surface and Interface Analysis, 2002. **33**: p. 796-806.

227. Baek, Y., and Frankel, G.S., *Electrochemical quartz crystal microbalance study of corrosion of phases in AA2024.* Journal of The Electrochemical Society, 2003. **150**(1): p. B1-B9.

228. Liu, Y., Skeldon, P., Thompson, G.E., Habazaki, H., and Shimizu, K., *Chromate conversion coatings on aluminium: influences of alloying.* Corrosion Science, 2004. **46**: p. 297-312.

229. Xia, L., Akiyama, E., Frankel, G., and McCreery, R., *Storage and release of soluble hexavalent chromium from chromate conversion coatings equilibrium aspects of CrVI concentration.* Journal of Electrochemical Society, 2000. **147**(7): p. 2556-2562.

230. Liu, Y., Skeldon, P., Thompson, G.E., Habazaki, H., and Shimizu, K., *Chromate conversion coatings on aluminium-copper alloys.* Corrosion Science, 2005. **47**(2): p. 341-354.

231. Schram, T., Goeminne, G., Terryn, H., and Vanhoolst, W., *Study of the composition of zirconium based chromium free conversion layers on aluminium.* Transactions of the Institute of Metal Finishing, 1995. **73**(3): p. 91-95.

232. Deck, P.D., Molly, M., and Sujdak, R.J., *Investigation of fluoacid based conversion coatings on aluminium.* Progress in Organic Coatings, 1998. **34**: p. 39-48.

233. Verdier, S., van der Laak, N., Dalard, F., Metson, J., and Delalande, S., *An electrochemical and SEM study of the mechanism of formation, morphology, and composition of titanium or zirconium fluoride-based coatings.* Surface and Coating Technology, 2006. **200**: p. 2955-2964.

234. Surviliene, S., Lisowska-Oleksiak, A., and Cesuniene, A., *Effect of ZrO_2 on corrosion behaviour of chromium coatings.* Corrosion Science, 2008. **50**: p. 338-344.

235. Lunder, O., Lapique, F., Johnsen, B., and Nisancioglu, K., *Effect of pre-treatment on the durability of epoxy-bonded AA6060 aluminium joints.* International Journal of Adhesion and Adhesives, 2004. **24**: p. 107-117.

236. Puomi, P., Fagerholm, H.M., Rosenholm, J.B. and Jyrkäs, K., *Comparison of different commercial pretreatment methods for hot-dip galvanised and Galfan coated steel.* Surface and Coatings Technology, 1999. **115**: p. 70-78.

237. Smit, M.A., Hunter, J.A., Sharman, J.D.B., Scamans, G.M. and Sykes, J.M., *Effect of organic additives on the performance of titanium-based conversion coatings.* Corrosion Science, 2003. **45**(9): p. 1903-1920.

238. Feliu, S., Galván, J.C., Feliu, S.Jr., Bastidas, J.M., Simancas, J., Morcillo, M. and Almeida, E.M., *An electrochemical impeadance study of the behaviour of some pretreatments applied to rusted steel surfaces.* Corrosion Science, 1993. **35**(5-8): p. 1351-1358.

239. Morcillo, M., Feliu, S., Simancas, J., Bastidas, J.M., Galvan, J.C., Feliu, S.Jr. and Almeida, E.M., *Corrosion of rusted steel in aqeous solutions of tannic acid.* Corrosion Engineering, 1992. **48**(12): p. 1032-1039.

240. Romero, M.A., Chabert, B., and Domard, A., *IR spectroscopy approach for the study of interactions between an oxidized aluminium surface and a poly (propylene-g-acrylic acid) film.* Journal of Applied Polymer Science 1993. **47**(3): p. 543-554.

241. Fedrizzi, L., Deflorian, F., and Bonora, P.L., *Corrosion behaviour of fluotitanate pretreated and painted aluminium sheets.* Electrochimica Acta 1997. **42**(6): p. 969-978.

242. Smit, M.A., Sykes, J.M., Hunter, J.A., Sharman, J.D.B. and Scamans, G.M., *Titanium based conversion coatings on aluminium alloy 3003.* Surface Engineering 1999. **15**(5): p. 407-410.

243. Danilidis, I., Sykes, J.M., Hunter, J.A. and Scamans, G.M., *Manganese based conversion treatment. 15(5):* . Surface Engineering, 1999. **15**(5): p. 401- 405.

244. Hamdy, A.S., and Beccaria, A.M., *Chrome-free pretreatment for aluminium composites.* Surface and Interface Analysis, 2002. **34**: p. 160-163.

245. Hughes, A.E., Gorman, J., Harvey, T.G., McCulloch, D., and Toh, S.K., *SEM and RBS characterisation of a cobalt-based conversion coating process on AA2024-T3 and AA7075-T6.* Surface and Interface Analysis, 2004. **36**: p. 1585-1591.

246. Haley, T.J., Komesu, N., Colvin, G., Koste, L., and Upham, H.C., *Pharmacology and toxicology of europium chloride.* Journal of Pharmaceutical Sciences, 1965. **54**(4): p. 643-645.

247. Campestrini, P., Terryn, H., Hovestad, A., and de Wit, J. H. W., *Formation of a cerium-based conversion coating on AA2024: relationship with the microstructure.* Surface and Coatings Technology, 2004. **176**(3): p. 365-381.

248. Arenas, M.A., Bethencourt, M., Botana, F. J., de Damborenea, J., and Marcos, M., *Inhibition of 5083 aluminium alloy and galvanised steel by lanthanide salts.* Corrosion Science, 2001. **43**(1): p. 157-170.

249. Hinton, B.R.W., *Corrosion inhibition with rare earth metal salts.* Journal of Alloys and Compounds, 1992. **180**: p. 15-25.

250. Davenport, A.J., Isaacs, H. S., and Kendig, M. W., *XANES investigation of the role of cerium compounds as corrosion inhibitors for aluminum.* Corrosion Science, 1991. **32**(5-6): p. 653-663.

251. Böhm, S., Greef, R., McMurray, H. N., Powell, S. M., and Worsley, D. A., *Kinetic and mechanistic studies of rare earth-rich protective film formation using in situ ellipsometry.* Journal of The Electrochemical Society, 2000. **147**(9): p. 3286-3293.

252. Aldykiewicz, A.J., Davenport, A.J. and Isaacs, H.S., *Studies of the formation of cerium-rich protective films using x-ray absorption near-edge spectroscopy and rotating disk electrode methods.* Journal of the Electrochemical Society 1996. **143**(1): p. 147-154.

253. Seon, F.M., *Rare earths for materials corrosion protection.* Journal of Less Common Metals, 1989. **148**: p. 73.

254. Hughes, A.E., Taylor, R.J., Hinton, B.R.W., and Wilson, L., *XPS and SEM characterization of hydrated cerium oxide conversion coatings.* Surface and Interface Analysis, 1995. **23**(7-8): p. 540-550.

255. Mansfeld, F., Wang, Y., and Shih, H., *The Ce---Mo process for the development of a stainless aluminum.* Electrochimica Acta, 1992. **37**(12): p. 2277-2282.

256. Mansfeld, F., and Wang, Y., *Development of "stainless" aluminum alloys by surface modification.* Materials Science and Engineering A, 1995. **198**(1-2): p. 51-61.

257. Wilson, L., Hinton, B.R.W., *A method of forming a corrosion resistant coating.* Patent WO 88/06639, 1988. .

258. Wang, C., Jiang, F., and Wang, F., *Cerium chemical conversion coating for aluminium alloy 2024-T3 and its corrosion resistance.* NACE: Corrosion Science Section, 2004. **60**(3): p. 237-243.

259. Online. 2006 [cited 2006 15/11/2006]]; Available from: http://es.epa.gov/ncer/sbir/success/pdf/environmentally.pdf.

260. EPA, *National Emission Standards for Hazardous Air Pollutants for Source Categories: Aerospace Manufacturing and Rework Facilities*, e.p.a. (EPA), Editor. 1995. p. 45947.

261. Xianglin, S., and Dalal, N.S., *Generation of hydroxyl radicals by chromate in biologically relevant systems: role of Cr(V) complexes versus tetraperoxochromate(V).* Environmental Health Perspectives, 1994. **102**(3): p. 231.

262. Skoog, D.A., Holler, F.J. and Nieman, T.A., *Principles of Instrumental Analysis*. 1998: Thompson Learning, Inc. .

263. Hensel, K.B., *Surface treatments: Electropolishing.* Metal Finishing, 1999. **97**(1): p. 440-448.

264. Caicedo-Martinez, C.E., Koroleva E.V., Thompson G.E., Skeldon P., Shimizu K., Habazaki H. and Hoellrigi G., *Surface nanotextures on aluminium.* Surface and Interface Analysis, 2002. **34**(1): p. 405-408.

265. Quintana, C., *Ultramicrotomy for cross-sections of nanostructure.* Micron 1997. **28**(3): p. 217-219.

266. Vastenhout, J.S.J., and Gnägi, H., *Ultramicrotomy of polymers using an oscillating diamond knife; improving polymer morphology.* Microscopy Microanalysis, 2002. **8**(Suppl. 2): p. 324-326.

267. Ericson, M.L., and Lindberg, H., *Design and potential of instrumented ultramicrotomy. 38(17):* . Polymer, 1997. **38**(17): p. 4485-4489.

268. Shimizu, K., Brown, G.M., Kobayashi, K., Skeldon, P., Thompson, G.E. and Wood, G.C., *Ultramicrotomy – a route towards the enhanced understanding of the corrosion and filming behaviour of aluminium and its alloys.* Corrosion Science 1998. **40**(7): p. 1049-1072.

269. Brown, G.M., Shimizu, K., Kobayashi, K., Thompson, G.E. and Wood, G.C., *The morphology, structure and mechanism of growth of chemical conversion coatings on aluminium.* Corrosion Science, 1992. **33**(9): p. 1371-1385.

270. Castle, J.E., and Zhdan, P.A., *Characterisation of surface topography by SEM and SFM: problems and solutions.* Journal physics. D: applied physics, 1997. **30**: p. 722-740.

271. Drzazga, W., Paluszynski, J., and Slowko, W., *Three-dimensional characterization of microstructures in a SEM.* Measurement Science and Technology, 2006. **17**: p. 28-31.

272. Sánchez, J., Fullea, J., Andrade, C., Gaitero, J.J., and Porro, A., *AFM study of the early corrosion of a high strength steel in a diluted sodium chloride solution.* Corrosion Science, 2008. **50**(7): p. 1820-1824.

273. West, P.E., *Introduction to atomic force microscopy*. 2007, Pacific Nanotechnology.

274. Wang, R., *An AFM and XPS study of corrosion caused by micro-liquid of dilute sulfuric acid on stainless steel.* Applied Surface Science, 2004. **227**(1-4): p. 399-409.

275. Martin, M.J., Calzada, M.L. and Mendiola, J., *Study by Rutherford Backscattering Spectroscopy of the heterostructure of lead titanate thin film* Journal of Sol-Gel Science and Technology 1998. **13**: p. 843-847.

276. Karl, H., Grosshans, I., Wenzel, A., Stritzker, B., Claessen, R., Strocov, V.N., Cirlin, G.E., Egorov, V.A., Polyakov, N.K., Samsonenko, Yu.B., Denisov, D.V., Ustinov, V.M. and Alferov, Zh.I., *Stoichiometry and absolute atomic concentration profiles obtained by combined Rutherford backscattering*

spectroscopy and secondary-ion mass spectroscopy: in As nanocrystals in Si. . Nanotechnology, 2002. **13**: p. 631-634.

277. Bubert, H., and Jenett, H., ed. *Surface and thin film analysis*. 2002, Wiley-VCH: Weinheim. p. 170-172.

278. Weiss, Z., *Emission yields and the standard model in glow discharge optical emission spectroscopy: Links to the underlying physics and analytical interpretation of the experimental data.* Spectrochimica Acta Part B: Atomic Spectroscopy, 2006. **61**(2): p. 121-133.

279. Weiss, Z., Steers, E.B.M., and Šmíd, P., *Excitation of zinc in a Grimm-type glow discharge: effects of hydrogen and other excitation-related matrix effects.* Journal of Analytical Atomic Spectrometry, 2005. **20**: p. 839-846.

280. Boumans, P.W.J.M., *Studies of sputtering in a glow discharge for spectrochemical analysis.* Journal of Analytical Chemistry, 1972. **44**: p. 1219-1228.

281. Wilken, L., Hoffmann, V., and Wetzig, K., *Erosion rate measurements for GD-OES.* Journal of Analytical Atomic Spectrometry, 2003. **18**(9): p. 1141-1145.

282. Klingenberg, C., and Jones, D., *What is salt spray (fog)? A detailed look at a common test.* Southern Metal Finishing, 2007. **5**(7): p. 1-5.

283. Liu, Y., and Cheng, Y.F., *Cathodic reaction kinetics and its implication on flow-assisted corrosion of aluminium alloy in aqueous ethylene glycol solution.* Journal of Applied electrochemistry, 2009. **39**: p. 1267-1272.

284. Kaiser, H., *Corrosion mechanisms*, ed. F. Mansfeld. 1987: Marcel Dekker Inc. p. 85.

285. Abd Rabbo, M.F., Wood, G.C., and Richardson, J.A., *A study of the interaction of oxide-coated aluminium with chloride solution using secondary ion mass spectrometry.* Corrosion Science, 1974. **14**: p. 645-650.

286. Richardson, J.A., and Wood, G.C., *A study of the pitting corrosion of Al by scanning electron microscopy.* Corrosion Science, 1970. **10**: p. 313-323.

287. Richardson, J.A., and Wood, G.C., *The interpretation of impedance changes on oxide-coated aluminium produced by immersion in inhibitive and corrosive aqueous media.* Journal of Electrochemical Society, 1973. **120**: p. 193-202.

288. Richardson, J.A., Wood, G.C., and Sutton, W.H., *The interpretation of impedance measurements on oxide-coated aluminium. Part 2. The effect of flaws in as-formed films.* Thin Solid Films, 1973. **16**: p. 99-116.

289. Mansfeld, F., Hengstenberg, D.H., and Kenkel, J.V., *Galvanic corrosion of Al alloys; I. effect of dissimilar metals.* Corrosion, 1974. **30**(10): p. 343-353.

290. Hollingsworth, E.H., and Hunsicker, H.Y., *Metals handbook.* 1987, ASM International, Metals Park, OH. p. 589.

291. Frankel, G.S., *Pitting corrosion of metals a review of the critical factors.* Journal of Electrochemical Society, 1998. **145**(6): p. 2186-2198.

292. Szklarska-Smialowska, Z., *Insight into the pitting behaviour of aluminium alloys.* Corrosion Science, 1992. **33**(8): p. 1193-1202.

293. Davis, G.D., Shaw, B.A., Rees, B.J., and Pecile, C.A., *Electrochemical behavior and surface chemistry of non-equilibrium aluminium-tantalum alloys: solute-rich interphase mechanism.* Surface and Interface Analysis, 1995. **23**: p. 609-617.

294. Frankel, G.S., Newman, R.C., Jahnes, C.V., and Russak, M.A., *On the pitting resistance of sputter-deposited aluminium alloys.* Journal of Electrochemical Society, 1993. **140**(8): p. 2192-2197.

295. Fin, N., Dodiuk, H., Yaniv, A. E., Drori, L., *Oxide treatments of Al 2024 for adhesive bonding- surface characterization.* Applied Surface Science, 1987. **28**(1): p. 11-33.

296. Sun, T.S., Chen, J. M., Venables, J. D., Hopping, R., *Effects of chemical and thermal treatments on the composition of 2024 aluminum adherend surfaces.* Applications Of Surface Science, 1978. **1**(2): p. 202-214.

297. Shimizu, K., Habazaki, H., Skeldon, P., Thompson, G. E., Wood, G. C., *GDOES depth profiling analysis of a thin surface film on aluminium.* Surface and Interface Analysis, 1999. **27**: p. 998-1002.

298. Furneaux, R.C., Thompson, G.E., and Wood, G.C., *An electronoptical study of the conversion coating formed on aluminium in a chromate/fluoride solution.* Corrosion Science, 1979. **19**: p. 63-71.

299. Pourbaix, M., *Atlas of electrochemical equilibria in aqueous solutions*. National association of corrosion engineers (NACE). 1974, Houston.

300. Newhard Jr., N.J., *Corrosion control coating*. Proceedings of corrosion control coating, ed. H. Leidheiser. 1979. p. 225.

301. Andreatta, F., Aldighieri, P., Paussa, L., Maggio, R.Di., Rossi, S., and Fedrizzi, L., *Electrochemical behaviour of ZrO_2 sol-gel pre-treatments on AA6060 aluminium alloy.* Electrochimica Acta, 2007. **52**: p. 7545-7555.